HAL open science

Finite element analysis of limit load and localized failure of structures

Jaka Dujc

To cite this version:

Jaka Dujc. Finite element analysis of limit load and localized failure of structures. Mechanics [physics.med-ph]. École normale supérieure de Cachan - ENS Cachan, 2010. English. NNT : . tel-00505153

HAL Id: tel-00505153

https://theses.hal.science/tel-00505153v1

Submitted on 22 Jul 2010

HAL is a multi-disciplinary open access archive for the deposit and dissemination of scientific research documents, whether they are published or not. The documents may come from teaching and research institutions in France or abroad, or from public or private research centers.

L'archive ouverte pluridisciplinaire **HAL**, est destinée au dépôt et à la diffusion de documents scientifiques de niveau recherche, publiés ou non, émanant des établissements d'enseignement et de recherche français ou étrangers, des laboratoires publics ou privés.

Univerza
v Ljubljani

Fakulteta za
gradbeništvo in
geodezijo

PODIPLOMSKI ŠTUDIJ
GRADBENIŠTVA

DOKTORSKI ŠTUDIJ

Kandidat:

JAKA DUJC, univ. dipl. inž. grad.

METODA KONČNIH ELEMENTOV ZA RAČUN MEJNE NOSILNOSTI IN LOKALIZIRANE PORUŠITVE PLOSKOVNIH KONSTRUKCIJ

Doktorska disertacija štev.: 200

FINITE ELEMENT ANALYSIS OF LIMIT LOAD AND LOCALIZED FAILURE OF STRUCTURES

Doctoral thesis No.: 200

Temo doktorske disertacije je odobrila Komisija za doktorski študij, po pooblastilu s 25. seje Senata Univerze v Ljubljani, dne 24. junija 2008 in imenovala mentorja izr.prof.dr. Boštjana Branka.

Ljubljana, 6. maj 2010

Univerza
v Ljubljani

Fakulteta za
gradbeništvo in
geodezijo

Komisijo za oceno ustreznosti teme doktorske disertacije v sestavi
izr.prof.dr. Boštjan Brank
izr.prof.dr. Jože Korelc
prof.dr. Miran Saje
prof.dr. Adnan Ibrahimbegović (ENS Francija)

je imenoval Senat Fakultete za gradbeništvo in geodezijo na 16. redni seji
dne 26. marca 2008.

Komisijo za oceno doktorske disertacije v sestavi
prof.dr. Miran Saje
izr.prof.dr. Jože Korelc
prof.dr. Delphine Brancherie, Universite de Technologie de Compiegne,
Compienge, Francija
prof.dr. Adnan Ibrahimbegović, Ecole Normale Superieure de Cachan,
Cachan, Francija

je imenoval Senat Fakultete za gradbeništvo in geodezijo na 8. redni seji
dne 24. februarja 2010.

Komisijo za zagovor doktorske disertacije v sestavi
prof.dr. Matjaž Mikoš, dekan UL FGG
izr.prof.dr. Boštjan Brank, mentor
prof.dr. Miran Saje
izr.prof.dr. Jože Korelc
prof.dr. Delphine Brancherie, Universite de Technologie de Compiegne,
Compienge, Francija
prof.dr. Adnan Ibrahimbegović, Ecole Normale Superieure de Cachan,
Cachan, Francija

je imenoval Senat Fakultete za gradbeništvo in geodezijo na 10. redni seji
dne 21. aprila 2010.

Univerza
v Ljubljani

Fakulteta za
gradbeništvo in
geodezijo

IZJAVA O AVTORSTVU

Podpisani **JAKA DUJC, univ. dipl. inž. grad.,** izjavljam, da sem avtor doktorske disertacije z naslovom: **»METODA KONČNIH ELEMENTOV ZA RAČUN MEJNE NOSILNOSTI IN LOKALIZIRANE PORUŠITVE PLOSKOVNIH KONSTRUKCIJ«.**

Ljubljana, 6. maj 2010

……..
(podpis)

BIBLIOGRAFSKO-DOKUMENTACIJSKA STRAN

UDK	**519.63:624.073(043.3)**
Avtor:	**Jaka Dujc**
Mentor:	**izr. prof. dr. Boštjan Brank**
Somentor:	**prof. dr. Adnan Ibrahimbegovic**
Naslov:	**Metoda končnih elementov za račun mejne nosilnosti in lokalizirane porušitve ploskovnih konstrukcij**
Obseg in oprema:	**211 str., 6 pregl., 100 sl., 429 en.**
Ključne besede:	**konstrukcije, metoda končnih elementov, armirani beton, jeklo, rezultante napetosti, elastoplastičnost, lokalna porušitev, vključena nezveznost**

Izvleček
V delu obravnavamo račun mejne nosilnosti in mejne duktilnosti konstrukcij z metodo končnih elementov. Ko je konstrukcija na meji svoje nosilnosti, so nekateri njeni deli v neelastičnem stanju, v najbolj kritičnih konstrukcijskih elementih pa se pojavi lokalizirana porušitev materiala, ki je povezana s koncentracijo neelastičnih deformacij na majhnem območju. Pri krhkih materialih predstavlja lokalizirano porušitev nastanek in razvoj večje razpoke, pri duktilnih materialih pa nastanek lokaliziranega nestabilnega plastičnega območja. Zato je račun mejne nosilnosti povezan tako z modeliranjem standardnih neelastičnih materialnih efektov, kot tudi z modeliranjem lokalizacijskih efektov v materialu, ki se jih pogosto označuje kot mehčanje materiala. V tem delu za modeliranje standardnih neelastičnih materialnih efektov izpeljemo in uporabljamo elastoplastične materialne modele, dotaknemo pa se tudi elastoviskoplastičnega materialnega modela za plošče in nelinearnega materialnega modela za armiranobetonske plošče. Skupno vsem izpeljanim in uporabljenim neelastičnim modelom je, da so definirani na nivoju rezultant napetosti. Za modeliranje pojava lokalizacij v materialu obstajajo različni matematični modeli in numerični algoritmi, ki pa so pogosto premalo natančni ali premalo učinkoviti. Zato v tem delu uporabimo novejšo metodo, ki temelji na končnih elementih z nezveznimi pomiki znotraj končnega elementa. Dokažemo, da je mogoče v okviru te metode izpeljati tudi kompleksnejše končne elemente - kompleksnejše tako v smislu zahtevnejše kinematike samega osnovnega modela, kot v smislu kompleksnejše aproksimacije nezveznih pomikov. Razvijemo več končnih elementov za račun različnih konstrukcijskih elementov. Najprej je predstavljen nelinearni končni element za račun mejne nosilnosti armiranobetonskih plošč, nato pa končni element za neelastično analizo kovinskih plošč, ki temelji na elastoplastičnem in elastoviskoplastičnem materialnem modelu z izotropnim in kinematičnim utrjevanjem. Pri slednjem izpeljemo računski algoritem, ki hkrati zajame obe neeleastični formulaciji. Nadalje izpeljemo končni element za kovinske lupine z elastoplastičnim materialnim modelom z izotropnim in kinematičnim utrjevanjem, ki temelji na rezultantah napetosti in na kriteriju plastičnega tečenja, ki ga določata dve ploskvi. Zadnja dva izpeljana končna elementa sta namenjena modeliranju lokalizirane porušitve materiala v nosilcih in ravninskih telesih. Elastoplastični končni element za Euler-Bernoullijeve nosilce ima vključeno nezveznost v rotacijah, njegovi konstitutivni parametri pa so določeni s posebnim postopkom, ki temelji na predhodni nelinearni analizi izbranega dela nosilca s podrobnejšim modelom. Zadnji izpeljani končni element je elastoplastični štirivozliščni končni element za ravninska telesa, ki ima vključene nezveznosti v pomikih. Kinematika nezveznosti je takšna, da omogoča linearne nezvezne skoke v pomikih tako v smeri normale, kot tudi v smeri tangente na črto nezveznosti. Numerični primeri dokazujejo, da je mogoče z izpeljanimi končnimi elementi in s pripadajočimi algoritmi učinkovito in na dokaj robusten način izračunati tako mejno nosilnost konstrukcije, kot simulirati popolno porušitev konstrukcije. Med drugim je predstavljen primer računa nastanka in širjenje razpoke v krhkem materialu in primer strižne porušitve v duktilnem materialu. Vse računalniške kode za izpeljane končne elemente so bile pripravljene v programskem okolju AceGen, ki omogoča razvoj programske kode v simbolnem zapisu in optimizacijo generirane kode. Numerični primeri so bili izračunani v programskem okolju AceFem.

BIBLIOGRAPHIC-DOCUMENTARY INFORMATION

UDC	**519.63:624.073(043.3)**
Author:	**Jaka Dujc**
Supervisor:	**assoc. prof. Boštjan Brank**
Co-supervisor:	**prof. Adnan Ibrahimbegovic**
Title:	**Finite element analysis of limit load and localized failure of structures**
Notes:	**211 p., 6 tab., 100 fig., 429 eq.**
Key words:	**structures, finite element method, reinforced concrete, steel, stress resultants, elastoplasticity, localized failure, embedded discontinuity**

Abstract
The dissertation deals with limit load and limit ductility analysis of structures by the finite element method. When structure is at its limit load, several structural components behave inelastically, while in the critical parts of the structure, due to localization of inelastic strains, failure of material appears. Localized effects in brittle materials are related to appearance and formation of a large (macro) crack, while failure in ductile materials is governed by localized shear bands. The study of limit load is thus related to modeling both standard inelastic material effects, as well as modeling of localized failure of material, often reffered to as material softening. Standard inelastic material effects are in this work described with elastoplastic, elastoviscoplastic and nonlinear elastic material models. All the material models are defined at the level of stress-resultants. Several mathematical approaches and numerical algorithms for modeling localized effects are at hand, but they are often inefficient or inaccurate. Therefor, we use an up-to-date approach, based on a finite element method with embedded discontinuity. We derive new finite element formulations with a quite complex kinematics of the basic elements, as well as rather complex description of discontinuous displacement fields. We derived several finite element formulations for analysis of different structural components. First we present a finite element for limit load analysis of reinforced concrete plates. Stress-resultant elastoplastic and elastoviscoplastic plate finite element formulation along with a unified computational procedure that covers both formulations are presented next. Further, a nonlinear shell finite element, based on a two-surface yield function, that includes both isotropic and kinematic material hardening is presented. The last two finite elements derived in this work are intended to model the localized failure in planar beams and 2D solids. The embedded discontinuity in rotations was built into elastoplastic Euler-Bernoulli beam finite element, and a procedure, based on a precomputed analysis of a part of a structure, by using a refined numerical model, is proposed to obtain the beam constitutive model parameters. Finally, we derive an elastoplastic quadrilateral two-dimensional finite element formulation with embedded strong discontinuity, whose kinematics can model linear jumps in both normal and tangential displacements along the discontinuity line. Numerical simulations show, that the derived finite elements, along with the accompanied numerical algorithms, are an efficient and a rather robust tool for limit load and failure analysis of structures. Among other examples, we present a simulation of crack growth in brittle material and a simulation of shear band failure in ductile material. All the computer codes of the finite element formulations presented in this work have been generated through the symbolic programming of the finite element computer code and the expression optimization in AceGen computer program. The performance of these elements has been presented in numerous numerical examples, all performed by the AceFem computer program.

INFORMATION BIBLIOGRAPHIQUE-DOCUMENTAIRE

CDU	**519.63:624.073(043.3)**
Auteur:	**Jaka Dujc**
Directeur de thèse:	**prof. Boštjan Brank**
Co-directeur de thèse:	**prof. Adnan Ibrahimbegovic**
Titre:	**Analyse Éléments Finis de la charge limite et de la rupture localisée des structures**
Notes:	**211 p., 6 tab., 100 fig., 429 éq.**
Mots clés:	**structures, méthode éléments finis, béton armé, acier, efforts généralisés, elastoplasticité, rupture localisée, enrichissement discontinu**

Résumé
Ce travail a pour objet l'analyse limite des structures par la méthode des éléments finis. Lorsqu'une structure atteint sa charge limite, certaines de ses composantes sont dans la phase inélastique de leur comportement, alors que dans les parties les plus critiques, du fait de la localisation des déformations inélastiques, se produit la rupture du matériau. Les effets de localisation sont, dans les matériaux fragiles liés à l'apparition et au développement de macro fissures alors qu'ils sont, dans les matériaux ductiles, gouvernés par les bandes de cisaillement localisées. L'étude de la charge limite est ainsi reliée à la modélisation du comportement inélastique standard du matériau mais également à la modélisation des effets localisés correspondant au comportement adoucissant des matériaux. Le comportement inélastique standard du matériau est, dans ce travail, décrit par des modèles élastoplastiques, élastoviscoplastiques ou élastiques non linéaires. Tous les modèles de comportement sont définis en termes d'efforts généralisés. Un certain nombre d'approches mathématiques et d'algorithmes numériques sont disponibles mais sont bien souvent inefficaces et manquent de précision. Ainsi, nous utilisons une approche développée plus récemment s'appuyant sur une méthode d'éléments finis enrichis de discontinuités. Nous avons développé de nouvelles formulations d'éléments standards prenant en compte des cinématiques et des descriptions des champs de déplacements discontinus complexes. Plusieurs formulations d'éléments finis ont été développées pour l'analyse de différents composants structurels. Nous présentons, dans un premier temps, un élément fini dédié à l'analyse limite des plaques en béton armé. La formulation d'un élément de plaque élastoplastique et élastoviscoplastique écrite en efforts généralisés associée à une procédure commune d'intégration sont présentées ensuite. Un élément de coque non linéaire, faisant intervenir une fonction seuil à deux surfaces incluant à la fois un écrouissage isotrope et un écrouissage cinématique est ensuite présenté. Les deux derniers éléments finis développés dans ce travail sont dédiés à la modélisation de la rupture localisée dans les poutres planes et les solides bidimensionnels. L'élément de poutre d'Euler-Bernouilli est enrichi par une discontinuité en rotation. Une stratégie s'appuyant sur l'analyse préalable, par un modèle raffiné, d'une partie de la structure est proposée afin d'obtenir les paramètres du modèle constitutif de la poutre. Enfin, nous présentons la formulation d'un élément quadrangulaire à discontinuité forte dont la cinématique permet de prendre en compte des sauts de déplacements linéaires dans les deux directions normale et tangentielle le long de la surface de discontinuité. Des résultats numériques montrent que les éléments développés ainsi que les algorithmes associés constituent un outil efficace et robuste d'analyse de la charge limite et de la rupture des structures. Parmi les exemples, nous présentons la simulation de la propagation d'une fissure dans un matériau fragile ainsi que le développement d'une bande de cisaillement dans un matériau ductile. Les codes numériques associés aux formulations présentées dans ce travail ont été générés par l'outil de programmation symbolique et d'optimisation de code AceGen. Les performances des éléments sont présentés à travers un grand nombre d'exemples numériques réalisés à partir du code AceFem.

ZAHVALA

Za pomoč pri pripravi doktorske disertacije se zahvaljujem izr. prof. Boštjanu Branku in prof. Adnanu Ibrahimbegoviću. Vajina vrata so mi bila vedno odprta, tudi ko ni šlo za reševanje strokovnih težav.

Posebna zahvala gre moji mami Silvestri in sestri Jerneji, ki sta mi vedno nudili podporo. Z besedami ne morem opisati, kako sem vama hvaležen.

Za podporo med študijem in številne nepozabne trenutke se iskreno zahvaljujem Ireni, Jožetu, Primožu, Urošu in Vidi.

Tekom študija sem se družil z veliko ljudmi, zaradi katerih sta bila delo na fakulteti in vsakdan prijetna in zanimiva. Seznam ljudi, katerim bi se rad zahvalil, je predolg, da bi ga lahko napisal na to stran. Moram pa izpostaviti Miho, Mateja in Vasjo, ki so mi nudili podporo, ko sem jo najbolj potreboval.

Zahvalil bi se tudi DDC svetovanje inženiring d.o.o, katerega štipendist sem bil v času dodiplomskega študija.

Na koncu bi se rad zahvalil še kolegom iz dodiplomskega študija, katere sem pri hitri izdelavi diplomske naloge nenamerno izpustil. Gorazd, Jernej, Marko, Matija, Uroš in že prej omenjena Miha in Vasja, hvala za nepozabna doživetja in druženje tekom dodiplomskega študija in v letih po njem. Vesel sem, da smo kljub geografskim razdaljam ohranili stike in da na sedaj že tradicionalnih srečanjih negujemo prijateljstva.

Contents

1 Introduction **1**
1.1 Motivation . . . 1
1.2 Background . . . 3
1.2.1 Limit load analysis . . . 3
1.2.2 Failure analysis . . . 5
1.3 Goals of the thesis . . . 7
1.4 Outline of the thesis . . . 8

2 Limit load analysis of reinforced concrete plates **11**
2.1 Introduction . . . 11
2.2 Constitutive model for reinforced concrete plates . . . 12
2.2.1 Basic idea . . . 12
2.2.2 Moment curvature relationship . . . 14
2.3 Isotropic and anisotropic reinforcement . . . 17
2.3.1 Isotropic reinforcement . . . 17
2.3.2 Anisotropic reinforcement . . . 18
2.4 Numerical examples . . . 21
2.4.1 Rectangular simply supported plate with anisotropic reinforcement 21
2.4.2 Simply supported square plate with anisotropic reinforcement . . . 22
2.4.3 Circular clamped plate with isotropic reinforcement . . . 23
2.4.4 Plate with two free edges . . . 23
2.4.5 Square plate with point supports in the corners . . . 24
2.5 Concluding remarks and chapter summary . . . 26

3 Inelastic analysis of metal plates **29**
3.1 Introduction . . . 29
3.2 Inelastic plate models . . . 29
3.2.1 Plate elastoplasticity . . . 31
3.2.2 Plate elastoviscoplasticity . . . 34

3.3 Finite element formulation 35
3.3.1 Space discretization 35
3.3.2 Computational issues for plasticity 38
3.3.3 Computational issues for viscoplasticity 41
3.4 Numerical examples 41
3.4.1 Limit load analysis of a rectangular plate 41
3.4.2 Limit load analysis of a circular plate 42
3.4.3 Elastoplastic analysis of a skew plate 47
3.4.4 Cyclic analysis of a circular plate 48
3.4.5 Elastoviscoplastic analysis of a circular plate 50
3.5 Concluding remarks and chapter summary 50

4 Inelastic analysis of metal shells 53
4.1 Introduction 53
4.2 Inelastic geometrically exact shell formulation 53
4.2.1 Geometry, kinematics and strains 54
4.2.2 Variational formulation 57
4.2.3 Stress-resultant constitutive equations for elastoplasticity 59
4.3 Finite element formulation 62
4.3.1 Space-domain discretization 62
4.3.2 Computational issues for plasticity 63
4.4 Numerical examples 73
4.4.1 Pinched cylinder with isotropic hardening 74
4.4.2 Half of a sphere 76
4.4.3 Limit load analysis of a rectangular plate 76
4.5 Concluding remarks and chapter summary 79

5 Illustration of embedded discontinuity concept for failure analysis 81
5.1 Introduction 81
5.2 1D finite element with embedded discontinuity 82
5.3 Computational procedure for failure analysis 90
5.4 Numerical examples 93
5.4.1 Tension test of a bar 94
5.4.2 Tension test of four parallel bars 95
5.5 Concluding remarks and chapter summary 96

6 Failure analysis of metal beams and frames 99
6.1 Introduction . . . 99
6.2 Beam element with embedded discontinuity . . . 101
6.2.1 Kinematics . . . 101
6.2.2 Equilibrium equations . . . 105
6.2.3 Constitutive relations . . . 106
6.3 Computation of beam plasticity material parameters . . . 110
6.4 Computational procedure . . . 114
6.5 Examples . . . 117
6.5.1 Computation of beam plasticity material parameters . . . 118
6.5.2 Push-over of a symmetric frame . . . 123
6.5.3 Push-over of an asymmetric frame . . . 125
6.5.4 Bending of beam under constant axial force . . . 127
6.5.5 Collapse of a simple frame . . . 129
6.5.6 Darvall-Mendis frame . . . 130
6.6 Concluding remarks and chapter summary . . . 135

7 Failure analysis of 2D solids 141
7.1 Introduction . . . 141
7.2 Family of ED elements for planar problems . . . 141
7.2.1 Kinematics . . . 142
7.2.2 Equilibrium equations . . . 147
7.2.3 Constitutive relations . . . 150
7.3 Computational procedure . . . 153
7.4 Examples . . . 159
7.4.1 Tension test . . . 159
7.4.2 Bending test . . . 161
7.4.3 Partial tension test . . . 161
7.4.4 Three point bending test . . . 162
7.4.5 Four point bending test . . . 166
7.4.6 Delamination . . . 168
7.4.7 Elasto-plastic tension test . . . 170
7.5 Concluding remarks and chapter summary . . . 173

8 Conclusion 177

Razširjeni povzetek 181

Bibliography **205**

List of Figures

2.1 Positive directions of the transverse displacement and rotations of the plate 12
2.2 Face with tensial stresses (darkened) caused by the positive bending moments 13
2.3 Moment curvature relationship for the principal direction 14
2.4 Layers of reinforcement and the effective area of the reinforcement in the principal direction 15
2.5 Equilibrium in the cross-section of the plate 16
2.6 Directions of the principal curvatures and the principal moments 18
2.7 Rectangular plate with anisotropic reinforcement under distributed load . . 22
2.8 Simply supported square plate with anisotropic reinforcement 23
2.9 Coarse (left) and fine (right) mesh of the circular plate 24
2.10 Load versus center displacement diagrams for circular plate 25
2.11 Geometry and loading of the plate with two free edges 25
2.12 Bending moment versus displacement at the center curves 25
2.13 Force versus displacement diagram for the square plate 26

3.1 Notation of the used finite element 36
3.2 Load - displacement diagram for simply supported rectangular plate 42
3.3 Load - displacement diagram for clamped rectangular plate 43
3.4 Load - displacement diagram for simply supported rectangular plate; α parameter case 43
3.5 Load - displacement diagram for clamped rectangular plate; α parameter case 44
3.6 Meshes used for: (a) rectangular plate - fine, (b) rectangular plate - coarse, (c) circular plate - fine and (d) circular plate - coarse 45
3.7 Simply supported circular plate - limit load analysis 45
3.8 Clamped circular plate - limit load analysis 46
3.9 Skew plate - (a) fine mesh, (b) coarse mesh 47
3.10 Skew plate - elastoplastic analysis 47
3.11 Spreading of plastic zones 48

3.12 Clamped circular plate - cyclic load 49
3.13 Loading curve for viscoplastic analyses 50
3.14 Time response for force-prescribed viscoplastic circular plate 51
3.15 Time response for displacement-prescribed viscoplastic circular plate 51

4.1 A sketch of a two-surface yield function 60
4.2 A sketch of a two-surface yield function and the closest point projection . . 69
4.3 Geometry, loading and boundary conditions for pinched cylinder 74
4.4 Load versus displacement curves for pinched cylinder 75
4.5 Initial and deformed configuration for pinched cylinder 75
4.6 Geometry, loading and boundary conditions of half of a sphere 76
4.7 Load versus displacement curves for half of a sphere 77
4.8 Initial, deformed fully loaded and deformed unloaded configuration for half of a sphere 77
4.9 Geometry for rectangular plate 78
4.10 Load versus displacement curves for the thin plate 78
4.11 Load versus displacement curves of the thick plate 79

5.1 Tension test of an idealized bar 81
5.2 Standard isoparametric 1d solid finite element 83
5.3 Isoparametric 1d solid finite element with embedded discontinuity 84
5.4 Strain distribution 85
5.5 Cohesive law at the discontinuity 88
5.6 One point numerical integration scheme 90
5.7 Tension test of one bar 94
5.8 Reaction force versus imposed displacement curve 94
5.9 Tension test of four parallel bars 95
5.10 Reaction versus imposed displacement of structure (left) and structural components (right) 96

6.1 Beam finite element with embedded discontinuity 101
6.2 Strain-free mode of the element 103
6.3 Rigid-plastic cohesive law at discontinuity 107
6.4 Evaluation of beam material parameters by using results of refined analysis 112
6.5 Uniaxial stress - strain curve 119
6.6 Boundary conditions for the shell model analysis 119
6.7 Failure mode of the representative part of the frame member as computed by the shell model 120

6.8 Bending moment versus rotation curves for the end cross-section 120
6.9 Plastic work versus end cross-section rotation curves 121
6.10 Approximation of the ultimate bending moment of the cross-section 122
6.11 Symmetric frame: geometry and loading 124
6.12 Load versus displacement and dissipated energy versus displacement curves for symmetric frame 124
6.13 Symmetric frame: deformed shape and locations of softening plastic hinges at $u_{top} \approx 60$ cm 125
6.14 Asymmetric frame: geometry and loading 126
6.15 Load versus displacement and dissipated energy versus displacement curves for asymmetric frame 126
6.16 Asymmetric frame: Deformed shape and locations of softening plastic hinges 127
6.17 Comparison of results for the bending of the beam under compressive axial force 128
6.18 Simple frame: the beam and the shell model 130
6.19 Comparison of results for simple frame example 131
6.20 Deformed shapes of the simple frame 131
6.21 Internal forces at the right support of the shell model 132
6.22 Geometry and loading of the portal frame. 133
6.23 Vertical load versus vertical deflection curves 134

7.1 Quadrilateral finite element with embedded discontinuity 142
7.2 Different element separation modes 144
7.3 Neighborhood of a point of interest at the discontinuity Γ^e 151
7.4 Numerical integration scheme 153
7.5 Rigid-plastic cohesive law with linear softening in tension 159
7.6 Tension test on a square block 160
7.7 Reaction force versus imposed displacement curves 160
7.8 Geometry of the bending test of the square block and the imposed displacement versus pseudo-time curves 161
7.9 Top reaction force versus imposed top displacement curves 162
7.10 Partial tension test of the square block 163
7.11 Stress at integration points in Ω^+ and Ω^- region versus imposed displacement curves 163
7.12 Three point bending test of a notched concrete beam 164
7.13 Rigid-plastic cohesive law with exponential softening in tension 164

7.14 Coarse (top) and fine (bottom) finite element meshes for the three point bending test . . . 165
7.15 Reaction force versus imposed displacement curves and scaled (100 times) deformed meshes . . . 165
7.16 Four point bending test . . . 166
7.17 Finite element mesh for the four point bending test . . . 167
7.18 Load versus crack mouth sliding displacement curves and the corresponding crack paths . . . 167
7.19 Scaled deformed mesh of the "n0 + m0" (left), "n0 + n1" (middle) and "n0" formulation . . . 168
7.20 Delamination test data . . . 169
7.21 Coarse (top) and fine (bottom) finite element meshes for the delamination test . . . 169
7.22 Reaction force versus imposed displacement diagram . . . 170
7.23 Deformed configuration of the coarse (left) and fine (right) mesh . . . 171
7.24 Tension test of a metal strip . . . 171
7.25 Rigid-plastic cohesive law with linear softening . . . 171
7.26 Total reaction force versus imposed displacement curves . . . 172
7.27 Discontinuity paths for several mesh sizes . . . 172
7.28 Scaled deformed configurations . . . 173

List of Tables

3.1 Limit load solutions for circular simply supported plate 44
3.2 Limit load solutions for circular clamped plate 46

5.1 The convegrence results 95

6.1 Summary of results of the shell model analyses 121
6.2 Comparison between approximations and shell analyses results 123
6.3 Comparison of the presented formulation with the literature 135

Chapter 1

Introduction

The objective of the first chapter is to motivate the reader and to outline the areas, which are aimed to be improved in this work. A brief background on accomplishments in the material nonlinear modeling and modeling of failure is provided. The goals of this thesis are presented and finally an outline of the manuscript is given.

1.1 Motivation

From the early days people were faced with a challenge to provide a safe shelter. Once people outgrew the natural shelters and started building man-made structures, the need to acquire the knowledge about materials and structures appeared. For millennia it was only possible to determine the material toughness and the behavior of structures by experimental observations and even nowadays the material properties and estimates regarding structural behavior are determined by experiments. Over the course of human history the understanding of laws of nature increased drastically and the theoretical models started to be used to describe the natural processes. With the uprise of computers in the second half of the twentieth century numerical simulations started playing the leading role in predicting the processes in nature. We are now able to obtain numerical solutions for problems where analytical results can no longer be attained. In particular, we can now simulate the behavior of complex structures, predict their limit load and even describe their behavior until complete failure. Given the short time frame and low cost of getting such computational solutions, when compared to obtaining experimental results, increase its importance ever since.

Currently the most widely used tool for analysis of structures is the finite element method. This is a numerical tool to solve differential equations characterizing a certain boundary value problem. The complete three-dimensional analysis of structure, that would have taken into account its exact geometry and all the phenomena related to

material geometrically nonlinear behavior (e.g. yielding of steel, cracking of concrete, slip between concrete and steel reinforcement, local failure of material, local and global buckling...) is due to the limited amount of computer power, and due to the limitation of numerical models, describing the above mentioned effects, currently impossible. Therefore a certain degree of mathematical idealization is needed. By considering certain kinematic assumptions we can model the 3D structure as 2D (plates, walls and shells) and 1D (bars, beams) by using plate, 2D solid, shell, bar and bream finite elements. Furthermore we can lower the computational costs by using simplified constitutive models.

In this work we derive several finite elements with inelastic material models that are suitable for limit load and failure analysis of different structural components. In order to obtain adequate solutions we derive elasto-plastic material models for analysis of steel beams, plates and shells and a nonlinear elastic model for analysis of reinforced concrete plates. These models are defined at the level of stress resultants, which makes them more robust and computationally cheaper. The novelty of this work is related to representation of material models. For instance, concerning the formulation for nonlinear analysis of reinforced concrete plates, Eurocode 2 recommendations for constitutive behavior of concrete were adopted. When analyzing plastic and viscoplastic stress-resultant plates, a unified computational procedure is presented that covers both formulations. Further, the stress-resultant plasticity for shells was revisited in order to provide a new view on return mapping algorithm for two-surface stress-resultant plasticity.

When one wants to determine the behavior of structures when the load produces localized material failure then the elasto-plastic and nonlinear elastic material models no longer suffice. The failure of structure or structure components usually begins due to very localized effects, which the continuum constitutive models are unable to capture adequately. As an example, one can think of a macro crack forming within a concrete wall, where the thickness of the crack is much smaller than the overall dimension of the wall itself. This makes the challenging task for the applied numerical method since the discontinuity in the wall has to be described. In order to simulate such problems, we incorporated singular fields, representing localized zones of failures, into the finite element framework, resulting in a finite element formulation with embedded strong discontinuities. Several contributions to this field are made in this work. The first one provides a new beam finite element with embedded rotational discontinuity, suitable for elastoplastic and failure analysis of planar frames. To determine beam hardening and softening parameters, a sequential multi-scale (shell-beam) procedure is proposed. The next contribution is a new formulation for an elastoplastic 2D solid finite element with embedded discontinuity. A quadrilateral finite element is derived that is suitable for nonlinear collapse analysis of 2D solids and can describe both brittle and ductile failure of the material.

1.2 Background

The number of contributions on the limit load analysis, inelastic analysis and the failure analysis in the literature is enormous. In the following a brief overview of the state of the art is given. In Section 1.2.1 we present approaches for the limit load analysis and in Section 1.2.2 we summarize the numerical developments on the modeling of failure.

1.2.1 Limit load analysis

Limit load analysis of structures has a significant practical value and there are numerous articles and books written on this topic. The most studied problems are limit load analysis of frames and plates. In the case of simple geometry of a reinforced concrete plate one can determine the limit load by using the plastic lines theory which is explained in numerous books (e.g. [Save and Massonet, 1972], [Nielsen, 1984], [Moy, 1996], [Park and Gamble, 2000], [Radosavljević and Bajić, 1990]). The basic principle in this method is the assumed plastic (breaking) lines that divide the plate into individual rigid parts that can only rotate around these lines. If we consider that the virtual work done by the fully plastic (breaking) bending moments acting at the plastic lines is equal to the virtual work done by the external load we can derive the limit load of the reinforced concrete plate. Note that this method gives the upper value of the limit load. The limitations of this approach become clear if the geometry of the plate is more complex. Note, that with this approach we only obtain the estimate of the limit load and there are no informations regarding the corresponding limit ductility.

For a more complex structural geometry, or when the limit load is not the only relevant quantity (e.g. one wants to know more on the displacement field, load-displacement history, irreversible deformation,...), one can use an inelastic (nonlinear) analysis based on the finite element method.

One already available option is the use of commercial programs that allow the nonlinear description of materials, e.g. of the reinforced concrete (e.g. [Hobbit et al., 2007]). When using the commercial software, we divide for example the plate in the thickness direction into layers of concrete and reinforcements, and use the standard elastoplastic material model for steel (see e.g. [Simo and Hughes, 1998], [Kojić and Bathe, 2005], [Lubliner, 1990], [Ibrahimbegovic, 2006], [Ibrahimbegovic, 2009]), to describe the behavior of reinforcement, and a rather sophisticated nonlinear material model to describe the behavior of the concrete. Such a nonlinear analysis requires the use of finite elements for shells and a knowledge of several parameters that describe the behavior of concrete. An alternative to the above approaches was presented in [Ibrahimbegovic et al., 1992], [Ibrahimbegovic and Frey, 1993b] and [Ibrahimbegovic and Frey, 1994]. This method is also based on

material nonlinear analysis of reinforced concrete plates, yet it uses a constitutive law that is based on stress resultants instead of stresses, which simplifies the analysis significantly. With this approach we can determine the limit load of the plate in the case of monotonically increasing loading. If the loading is such that includes significant amount of loading and unloading, one should use a different approach to compute the limit load. A similar approach, that is capable of describing the cyclic and even dynamic loading is considered in [Koechlin and Potapov, 2007]. Here, the constitutive relations are also written in terms of stress resultants, in particular a yield function is used, which considers the damage model for concrete and elastoplastic model for steel reinforcement.

The standard approach for the inelastic analysis of metal plates and shells is the use of finite elements for shells that require through the thickness integration, see e.g. [Brank et al., 1997]. Such elements are included in most of the commercial finite element based programs (e.g. [Hobbit et al., 2007]). When using the finite elements with through the thickness integration, we divide the shell in the thickness direction into several layers, determine the stress state in each layer by using the standard elastoplastic material model for steel and then by numerical integration along the thickness direction determine the values of stress resultants for a particular cross-section. Such a nonlinear analysis is computational quite expensive, since we need to determine and store the values of internal variables (plastic strain and hardening variables) for all the integration points in the thickness direction. Another way, which is less common, introduces the elastoplastic constitutive equations directly in the 2D stress resultant form; see e.g. [Simo and Kennedy, 1992], [Skallerud et al., 2001], [Crisfield and Peng, 1992] for the shell case. The latter approach is on one hand computationally much faster than the former one, but on the other hand it fails to describe the spreading of the plastification through the plate thickness, see e.g. [Auricchio and Taylor, 1994]. This drawback can be removed (to a certain extent) by a pseudo-time dependent value of the yield parameter associated with the plate bending response. This was first suggested by Crisfield, see e.g. [Crisfield, 1981] and references therein, and was later used e.g. by [Shi and Voyiadjis, 1992] for plates and [Zeng et al., 2001] and [Voyiadjis and Woelke, 2006] for shells. Another way to approximately describe the 3d effect of spreading of plasticity throughout the plate is to use the generalized plasticity model for plates, which is based on two functions (both defined in terms of stress resultants), the yield function and the limit function, see e.g. [Auricchio and Taylor, 1994]. However, if one wants to evaluate only the limit load of the metal plate, the above mentioned modifications are unnecessary, since both the stress resultant formulation and the stress based formulation with the through-the-thickness numerical integration provide the same result.

1.2.2 Failure analysis

In the above section we have mentioned some of the approaches that are suitable to determine the behavior of a structure up to the limit load. The question now arises how can one include the effects that are related to material failure. The failure of material is related to the appearance of a discontinuity in the displacement field (e.g. cracks in brittle materials or shear bands in ductile materials) which is in contradiction with the smooth nature of the finite element method.

The most trivial approach, that is also incorporated in most commercial finite element programs, is *element deletion*. The basic idea behind this procedure is simple. Once we detect that the strength of the material has been reached within a single element, e.g. maximum principal stress at the integration point of the element was surpassed, we consider this element to be totally damaged and that it no longer contributes to the resulting system of equations. The discontinuity is in this case represented by the deleted finite element. It is clear that this approach has a drawback of being dependent on the finite element discretization.

Instead of deleting the element, once the strength of material is surpassed, one can at the integration points of this element apply a softening stress - strain law in which the stress tends to zero with the growing strain. These procedures are often denoted as *softening models*. Softening models are problematic since multiple strain states are possible for a certain stress field leading to an ill-posed mathematical problem and similarly as for the element deletion, the finite element solution is pathologically dependent on the mesh size.

This drawback can be circumvented if the element size is included in the constitutive relations in terms of the characteristic length, leading to the so called *smeared crack approach* first proposed in [Rashid, 1968] and is often used to analyze the failure of brittle materials. In this method the continuum model can capture the softening response objectively, since the proper element softening dissipation is achieved by the definition of the softening law being dependent on the element size.

The proper energy dissipation distributed over the volume of the element was achieved in [Bažant and Oh, 1983] and [Rots et al., 1985] leading to a *band smeared crack approach*.

Alternative approaches where the characteristic length is also included in the constitutive law are among others: *non-local continuum* ([Bažant et al., 1984]), *higher-gradient models* ([Coleman and Hodgon, 1985]) and *Cosserat continuum* ([de Borst and Sluys, 1991]).

In all the above mentioned procedures the actual discontinuity is not present in the model and we only model its influence on the continuum. The first papers that considered

the actual discontinuity as a geometric entity in the finite element formulation are [Ngo and Scordelis, 1967] and later [Hillerborg, 1976] introducing the *discrete crack approach*. Within this formulation the force - displacement relations are enforced along the finite element edges, in particular at the element nodes. Once the nodal force at the node ahead of the discontinuity tip exceeds the strength of the material the node splits into two new nodes and the discontinuity can now propagate to the next node. The position of the discontinuity is thus restricted to the finite element boundary which makes the procedure mesh dependent. A better result is obtained if the crack path is predefined with an appropriate mesh alignment or if the remeshing is used, see e.g. [Ingraffea and Saouma, 1985]. In [de Borst et al., 2004] a comparison of smeared and discrete crack approaches is given.

Similar to the discrete crack approach is the *cohesive zone model* developed in [Needleman, 1987]. In this approach the boundaries of the finite elements are modeled by the cohesive finite elements that have a certain traction-separation law incorporated. The formulation was further developed in [Tvergaard, 1990] to include both normal and tangential separation and a further improvement in [Xu and Needleman, 1994] allowed to deal with the crack branching. If the cohesive elements are included in the finite element mesh at the beginning of the simulation, the solution is influenced by cohesive elements' stiffness. This can be avoided if the elements are included only after reaching a failure criterion, see e.g. [Camacho and Ortiz, 1996] and [Ortiz and Pandolfi, 1999]. Similarly as for the discrete crack approach the cohesive zone model also suffers to be mesh objective and several techniques to diminish this drawback can be used, see e.g. [Carter et al., 2000], [Bittencourt et al., 1996], [Ortiz and Quigley, 1991], [Marusich and Ortiz, 1995] and [Ingraffea and Saouma, 1985].

In [Ortiz et al., 1987], the first time the discontinuity in the strain field was introduced into the bulk of a finite element to employ the strain localization. The displacement field in this approach remained continuous and the method became known as the *weak discontinuity approach*.

The *strong discontinuity approach*, in a sense, that the displacement field in the finite element framework is discontinues itself, was for the first time accomplished in [Dvorkin et al., 1990] and [Simo et al., 1993] and it was further developed e.g. in [Simo and Oliver, 1994], [Oliver and Simo, 1994], [Oliver, 1995], [Oliver, 1996a] and [Oliver, 1996b]. The main advantage of the method is in the way it incorporates the discontinuity in the finite element framework. Namely, once the discontinuity propagation criterion was reached in a particular finite element, additional parameters are introduced in this finite element only. These local unknowns, which one can interpret as the jumps in the displacement field, can be condensed out at the element level, thus leaving the global system of equations

unchanged. Since the strong discontinuity with all the related parameters is embedded within individual finite elements, this method is often denoted as the *embedded discontinuity finite element method* (ED-FEM). ED-FEM approach received a lot of attention in the past two decades and numerous authors took part in developing and improving it in various fields of finite elements. The embedded discontinuity approach was successfully included in the beam finite element formulation in the works of [Ehrlich and Armero, 2005], [Armero and Ehrlich, 2006b], [Armero and Ehrlich, 2004], [Wackerfuss, 2008] and [Dujc et al., 2009] among others. The theoretical formulation of the localized failure in the Reisner-Mindlin plate theory was presented in [Armero and Ehrlich, 2006a] and built into triangular and quadrilateral plate finite elements. The theoretical formulation of combined hardening and softening plasticity model was presented in [Ibrahimbegovic and Brancherie, 2003] and applied into 2D solid finite elements. This formulation along with the formulation that includes damage constitutive model for the bulk response and the damage constitutive model for the discontinuity was presented in [Brancherie, 2003]. The modeling of failure in solids was also studied in [Brancherie and Ibrahimbegovic, 2008], [Manzoli and Shing, 2006], [Linder and Armero, 2007], [Dujc et al., 2010] and [Linder, 2007], where also a detailed review on the history of theoretical and numerical modeling of failure is presented. Recently, in [Ibrahimbegovic and Melnyk, 2007] the approach of modeling of localized failure in heterogeneous materials was considered where both strong and weak discontinuity approach was incorporated. For a review on approaches to derivation of embedded discontinuity model we also refer to [Jirasek, 2000] and [Jirasek and Zimmermann, 2001].

Similar to ED-FEM approach is the *extended finite element method* (X-FEM), whose concepts are based on the partition of unity ([Melenk and Babuška, 1996] and [Babuška and Melenk, 1997]). Contrary to ED-FEM, the parameters describing the behavior of discontinuity are in X-FEM treated globally. This means that the number of global equilibrium equations is not fixed during the simulation but it grows with the formation of the discontinuity path. A comparison of the ED-FEM and the X-FEM is for example given in [Jirasek, 2000] and [Ibrahimbegovic and Melnyk, 2007].

1.3 Goals of the thesis

The particular goals of the thesis follow the main goal, which is to study and develop numerical tools for analysis of limit load, limit ductility and complete failure of structures and structural components. The particular goals can be summarized as follows:

- The first goal is to apply the Eurocode 2 [Eurocode 2, 2004] recommendations to de-

scribe the constitutive behavior of reinforced concrete plates presented in [Ibrahimbegovic et al., 1992], [Ibrahimbegovic and Frey, 1993b] and [Ibrahimbegovic and Frey, 1994], and to include the resulting constitutive model into the AceGen [Korelc, 2007b] code of the existing Reissner-Mindlin plate finite element presented in [Bohinc et al., 2009].

- The second goal is to derive the small strain stress resultant elastoplastic plate finite element that includes both isotropic and kinematic hardening, further extend the plasticity formulation into the visoplasticy formulation of Perzyna type and include the constitutive relations into the AceGen code [Korelc, 2007b] of the existing Reissner-Mindlin plate finite element presented in [Bohinc et al., 2009].

- The third goal is to derive the inelastic geometrically exact shell formulation and upgrade the existing shell finite element (see [Brank et al., 1995] and [Brank and Ibrahimbegovic, 2001]) programed in AceGen [Korelc, 2007b], to include the return mapping algorithms needed for shell stress-resultant plasticity with isotropic and kinematic hardening.

- Fourth goal is to derive a new elastoplastic Euler-Bernoulli beam finite element with embedded discontinuity for push over analysis of steel frame structures. In this context an approach to determine the material parameters needed for an analysis of newly derived Euler-Bernoulli beam had to be derived.

- The last goal of the thesis is to derive the family of quadrilateral finite elements for analysis of 2D solids, including both hardening and the localized softening effects, where the opening of the discontinuity is considered as linear in normal and in tangential direction. The element should be suitable for failure analysis of brittle as well as ductile solids.

1.4 Outline of the thesis

In addition to Section 1 the thesis consists of seven chapters, where we consider different topics related to the limit load analysis and the failure analysis of structures.

The limit load analysis of reinforced concrete plates is considered in Chapter 2. Kinematic quantities with dual strain variables related to plate boundary value problem are presented, followed by a detailed description of nonlinear elastic constitutive relations for reinforced concrete plates. With respect to the pattern of reinforcement we differ between the case of isotropic reinforcement and the case of anisotropic reinforcement. Concep-

tual algorithms for both cases are presented, followed by several numerical simulations. Concluding remarks and a short summary end this chapter.

In Chapter 3 we derive small strain elastoplastic plate finite element formulation in terms of stress resultants. Nonlinear isotropic and linear kinematic hardening are considered. We further extend the plasticity formulation into the visoplasticy formulation of Perzyna type. Both elastoplastic and elastoviscoplastic stress resultant plate formulations are derived by exploiting the hypotheses of instantaneous elastic response and the principle of maximum plastic dissipation (plasticity) or the penalty-like form of the principle of maximum plastic dissipation (viscoplasticity). The performance of the finite element is shown by several numerical examples. We conclude the chapter with concluding remarks and a short summary.

Elastoplastic analysis of thin metal shells is presented in Chapter 4. First we describe the kinematics and the variational formulation of the geometrically exact shell. By the thermodynamics consideration and the use of modified version of the classical Ilyushin-Shapiro yield function we derive the evolution equations for generalized plastic strain, internal variable related to isotropic hardening and the internal variables related to kinematic hardening. Next we present the spatial finite element discretization and computational algorithms related to shell stress resultant multi-surface plasticity. The results of several numerical simulations, accompanied by the results from literature are further presented. The chapter closes with concluding remarks and a short summary.

In Chapter 5 we present the finite element method with embedded discontinuity for failure analysis in 1D solids. With the introduction of one additional kinematic parameter into the standard 1D solid isoparametric finite element, we derive the enriched strain field and by considering the principle of virtual work we obtain the mesh related equilibrium equations along with the local element-wise equations that arise due to strain enrichment. The response of the bulk material is linear elastic, while the response of the discontinuity is considered to be rigid plastic, where all the necessary ingredients are obtained by considering the principles of thermodynamics. Next we present the computational procedure that determines the new values of nodal displacements and the new values of local (element) variables. Two numerical simulations are presented. We conclude the chapter with concluding remarks and a short summary. We note that this chapter is included in the thesis only for illustrative purposes.

The principles that were presented in Chapter 5 for 1D solids are in Chapter 6 incorporated in elastoplastic Euler-Bernoulli beam finite element. First we consider the kinematics of Euler-Bernoulli beam finite element with discontinuities in the rotation field and in the axial displacement field and derive the operators needed to enrich the generalized strain field. Again we use the principle of virtual work to obtain the global

and the local equilibrium equations. Next we considered the elasto-plastic response of the bulk material of the beam and a rigid plastic response of the discontinuity. The remaining ingredients of the elastoplasticity with hardening and the rigid-plasticity with softening are obtained from the consideration of thermodynamics of associative plasticity and the principle of maximum plastic dissipation. Next we discuss computation of the beam hardening and softening parameters by using the shell model. We present the details of the computational procedure and show the performance of our approach by several numerical simulations. Concluding remarks and a short summary close the chapter.

The failure analysis of 2D solids is presented in Chapter 7. Within the standard isoparametric quadrilateral finite element we introduce a discontinuity line with four additional parameters representing four modes of separation. We determine the interpolation matrices related to the additional parameters and with the derivation of the enriched displacement field we obtain the strain field and the strain field operators related to the parameters of the discontinuity. By considering that the additional parameters can be viewed as the incompatible degrees of freedom, we obtain the operators related to virtual strain and with them by considering the principle of virtual work we derive the local and the global equilibrium equations. Next we considered the elasto-plastic response of the bulk material and a rigid plastic response of the discontinuity. All the remaining ingredients are obtained from the consideration of thermodynamics of associative plasticity and the principle of maximum plastic dissipation. In Section 7.3 we present the procedure to determine the new values of the nodal displacement, hardening plasticity variables related to integration points of the element and the local softening plasticity variables related to integration points of the discontinuity along with the procedure that determines the discontinuity propagation within the finite element mesh. Several numerical simulations are presented. We conclude this chapter with concluding remarks and a short summary.

Concluding remarks of the thesis are given in Chapter 8.

Remark 1.1. *In all chapters, the notation is specialized to the topic of the particular chapter. Therefore the validity of notation ends with the chapter end.*

Chapter 2

Limit load analysis of reinforced concrete plates

2.1 Introduction

In this chapter we present the approach for a nonlinear analysis of concrete plates by using the finite element method. We use a constitutive law that is based on stress resultants instead of stress, which makes the analysis computationally much cheaper. The idea is taken from [Ibrahimbegovic et al., 1992], [Ibrahimbegovic and Frey, 1993b], [Ibrahimbegovic and Frey, 1994]; the difference is that we apply the Eurocode 2 [Eurocode 2, 2004] recommendations to describe the constitutive behavior of reinforced concrete.

With this approach we can determine the limit load of the plate in the case of monotonically increasing loading. If the loading is such that includes significant amount of loading and unloading one should use a different approach to compute the limit load. We consider that the local effects related to the change of stiffness of plate and the redistribution of loading are small and negligible. We also assume that the displacements of the plate are small enough, that we can neglect the membrane forces in the plate.

The chapter is organized as follows: in Section 2.2 we present the kinematics of the Reissner-Mindlin plate model, define the stress resultants and describe the details of the nonlinear elastic constitutive relations for reinforced concrete plates. With respect to the pattern of reinforcement we distinguish between the case of isotropic reinforcement and the case of anisotropic reinforcement and present the computational algorithms for both cases, in Section 2.3. In Section 2.4 several numerical simulations are presented. Finally, in Section 2.5 concluding remarks and a short summary are provided.

2.2 Constitutive model for reinforced concrete plates

2.2.1 Basic idea

According to Reissner-Mindlin plate theory we model the plate as a surface in the x_1x_2 plane that has at each point three degrees of freedom: displacement in the x_3 direction and two rotations of the plate normal around axis x_1 and axis x_2 (see Figure 2.1). We can then express the curvature vector $\boldsymbol{\kappa}$ and the vector of transverse shear deformations $\boldsymbol{\gamma}$ as

$$\boldsymbol{\kappa} = [-\frac{\partial\theta_2}{\partial x_1}, \frac{\partial\theta_1}{\partial x_2}, \frac{\partial\theta_1}{\partial x_1} - \frac{\partial\theta_2}{\partial x_2}]^T = [\kappa_{11}, \kappa_{22}, 2\kappa_{12}]^T, \tag{2.1}$$

$$\boldsymbol{\gamma} = [\frac{\partial w}{\partial x_1} + \theta_2, \frac{\partial w}{\partial x_2} - \theta_1]^T. \tag{2.2}$$

With the proposed constitutive law for reinforced concrete we relate the total values of deformations (curvatures and shear strains) with the plate stress resultants

$$\boldsymbol{m} = [m_{11}, m_{22}, m_{12}]^T \ , \ \boldsymbol{q} = [q_1, q_2]^T, \tag{2.3}$$

where $\boldsymbol{m}$ is the vector of bending moments and $\boldsymbol{q}$ is the vector of shear forces per unit length. With the chosen coordinate system and the chosen cinematic and constitutive relations we obtain positive values of bending moments, when we have tensial stress on the lower face of the plate, t.i. the face with the normal $\boldsymbol{n}$ in the $-x_3$ direction (Figure 2.2).

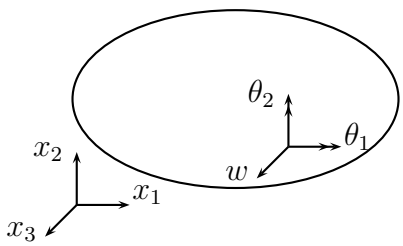

Figure 2.1: Positive directions of the transverse displacement and rotations of the plate

Slika 2.1: Pozitivne smeri prečnega pomika in zasukov plošče

We treat the bending and the shear part of the constitutive law separately. The shear forces are computed according to standard linear elastic constitutive relations for isotropic material

$$\boldsymbol{q} = \boldsymbol{C}_S\boldsymbol{\gamma} \ , \ \boldsymbol{C}_S = \frac{5}{6}\frac{E_c h}{2(1+\nu_c)}\begin{bmatrix} 1 & 0 \\ 0 & 1 \end{bmatrix}, \tag{2.4}$$

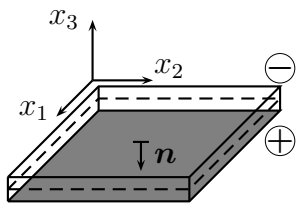

Figure 2.2: Face with tensial stresses (darkened) caused by the positive bending moments

Slika 2.2: Nategnjena stran plošče (potemnjena), ko so momenti pozitivni

where E_c is the Young's modulus of the concrete, h is the thickness of the plate and ν_c is the Poisson ratio of the concrete. Therefore, the derived model for reinforced concrete plate is unable to describe the shear failure of the plate.

Regarding bending we consider two distinguished states: I the state before cracking of the concrete and II the cracked state, when the cracks due to tensial failure of the concrete are already present in the plate. For the intact concrete (state I) we consider the linear elastic relations between the bending moments and the curvatures. If we neglect the contribution of the reinforcement we get

$$\boldsymbol{m} = \boldsymbol{C}_B \boldsymbol{\kappa} \ , \ \boldsymbol{C}_B = \frac{E_c h^3}{12(1-\nu_c^2)} \begin{bmatrix} 1 & \nu_c & 0 \\ \nu_c & 1 & 0 \\ 0 & 0 & \frac{1-\nu_c}{2} \end{bmatrix} . \tag{2.5}$$

The state II starts when one of the moments in one of the prescribed orthogonal directions, determined with the angles ϕ and $\phi + \frac{\pi}{2}$ (see Figure 2.4), reaches the value $m_{crack} = f_{ct}\frac{h^2}{6}$, where f_{ct} is the tensial strength of the concrete. In other words, we check for the crack initiation in the two orthogonal directions, where one can interpret m_{crack} as the bending moment that initiates crack in the planar beam with the unit width. The two orthogonal directions can be either in the directions of the principal curvatures,in the directions of the principal bending moments or in the directions of the maximum resistance of the plate. More on the choice of crack directions will be explained in Section 2.3.

Even in the subsequent phase of the loading, after the cracking has been initiated (in state II), we check for the progress of cracks along the two orthogonal directions, that are not necessary equal to the directions at the first appearance of the crack.

In the cracked state we disregard the influence of Poisson's ratio and assume independent responses for the two orthogonal directions. Further details will be addressed in Section 2.2.2 below.

2.2.2 Moment curvature relationship

In what fallows we present the approach that gives us the relationship between the bending moment $\overline{m}$ and the corresponding curvature $\overline{\kappa}$ for the direction that is determined with the angle ϕ (Figure 2.4). First we provide the values of $\overline{m}$ and $\overline{\kappa}$ for three distinguished states of the reinforced concrete cross-section (Figure 2.3):

- appearance of the first crack in the concrete (point A, $\overline{m} = m_{crack}$, $\overline{\kappa} = \kappa_{crack}$),
- start of yielding of the reinforcement (point B, $\overline{m} = m_y$, $\overline{\kappa} = \kappa_y$),
- and the failure of the concrete in compression (point C, $\overline{m} = m_f$, $\overline{\kappa} = \kappa_f$).

Once we have points A, B and C determined we simply connect them and obtain the peace-wise linear constitutive relation. The key parameter that determines the shape

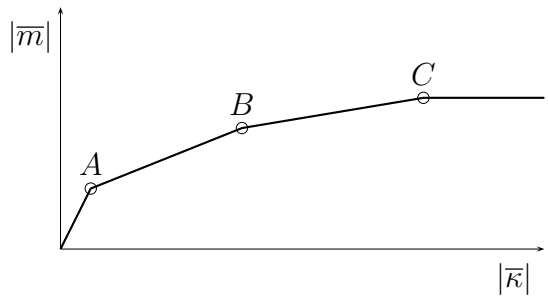

Figure 2.3: Moment curvature relationship for the principal direction

Slika 2.3: Diagram moment ukrivljenost za glavno smer

of the diagram in Figure 2.3 is the effective area of the reinforcement in the principal direction determined with the angle ϕ, which we compute according to

$$a_\phi = \sum a_i \cos^2(\phi - \alpha_i), \tag{2.6}$$

where a_i is the area of the reinforcement layer i with the orientation angle α_i (Figure 2.4).

In order to obtain the points A, B and C we adopt the Eurocode 2 recommendations for the constitutive relations for concrete and steel. For the concrete in compression we use the following relation between the stress σ_c and strain ε_c

$$\sigma_c = \begin{cases} f_{ck}(1 - (1 - \frac{\varepsilon_c}{\varepsilon_{c2}})^n) & \text{za } 0 \leq \varepsilon_c \leq \varepsilon_{c2} \\ f_{ck} & \text{za } \varepsilon_{c2} \leq \varepsilon_c \leq \varepsilon_{cu3} \end{cases}, \tag{2.7}$$

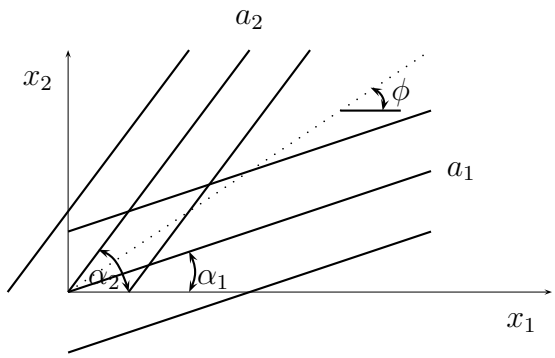

Figure 2.4: Layers of reinforcement and the effective area of the reinforcement in the principal direction

Slika 2.4: Plasti armature in efektivna količina armature v glavni smeri

where $\varepsilon_{c2} = 0.002$, $\varepsilon_{cu3} = 0.0035$, $n = 2$ for concrete $f_{ck} \leq 50$ and f_{ck} is the compressive strength of concrete. The tensile strength and the corresponding strain are according to Eurocode 2 $f_{ct} = f_{ct}(f_{ck})$ and $\varepsilon_{ct} = \frac{f_{ct}}{E_c}$. We adopt the standard bilinear relationship between the reinforcement strain ε_s and the reinforcement stress σ_s

$$\sigma_s = \begin{cases} E_s\varepsilon_s & \text{za } \varepsilon_s \leq \frac{f_y}{E_s} \\ f_y & \text{za } \varepsilon_s > \frac{f_y}{E_s} \end{cases} , \tag{2.8}$$

where f_y is the tensial strength of steel and $E_s = 20000kN/cm^2$ is the Young's modulus of steel.

Characteristic points for moment curvature diagrams

In order to obtain the characteristic points A, B and C in Figure 2.3 we need the following data: the tensile strength of steel f_y, the Young's modulus of steel E_s, the effective area of the reinforcement $a_\phi[cm^2/cm]$, the compressive strength of concrete f_{ck}, the tensile strength of concrete f_{ct} or its corresponding strain $\varepsilon_{ct} = \frac{f_{ct}}{E_c}$, the Young's modulus of concrete E_c, the thickness of the plate h and the effective height of the plate $d = h - a$, where a is the distance from the bottom face of the plate to the reinforcement. In Figure 2.5 ε_{cc} denotes the strain at the face in compression, ε_{ct} is the strain at the face in tension, ε_s is the strain at the position of reinforcement, F_c is the resultant force arising from the compressive stress in concrete, F_s is the force in the reinforcement and x is the distance between the neutral axis and the plate mid-plane.

Bending moment and the corresponding curvature at the crack initiation are

$$m_{crack} = f_{ct}\frac{h^2}{6} \ , \ \kappa_{crack} = 2\frac{\varepsilon_{ct}}{h} = 2\frac{f_{ct}}{E_c h}. \tag{2.9}$$

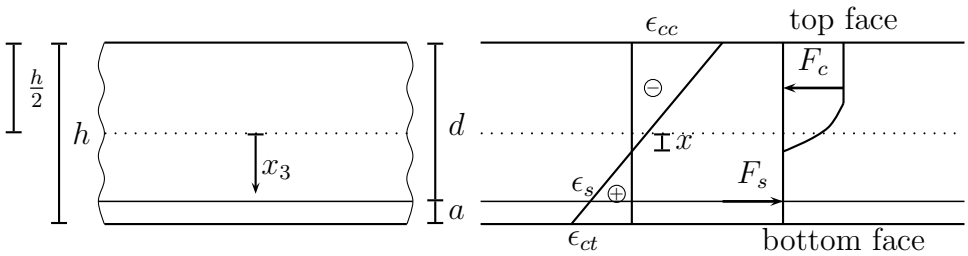

Figure 2.5: Equilibrium in the cross-section of the plate

Slika 2.5: Ravnotežje v prerezu plošče

The strain in the reinforcement that corresponds to the start of yielding is equal to $\varepsilon_s = \frac{f_y}{E_s}$ and the force in the reinforcement at that time is $F_s = f_y a_\phi$. By considering, that the compressive force in the concrete is equal to the force in reinforcement

$$F_c = F_s \ , \ F_c(x) = \int_{-\frac{h}{2}}^{x} \sigma_c dx_3, \tag{2.10}$$

we obtain the position of the neutral axis x that satisfies the equilibrium in (2.10). We can then provide the edge (face) values of the strains in concrete $\varepsilon_{cc}(x, \varepsilon_s)$ and $\varepsilon_{ct}(x, \varepsilon_s)$ (Figure 2.5). The values of the bending moment and the curvature at the start of yielding of the reinforcement are then

$$m_y = \int_{-\frac{h}{2}}^{x} \sigma_c x_3 dx_3 + (\frac{h}{2} - a)F_s \ , \ \kappa_y = \frac{\varepsilon_{ct} + \varepsilon_{cc}}{h}. \tag{2.11}$$

The strain in concrete at the face in compression that corresponds to the bending moment at the start of failure of concrete in compression is $\varepsilon_{cc} = \varepsilon_{cu3}$. The reinforcement is already plastified, thus we obtain the force in the reinforcement as $F_s = f_y a_\phi$. Similarly as above we now look for the position of the neutral axis by solving (2.10). The bending moment at the start of failure of concrete in compression and the corresponding curvature are

$$m_f = \int_{-\frac{h}{2}}^{x} \sigma_c x_3 dx_3 + (\frac{h}{2} - a)F_s \ , \ \kappa_f = \frac{\varepsilon_{ct} + \varepsilon_{cc}}{h}. \tag{2.12}$$

Note that we assumed that the amount of reinforcement is such that ensures that the yielding of the reinforcement appears prior to the failure of the cross-section due to crushing of concrete in compression.

In the case that reinforcement is negative (i.e. close to the top face) the corresponding $\overline{m}(-\overline{\kappa})$ relationship is derived in a similar way. In the case of double reinforced cross-section the above procedure should be slightly (but trivially) modified.

2.3 Isotropic and anisotropic reinforcement

In Section 2.2 we have presented the constitutive law for reinforced concrete plates, in particular we have explained the moment curvature relationship that we use to determine the response of the plate in state II. The relationship $\overline{m}(\overline{\kappa})$ was derived for an arbitrary angle ϕ (Figure 2.4). In what follows we will take a look at the options that are available for a particular choice of angle ϕ with respect to the different pattens of plate reinforcement.

2.3.1 Isotropic reinforcement

An isotropic reinforcement corresponds to the effective reinforcement area a_ϕ (Equation (2.6)) being the same in any direction ϕ:

$$a_\phi^{isotropic} = \sum_i a_i \cos^2(\phi - \alpha_i) = const. \quad \text{for} \quad \forall\phi. \tag{2.13}$$

For example an orthogonal reinforcement net with the same area a_1 in each direction results in an isotropic reinforcement:

$$a_\phi = a_1 \cos^2(\phi - \alpha) + a_1 \cos^2(\phi - \alpha + \frac{\pi}{2}) = a_1 \quad \text{for} \quad \forall\phi. \tag{2.14}$$

In the case of isotropic reinforcement we can pre-compute the relationship $\overline{m}(\overline{\kappa})$ (Figure 2.3) and store it for subsequent use. Namely the relationship $\overline{m}(\overline{\kappa})$ is independent on ϕ.

The algorithm that we use to analyze the plates with isotropic reinforcement is the following:

1. At each gauss integration point do the following computations: at the given values of displacements $\boldsymbol{u} = [w, \theta_1, \theta_2]^T$ compute the curvature in the global x_1x_2 coordinate system
$$\boldsymbol{\kappa} = \boldsymbol{\kappa}(\boldsymbol{u}) = [\kappa_{11}, \kappa_{22}, 2\kappa_{12}]^T. \tag{2.15}$$

2. Compute the values of principal curvatures
$$\kappa_{1,2} = \frac{\kappa_{11} + \kappa_{22}}{2} \pm \sqrt{(\frac{\kappa_{11} - \kappa_{22}}{2})^2 + (\kappa_{12})^2}. \tag{2.16}$$

3. From the pre-computed relationship $\overline{m}(\overline{\kappa})$ determine the principal moments
$$m_1 = \overline{m}(\kappa_1), \quad m_2 = \overline{m}(\kappa_2). \tag{2.17}$$

4. Compute the shear strains and shear forces in the $x_1x_2x_3$ coordinate system
$$\boldsymbol{\gamma} = \boldsymbol{\gamma}(\boldsymbol{u}) = [\gamma_1, \gamma_2]^T, \quad \boldsymbol{q} = [q_1, q_2]^T = \boldsymbol{C}_S\boldsymbol{\gamma}. \tag{2.18}$$

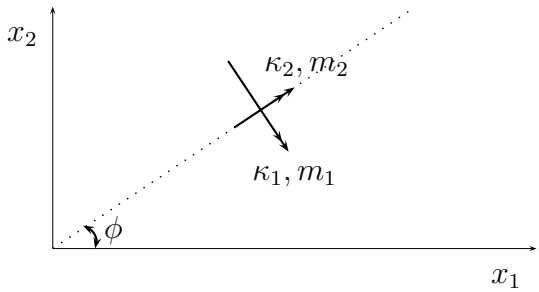

Figure 2.6: Directions of the principal curvatures and the principal moments

Slika 2.6: Smeri glavnih ukrivljenosti in momentov

5. Use the principle of virtual work $\delta\Pi$ as the basis for the finite element method analysis

$$\delta\Pi(\mathbf{u}, \delta\mathbf{u}) = \sum_e \int_{\Omega^e} (m_1\delta\kappa_1 + m_2\delta\kappa_2 + q_1\delta\gamma_1 + q_2\delta\gamma_2)d\Omega - \sum_e \int_{\Omega^e} p\delta w d\Omega, \quad (2.19)$$

where $\delta\boldsymbol{u} = [\delta w, \delta\theta_1, \delta\theta_2]^T$ are the virtual displacement, $\delta\kappa_1$ and $\delta\kappa_2$ are the virtual principal curvatures, $\delta\gamma_1$ and $\delta\gamma_2$ are virtual shear strains, p is the surface loading and Ω^e is the domain in the x_1x_2 plain that is occupied by the mid-plane of the finite element with index e. Details of the finite element discretization are omitted here and are presented in details in Section 3.3.1.

2.3.2 Anisotropic reinforcement

If the effective area of reinforcement depends of the angle ϕ we have the case of anisotropic reinforcement:

$$a_\phi(\phi) \neq const. \quad (2.20)$$

This is the case for example if we have reinforcement only in one direction or if we have an orthogonal reinforcement with different areas of reinforcement in each direction. There are two ways of analysis and we denote them as the (i) the fixed crack approach, when we have predetermined direction of the crack formation and (ii) the rotating crack approach, when the direction of the crack changes during the analysis.

Fixed crack

We assume that the cracks form in the direction of the maximum resistance of the plate. With the chosen reinforcement we assume that the crack direction corresponds to $\phi = \phi_r$,

where

$$\tan 2\phi_r = \frac{\sum_{i=1}^{nrl} m_{f\,i} \sin 2\alpha_i}{\sum_{i=1}^{nrl} m_{f\,i} \cos 2\alpha_i}. \tag{2.21}$$

In general all the components of the curvature vector $\boldsymbol{\kappa}_r$ written in the nt orthogonal coordinate system, which is determined with the angle ϕ_r, are nonzero

$$\kappa_n \neq 0 \ , \ \kappa_t \neq 0 \ , \ \kappa_{nt} \neq 0. \tag{2.22}$$

For the n and t directions we compute the effective areas of reinforcement a_n and a_t and determine the relationships $\overline{m}_n(\overline{\kappa}_n)$ and $\overline{m}_t(\overline{\kappa}_t)$ according to the procedure described in Section 2.2.2. For the component m_{nt} we assume the following relation

$$m_{nt} = \beta(\kappa_n, \kappa_t)\frac{G_c t^3}{12}\kappa_{nt}, \quad G_c = \frac{E_c}{2(1-\nu)}, \tag{2.23}$$

where the parameter $\beta(\kappa_n, \kappa_t)$ could account for the gradual reduction of shear resistance due to crack initiation. For simplicity we often adopt the constant value for β (in the numerical simulations in Section 2.4 we used $\beta = 1$).

The algorithm for the fixed crack approach is the following:

1. At each gauss integration point do the following computations: at the given values of displacements $\boldsymbol{u} = [w, \theta_1, \theta_2]^T$ compute the curvature in the global x_1x_2 coordinate system

$$\boldsymbol{\kappa} = \boldsymbol{\kappa}(\boldsymbol{u}) = [\kappa_{11}, \kappa_{22}, 2\kappa_{12}]^T. \tag{2.24}$$

2. Compute the values of curvatures in the nt coordinate system

$$\boldsymbol{\kappa}_r = T_r^T \boldsymbol{\kappa}, \quad \boldsymbol{\kappa}_r = [\kappa_n, \kappa_t, \kappa_{nt}]^T, \tag{2.25}$$

$$T_r = \begin{bmatrix} \cos^2\phi_r & \sin^2\phi_r & -\sin 2\phi_r \\ \sin^2\phi_r & \cos^2\phi_r & \sin 2\phi_r \\ \sin\phi_r\cos\phi_r & -\sin\phi_r\cos\phi_r & \cos 2\phi_r \end{bmatrix}. \tag{2.26}$$

3. Compute the bending moments in the nt coordinate system:

$$m_n = \overline{m}_n(\kappa_n), \quad m_t = \overline{m}_t(\kappa_t), \quad m_{nt} = \beta(\kappa_n, \kappa_t)\frac{G_c t^3}{12}\kappa_{nt}. \tag{2.27}$$

4. Compute the shear strains and shear forces in the x1x2x3 coordinate system

$$\boldsymbol{\gamma} = \boldsymbol{\gamma}(\boldsymbol{u}) = [\gamma_1, \gamma_2]^T \quad \boldsymbol{q} = [q_1, q_2]^T = \boldsymbol{C}_S\boldsymbol{\gamma}. \tag{2.28}$$

5. Use the principle of virtual work $\delta\Pi$ as the basis for the finite element method analysis

$$\delta\Pi(\mathbf{u},\delta\mathbf{u}) = \sum_e \int_{\Omega^e} (m_n\delta\kappa_n + m_t\delta\kappa_t + m_{nt}\delta\kappa_{nt} + q_1\delta\gamma_1 + q_2\delta\gamma_2)d\Omega - \sum_e \int_{\Omega^e} p\delta w d\Omega, \tag{2.29}$$

where $\delta\kappa_n$, $\delta\kappa_t$, $\delta\kappa_{nt}$ are the virtual curvatures.

Rotating crack

We assume the crack initiation in the direction of the principal curvature, which can change during the analysis.

The algorithm for the rotating crack approach is the following:

1. At each gauss integration point do the following computations: at the given values of displacements $\boldsymbol{u} = [w, \theta_1, \theta_2]^T$ compute the curvature in the global x_1x_2 coordinate system

$$\boldsymbol{\kappa} = \boldsymbol{\kappa}(\boldsymbol{u}) = [\kappa_{11}, \kappa_{22}, 2\kappa_{12}]^T. \tag{2.30}$$

2. Compute the values of principal curvatures

$$\kappa_{1,2} = \frac{\kappa_{11}+\kappa_{22}}{2} \pm \sqrt{(\frac{\kappa_{11}-\kappa_{22}}{2})^2 + (\kappa_{12})^2}. \tag{2.31}$$

3. Compute the direction of principle curvatures

$$\phi = 1/2\arctan(\frac{2\kappa_{12}}{\kappa_{11}-\kappa_{22}}) + k\frac{\pi}{2}\ , k = \begin{cases} 1 & \text{for } \kappa_{11}-\kappa_{22} < 0 \\ 0 & \text{else} \end{cases}. \tag{2.32}$$

4. Compute the effective area of reinforcement for both directions

$$a_1 = a_\phi = \sum_i a_i \cos^2(\phi - \alpha_i), \quad a_2 = a_{\phi+\frac{\pi}{2}} = \sum_i a_i \cos^2(\phi + \frac{\pi}{2} - \alpha_i). \tag{2.33}$$

5. Determine the relationships $\overline{m}_1(\overline{\kappa}_1)$ and $\overline{m}_2(\overline{\kappa}_2)$.

6. Determine the values of principal moments

$$m_1 = \overline{m}_1(\kappa_1), \quad m_2 = \overline{m}_2(\kappa_2). \tag{2.34}$$

7. Compute the shear strains and shear forces in the $x_1x_2x_3$ coordinate system

$$\boldsymbol{\gamma} = \boldsymbol{\gamma}(\boldsymbol{u}) = [\gamma_1, \gamma_2]^T, \quad \boldsymbol{q} = [q_1, q_2]^T = \boldsymbol{C}_S\boldsymbol{\gamma}. \tag{2.35}$$

8. Use the principle of virtual work $\delta\Pi$ as the basis for the finite element method analysis

$$\delta\Pi(\hat{\mathbf{u}},\delta\hat{\mathbf{u}}) = \sum_e \int_{\Omega^e} (m_1\delta\kappa_1 + m_2\delta\kappa_2 + q_1\delta\gamma_1 + q_2\delta\gamma_2)d\Omega - \sum_e \int_{\Omega^e} p\delta w d\Omega. \tag{2.36}$$

2.4 Numerical examples

The presented constitutive model and the corresponding algorithms were compiled with the quadrilateral finite element for plates with quadratic interpolation of transverse displacement w and linear interpolation of rotations θ_1 and θ_2, which was presented in [Bohinc and Ibrahimbegovic, 2005] and is described in detail in Section 3.3.1. The computer code was generated by using symbolic manipulation code AceGen and the examples were computed by using finite element program AceFem, both developed by Korelc, see [Korelc, 2002], [Korelc, 2007b] and [Korelc, 2007a].
In the cases with isotropic reinforcement the results obtained with the isotropic model are completely the same as the ones obtained with the anisotropic model with rotating crack. The only difference is in the computation time, which is shorter for the isotropic model, since less numerical operations are needed.

It is assumed in the following examples that the positive or negative reinforcement is the same at any point of the plate.

2.4.1 Rectangular simply supported plate with anisotropic reinforcement

We consider a rectangular simply supported plate under distributed load. The properties of the plate are: the thickness $h = 80\ mm$, the length $l = 300\ cm$ and the width $b = 200\ cm$. The plate reinforcement is orthogonal with the area of the reinforcement in the first direction $a_1 = 251\ mm^2/m$ and in the second direction $a_2 = 559\ mm^2/m$. The position of reinforcement is at a distance $c_1 = c_2 = 14\ mm$ from the bottom face of the plate. The material properties are: $E_c = 24\ kN/mm^2$, $f_{ck} = 26.5\ N/mm^2$, $f_{ct} = 2.5\ N/mm^2$, $E_s = 205\ kN/mm^2$ in $f_y = 460\ N/mm^2$. The finite element mesh used in our simulations consist of 8×8 finite elements. Two numerical simulations were performed; one with the fixed crack approach and the second with the rotating crack approach. In Figure 2.7 we present the total load versus displacement at the center obtained in numerical simulations along with experimental results adopted from [Ibrahimbegovic and Frey, 1994]. We can see from Figure 2.7 that there is a reasonable agreement between the rotating crack approach and the experimental data and that the prediction of the limit load is fairly accurate whereas the fixed crack approach significantly over-estimates the true resistance of the plate. The reason for that is that the directions of principal action do not coincide with the directions of the plate reinforcement. The fixed crack approach would give reasnoble results only in the case, where these two directions would coincide, i.e. in the case of optimally designed plate. Since this approach in general leads to a large over-estimate of the plate resistance it is not suitable for numerical simulations.

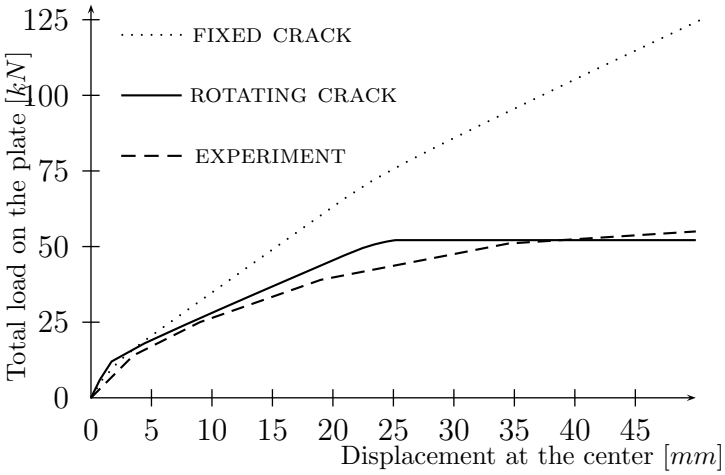

Figure 2.7: Rectangular plate with anisotropic reinforcement under distributed load

Slika 2.7: Pravokotna anizotropno armirana plošča pod vplivom ploskovne obtežbe

2.4.2 Simply supported square plate with anisotropic reinforcement

In this example we consider a simply supported square plate with anisotropic reinforcement under distributed loading. The plate's thickness is $h = 5.1\ cm$ and the side of the plate is $a = 183\ cm$. The plate reinforcement is orthogonal where the area of the reinforcement in the first direction is $a_1 = 2.81\ cm^2/m$ and in the second direction is $a_2 = 2.35\ cm^2/m$. The position of reinforcement is determined with $d_1 = 3.9\ cm$ for the first direction and with $d_2 = 4.39\ cm$ for the second direction, where d_i is the distance form the top face of the plate to the position of the reinforcement. The material properties are: $E_c = 3242\ kN/cm^2$, $f_{ck} = 3.5\ kN/cm^2$, $f_{ct} = 0.379\ kN/cm^2$, $\nu_c = 0.18$, $E_s = 20691\ kN/cm^2$ in $f_y = 37.59\ kN/cm^2$. The numerical simulations were performed with the mesh of 8×8 finite elements. In the simulations we assumed that both layers of reinforcement are positioned at the same distance from the top face of the plate: $\overline{d} = \frac{d_1+d_2}{2} = 4.15\ cm$. In the corner nodes of the plate we did not support the vertical displacement which was in agreement with the experimental boundary conditions, see [Ibrahimbegovic et al., 1992]. Figure 2.8 presents the load versus displacement at the center curves. We can see that there is a good agreement of results in the region of small displacements (up to cca. 20 mm). When the displacements get bigger, the membrane effects significantly increase the resistance of the plate, which is not accounted for in our model.

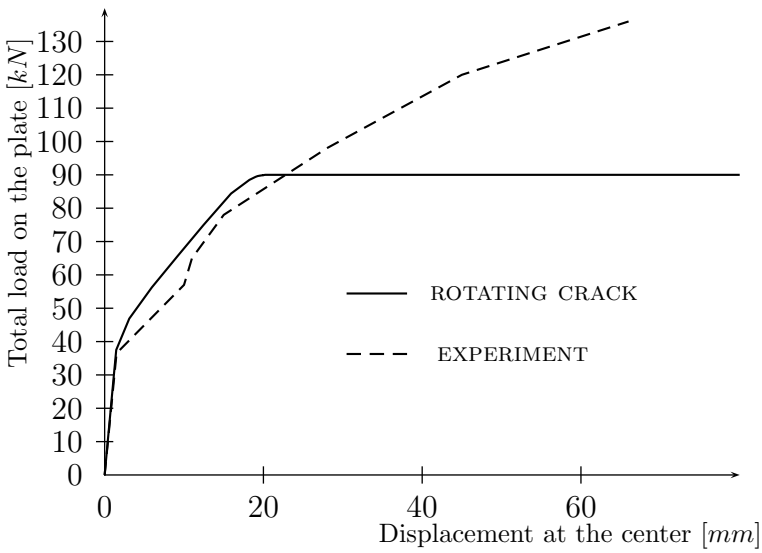

Figure 2.8: Simply supported square plate with anisotropic reinforcement

Slika 2.8: Kvadratna anizotropno armirana plošča pod vplivom ploskovne obtežbe

2.4.3 Circular clamped plate with isotropic reinforcement

We consider a circular plate with isotropic reinforcement. The thickness of the plate is $h = 1\ m$ and its radius is $R = 10\ m$. The material properties are: $E_c = 2000\ kN/cm^2$, $f_{ck} = 3.5\ kN/cm^2$, $f_{ct} = 0.56\ kN/cm^2$, $\nu_c = 0.16$, $E_s = 21000\ kN/cm^2$ in $f_y = 46\ kN/cm^2$. The plate has an isotropic reinforcement with $\mu = \mu' = 1\%$ reinforcement in each direction, placed at $a = a' = 3\ cm$ from the top and bottom face of the plate. In Figure 2.9 we present the coarse (left) and the fine (right) finite element mesh that we used in the numerical simulations. The plate is built in, i.e. the edge nodes have prescribed all the degrees of freedom ($w = \theta_1 = \theta_2 = 0$). In Figure 2.10 we present the load versus transverse displacement at the center curves. Along with the results of our simulations we also present the results obtained by the 3-D solid finite elements (see [Ibrahimbegovic et al., 1992]). We can see that there is hardly any difference in results obtained by the course and the fine mesh and despite the simplicity of our approach, we have a good agreement with the results obtained by the more sophisticated approach.

2.4.4 Plate with two free edges

In this example we consider a rectangular plate that is simply supported along the shorter edges while the longer edges are free, see Figure 2.11. The geometric properties of the plate are: the length of the shorter edges $l_1 = 45.72\ cm$, the length of the longer edges $l_2 = 76.2\ cm$, the thickness $h = 3.81\ cm$ and the distance from the top face of the plate

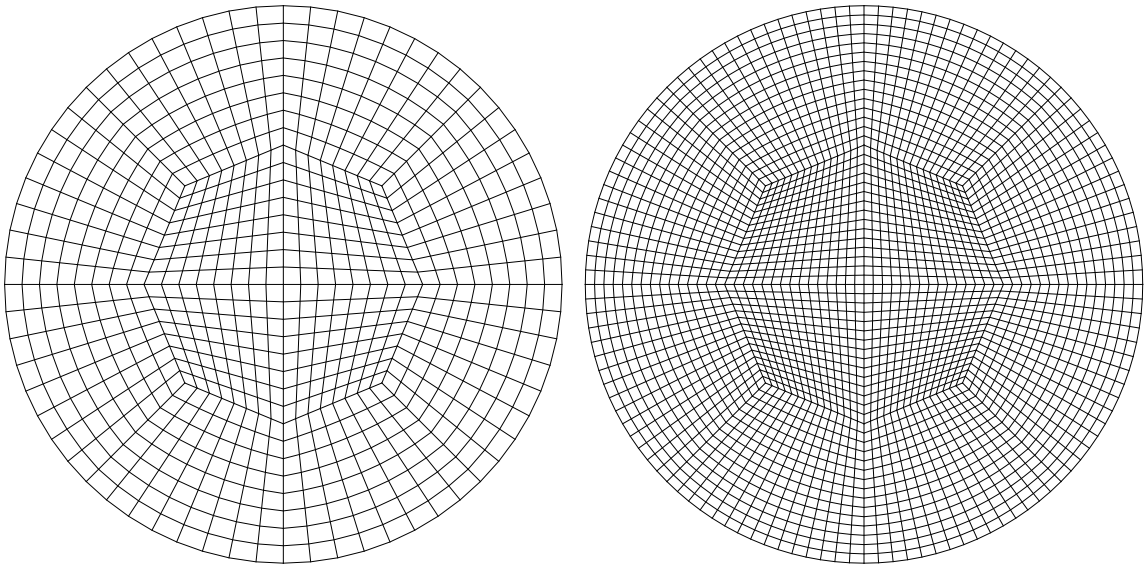

Figure 2.9: Coarse (left) and fine (right) mesh of the circular plate

Slika 2.9: Groba (levo) in fina (desno) mreža končnih elementov pri krožni plošči

to the reinforcement $d = 3.1\ cm$. The material properties are: $E_c = 2900\ kN/cm^2$, $f_{ck} = 3.2\ kN/cm^2$, $f_{ct} = 0.2\ kN/cm^2$, $\nu_C = 0.18$, $E_s = 20000\ kN/cm^2$ and $f_y = 22\ kN/cm^2$. The plate is loaded with the line load P (Figure 2.11). The reinforcement is placed only in the direction parallel to the longer edges where $a_1 = 2,74\ cm^2/m$. The numerical simulation is performed with the finite element mesh of 10×10 elements. In Figure 2.12 we compare the results of our approach with the results obtained by the commercial program Abaqus [Hobbit et al., 2007], where the behavior of the reinforcement was described with the elastoplastic material model for steel and the behavior of the concrete was described with the damage material model. We can see that there is a reasonable agreement in the results.

2.4.5 Square plate with point supports in the corners

We consider a square plate with point supports in the corners. The plate is loaded with the point load at the center of the plate. The plate's properties are: the thickness $h = 4.4\ cm$, the length of the side of the plate $l = 91.4\ cm$, the amount of isotropic reinforcement $\mu = 0.85\%$ and the distance from the top face of the plate to the position of reinforcement $d = 3.3\ cm$. The properties of steel and concrete are: $f_{ck} = 3.8\ kN/cm^2$, $E_c = 3600\ kN/cm^2$, $\nu_c = 0.15$, $f_{ct} = 0.53\ kN/cm^2$, $E_s = 20000\ kN/cm^2$ and $f_y = 34.5\ kN/cm^2$. The numerical simulation is performed with a mesh of 20×20 elements.

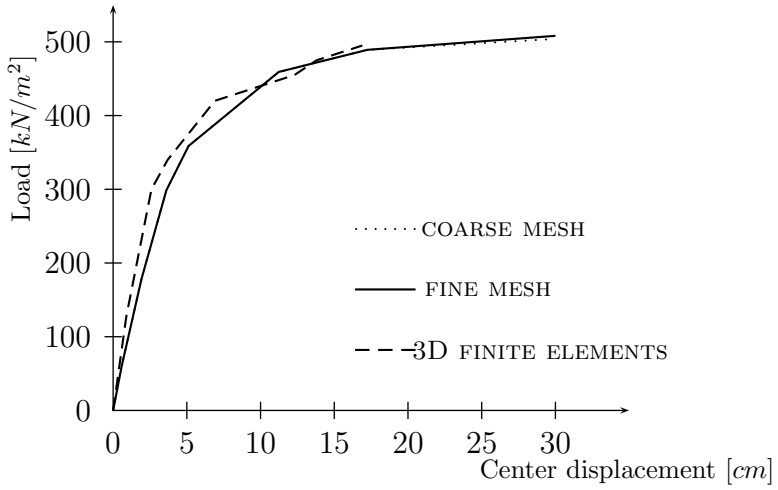

Figure 2.10: Load versus center displacement diagrams for circular plate

Slika 2.10: Krivulje obtežba - pomik pri krožni plošči

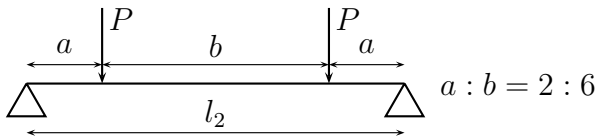

Figure 2.11: Geometry and loading of the plate with two free edges

Slika 2.11: Geometrija in obtežba plošče z dvema prostima robovoma

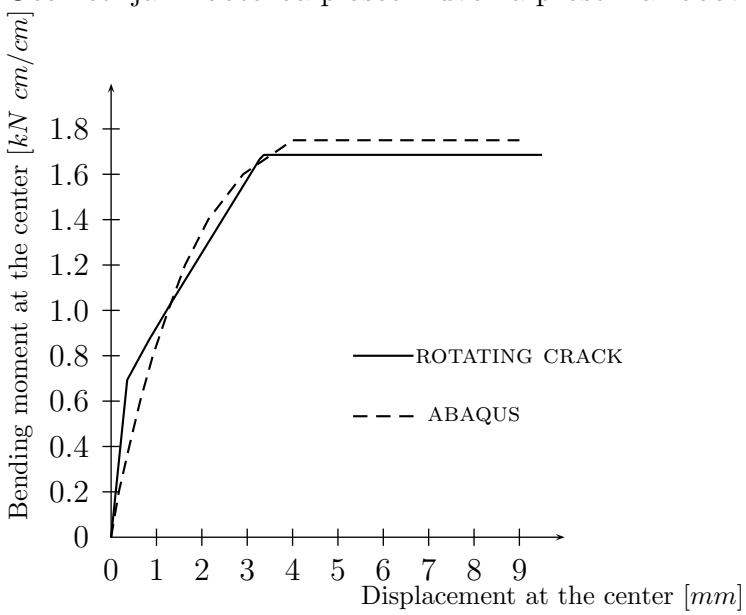

Figure 2.12: Bending moment versus displacement at the center curves

Slika 2.12: Krivulje upogibnega momenta v odvisnosti od prečnega pomika na sredini plošče

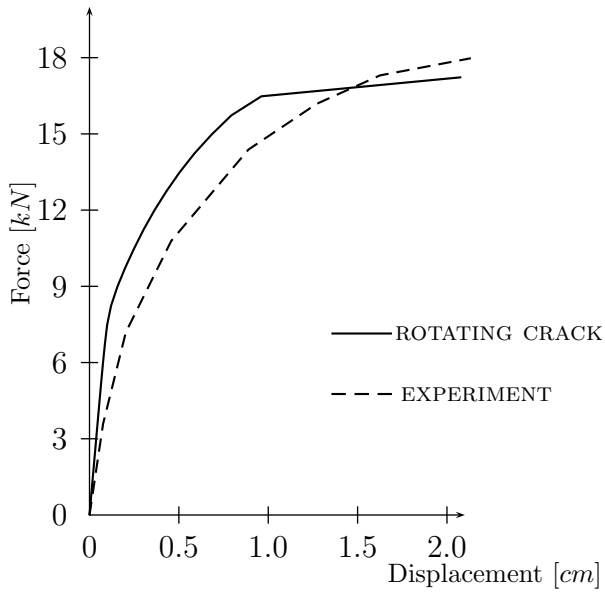

Figure 2.13: Force versus displacement diagram for the square plate

Slika 2.13: Krivulje sila pomik pri kvadratni plošči

In Figure 2.13 we present the transverse displacement of the point that is at a distance $\frac{l}{10}$ from the center point of the plate in the x_1 direction. This example also shows that the presented approach gives results that are in reasnoble agreement with the experimentally obtained results (see [Zahlten, 1993]).

2.5 Concluding remarks and chapter summary

In this chapter the analysis of reinforced concrete plates is considered where we distinguish between the uncracked state I of the plate and the cracked state II of the plate, activated by the tensile failure of the concrete. In state I we consider the standard linear elastic constitutive relations for isotropic material

$$\boldsymbol{q} = \boldsymbol{C}_S \boldsymbol{\gamma}, \quad \boldsymbol{m} = \boldsymbol{C}_B \boldsymbol{\kappa}.$$

In state II we again consider a linear elastic response for the shear while for the bending part we disregard the influence of Poisson's ratio and assume independent responses for the two orthogonal directions defined by ϕ and $\phi + \frac{\pi}{2}$ of the form

$$\overline{m} = \overline{m}(\overline{\kappa}).$$

The response in those two directions is determined with the effective area of reinforcement in that direction

$$a_\phi = \sum_i a_i \cos^2(\phi - \alpha_i), \quad a_{\phi+\frac{\pi}{2}} = \sum_i a_i \cos^2(\phi + \frac{\pi}{2} - \alpha_i),$$

and a peace-wise linear diagram determined with three distinguished states of the reinforced concrete cross-section:

- appearance of the first crack in the concrete (point A in Figure 2.3),
- start of yielding of the reinforcement (point B in Figure 2.3),
- the failure of the concrete in compression (point C in Figure 2.3).

With respect to the different patterns of plate reinforcement we provide the algorithm for the isotropic reinforcement with the constant effective area in any direction

$$a_{\phi}^{isotropic} = const.,$$

and for the case of anisotropic reinforcement

$$a_{\phi}(\phi) \neq const.,$$

a fixed crack and a rotating crack algorithm is provided.

The results of the presented approach for the analysis of limit load of reinforced concrete plates are in good agreement with the available experimental results (which are available in the literature) for those plates, where the load is monotonically increased until the failure of the plate. The essence of this approach is that it takes into account the gradual degradation of reinforced concrete due to crushing of the concrete and the yielding of the reinforcement. Although the approach is based on the nonlinear finite element method it is robust and relatively simple.

Chapter 3

Inelastic analysis of metal plates

3.1 Introduction

In this chapter we derive small strain elastoplastic plate finite element formulation in terms of stress resultants. Nonlinear isotropic and linear kinematic hardening are considered. We further extend the plasticity formulation into the visoplasticy formulation of Perzyna type, e.g. [Kojić and Bathe, 2005], [Kleiber and Kowalczyk, 1996]. Both elastoplastic and elastoviscoplastic stress resultant plate formulations are derived by exploiting the hypotheses of instantaneous elastic response and the principle of maximum plastic dissipation (plasticity) or the penalty-like form of the principle of maximum plastic dissipation (viscoplasticity); see e.g. [Ibrahimbegovic et al., 1998] for 3d setting of those topics. We show that with such an approach a unified computational framework for elastoplastic and elastoviscoplastic stress resultant plate analysis can be obtained.

The chapter is organized as follows: In section 3.2 we systematically derive basic equations of elastoplastic and elastoviscoplastic plate models. In section 3.3 we present spatial finite element discretization and numerical procedure for integration of elastoplastic and elastoviscoplastic evolution equations. The finite element that is used is the simplest of the family of the plate elements presented in [Bohinc et al., 2009] and [Ibrahimbegovic, 1993], which share the property that the interpolation of transverse displacement is one order higher than the interpolation of rotations. Numerical examples are presented in Section 3.4 and concluding remarks and chapter summary are given in Section 3.5.

3.2 Inelastic plate models

We model a plate as a 2d body occupying a domain Ω in the x_1x_2 plane. The weak form of the equilibrium equations is for the inelastic geometrically linear Reissner-Mindlin plate

model given as

$$G\left(m_{\alpha\beta}, q_\alpha; \widehat{w}, \widehat{\theta}_\gamma\right) = \int_\Omega \widehat{\kappa}_{\alpha\beta}\left(\widehat{\theta}_\gamma\right) m_{\alpha\beta} d\Omega + \int_\Omega \widehat{\gamma}_\alpha\left(\widehat{w}, \widehat{\theta}_\gamma\right) q_\alpha d\Omega, \quad (3.1)$$
$$-\int_\Omega \widehat{w} p d\Omega - G_{ext,b}\left(\overline{m}_\alpha, \overline{q}_\alpha; \widehat{w}, \widehat{\theta}_\gamma\right) = 0, \qquad \alpha, \beta, \gamma \in \{1, 2\},$$

where w is transverse displacement (i.e. displacement in the direction of x_3 coordinate), θ_γ is rotation of a plate normal (i.e. unit vector in the direction of x_3 coordinate) around x_γ axis, $\kappa_{\alpha\beta}$ are bending strains, γ_α are shear strains

$$\kappa_{\alpha\beta} = \frac{1}{2}\left(\frac{\partial \beta_\alpha}{\partial x_\beta} + \frac{\partial \beta_\beta}{\partial x_\alpha}\right), \qquad \beta_\alpha = e_{\alpha\beta}\theta_\beta \Rightarrow \begin{pmatrix} \beta_1 \\ \beta_2 \end{pmatrix} = \begin{bmatrix} 0 & -1 \\ 1 & 0 \end{bmatrix} \begin{pmatrix} \theta_1 \\ \theta_2 \end{pmatrix}, \quad (3.2)$$
$$\gamma_\alpha = \frac{\partial w}{\partial x_\alpha} - \beta_\alpha, \quad (3.3)$$

$m_{\alpha\beta}$ are bending moments, q_α are transverse forces, p is transverse plate loading (i.e. loading in the direction of x_3 coordinate), $G_{ext,b}$ is virtual work of external moments $\overline{m}_\alpha$ and external forces $\overline{q}_\alpha$ acting on the plate boundary, and $(\widehat{\circ})$ is virtual quantity that corresponds to $(\circ)$. We consider displacement w, rotations θ_γ, stress resultants $m_{\alpha\beta}$, q_α and load as functions of position $\boldsymbol{x} = [x_1, x_2]^T \in \Omega$ and pseudo-time $t \in [0, T]$, i.e. $w = w(\boldsymbol{x}, t)$, $\theta_\gamma = \theta_\gamma(\boldsymbol{x}, t)$, $m_{\alpha\beta} = m_{\alpha\beta}(\boldsymbol{x}, t)$, $q_\alpha = q_\alpha(\boldsymbol{x}, t)$, $p = p(\boldsymbol{x}, t)$, $\overline{m}_\alpha = \overline{m}_\alpha(\boldsymbol{x}, t)$, $\overline{q}_\alpha = \overline{q}_\alpha(\boldsymbol{x}, t)$. Equation (3.1) can be written in matrix form as

$$G\left(\boldsymbol{m}, \boldsymbol{q}; \widehat{w}, \widehat{\boldsymbol{\theta}}\right) = \int_\Omega \widehat{\boldsymbol{\kappa}}^T \boldsymbol{m} d\Omega + \int_\Omega \widehat{\boldsymbol{\gamma}}^T \boldsymbol{q} d\Omega - \int_\Omega \widehat{w} p d\Omega - G_{ext,b} = 0, \quad (3.4)$$

where the following mappings have been defined

$$\begin{aligned}
\theta_\gamma &\mapsto \boldsymbol{\theta} = [\theta_1, \theta_2]^T, \\
\kappa_{\alpha\beta} &\mapsto \boldsymbol{\kappa} = [\kappa_{11}, \kappa_{22}, 2\kappa_{12}]^T = \left[-\frac{\partial \theta_2}{\partial x_1}, \frac{\partial \theta_1}{\partial x_2}, \frac{\partial \theta_1}{\partial x_1} - \frac{\partial \theta_2}{\partial x_2}\right]^T, \\
\gamma_\alpha &\mapsto \boldsymbol{\gamma} = [\gamma_1, \gamma_2]^T = \left[\frac{\partial w}{\partial x_1} + \theta_2, \frac{\partial w}{\partial x_2} - \theta_1\right]^T, \\
m_{\alpha\beta} &\mapsto \boldsymbol{m} = [m_{11}, m_{22}, m_{12}]^T, \qquad q_\alpha \mapsto \boldsymbol{q} = [q_1, q_2]^T.
\end{aligned} \quad (3.5)$$

For further use we also define the following strain and stress resultant vectors

$$\begin{aligned}
\boldsymbol{\varepsilon} &= \left[\boldsymbol{\kappa}^T, \boldsymbol{\gamma}^T\right]^T = [\kappa_{11}, \kappa_{22}, 2\kappa_{12}, \gamma_1, \gamma_2]^T, \\
\boldsymbol{\sigma} &= \left[\boldsymbol{m}^T, \boldsymbol{q}^T\right]^T = [m_{11}, m_{22}, m_{12}, q_1, q_2]^T.
\end{aligned} \quad (3.6)$$

Having defined the weak form of equilibrium equations and the kinematic relations, we proceed with stress resultant inelastic constitutive relations for small strain plate bending problems.

3.2.1 Plate elastoplasticity

We consider the following internal variables to describe the irreversible nature of the plastic process during the plate bending: the plastic strain $\boldsymbol{\varepsilon}^p$, the scalar parameter ξ, which controls the isotropic hardening mechanism, and the strain-like parameters $\varkappa_{ij}$, $i, j \in \{1, 2, 3\}$, which control the kinematic hardening mechanism. The state variables are functions of position $\boldsymbol{x}$ and pseudo-time t, i.e. $\boldsymbol{\varepsilon}^p = \boldsymbol{\varepsilon}^p(\boldsymbol{x}, t)$, $\xi = \xi(\boldsymbol{x}, t)$ and $\varkappa_{ij} = \varkappa_{ij}(\boldsymbol{x}, t)$.

A usual additive split of reversible (elastic) and irreversible (plastic) strains is assumed

$$\boldsymbol{\varepsilon} = \boldsymbol{\varepsilon}^e + \boldsymbol{\varepsilon}^p, \tag{3.7}$$

where, according to (3.6), $\boldsymbol{\varepsilon}^e = \left[\boldsymbol{\kappa}^{e,T}, \boldsymbol{\gamma}^{e,T}\right]^T$ and $\boldsymbol{\varepsilon}^p = \left[\boldsymbol{\kappa}^{p,T}, \boldsymbol{\gamma}^{p,T}\right]^T$. The strain energy function is assumed to be of the following (quadratic) form

$$\psi(\boldsymbol{\varepsilon}^e, \xi, \check{\varkappa}) = \frac{1}{2}\boldsymbol{\varepsilon}^{e,T}\boldsymbol{C}\boldsymbol{\varepsilon}^e + \Xi(\xi) + \frac{1}{2}\left(\frac{2}{3}H_{kin}\right)\check{\varkappa}^T\boldsymbol{D}\check{\varkappa}, \tag{3.8}$$

where the mapping $\varkappa_{ij} \mapsto \check{\varkappa} = [\varkappa_{11}, \varkappa_{22}, 2\varkappa_{12}, 2\varkappa_{13}, 2\varkappa_{23}]^T$ has been defined, and the following matrices have been introduced (we assume the isotropic elastic response of a plate)

$$\boldsymbol{C} = \begin{bmatrix} \boldsymbol{C}^b & \boldsymbol{0} \\ \boldsymbol{0} & \boldsymbol{C}^s \end{bmatrix}, \quad \boldsymbol{C}^b = k^b \begin{bmatrix} 1 & \nu & 0 \\ \nu & 1 & 0 \\ 0 & 0 & \frac{1-\nu}{2} \end{bmatrix}, \quad \boldsymbol{C}^s = k^s \begin{bmatrix} 1 & 0 \\ 0 & 1 \end{bmatrix}. \tag{3.9}$$

Matrix $\boldsymbol{D}$ in (3.8) is such that $\check{\varkappa}^T\boldsymbol{D}\check{\varkappa} = \varkappa_{ij}\varkappa_{ij}$, $ij \neq 33$, i.e.

$$\boldsymbol{D} = \begin{bmatrix} \boldsymbol{I}_2 & \boldsymbol{0} \\ \boldsymbol{0} & \frac{1}{2}\boldsymbol{I}_3 \end{bmatrix}, \quad \boldsymbol{I}_2 = \begin{bmatrix} 1 & 0 \\ 0 & 1 \end{bmatrix}, \quad \boldsymbol{I}_3 = \begin{bmatrix} 1 & 0 & 0 \\ 0 & 1 & 0 \\ 0 & 0 & 1 \end{bmatrix}. \tag{3.10}$$

In (3.8) we assumed a general (nonlinear) form of isotropic hardening and a linear form of kinematic hardening with hardening modulus H_{kin}. The constants in (3.9) are $k^b = \frac{Eh^3}{12(1-\nu^2)}$, $k^s = \frac{cEh}{2(1+\nu)}$, where E is elastic modulus, ν is Poisson's ratio, h is plate thickness, and c is shear correction factor, usually set to 5/6.

We denote the stress-like internal variables, which correspond to the strain-like internal variables ξ and $\varkappa_{ij}$, as q and α_{ij}, respectively. These dual variables are used to define yield function. In this work we use a stress resultant approximation of the von Mises yield function, which can be for the Reissner-Mindlin plate model written in a non-dimensional form as

$$\phi(\boldsymbol{\sigma}, q, \boldsymbol{\alpha}) = (\boldsymbol{\sigma} + \boldsymbol{\alpha})^T\boldsymbol{A}(\boldsymbol{\sigma} + \boldsymbol{\alpha}) - \left(1 - \frac{q}{\sigma_y}\right)^2 = 0, \tag{3.11}$$

where $\boldsymbol{\sigma}$ is defined in (3.6), $\boldsymbol{\alpha}$ (the negative of the back stress resultants) is defined by mapping $\alpha_{ij} \mapsto \boldsymbol{\alpha} = [\alpha_{11}, \alpha_{22}, \alpha_{12}, \alpha_{13}, \alpha_{23}]^T$, σ_y is uniaxial yield stress, matrix $\boldsymbol{A}$ is for isotropic plastic response equal to

$$\boldsymbol{A} = \begin{bmatrix} \frac{1}{m_0^2}\boldsymbol{P} & \boldsymbol{0} \\ \boldsymbol{0} & \frac{1}{q_0^2}\boldsymbol{I}_2 \end{bmatrix}, \qquad \boldsymbol{P} = \frac{1}{2}\begin{bmatrix} 2 & -1 & 0 \\ -1 & 2 & 0 \\ 0 & 0 & 6 \end{bmatrix}, \tag{3.12}$$

and m_0 and q_0 are yield parameters associated with bending and transverse shear, respectively. They are usually set to the fully plastic uniaxial plate bending moment $m_0 = \frac{\sigma_y h^2}{4}$ and to the fully plastic transverse shear force $q_0 = \frac{\sigma_y h}{\sqrt{3}}$. The yield function (3.11) is special case of generalized (since it includes hardening) Ilyushin-Shapiro stress resultant yield function for shells; see e.g. [Crisfield and Peng, 1992], [Simo and Kennedy, 1992] and references therein for discussion on stress resultant yield functions for shells. A similar form, but without description of kinematic hardening mechanism and with the choice of linear isotropic hardening, was used in [Ibrahimbegovic and Frey, 1993a], [Shi and Voyiadjis, 1992].

Remark 3.1. *The yield function (3.11) does not allow to simulate the spreading of plasticity through the plate thickness. One possibility to take through-the-thickness distribution of plasticity into account, while still using a stress resultant form of the yield function, is to multiply the value of m_0 by a parameter α, such that αm_0 follows an experimental uniaxial moment-plastic curvature relation. Some authors, see e.g. [Shi and Voyiadjis, 1992], [Zeng et al., 2001], used the proposal of [Crisfield, 1981] who suggested the following form of α*

$$\alpha(t) = 1 - \frac{1}{3}\exp\left(-\frac{8}{3}\check{\kappa}^p(t)\right), \tag{3.13}$$

where

$$\check{\kappa}^p(t) = \frac{Eh}{\sqrt{3}\sigma_y}\int_0^t \left[(\dot{\kappa}_{11}^p)^2 + (\dot{\kappa}_{22}^p)^2 + \dot{\kappa}_{11}^p\dot{\kappa}_{22}^p + (\dot{\kappa}_{12}^p)^2/4\right]^{\frac{1}{2}} d\tau \tag{3.14}$$

plays the role of equivalent plastic curvature. In (3.14) $(\dot{\circ}) = \frac{\partial(\circ)}{\partial t}$. Note that for $\check{\kappa}^p = 0$ one has $\alpha = 2/3$, and for $\check{\kappa}^p \to \infty$ one gets $\alpha \to 1$.

Remark 3.2. *The general quadratic form of the yield condition (3.11) is also suitable to express stress resultant approximation of the anisotropic criterion of Hill. In such a case one needs to define the corresponding form of matrix $\boldsymbol{A}$, see e.g. [Zeng et al., 2001] for details.*

Having defined plastic strains, strain energy function and yield function, we proceed with derivation of the remaining ingredients of the stress resultant elastoplasticity for

plates. For the isothermal case we can write the following rate of material dissipation

$$\mathcal{D} = \boldsymbol{\sigma}^T \dot{\boldsymbol{\varepsilon}} - \frac{d}{dt}\psi\left(\boldsymbol{\varepsilon}^e, \xi, \check{\varkappa}\right) = \boldsymbol{\sigma}^T \dot{\boldsymbol{\varepsilon}} - \left(\frac{\partial \psi}{\partial \boldsymbol{\varepsilon}^e}\right)^T \left(\dot{\boldsymbol{\varepsilon}} - \dot{\boldsymbol{\varepsilon}}^p\right) - \frac{\partial \psi}{\partial \xi}\dot{\xi} - \left(\frac{\partial \psi}{\partial \check{\varkappa}}\right)^T \dot{\check{\varkappa}} \geqslant 0, \quad (3.15)$$

which is assumed to be non-negative. Note that equation (3.15) can be derived from the second law of thermodynamics, see e.g. [Khan and Huang, 1995], [Simo and Kennedy, 1992]. By assuming that the elastic process is non-dissipative (i.e. the state variables do not change during that process and $\mathcal{D} = 0$) one has

$$\boldsymbol{\sigma} = \frac{\partial \psi}{\partial \boldsymbol{\varepsilon}^e} = \boldsymbol{C}\boldsymbol{\varepsilon}^e. \quad (3.16)$$

By further consideration of (3.15) one can define the dual variables, i.e. the hardening variable q and the variables that control kinematic hardening $\boldsymbol{\alpha}$, as

$$q = -\frac{\partial \psi}{\partial \xi} = -\frac{d\Xi\left(\xi\right)}{d\xi} = -\Xi'\left(\xi\right), \qquad \boldsymbol{\alpha} = -\frac{\partial \psi}{\partial \check{\varkappa}} = -\frac{2}{3}H_{kin}\boldsymbol{D}\check{\varkappa} = -\frac{2}{3}H_{kin}\boldsymbol{\varkappa}, \quad (3.17)$$

where $\boldsymbol{\varkappa} = \left[\varkappa_{11}, \varkappa_{22}, \varkappa_{12}, \varkappa_{13}, \varkappa_{23}\right]^T$. By using (3.16) and (3.17) in (3.15) we obtain the reduced material dissipation (i.e. the dissipation of the plastic process) as

$$\mathcal{D}^p = \boldsymbol{\sigma}^T \dot{\boldsymbol{\varepsilon}}^p + q\dot{\xi} + \boldsymbol{\alpha}^T \dot{\boldsymbol{\varkappa}} \geqslant 0. \quad (3.18)$$

The principle of maximum plastic dissipation states that among all the dual variables $(\boldsymbol{\sigma}, q, \boldsymbol{\alpha})$ that satisfy the yield criteria, one should choose those that maximize plastic dissipation. The problem can be written in the following form: Find minimum of $\mathcal{L}^p\left(\boldsymbol{\sigma}, q, \boldsymbol{\alpha}, \dot{\gamma}\right)$, where

$$\mathcal{L}^p\left(\boldsymbol{\sigma}, q, \boldsymbol{\alpha}, \dot{\gamma}\right) = -\mathcal{D}^p\left(\boldsymbol{\sigma}, q, \boldsymbol{\alpha}\right) + \dot{\gamma}\phi\left(\boldsymbol{\sigma}, q, \boldsymbol{\alpha}\right), \quad (3.19)$$

and $\dot{\gamma} \geqslant 0$ plays the role of Lagrange multiplier. From the above minimization problem and (3.11) we obtain explicit forms of evolution equations for the internal variables

$$\begin{aligned}
\frac{\partial \mathcal{L}^p}{\partial \boldsymbol{\sigma}} &= -\dot{\boldsymbol{\varepsilon}}^p + \dot{\gamma}\frac{\partial \phi}{\partial \boldsymbol{\sigma}} = 0 \Longrightarrow \dot{\boldsymbol{\varepsilon}}^p = \dot{\gamma}\underbrace{2\boldsymbol{A}\left(\boldsymbol{\sigma} + \boldsymbol{\alpha}\right)}_{\boldsymbol{\nu}}, \\
\frac{\partial \mathcal{L}^p}{\partial q} &= -\dot{\xi} + \dot{\gamma}\frac{\partial \phi}{\partial q} = 0 \Longrightarrow \dot{\xi} = \dot{\gamma}\underbrace{\frac{2}{\sigma_y}\left(1 - \frac{q}{\sigma_y}\right)}_{\beta} \overset{(3.11)}{=} \dot{\gamma}\underbrace{\frac{2}{\sigma_y}\sqrt{\left(\boldsymbol{\sigma} + \boldsymbol{\alpha}\right)^T \boldsymbol{A}\left(\boldsymbol{\sigma} + \boldsymbol{\alpha}\right)}}_{\beta}, \quad (3.20) \\
\frac{\partial \mathcal{L}^p}{\partial \boldsymbol{\alpha}} &= -\dot{\boldsymbol{\varkappa}} + \dot{\gamma}\frac{\partial \phi}{\partial \boldsymbol{\alpha}} = 0 \Longrightarrow \dot{\boldsymbol{\varkappa}} = \dot{\gamma}\underbrace{2\boldsymbol{A}\left(\boldsymbol{\sigma} + \boldsymbol{\alpha}\right)}_{\boldsymbol{\nu}}.
\end{aligned}$$

Note that $\dot{\boldsymbol{\varkappa}} = \dot{\boldsymbol{\varepsilon}}^p$.

Remark 3.3. *Equation (3.20)$_2$ is generalization of the equivalent plastic work variable $W^p = \boldsymbol{\sigma}^T \dot{\boldsymbol{\varepsilon}}^p$. Namely, by inserting $\dot{\boldsymbol{\varkappa}} = \dot{\boldsymbol{\varepsilon}}^p$ and (3.20)$_1$ into (3.18), and using (3.11), one gets $\mathcal{D}^p = \dot{\gamma} 2 \left(1 - \frac{q}{\sigma_y}\right)$, which implies, see (3.20)$_2$, that $\dot{\xi} = \frac{1}{\sigma_y}\mathcal{D}^p$.*

The loading/unloading conditions follow from the demands that $\dot{\gamma}$ is non-negative, ϕ is non-positive, and the plastic dissipation $\mathcal{D}^p$ equals zero for elastic process when $\phi < 0$

$$\dot{\gamma} \geqslant 0, \qquad \phi \leqslant 0, \qquad \dot{\gamma}\phi = 0. \tag{3.21}$$

In addition to (3.21) we have the condition $\dot{\phi} = 0$ if $\dot{\gamma} > 0$ (the consistency condition). It guarantees the admissibility of the subsequent state in the case of change of state variables. The consistency condition

$$\dot{\gamma} > 0; \quad \dot{\phi} = 0 = \left(\frac{\partial \phi}{\partial \boldsymbol{\sigma}}\right)^T \dot{\boldsymbol{\sigma}} + \frac{\partial \phi}{\partial q}\dot{q} + \left(\frac{\partial \phi}{\partial \boldsymbol{\alpha}}\right)^T \dot{\boldsymbol{\alpha}}, \tag{3.22}$$

pseudo-time derivatives of (3.16) and (3.17), $\dot{\boldsymbol{\sigma}} = \boldsymbol{C}\left(\dot{\boldsymbol{\varepsilon}} - \dot{\boldsymbol{\varepsilon}}^p\right)$, $\dot{q} = -\Xi''(\xi)\dot{\xi}$, $\dot{\boldsymbol{\alpha}} = -\frac{2}{3}H_{kin}\dot{\boldsymbol{\varkappa}}$, and equations (3.20) lead to the following expression for $\dot{\gamma}$

$$\dot{\gamma} = \frac{1}{\left(\boldsymbol{\nu}^T \boldsymbol{C}\boldsymbol{\nu} + \Xi''(\xi)\beta^2 + \frac{2}{3}H_{kin}\boldsymbol{\nu}^T\boldsymbol{\nu}\right)}\boldsymbol{\nu}^T\boldsymbol{C}\dot{\boldsymbol{\varepsilon}}. \tag{3.23}$$

If (3.23) and (3.20) are used in $\dot{\boldsymbol{\sigma}} = \boldsymbol{C}\left(\dot{\boldsymbol{\varepsilon}} - \dot{\boldsymbol{\varepsilon}}^p\right)$, one can write $\dot{\boldsymbol{\sigma}} = \boldsymbol{C}^{ep}\dot{\boldsymbol{\varepsilon}}$, where

$$\boldsymbol{C}^{ep} = \begin{cases} \boldsymbol{C} & \text{if } \dot{\gamma} = 0 \\ \boldsymbol{C} - \frac{\boldsymbol{C}\boldsymbol{\nu}\boldsymbol{\nu}^T\boldsymbol{C}}{\boldsymbol{\nu}^T\boldsymbol{C}\boldsymbol{\nu} + \Xi''(\xi)\beta^2 + \frac{2}{3}H_{kin}\boldsymbol{\nu}^T\boldsymbol{\nu}} & \text{if } \dot{\gamma} > 0 \end{cases} \tag{3.24}$$

is elastoplastic tangent modulus of the elastoplastic plate model.

By computation of the internal variables (i.e. by integration of (3.20)) and by using (3.16) one recovers the stress resultants $\boldsymbol{\sigma}(\boldsymbol{x}, t) = \left[\boldsymbol{m}^T, \boldsymbol{q}^T\right]^T$ appearing in the weak form of the equilibrium equations (3.4).

3.2.2 Plate elastoviscoplasticity

A stress resultant viscoplastic constitutive equations for plates of Perzyna type are obtained by a modification of the elastoplasticity model presented in the previous section. The basic difference between the viscoplasticity and plasticity is that in the former model the stress states $\{\boldsymbol{\sigma}, q, \boldsymbol{\alpha}\}$, such that $\phi(\boldsymbol{\sigma}, q, \boldsymbol{\alpha}) > 0$, are permissible, while in the latter are not. The state variables remain the same, except for the viscoplastic strain $\boldsymbol{\varepsilon}^{vp}$, which replaces $\boldsymbol{\varepsilon}^p$. The constrained minimization problem (3.19) for plasticity is here replaced by the penalty form of the principle of maximum plastic dissipation (see e.g. [Simo and

Hughes, 1998] section 2.7 and [Ibrahimbegovic et al., 1998] for details), which can be stated as: Find minimum of $\mathcal{L}^{vp}(\boldsymbol{\sigma}, q, \boldsymbol{\alpha})$, where

$$\mathcal{L}^{vp}(\boldsymbol{\sigma}, q, \boldsymbol{\alpha}) = -\mathcal{D}^{vp}(\boldsymbol{\sigma}, q, \boldsymbol{\alpha}) + \frac{1}{\eta} g(\phi(\boldsymbol{\sigma}, q, \boldsymbol{\alpha})), \tag{3.25}$$

$\eta \in (0, \infty)$ is penalty parameter (also called viscosity coefficient or fluidity parameter), $\mathcal{D}^{vp}$ is viscoplastic dissipation of the same form as (3.18) and g is penalized functional. A usual choice for g is

$$g(\phi) = \begin{cases} \frac{1}{2}\phi^2 & \text{if } \phi \geq 0 \\ 0 & \text{if } \phi < 0 \end{cases}. \tag{3.26}$$

With this choice for g the minimization of (3.25) leads to

$$\frac{\partial \mathcal{L}^{vp}}{\partial \boldsymbol{\sigma}} = -\dot{\boldsymbol{\varepsilon}}^{vp} + \frac{1}{\eta}\langle\phi\rangle \frac{\partial \phi}{\partial \boldsymbol{\sigma}} = 0, \ \frac{\partial \mathcal{L}^{vp}}{\partial q} = -\dot{\xi} + \frac{1}{\eta}\langle\phi\rangle \frac{\partial \phi}{\partial q} = 0, \ \frac{\partial \mathcal{L}^{vp}}{\partial \boldsymbol{\alpha}} = -\dot{\boldsymbol{\varkappa}} + \frac{1}{\eta}\langle\phi\rangle \frac{\partial \phi}{\partial \boldsymbol{\alpha}} = 0, \tag{3.27}$$

where $\langle\phi\rangle = g\prime(\phi) = \frac{dg}{d\phi}$. Equations (3.27) provide the corresponding evolution equations of the state variables for the viscoplastic plate model.

If one defines the viscoplastic multiplier $\dot{\gamma}$ as $\dot{\gamma} = \frac{1}{\eta}\langle\phi\rangle$ then the evolution equations for viscoplastic model can be written as those for elastoplastic model, see (3.20). Their integration, which leads to stress resultants $\boldsymbol{\sigma}(\boldsymbol{x}, t) = \left[\boldsymbol{m}^T, \boldsymbol{q}^T\right]^T$, can be performed in very similar manner as for plasticity, as shown below.

3.3 Finite element formulation

3.3.1 Space discretization

In the finite element solution of the plate bending problem a domain under consideration Ω is discretized by a mesh of finite elements so that $\Omega^h = \bigcup_{e=1}^{nel} \Omega^e$, where nel is number of elements in the mesh. In this work we use one of the quadrilateral plate elements originally introduced in [Ibrahimbegovic, 1993]. Its geometry is defined by the bilinear mapping $\boldsymbol{\xi} \mapsto \boldsymbol{x}^h$ ($\boldsymbol{\xi} \in [-1, 1] \times [-1, 1]$; $\boldsymbol{x}^h \in \Omega^e$) with

$$\boldsymbol{x}^h(\boldsymbol{\xi})\,|_{\Omega^e} = \sum_{a=1}^{4} N_a(\boldsymbol{\xi})\,\boldsymbol{x}_a, \qquad \boldsymbol{x}_a = [x_{1a}, x_{2a}]^T, \qquad \boldsymbol{\xi} = \left[\xi^1, \xi^2\right]^T, \tag{3.28}$$

where $\boldsymbol{x}_a$ are coordinates of the finite element node a and

$$N_a\left(\xi^1, \xi^2\right) = \frac{1}{4}\left(1 + \xi_a^1\xi^1\right)\left(1 + \xi_a^2\xi^2\right), \qquad \begin{array}{cccc} a & 1 & 2 & 3 & 4 \\ \hline \xi_a^1 & -1 & 1 & 1 & -1 \\ \hline \xi_a^2 & -1 & -1 & 1 & 1 \end{array}. \tag{3.29}$$

The subscript h is used to denote the discretely approximated quantities. Interpolation of the rotations is based on bilinear polynomials (3.29)

$$\begin{pmatrix} \theta_1^h \\ \theta_2^h \end{pmatrix} = \boldsymbol{\theta}^h(\boldsymbol{\xi}, t)\,|_{\Omega^e} = \sum_{a=1}^{4} N_a(\boldsymbol{\xi})\,\boldsymbol{\theta}_a(t)\,, \qquad \boldsymbol{\theta}_a = [\theta_{1a}, \theta_{2a}]^T\,, \tag{3.30}$$

while interpolation of the transverse displacement is performed in more elaborated way as

$$w^h(\boldsymbol{\xi}, t)\,|_{\Omega^e} = \sum_{a=1}^{4} N_a(\boldsymbol{\xi})\,w_a(t) + \sum_{E=5}^{8} N_E(\boldsymbol{\xi})\,\frac{l_{JK}}{8}\boldsymbol{n}_{JK}^T\left(\boldsymbol{\theta}_J(t) - \boldsymbol{\theta}_K(t)\right). \tag{3.31}$$

The second term in (3.31) is such that the shear distribution along each element edge is constant. In (3.31) $l_{JK} = \left((x_{1K} - x_{1J})^2 + (x_{2K} - x_{2J})^2\right)^{1/2}$, $\boldsymbol{n}_{JK} = [\cos\alpha_{JK}, \sin\alpha_{JK}]^T$ (see Figure 3.1) and

$$\begin{array}{ll} N_E(\boldsymbol{\xi}) = \frac{1}{2}(1-\xi^1)^2(1+\xi_J^2\xi^2)\,, & E = 5,7 \\ N_E(\boldsymbol{\xi}) = \frac{1}{2}(1-\xi^2)^2(1+\xi_J^1\xi^1)\,, & E = 6,8 \end{array}\,, \quad \begin{array}{cccc} E & 5 & 6 & 7 & 8 \\ \hline J & 1 & 2 & 3 & 4 \\ \hline K & 2 & 3 & 4 & 1 \end{array}\,. \tag{3.32}$$

Interpolation of bending strains follows from $(3.5)_2$ and (3.30)

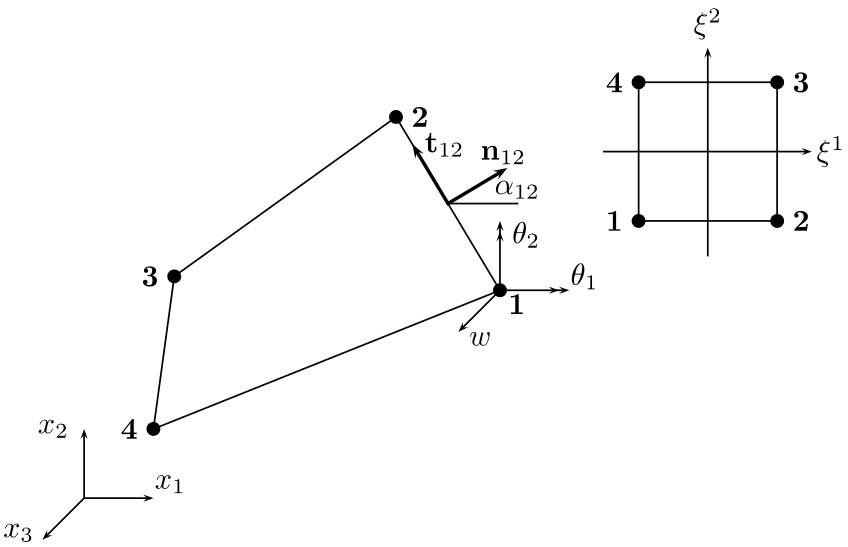

Figure 3.1: Notation of the used finite element

Slika 3.1: Notacija pri uporabljenem končnem elementu

$$\boldsymbol{\kappa}^h(\boldsymbol{\xi}, t)\,|_{\Omega^e} = \sum_{a=1}^{4} \boldsymbol{B}_a(\boldsymbol{\xi})\,\boldsymbol{\theta}_a(t)\,, \qquad \boldsymbol{B}_a = \begin{bmatrix} 0 & -N_{a,x_1} \\ N_{a,x_2} & 0 \\ N_{a,x_1} & -N_{a,x_2} \end{bmatrix}, \tag{3.33}$$

where notation $N_{a,x_i} = \frac{\partial N_a}{\partial \xi^j}\frac{\partial \xi^j}{\partial x_i}$ has been used. We further choose a bilinear distribution over the element for the shear strains

$$\begin{pmatrix} \gamma_1^h \\ \gamma_2^h \end{pmatrix} = \boldsymbol{\gamma}^h(\boldsymbol{\xi},t)\,|_{\Omega^e} = \sum_{I=1}^{4} N_I(\boldsymbol{\xi})\,\boldsymbol{\gamma}_I(t), \qquad \boldsymbol{\gamma}_I = [\gamma_{1I},\gamma_{2I}]^T, \tag{3.34}$$

where the nodal shear strains $\boldsymbol{\gamma}_I$ are obtained from (3.3), (3.30) and (3.31) as

$$\boldsymbol{\gamma}_I = \frac{1}{\boldsymbol{t}_{IJ}^T\boldsymbol{n}_{IK}}\begin{bmatrix} \frac{1}{l_{IK}}\boldsymbol{n}_{IJ}w_K + \frac{1}{l_{IJ}}\boldsymbol{n}_{IK}w_J - \left(\frac{1}{l_{IK}}\boldsymbol{n}_{IJ} + \frac{1}{l_{IJ}}\boldsymbol{n}_{IK}\right)w_I + \\ \frac{1}{2}\boldsymbol{n}_{IJ}\boldsymbol{n}_{IK}^T\boldsymbol{\theta}_K - \frac{1}{2}\boldsymbol{n}_{IK}\boldsymbol{n}_{IJ}^T\boldsymbol{\theta}_J + \frac{1}{2}\left(\boldsymbol{n}_{IJ}\boldsymbol{n}_{IK}^T - \boldsymbol{n}_{IK}\boldsymbol{n}_{IJ}^T\right)\boldsymbol{\theta}_I \end{bmatrix}, \quad \begin{array}{cccc} I & 1 & 2 & 3 & 4 \\ \hline J & 4 & 1 & 2 & 3 \\ \hline K & 2 & 3 & 4 & 1 \end{array}. \tag{3.35}$$

The notation for strains and transverse displacement can be further simplified as

$$\begin{aligned} \boldsymbol{\kappa}^h(\boldsymbol{\xi},t) \;\;|_{\;\Omega^e} &= \sum_{a=1}^{4}\widetilde{\boldsymbol{B}}_a(\boldsymbol{\xi})\,\boldsymbol{u}_a(t), \qquad \boldsymbol{\gamma}^h(\boldsymbol{\xi},t)\,|_{\Omega^e} = \sum_{a=1}^{4}\boldsymbol{G}_a(\boldsymbol{\xi})\,\boldsymbol{u}_a(t), \\ w^h(\boldsymbol{\xi},t) \;\;|_{\;\Omega^e} &= \sum_{a=1}^{4}\boldsymbol{M}_a(\boldsymbol{\xi})\,\boldsymbol{u}_a(t), \qquad \boldsymbol{u}_a = \begin{pmatrix} w_a \\ \boldsymbol{\theta}_a \end{pmatrix}, \end{aligned} \tag{3.36}$$

where $\widetilde{\boldsymbol{B}}_a$ follows from (3.33), $\boldsymbol{G}_a$ from (3.34) and (3.35) and $\boldsymbol{M}_a$ from (3.31). The virtual quantities $\widehat{\boldsymbol{\kappa}}^h(\boldsymbol{\xi})$, $\widehat{\boldsymbol{\gamma}}^h(\boldsymbol{\xi})$ and $\widehat{w}^h(\boldsymbol{\xi})$ are interpolated in the same manner as corresponding quantities in (3.36). One can also introduce more compact notation: $\boldsymbol{\varepsilon}^h = \left[\boldsymbol{\kappa}^{h,T},\boldsymbol{\gamma}^{h,T}\right]^T = \widetilde{\widetilde{\boldsymbol{B}}}_a^T\boldsymbol{u}_a$, $\widehat{\boldsymbol{\varepsilon}}^h = \widetilde{\widetilde{\boldsymbol{B}}}_a^T\widehat{\boldsymbol{u}}_a$, $\widetilde{\widetilde{\boldsymbol{B}}}_a^T = \left[\widetilde{\boldsymbol{B}}_a^T,\boldsymbol{G}_a^T\right]$.

When the above interpolations are introduced in the weak form of equilibrium equations (3.4) one gets for an element (e) the following discretized equation (we assume that only load $p = p(\boldsymbol{\xi},t)$ is active)

$$G^{(e)}\left(w^h(\boldsymbol{\xi},t),\boldsymbol{\theta}^h(\boldsymbol{\xi},t);\widehat{w}_a,\widehat{\boldsymbol{\theta}}_a\right) = \sum_{a=1}^{4}\widehat{\boldsymbol{u}}_a^{(e),T}\left(\widehat{w}_a,\widehat{\boldsymbol{\theta}}_a\right)\boldsymbol{r}_a^{(e)}\left(w^h(\boldsymbol{\xi},t),\boldsymbol{\theta}^h(\boldsymbol{\xi},t)\right), \tag{3.37}$$

where $\widehat{\boldsymbol{u}}_a = \left[\widehat{w}_a,\widehat{\boldsymbol{\theta}}_a^T\right]^T$,

$$\boldsymbol{r}_a^{(e)} = \begin{array}{l} \int_{\Omega^{(e)}}\widetilde{\widetilde{\boldsymbol{B}}}_a^T(\boldsymbol{\xi})\,\boldsymbol{\sigma}\left(\boldsymbol{\varepsilon}^h(\boldsymbol{\xi},t),\boldsymbol{\varepsilon}^p(\boldsymbol{\xi},t),\xi(\boldsymbol{\xi},t),\varkappa(\boldsymbol{\xi},t)\right)d\Omega^{(e)} - \\ \int_{\Omega^{(e)}}\boldsymbol{M}_a^T(\boldsymbol{\xi})\,\boldsymbol{p}(\boldsymbol{\xi},t)\,d\Omega^{(e)} \end{array}, \tag{3.38}$$

$\boldsymbol{p} = \left[p^h,0,0\right]^T$, $\boldsymbol{\varepsilon}^h(\boldsymbol{\xi},t) = \boldsymbol{\varepsilon}^h\left(\boldsymbol{\theta}^h(\boldsymbol{\xi},t),\boldsymbol{\gamma}^h(\boldsymbol{\xi},t)\right)$, etc. Numerical integration of (3.38) (2×2 Gauss integration points are used for the present element) leads to

$$\boldsymbol{r}_a^{(e)} = \sum_{G=1}^{4} W_G\begin{pmatrix} \widetilde{\widetilde{\boldsymbol{B}}}_a^T(\boldsymbol{\xi}_G)\,\boldsymbol{\sigma}\left(\boldsymbol{\varepsilon}^h(\boldsymbol{\xi}_G,t),\boldsymbol{\varepsilon}^p(\boldsymbol{\xi}_G,t),\xi(\boldsymbol{\xi}_G,t),\varkappa(\boldsymbol{\xi}_G,t)\right) - \\ \boldsymbol{M}_a^T(\boldsymbol{\xi}_G)\,\boldsymbol{p}(\boldsymbol{\xi}_G,t) \end{pmatrix}\det\boldsymbol{J}(\boldsymbol{\xi}_G), \tag{3.39}$$

where $\boldsymbol{\xi}_G$ are $\boldsymbol{\xi}$ coordinates evaluated at the Gauss point, W_G is Gauss point weight, and $\boldsymbol{J}$ is Jacobian matrix of the mapping $\boldsymbol{\xi} \mapsto \boldsymbol{x}^h$. It can be seen that the values of state variables need to be obtained only at the integration points for a particular value of pseudo-time. The component of the element consistent tangent stiffness matrix are

$$\boldsymbol{K}_{ab}^{(e)} = \frac{\partial \boldsymbol{r}_a^{(e)}}{\partial \boldsymbol{u}_b} = \sum_{G=1}^{4} W_G \tilde{\tilde{\boldsymbol{B}}}_a^T \left(\boldsymbol{\xi}_G\right) \underbrace{\frac{\partial \boldsymbol{\sigma}\left(\boldsymbol{\xi}_G, t\right)}{\partial \boldsymbol{\varepsilon}^h}}_{\dot{\boldsymbol{\sigma}}\dot{\boldsymbol{\varepsilon}}^{-1}(\boldsymbol{\xi}_G,t)=\boldsymbol{C}^{ep}(\boldsymbol{\xi}_G,t)} \underbrace{\frac{\partial \boldsymbol{\varepsilon}^h\left(\boldsymbol{\xi}_G, t\right)}{\partial \boldsymbol{u}_b}}_{\tilde{\tilde{\boldsymbol{B}}}_b(\boldsymbol{\xi}_G)} \det \boldsymbol{J}\left(\boldsymbol{\xi}_G\right). \tag{3.40}$$

The element consistent stiffness matrix and the element residual vector follow from (3.39) and (3.40) as

$$\boldsymbol{K}^{(e)} = \left[\boldsymbol{K}_{ab}^{(e)}\right], \qquad \boldsymbol{r}^{(e)} = \left[\boldsymbol{r}_a^{(e),T}\right]^T, \qquad a, b = 1, 2, 3, 4\ . \tag{3.41}$$

The assembly procedure follows the usual approach explained in the finite element textbooks, e.g. [Ibrahimbegovic, 2006]. The resulting nonlinear equations for nodal displacements/rotations of the chosen finite element mesh are solved by incremental/iterative Newton-Raphson solution procedure.

3.3.2 Computational issues for plasticity

As a result of space discretization, addressed in the previous section, the evolution equations (3.20) become ordinary differential equations in time that need to be integrated numerically at each integration point. Backward Euler integration scheme is used for that end. The solution is searched for at discrete pseudo-time points $0 < t_1 < \ldots t_n < t_{n+1} \ldots < T$. At a typical pseudo-time increment $\Delta t = t_{n+1} - t_n$ and typical integration point located at $\boldsymbol{x}^h\left(\boldsymbol{\xi}_G\right) \in \Omega^e$ the problem can be stated as: By knowing the values of the internal variables at the beginning of the pseudo-time increment, i.e. $\boldsymbol{\varepsilon}_n^p, \xi_n$, $\varkappa_n$, find values of the internal variables at the end of the pseudo-time increment, i.e. $\boldsymbol{\varepsilon}_{n+1}^p, \xi_{n+1}$, $\varkappa_{n+1}$, which should satisfy the yield criterion. In the spirit of the operator split method [Ibrahimbegovic, 2006] one assumes that the best iterative guess for strains at the end of the pseudo-time increment, $\boldsymbol{\varepsilon}_{n+1}^{(i)}$, is given data. Here (i) is iteration counter of the (global) Newton-Raphson solution procedure.

Prior to the integration of evolution equations, the following test is performed: assume that the pseudo-time step from t_n to t_{n+1} remains elastic and evaluate the trial (test) values of strain-like and stress-like internal variables

$$\boldsymbol{\sigma}_{n+1}^{trial} = \boldsymbol{C}\left(\boldsymbol{\varepsilon}_{n+1}^{(i)} - \underbrace{\boldsymbol{\varepsilon}_{n+1}^{p,trial}}_{\boldsymbol{\varepsilon}_n^p}\right), \qquad q_{n+1}^{trial} = -\Xi'\left(\underbrace{\xi_{n+1}^{trial}}_{\xi_n}\right), \qquad \boldsymbol{\alpha}_{n+1}^{trial} = -\frac{2}{3} H_{kin} \underbrace{\varkappa_{n+1}^{trial}}_{\varkappa_n}. \tag{3.42}$$

If the yield function evaluated with those trial variables $\phi_{n+1}^{tr} = \phi\left(\boldsymbol{\sigma}_{n+1}^{trial}, q_{n+1}^{trial}, \boldsymbol{\alpha}_{n+1}^{trial}\right) \leq 0$, then, see (3.21), $\gamma_{n+1} = \dot{\gamma}\Delta t = 0$. The final values at the end of the pseudo-time increment (marked with the bar) equal the trial values, i.e. $\overline{\boldsymbol{\varepsilon}}_{n+1}^{p} = \boldsymbol{\varepsilon}_{n+1}^{p,trial}$, $\overline{\xi}_{n+1} = \xi_{n+1}^{trial}$ and $\overline{\varkappa}_{n+1} = \varkappa_{n+1}^{trial}$. The pseudo-time step is indeed elastic.

In the case that the yield function for those trial variables is violated, then $\gamma_{n+1} > 0$ and $\phi_{n+1} = 0$. Backward Euler integration of evolution equations is performed, i.e.

$$\boldsymbol{\varepsilon}_{n+1}^{p} = \boldsymbol{\varepsilon}_{n}^{p} + \gamma_{n+1}\boldsymbol{\nu}_{n+1}, \qquad \xi_{n+1} = \xi_n + \gamma_{n+1}\beta_{n+1}, \qquad \varkappa_{n+1} = \varkappa_n + \gamma_{n+1}\boldsymbol{\nu}_{n+1}. \tag{3.43}$$

Equations (3.43) and $\phi_{n+1} = 0$ can be written as the following set of nonlinear equations (with respect to $\boldsymbol{\varepsilon}_{n+1}^{p} = \varkappa_{n+1}$, ξ_{n+1} and γ_{n+1})

$$\begin{gathered}
\boldsymbol{\varepsilon}_{n+1}^{p} - \boldsymbol{\varepsilon}_{n}^{p} - \gamma_{n+1} 2\boldsymbol{A}\left(\boldsymbol{C}\left(\boldsymbol{\varepsilon}_{n+1}^{(i)} - \boldsymbol{\varepsilon}_{n+1}^{p}\right) - \frac{2}{3}H_{kin}\boldsymbol{\varepsilon}_{n+1}^{p}\right) = \boldsymbol{0}, \\
\xi_{n+1} - \xi_n - \gamma_{n+1}\frac{2}{\sigma_y}\left(1 + \frac{\Xi'\left(\xi_{n+1}\right)}{\sigma_y}\right) = 0, \\
\left(\boldsymbol{C}\left(\boldsymbol{\varepsilon}_{n+1}^{(i)} - \boldsymbol{\varepsilon}_{n+1}^{p}\right) - \frac{2}{3}H_{kin}\boldsymbol{\varepsilon}_{n+1}^{p}\right)^T \boldsymbol{A}\left(\boldsymbol{C}\left(\boldsymbol{\varepsilon}_{n+1}^{(i)} - \boldsymbol{\varepsilon}_{n+1}^{p}\right) - \frac{2}{3}H_{kin}\boldsymbol{\varepsilon}_{n+1}^{p}\right) - \left(1 + \frac{\Xi'\left(\xi_{n+1}\right)}{\sigma_y}\right)^2 = 0,
\end{gathered} \tag{3.44}$$

which can be solved iteratively by Newton procedure to get the final values $\overline{\boldsymbol{\varepsilon}}_{n+1}^{p}$, $\overline{\xi}_{n+1}$ and $\overline{\gamma}_{n+1}$.

For more effective solution of (3.43) one can write relations (3.16) and (3.17) as, see (3.20)

$$\begin{aligned}
\boldsymbol{\sigma}_{n+1} &= \boldsymbol{C}\left(\boldsymbol{\varepsilon}_{n+1}^{(i)} - \boldsymbol{\varepsilon}_{n+1}^{p,trial}\right) = \boldsymbol{\sigma}_{n+1}^{trial} - \gamma_{n+1}\boldsymbol{C}\underbrace{2\boldsymbol{A}\left(\boldsymbol{\sigma}_{n+1} + \boldsymbol{\alpha}_{n+1}\right)}_{\boldsymbol{\nu}_{n+1}}, \\
q_{n+1} &= -\Xi'(\xi_{n+1}), \quad \xi_{n+1} = \xi_n + \gamma_{n+1}\underbrace{\frac{2}{\sigma_y}\sqrt{\left(\boldsymbol{\sigma}_{n+1} + \boldsymbol{\alpha}_{n+1}\right)^T \boldsymbol{A}\left(\boldsymbol{\sigma}_{n+1} + \boldsymbol{\alpha}_{n+1}\right)}}_{\beta_{n+1}}, \\
\boldsymbol{\alpha}_{n+1} &= -\frac{2}{3}H_{kin}\varkappa_{n+1} = \boldsymbol{\alpha}_{n+1}^{trial} - \gamma_{n+1}\frac{2}{3}H_{kin}\underbrace{2\boldsymbol{A}\left(\boldsymbol{\sigma}_{n+1} + \boldsymbol{\alpha}_{n+1}\right)}_{\boldsymbol{\nu}_{n+1}},
\end{aligned} \tag{3.45}$$

which leads to

$$\begin{aligned}
\left(\boldsymbol{\sigma}_{n+1} + \boldsymbol{\alpha}_{n+1}\right) &= \underbrace{\left[\boldsymbol{I}_5 + \gamma_{n+1}\left(2\boldsymbol{C}\boldsymbol{A} + \frac{4}{3}H_{kin}\boldsymbol{A}\right)\right]^{-1}}_{\boldsymbol{W}_{n+1}(\gamma_{n+1})}\left(\boldsymbol{\sigma}_{n+1}^{trial} + \boldsymbol{\alpha}_{n+1}^{trial}\right), \\
q_{n+1} &= q_{n+1}\left(\gamma_{n+1}\right).
\end{aligned} \tag{3.46}$$

A closed form expression for the inverse of the matrix in (3.46) can be obtained by using spectral decomposition of $\boldsymbol{C}$ and $\boldsymbol{A}$; the procedure is very similar to the one at the plane stress situation, see [Ibrahimbegovic and Frey, 1993a], [Simo and Hughes, 1998], [Simo

and Kennedy, 1992], [Kleiber and Kowalczyk, 1996], and will not be repeated here, see e.g. [Brank, 1994] for details. Explicit inversion of $\boldsymbol{W}_{n+1}$ enables expressing $(\boldsymbol{\sigma}_{n+1} + \boldsymbol{\alpha}_{n+1})$ in terms of single unknown γ_{n+1}. Since $\gamma_{n+1}\phi_{n+1} = 0$, see (3.21), one gets a single nonlinear equation in terms of γ_{n+1}

$$\phi_{n+1}((\boldsymbol{\sigma}_{n+1} + \boldsymbol{\alpha}_{n+1})(\gamma_{n+1}), q_{n+1}(\gamma_{n+1})) = \phi_{n+1}(\gamma_{n+1}) = 0. \tag{3.47}$$

The solution of (3.47) is obtained by Newton iterative procedure

$$-\phi'^{(k)}_{n+1}\Delta\gamma^{(k)}_{n+1} = \phi^{(k)}_{n+1}, \qquad \gamma^{(k+1)}_{n+1} = \gamma^{(k)}_{n+1} + \Delta\gamma^{(k)}_{n+1}, \tag{3.48}$$

where (k) is iteration counter and $\phi'_{n+1} = \frac{d\phi_{n+1}}{d\gamma_{n+1}}$. The final (converged) solution of (3.47) is marked by the bar, i.e. $\overline{\gamma}_{n+1}$. The final values at the end of the pseudo-time increment are also marked with the bar; for example $\overline{\boldsymbol{\varepsilon}}^p_{n+1} = \overline{\varkappa}_{n+1}$ and $\overline{\xi}_{n+1}$ can be computed from (3.46) and (3.43) by using $\overline{\gamma}_{n+1}$.

Remark 3.4. *Numerical experiments show that for the present case the function $\phi^{(k)}_{n+1}$ may be very steep; i.e. very large differences in function value can be obtained for small differences in function argument. However, no difficulties in computation of the numerical examples presented below were observed if the convergence criterion was based on the value of $\phi^{(k)}_{n+1}$; we used $\phi^{(k)}_{n+1} < 10^{-12}$ for convergence criterion.*

Remark 3.5. *When yield function with $\alpha(t)$, see (3.13), was used in the numerical computations, the equivalent plastic curvature (3.14) of the pseudo-time increment $[t_n, t_{n+1}]$ was evaluated with $\check{\kappa}^p_n$ and α_n. The $\check{\kappa}^p_{n+1}$ for the next time step was calculated with numerical integration of equation (3.14)*

$$\check{\kappa}^p_{n+1} = \check{\kappa}^p_n + \frac{Eh}{\sqrt{3}\sigma_y}\left[(\Delta\overline{\kappa}^p_{11,n+1})^2 + (\Delta\overline{\kappa}^p_{22,n+1})^2 + \Delta\overline{\kappa}^p_{11,n+1}\,\Delta\overline{\kappa}^p_{22,n+1} + (\Delta\overline{\kappa}^p_{12,n+1})^2/4\right]^{\frac{1}{2}}, \tag{3.49}$$

where $\Delta\overline{\kappa}^p_{11,n+1}, \Delta\overline{\kappa}^p_{22,n+1}, \Delta\overline{\kappa}^p_{12,n+1}$ are the first three components of $\Delta\overline{\boldsymbol{\varepsilon}}^p_{n+1} = \overline{\gamma}_{n+1}\overline{\boldsymbol{\nu}}_{n+1}$.

To complete the elastoplastic implementation issues the consistent tangent matrix $d\boldsymbol{\sigma}_{n+1}/d\boldsymbol{\varepsilon}^{(i)}_{n+1}$ has to be derived for $\gamma_{n+1} > 0$. It is obtained by differentiation of $\boldsymbol{\varepsilon}^{(i)}_{n+1} = \boldsymbol{C}^{-1}\boldsymbol{\sigma}_{n+1} + \boldsymbol{\varepsilon}^p_{n+1}$, eqs. (3.43), and consistency condition $d\phi_{n+1} = 0$. After some manipulation one can have

$$d\boldsymbol{\sigma}_{n+1} = \left[\boldsymbol{C}^{-1} + 2\overline{\gamma}_{n+1}\boldsymbol{H}_{n+1}\boldsymbol{A} + \frac{3}{2\overline{f}_{n+1}H_{kin} + 6\overline{c}_{n+1}}\boldsymbol{H}_{n+1}\overline{\boldsymbol{\nu}}_{n+1}\overline{\boldsymbol{\nu}}^T_{n+1}\boldsymbol{H}_{n+1}\right]^{-1} d\boldsymbol{\varepsilon}^{(i)}_{n+1}, \tag{3.50}$$

where

$$\boldsymbol{H}_{n+1}^{-1} = \boldsymbol{I}_5 + \frac{4}{3}\gamma_{n+1} H_{kin} \boldsymbol{A},\ \overline{f}_{n+1} = \overline{\boldsymbol{\nu}}_{n+1}^T \boldsymbol{H}_{n+1} \overline{\boldsymbol{\nu}}_{n+1},\ \overline{c}_{n+1} = \frac{2\left(1 + \frac{\Xi'(\overline{\xi}_{n+1})}{\sigma_y}\right)^2 \Xi''\left(\overline{\xi}_{n+1}\right)}{\sigma_y^2 - 2\overline{\gamma}_{n+1}\Xi''\left(\overline{\xi}_{n+1}\right)}. \tag{3.51}$$

The inverse of $\boldsymbol{H}_{n+1}^{-1}$ can be obtained in closed form. The matrix in (3.50) can be obtained in closed form as well by using Sherman-Morrison formula, see e.g. [Press et al., 1992].

3.3.3 Computational issues for viscoplasticity

The above discussed viscoplastic plate model allows one to define a unified framework for both stress resultant elastoplasticity and stress resultant viscoplasticity for plates. Namely, the integration procedure for the plate viscoplasticity is essentially the same as for the plate plasticity, except that for $\phi_{n+1}^{tr} > 0$ one looks for $\gamma_{n+1} = \frac{\Delta t}{\eta}\langle\phi_{n+1}\rangle > 0$. Its final value is obtained by iterative solution of nonlinear equation

$$-\frac{\eta}{\Delta t}\gamma_{n+1} + \phi_{n+1}\left(\gamma_{n+1}\right) = 0 \rightarrow \overline{\gamma}_{n+1}. \tag{3.52}$$

The consistent tangent matrix is obtained in the same manner as for plasticity except that one has to replace in its derivation the consistency condition $d\phi_{n+1} = 0$ by $d\phi_{n+1} - \frac{\eta}{\Delta t} d\gamma_{n+1} = 0$. The form of the consistent tangent matrix is the same as (3.50) except that $\overline{c}_{n+1}$ is replaced by $\overline{c}_{n+1} + \frac{\eta}{\Delta t}$.

3.4 Numerical examples

The finite element code for inelastic plate analysis was generated by using symbolic code manipulation program AceGen developed by Korelc [Korelc, 2007b] and implemented into the finite element analysis program AceFEM, see [Korelc, 2007a]. We note that the plate element used in this work is locking-free as shown in [Ibrahimbegovic, 1993] (see results for PQ2 element).

3.4.1 Limit load analysis of a rectangular plate

A rectangular plate of elastic-perfectly plastic material under uniformly distributed load is analyzed for two sets of boundary conditions: simple supported (of hard type) and clamped (of hard type). The plate characteristics are: thickness $h = 0.5\ cm$, length $l = 150\ cm$, width $b = 100\ cm$. Material parameters are: Young's modulus $E = 21000\ kN/cm^2$, Poisson's ration $\nu = 0.3$ and yield stress $\sigma_y = 40\ kN/cm^2$. Numerical analysis was performed with a coarse mesh of 8×8 and with a fine mesh of 60×40 elements, see Figure 3.6. We compare our results with those obtained by ABAQUS' [Hobbit

et al., 2007] quadrilateral shell element (S4R element) with through-the-thickness stress integration (with 5 integration points) and von Mises yield criterion. Load-displacement

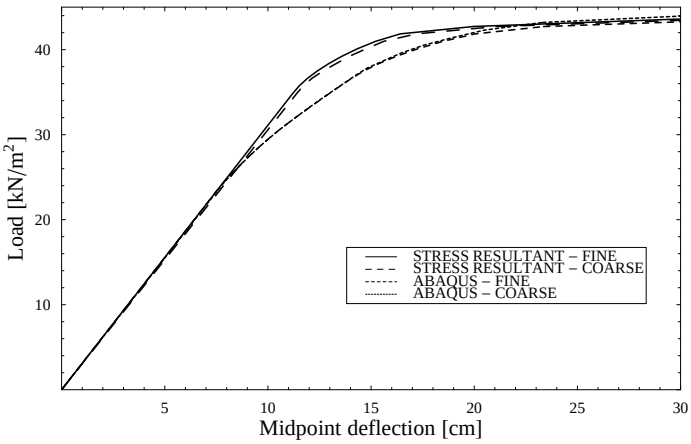

Figure 3.2: Load - displacement diagram for simply supported rectangular plate

Slika 3.2: Diagram obtežba pomik pri prostoležeči pravokotni plošči

curves are presented in Figures 3.2 and 3.3. There is a difference in results of both analyses since the stress resultant formulation does not account for gradual through-the-thickness plastification. However, equal limit load is obtained in both cases. It is interesting to see that the mesh density plays more important role in the accuracy of the limit load computation than the chosen way of definition of elastoplastic constitutive model. Namely, the difference between the coarse and fine mesh in predicting the limit load is around 20 % for the clamped plate, see Figure 3.3. By replacing m_0 with αm_0, we can estimate gradual spreading of plastic zones through the thickness. In Figures 3.4 and 3.5 we present load-displacement curves obtained by using α parameter and coarse mesh. We used a constant value of α across one time increment and therefore the yield criterion is no longer smooth in pseudo-time. To reduce the influence of this effect we used small time increments. In case of simply supported plate (Figure 3.4) the first yield is well predicted, yet the curve in subsequent states is below the ABAQUS' curve. Results for clamped plate are much better since one can hardly distinguish between ABAQUS and stress resultant formulation when using time increment $\Delta t = 0.0025$.

3.4.2 Limit load analysis of a circular plate

We analyze a uniformly loaded circular plate of the same elastic-perfectly plastic material as in the previous example. Again we consider simply supported and clamped plates.

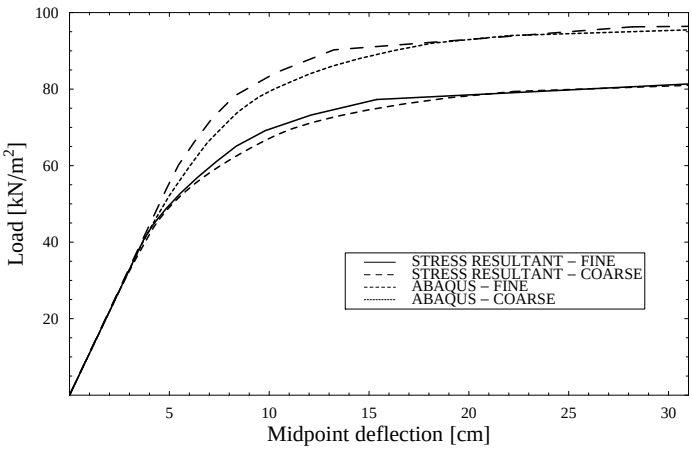

Figure 3.3: Load - displacement diagram for clamped rectangular plate

Slika 3.3: Diagram obtežba pomik pri vpeti pravokotni plošči

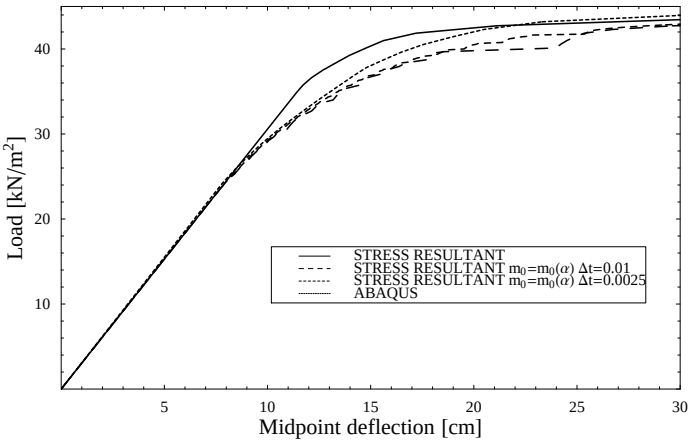

Figure 3.4: Load - displacement diagram for simply supported rectangular plate; α parameter case

Slika 3.4: Diagram obtežba pomik pri prostoležeči pravokotni plošči v primeru uporabe parametra α

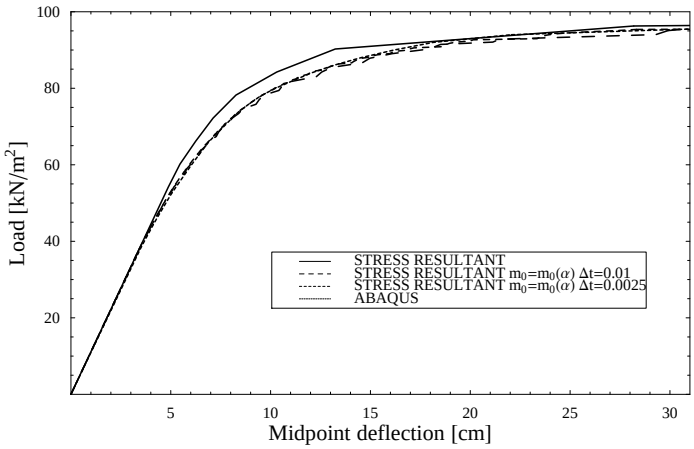

Figure 3.5: Load - displacement diagram for clamped rectangular plate; α parameter case

Slika 3.5: Diagram obtežba pomik pri vpeti pravokotni plošči v primeru uporabe parametra α

The radius of the plate is $r = 50\ cm$ and the thickness is $h = 0.5\ cm$. The meshes are shown in Figure 3.6. In Figures 3.7 and 3.8 we plot load-displacement curves. Again we see that the coarse mesh overestimates limit load in the case of clamped plate. Overall correspondence of two formulations is reasonable. In Tables 3.1 and 3.2 we compare our

Limit load	Yield criterion	Reference
$q = 1.629\frac{h^2}{r^2}\sigma_y$	present	present (fine mesh)
$q = 1.625\frac{h^2}{r^2}\sigma_y$	-	[Eurocode 3, 2007]
$q = 1.500\frac{h^2}{r^2}\sigma_y$	Tresca (analytical solution)	[Lubliner, 1990], [Sawczuk, 1989]
$q = 1.629\frac{h^2}{r^2}\sigma_y$	Von Mises (analytical solution)	[Sawczuk, 1989]
$q = 2.000\frac{h^2}{r^2}\sigma_y$	Von Mises (analytical upper bound)	[Sawczuk, 1989]
$q = 1.500\frac{h^2}{r^2}\sigma_y$	Von Mises (analytical lower bound)	[Sawczuk, 1989]

Table 3.1: Limit load solutions for circular simply supported plate

Tabela 3.1: Mejne obtežbe pri prostoležeči krožni krožni plošči

results for limit load with analytical solutions found in textbooks on plasticity [Lubliner, 1990], [Sawczuk, 1989] and Eurocode [Eurocode 3, 2007]. Our result for simply supported plate is in complete agreement with solution based on von Mises yield criterion, see Table 3.1. In the case of clamped plate our result is slightly greater than the von Mises yield based solution, see Table 3.2.

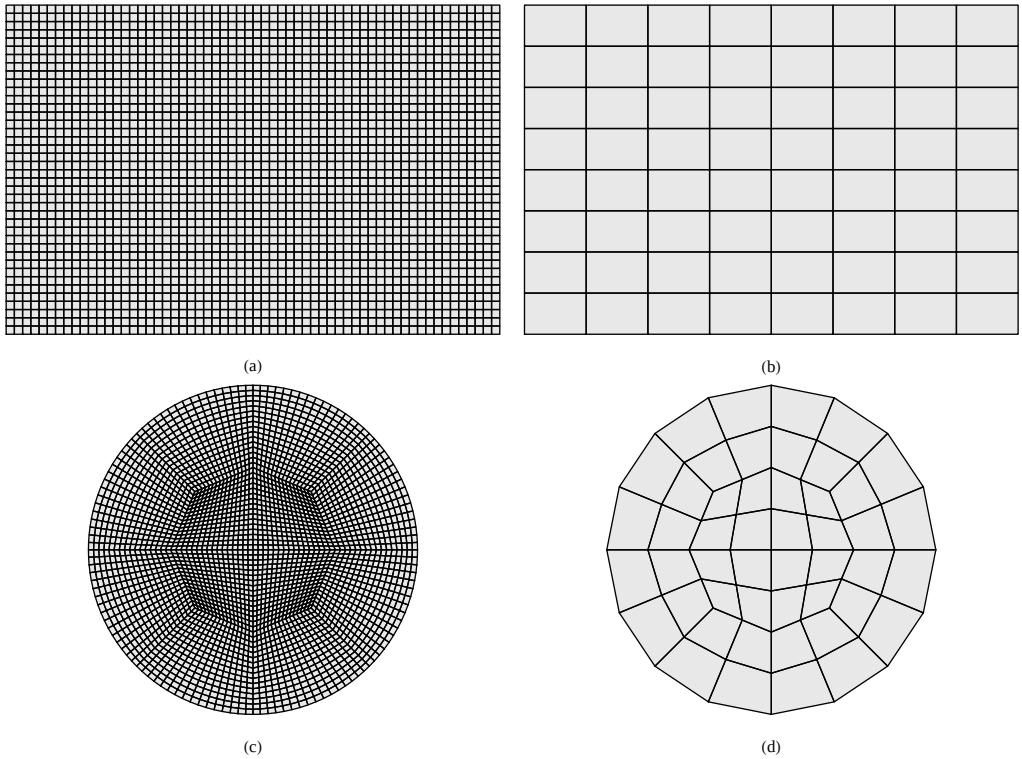

Figure 3.6: Meshes used for: (a) rectangular plate - fine, (b) rectangular plate - coarse, (c) circular plate - fine and (d) circular plate - coarse

Slika 3.6: Uporabljene mreže: (a) pravokotna plošča - fina, (b) pravokotna plošča - groba, (c) krožna plošča - fina in (d) krožna plošča - groba

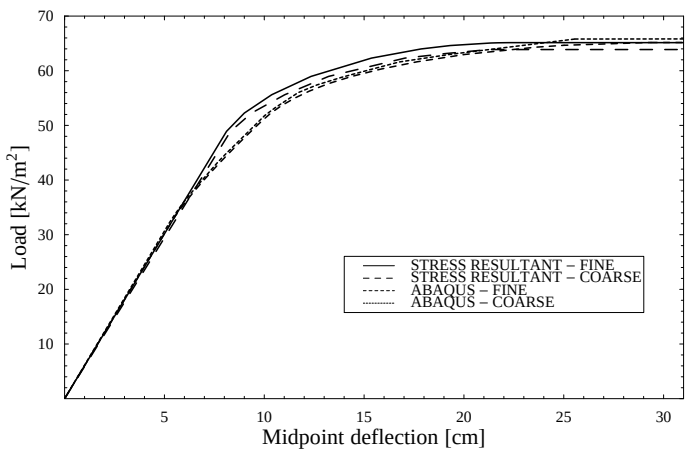

Figure 3.7: Simply supported circular plate - limit load analysis

Slika 3.7: Prostoležeča krožna plošča - analiza mejne obtežbe

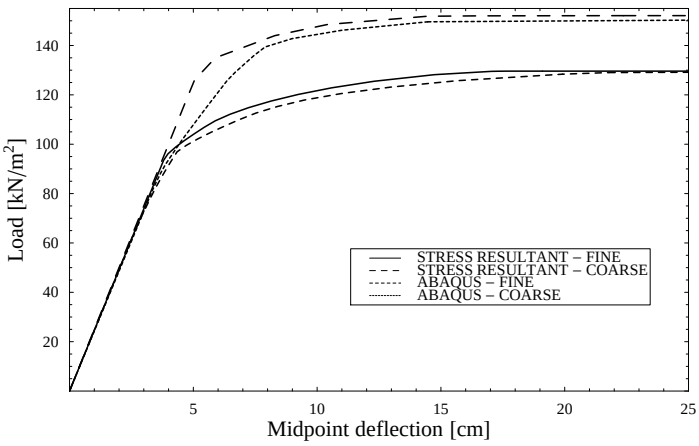

Figure 3.8: Clamped circular plate - limit load analysis

Slika 3.8: Vpeta krožna plošča - analiza mejne obtežbe

Limit load	Yield criterion	Reference
$q = 3.240\frac{h^2}{r^2}\sigma_y$	present	present (fine mesh)
$q = 3.125\frac{h^2}{r^2}\sigma_y$	-	[Eurocode 3, 2007]
$q = 2.815\frac{h^2}{r^2}\sigma_y$	Tresca (analytical solution)	[Lubliner, 1990], [Sawczuk, 1989]
$q = 3.138\frac{h^2}{r^2}\sigma_y$	Von Mises (analytical solution)	[Sawczuk, 1989]

Table 3.2: Limit load solutions for circular clamped plate

Tabela 3.2: Mejne obtežbe pri vpeti krožni krožni plošči

3.4.3 Elastoplastic analysis of a skew plate

We consider a skew plate of elastic-plastic material with hardening under uniformly distributed load. The plate thickness is $h = 0.5\ cm$, the longer side is $a = 150\ cm$, the shorter one is $b = 135\ cm$ and the in-between angle is $\phi = 45°$. All material properties are the same as in the above examples, except for isotropic hardening modulus, which is now $H_{iso} = 0.1E = 2100kN/cm^2$. The plate is supported along the shorter edges with five equally spaced point supports restraining displacements and allowing both rotations. Mesh is shown in Figure 3.9. Load versus centre displacement diagrams are presented

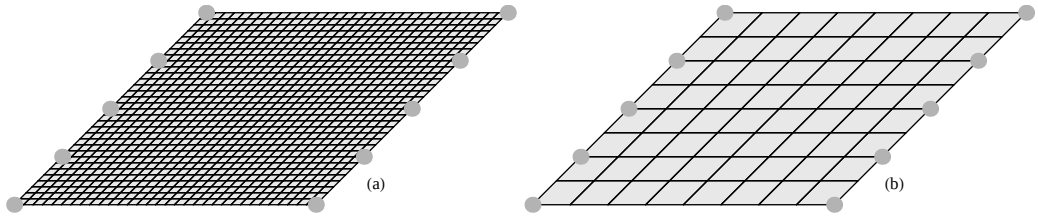

Figure 3.9: Skew plate - (a) fine mesh, (b) coarse mesh

Slika 3.9: Romboidna plošča - (a) fina mreža, (b) groba mreža

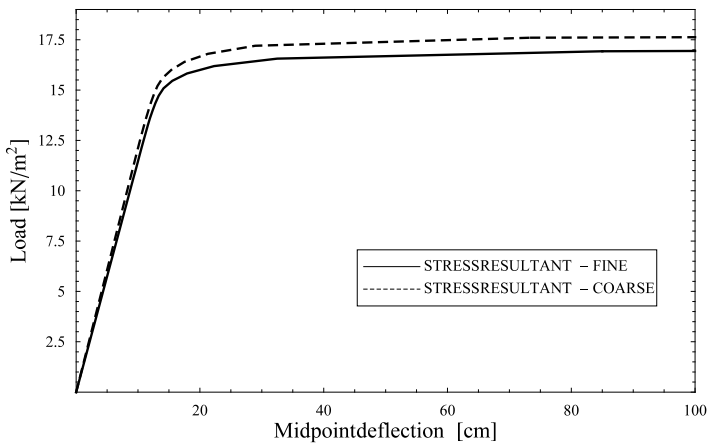

Figure 3.10: Skew plate - elastoplastic analysis

Slika 3.10: Romboidna plošča - elastoplastična analiza

in Figure 3.10. Both curves have similar shapes, yet the curve obtained with the coarse mesh is again above the curve obtained with the fine mesh. We see that the yielding of the plate significantly reduces its stiffness, yet the limit load is never reached because of the isotropic hardening. When using stress resultant plasticity model one can easily track

the spreading of plastic zones. In Figure 3.11 we see that the yielding starts in the corners

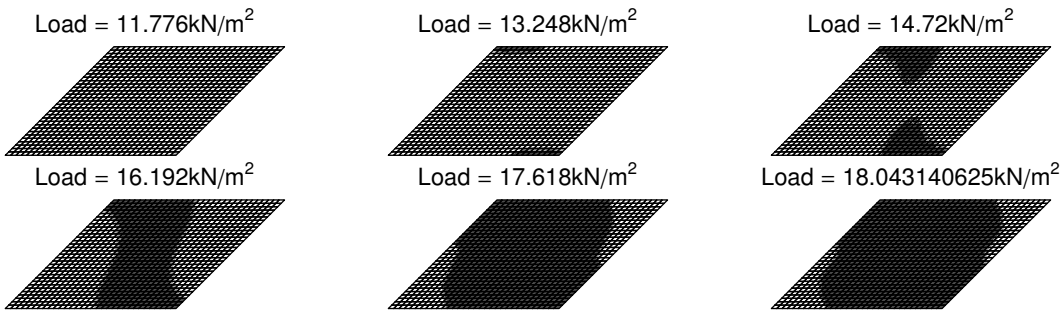

Figure 3.11: Spreading of plastic zones

Slika 3.11: Širjenje plastificiranega območja

of the shorter diagonal, then it reaches the centre of the plate and spreads in the direction of longer diagonal corners.

3.4.4 Cyclic analysis of a circular plate

We consider a clamped circular plate under cyclic loading conditions. The plate is loaded with uniformly distributed load with the amplitude that corresponds to twice of the load at the first yield $p_{max} = 2\left(1.5(\frac{h}{r})^2\sigma_y\right)$. We examine three hardening cases: (i) isotropic hardening ($H_{iso} = 2100\ kN/cm^2$, $H_{kin} = 0\ kN/cm^2$), (ii) kinematic hardening ($H_{iso} = 0\ kN/cm^2$, $H_{kin} = 2100\ kN/cm^2$), (iii) combined isotropic and kinematic hardening ($H_{iso} = H_{kin} = 1050\ kN/cm^2$). The remaining material and geometry parameters are the same as those adopted for the limit load analysis, except for plate thickness which is now $h = 4\ cm$. In Figure 3.12 the load-displacement curves for the first two cycles are presented for stress resultant formulation and stress resultant formulation with parameter α. Isotropic hardening enlarges the yield surface which can be seen in Figure 3.12 where the curve appears as a closed loop after the first cycle. After the initial cycle the plate can sustain greater stress resultants and still remain elastic. The shift of the initial curve to the right represents the plastic deformation. Purely kinematic hardening curve is wider and is virtually unchanged from one cycle to another. In this case the size of the yield surface is unchanged whereas the effect of kinematic hardening changes the position of it. We can look at the combined hardening curve as a combination of the purely isotropic and purely kinematic hardening curves. Isotropic hardening effects prevail and after the first cycle the plate remains in elastic state.

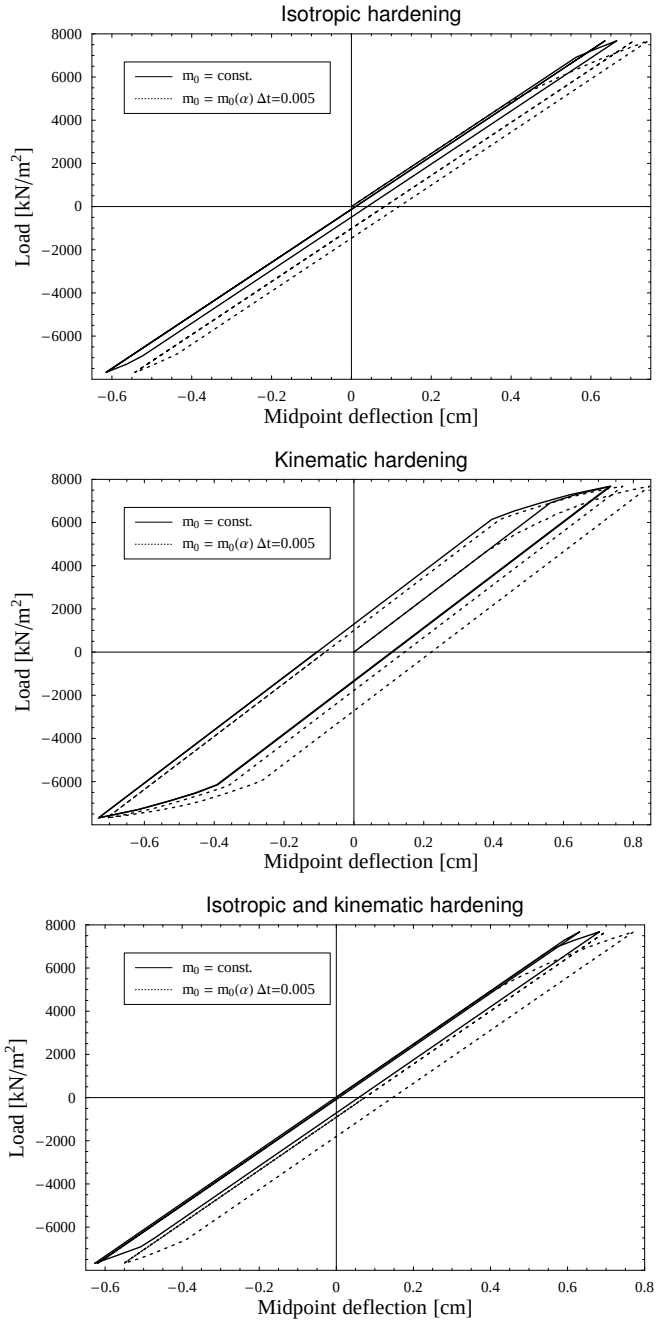

Figure 3.12: Clamped circular plate - cyclic load

Slika 3.12: Vpeta krožna plošča - ciklična obremenitev

For further elastoplastic numerical examples we direct the reader to [Dujc and Brank, 2006].

3.4.5 Elastoviscoplastic analysis of a circular plate

In this example we consider a clamped circular plate of elastoviscoplastic material. All material and geometry parameters are the same as in the case of limit load analysis. Three different values of viscosity parameter are chosen, $\eta = 0$, $\eta = 1$, $\eta = 10$, for two sets of loading conditions. In the first set we gradually apply a point load in the center of the plate until it reaches its final value $F = 22\ kN$ at time $t = 1$. The second set is displacement driven with a prescribed final value of midpoint deflection $w = 11\ cm$. Loading curves

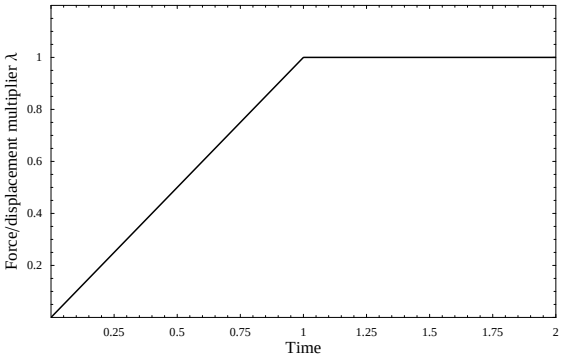

Figure 3.13: Loading curve for viscoplastic analyses

Slika 3.13: Obtežne krivulje za viskoplastične analize

for both loading sets are presented in Figure 3.13. We show the time-deflection curve of the plate under first loading condition in Figure 3.14. The viscosity coefficient η has a significant effect on a nature of inelastic response. The value $\eta = 0$ corresponds to plasticity whereas for values $\eta > 0$ the inelastic deformations are time dependent. One can note that the strain in elastoviscoplastic material held at constant stress will gradually reach the level of strain in a time independent material. Time response of the plate for the strain driven loading is presented in Figure 3.15. We see a hardening like response in viscoplastic materials ($\eta > 0$) but resistance is slowly dropping to the value corresponding to the time independent material.

3.5 Concluding remarks and chapter summary

The stress resultant plasticity for plates has been revisited and reformulated in this chapter. The basic ingredients of the constitutive law are the usual additive split of elastic

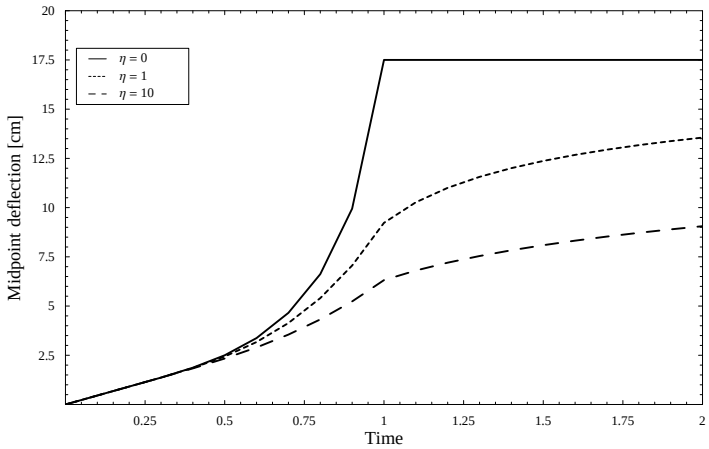

Figure 3.14: Time response for force-prescribed viscoplastic circular plate

Slika 3.14: Časovni odziv krožne plošče pri predpisani obtežbi

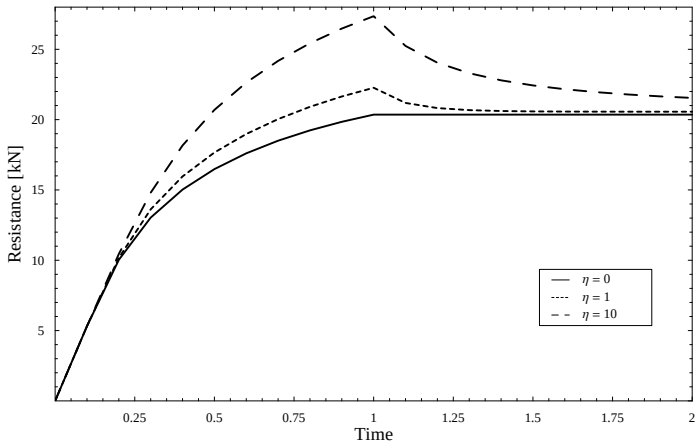

Figure 3.15: Time response for displacement-prescribed viscoplastic circular plate

Slika 3.15: Časovni odziv krožne plošče pri predpisanih pomikih

and plastic (viscoplastic) strains

$$\boldsymbol{\varepsilon} = \boldsymbol{\varepsilon}^{e} + \boldsymbol{\varepsilon}^{p,vp},$$

the strain energy function including isotropic and kinematic hardening

$$\psi\left(\boldsymbol{\varepsilon}^{e}, \xi, \check{\varkappa}\right) = \frac{1}{2}\boldsymbol{\varepsilon}^{e,T}\boldsymbol{C}\boldsymbol{\varepsilon}^{e} + \Xi\left(\xi\right) + \frac{1}{2}\left(\frac{2}{3}H_{kin}\right)\check{\varkappa}^{T}\boldsymbol{D}\check{\varkappa},$$

stress resultant yield function

$$\phi\left(\boldsymbol{\sigma}, q, \boldsymbol{\alpha}\right) = \left(\boldsymbol{\sigma} + \boldsymbol{\alpha}\right)^{T}\boldsymbol{A}\left(\boldsymbol{\sigma} + \boldsymbol{\alpha}\right) - \left(1 - \frac{q}{\sigma_y}\right)^{2} = 0,$$

and the principle of maximum plastic dissipation for the plasticity case

$$\mathcal{L}^{p}\left(\boldsymbol{\sigma}, q, \boldsymbol{\alpha}, \dot{\gamma}\right) = -\mathcal{D}^{p}\left(\boldsymbol{\sigma}, q, \boldsymbol{\alpha}\right) + \dot{\gamma}\phi\left(\boldsymbol{\sigma}, q, \boldsymbol{\alpha}\right),$$

which is in the viscoplastic case replaced by

$$\mathcal{L}^{vp}\left(\boldsymbol{\sigma}, q, \boldsymbol{\alpha}\right) = -\mathcal{D}^{vp}\left(\boldsymbol{\sigma}, q, \boldsymbol{\alpha}\right) + \frac{1}{\eta}g\left(\phi\left(\boldsymbol{\sigma}, q, \boldsymbol{\alpha}\right)\right),$$

where

$$g\left(\phi\right) = \begin{cases} \frac{1}{2}\phi^{2} & \text{if } \phi \geq 0 \\ 0 & \text{if } \phi < 0 \end{cases},$$

is the penalized functional. The update of plastic internal variables is carried out by solving only one equation

$$\phi_{n+1}(\left(\boldsymbol{\sigma}_{n+1} + \boldsymbol{\alpha}_{n+1}\right)\left(\gamma_{n+1}\right), q_{n+1}\left(\gamma_{n+1}\right)) = \phi_{n+1}\left(\gamma_{n+1}\right) = 0 \rightarrow \overline{\gamma}_{n+1},$$

while in the viscoplastic case this equation is replaced by

$$-\frac{\eta}{\Delta t}\gamma_{n+1} + \phi_{n+1}\left(\gamma_{n+1}\right) = 0 \rightarrow \overline{\gamma}_{n+1}.$$

By setting $\eta = 0$ in the viscoplastic equation we obtain the plastic case, thus both inelastic formulations can be treated within one computational framework. Numerical results of the presented formulation have been compared with the stress formulation (ABAQUS [Hobbit et al., 2007]) as well as with the stress resultant formulation with α parameter that takes into account gradual spreading of through-the-thickness plastification. It has been shown that, regarding the accuracy of the limit load computation, the mesh density plays more important role than the type of elastoplastic formulation. An extension of this work to geometrically nonlinear shells will be addressed in Chapter 4.

Chapter 4

Inelastic analysis of metal shells

4.1 Introduction

In this chapter we present an approach for an elastoplastic analysis of metal shells by using the finite element method. In our approach we use a constitutive law that is based on stress resultants, thus reducing the number of required numerical integration points in the thickness direction to only one, which makes the analysis computationally much faster with respect to the approach dealing with stress, see e.g. [Brank et al., 1997]. A similar approach was already presented in [Simo and Kennedy, 1992], with the use of a different shell finite element and a different hardening law.

In Section 4.2 we first describe the kinematics and the variational formulation of the geometrically exact shell (note that this part is included to ensure the complete description of the derived finite element, while the emphasis of this chapter is on the constitutive relations presented and the return mapping algorithms) followed by the constitutive equations for stress-resultant elastoplasticity for shells. In Section 4.3 we present the spatial finite element discretization and computational algorithms related to shell stress resultant multi-surface plasticity. The results of several numerical simulations are presented in Section 4.4. We close the chapter with concluding remarks and a short summary in Section 4.5.

4.2 Inelastic geometrically exact shell formulation

In this section we present inelastic nonlinear shell model that is formulated entirely in stress resultants and can accommodate large displacements and large rotations.

4.2.1 Geometry, kinematics and strains

We model a shell as a surface that has an inextensible unit vector (called shell director) attached at its every point. The surface, which will be called midsurface, since it represents the middle-surface of the shell, is embedded in the 3d space. The position vector of a material point in the initial (undeformed, reference) stress-free shell configuration is then defined by

$$\boldsymbol{X}\left(\xi^1,\xi^2,\xi\right)=\boldsymbol{\varphi}_0\left(\xi^1,\xi^2\right)+\xi\boldsymbol{T}\left(\xi^1,\xi^2\right),\qquad \left(\xi^1,\xi^2\right)\in\mathcal{A},\qquad \xi\in\mathcal{F}. \tag{4.1}$$

Here, ξ^1 and ξ^2 are convective curvilinear coordinates that parametrize the midsurface; $\mathcal{A}$ is the domain of that parametrization; $\boldsymbol{T}$, $\|\boldsymbol{T}\|=1$, is the shell director that coincides with the normal vector to the midsurface; and ξ is through-the-thickness convective coordinate defined in the domain $\mathcal{F}=[-h/2,h/2]$, where h represents initial shell thickness, here assumed to be constant. In what follows, we always determine the components of the above vectors with respect to the fixed orthonormal basis $\boldsymbol{e}_i=\boldsymbol{e}^i$, $i=1,2,3$, in the 3d space, i.e. $\boldsymbol{X}=X^i\boldsymbol{e}_i$, $\boldsymbol{\varphi}_0=\varphi_0^i\boldsymbol{e}_i$, $\boldsymbol{T}=T^i\boldsymbol{e}_i$. We further define the shell director as $\boldsymbol{T}=\boldsymbol{\Lambda}_0\boldsymbol{e}_3$, where $\boldsymbol{\Lambda}_0$ is a given (initial) rotation tensor, $\boldsymbol{\Lambda}_0^{-1}=\boldsymbol{\Lambda}_0^T$, $\det\boldsymbol{\Lambda}_0=1$. If one introduces at a point of midsurface an orthonormal basis $\widehat{\boldsymbol{e}}_i=\widehat{\boldsymbol{e}}^i$ as

$$\widehat{\boldsymbol{e}}_3\equiv\boldsymbol{T},\quad \widehat{\boldsymbol{e}}_1\perp\widehat{\boldsymbol{e}}_3,\quad \|\widehat{\boldsymbol{e}}_1\|=1,\quad \widehat{\boldsymbol{e}}_2=\widehat{\boldsymbol{e}}_3\times\widehat{\boldsymbol{e}}_1, \tag{4.2}$$

the rotation tensor $\boldsymbol{\Lambda}_0$ at that point can be represented as $\boldsymbol{\Lambda}_0=[\widehat{\boldsymbol{e}}_1,\widehat{\boldsymbol{e}}_2,\boldsymbol{T}]$. It is further assumed that the position vector to the material point in the deformed configuration is given by

$$\boldsymbol{x}\left(\xi^1,\xi^2,\xi\right)=\underbrace{\left[\boldsymbol{\varphi}_0\left(\xi^1,\xi^2\right)+\boldsymbol{u}\left(\xi^1,\xi^2\right)\right]}_{\boldsymbol{\varphi}(\xi^1,\xi^2)}+\xi\boldsymbol{t}\left(\xi^1,\xi^2\right),\qquad \|\boldsymbol{t}\|=1. \tag{4.3}$$

In (4.3) $\boldsymbol{u}$ is a displacement vector of a midsurface point, and $\boldsymbol{t}$ is new position of shell director at the deformed configuration. We will define $\boldsymbol{t}$ as the following sequence of two rotations $\boldsymbol{t}=\boldsymbol{\Lambda}_0\boldsymbol{\Lambda}\boldsymbol{e}_3$. The components of newly defined vectors in (4.3) are also determined with respect to the fixed orthonormal basis $\boldsymbol{e}_i$, i.e. $\boldsymbol{x}=x^i\boldsymbol{e}_i$, $\boldsymbol{\varphi}=\varphi^i\boldsymbol{e}_i$, $\boldsymbol{u}=u^i\boldsymbol{e}_i$, and $\boldsymbol{t}=t^i\boldsymbol{e}_i$. The rotation tensor $\boldsymbol{\Lambda}$ is viewed in this work as a function of a constrained rotation vector $\boldsymbol{\vartheta}$, i.e. $\boldsymbol{\Lambda}=\widetilde{\boldsymbol{\Lambda}}\left(\boldsymbol{\vartheta}\right)$, see e.g. [Brank and Ibrahimbegovic, 2001] and [Brank et al., 1997] for details. Since the rotation around the shell director (i.e. drilling rotation) plays no role in the present theory, the constrained rotation vector has only two components with respect to the basis $\widehat{\boldsymbol{e}}_i$, i.e. $\boldsymbol{\vartheta}=\vartheta^\alpha\widehat{\boldsymbol{e}}_\alpha$, $\alpha=1,2$. By using the Rodrigues formula for the representation of $\widetilde{\boldsymbol{\Lambda}}\left(\boldsymbol{\vartheta}\right)$, one ends up with the following expression for $\boldsymbol{t}=\boldsymbol{t}\left(\boldsymbol{\vartheta}\right)$, see [Brank and Ibrahimbegovic, 2001]

$$\boldsymbol{t}=\boldsymbol{\Lambda}_0\left(\cos\vartheta\boldsymbol{e}_3+\frac{\sin\vartheta}{\vartheta}\boldsymbol{\vartheta}\times\boldsymbol{e}_3\right),\qquad \vartheta=\|\boldsymbol{\vartheta}\|. \tag{4.4}$$

The vectors of the convected basis $\boldsymbol{G}_i$ at the initial configuration are related to the position vector $\boldsymbol{X}$ and to the convected coordinates ξ^α, ξ as

$$\boldsymbol{G}_\alpha = \frac{\partial \boldsymbol{X}}{\partial \xi^\alpha} = \frac{\partial \boldsymbol{\varphi}_0}{\partial \xi^\alpha} + \xi \frac{\partial \boldsymbol{T}}{\partial \xi^\alpha}, \qquad \boldsymbol{G}_3 = \frac{\partial \boldsymbol{X}}{\partial \xi} = \boldsymbol{T}. \tag{4.5}$$

Similarly, the vectors of the convected basis $\boldsymbol{g}_i$ at the deformed configuration are

$$\boldsymbol{g}_\alpha = \frac{\partial \boldsymbol{x}}{\partial \xi^\alpha} = \frac{\partial \boldsymbol{\varphi}}{\partial \xi^\alpha} + \xi \frac{\partial \boldsymbol{t}}{\partial \xi^\alpha}, \qquad \boldsymbol{g}_3 = \frac{\partial \boldsymbol{x}}{\partial \xi} = \boldsymbol{t}. \tag{4.6}$$

The corresponding dual base vectors $\boldsymbol{G}^i$ and $\boldsymbol{g}^i$ are defined through the relationships $\boldsymbol{G}_i \cdot \boldsymbol{G}^j = \delta_i^j$ and $\boldsymbol{g}_i \cdot \boldsymbol{g}^j = \delta_i^j$, where δ_i^j is a Kronecker symbol. Note that $\boldsymbol{G}^3 = \boldsymbol{G}_3$. The identity tensor of the shell reference configuration (or the shell metric tensor) is $\boldsymbol{G} = \boldsymbol{G}_i \otimes \boldsymbol{G}^j = G_{ij}\boldsymbol{G}^i \otimes \boldsymbol{G}^j$, where $G_{ij} = \boldsymbol{G}_i \cdot \boldsymbol{G}_j$. The differential volume element is given as $dV = \sqrt{G} d\xi d\xi^1 d\xi^2$, where $\sqrt{G} = \boldsymbol{G}_3 \cdot (\boldsymbol{G}_1 \times \boldsymbol{G}_2)$. The base vectors at the reference midsurface and at the deformed midsurface are obtained by setting $\xi = 0$ in (4.5) and (4.6), respectively, i.e. $\boldsymbol{A}_i = \boldsymbol{G}_i|_{\xi=0}$, and $\boldsymbol{a}_i = \boldsymbol{g}_i|_{\xi=0}$. For the reference configuration we have

$$\boldsymbol{A}_\alpha = \frac{\partial \boldsymbol{\varphi}_0}{\partial \xi^\alpha}, \qquad \boldsymbol{A}_3 = \boldsymbol{T}. \tag{4.7}$$

The corresponding dual base vectors of $\boldsymbol{A}^i$ and $\boldsymbol{a}^i$ are defined as $\boldsymbol{A}_i \cdot \boldsymbol{A}^j = \delta_i^j$ and $\boldsymbol{a}_i \cdot \boldsymbol{a}^j = \delta_i^j$, respectively. Note that $\boldsymbol{A}^3 = \boldsymbol{A}_3$. The identity (or metric) tensor of the shell reference midsurface is $\boldsymbol{A} = \boldsymbol{A}_\alpha \otimes \boldsymbol{A}^\beta = A_{\alpha\beta}\boldsymbol{A}^\alpha \otimes \boldsymbol{A}^\beta = A_{\alpha\beta}\left(\boldsymbol{A}^\alpha\right)_\gamma \left(\boldsymbol{A}^\beta\right)_\delta \boldsymbol{e}_\gamma \otimes \boldsymbol{e}_\delta = \delta_\alpha^\beta \boldsymbol{e}_\alpha \otimes \boldsymbol{e}_\beta$, where $A_{\alpha\beta} = \boldsymbol{A}_\alpha \cdot \boldsymbol{A}_\beta$ and $A^{\alpha\beta} = \boldsymbol{A}^\alpha \cdot \boldsymbol{A}^\beta$. The differential surface element is given as $dA = \sqrt{A} d\xi^1 d\xi^2$, where $\sqrt{A} = \|\boldsymbol{A}_1 \times \boldsymbol{A}_2\|$. We can further define a tensor, called shifter, which transforms the base vectors of the midsurface to the base vectors of the shell body. The shifter from the shell reference configuration, denoted as $\boldsymbol{Z}$, shifts $\boldsymbol{A}_i$ and $\boldsymbol{A}^i$ (defined at a midsurface point) to $\boldsymbol{G}_i$ and $\boldsymbol{G}^i$, respectively, i.e. $\boldsymbol{G}_i = \boldsymbol{Z}\boldsymbol{A}_i$ and $\boldsymbol{G}^i = \boldsymbol{Z}^{-T}\boldsymbol{A}^i$. In what follows, we assume that a shell is suficently thin that $\boldsymbol{Z} \approx \boldsymbol{I}$.

Having defined the base vectors, we can proceed with the expression for the deformation gradient

$$\boldsymbol{F} = \frac{\partial \boldsymbol{x}}{\partial \boldsymbol{X}} = \frac{\partial \boldsymbol{x}}{\partial \xi^i}\left[\frac{\partial \boldsymbol{X}}{\partial \xi^i}\right]^{-1} = \boldsymbol{g}_i \otimes \boldsymbol{G}^i. \tag{4.8}$$

In (4.8) we used notation $\xi^3 = \xi$. By knowing $\boldsymbol{F}$, we can obtain the components of the Green-Lagrange strain tensor with respect to the convected basis $\boldsymbol{A}^i$

$$\begin{aligned} \boldsymbol{E} &= \frac{1}{2}\left(\boldsymbol{F}^T\boldsymbol{F} - \boldsymbol{G}\right) = \frac{1}{2}\left[\left(\boldsymbol{G}^i \otimes \boldsymbol{g}_i\right)\left(\boldsymbol{g}_j \otimes \boldsymbol{G}^j\right) - \boldsymbol{G}_i \cdot \boldsymbol{G}_j\left(\boldsymbol{G}^i \otimes \boldsymbol{G}^j\right)\right] \\ &= \frac{1}{2}\left(\boldsymbol{g}_i \cdot \boldsymbol{g}_j - \boldsymbol{G}_i \cdot \boldsymbol{G}_j\right)\boldsymbol{G}^i \otimes \boldsymbol{G}^j = E_{ij}\boldsymbol{G}^i \otimes \boldsymbol{G}^j \underbrace{\approx}_{\boldsymbol{Z}\approx\boldsymbol{I}} E_{ij}\boldsymbol{A}^i \otimes \boldsymbol{A}^j. \end{aligned} \tag{4.9}$$

By evaluation of the dot products in (4.9) one can get the strains E_{ij}, which are varying quadratically with respect to the ξ coordinate

$$E_{ij} = \varepsilon_{ij} + \xi\kappa_{ij} + (\xi)^2 \eta_{ij}. \tag{4.10}$$

Note, that $\varepsilon_{33} = \kappa_{33} = \eta_{\alpha 3} = \eta_{3\alpha} = \eta_{33} = 0$. In this work we will truncate the strains $E_{\alpha\beta}$ after the linear term, and the transverse shear strains $E_{\alpha 3} = E_{3\alpha}$ after the constant term, i.e.

$$\begin{aligned} E_{\alpha\beta} &\to \varepsilon_{\alpha\beta} + \xi\kappa_{\alpha\beta}, \\ E_{\alpha 3} &\to \varepsilon_{\alpha 3}. \end{aligned} \tag{4.11}$$

The Green-Lagrange tensor that we will work with will have the following components in basis $\boldsymbol{A}^i$

$$\boldsymbol{E} \approx E_{ij}\boldsymbol{A}^i \otimes \boldsymbol{A}^j = \varepsilon_{\alpha\beta}\boldsymbol{A}^\alpha \otimes \boldsymbol{A}^\beta + \xi\kappa_{\alpha\beta}\boldsymbol{A}^\alpha \otimes \boldsymbol{A}^\beta + \varepsilon_{\alpha 3}\left(\boldsymbol{A}^\alpha \otimes \boldsymbol{T} + \boldsymbol{T} \otimes \boldsymbol{A}^\alpha\right). \tag{4.12}$$

Expressions for $\varepsilon_{\alpha\beta}$, $\kappa_{\alpha\beta}$ and $2\varepsilon_{\alpha 3}$ in (4.11) are the classical expressions for the shell membrane, the shell bending and the shell transverse shear strains, respectively. Their explicit forms follow from using $\boldsymbol{g}_i$ and $\boldsymbol{G}_i$ in (4.9)

$$\begin{aligned} \varepsilon_{\alpha\beta} &= \frac{1}{2}\left(\boldsymbol{\varphi}_{,\alpha}\cdot\boldsymbol{\varphi}_{,\beta} - \boldsymbol{\varphi}_{0,\alpha}\cdot\boldsymbol{\varphi}_{0,\beta}\right), \qquad 2\varepsilon_{\alpha 3} = \gamma_\alpha = \boldsymbol{\varphi}_{,\alpha}\cdot\boldsymbol{t} - \underbrace{\boldsymbol{\varphi}_{0,\alpha}\cdot\boldsymbol{T}}_{0}, \\ \kappa_{\alpha\beta} &= \frac{1}{2}\left(\boldsymbol{\varphi}_{,\alpha}\cdot\boldsymbol{t}_{,\beta} + \boldsymbol{\varphi}_{,\beta}\cdot\boldsymbol{t}_{,\alpha} - \boldsymbol{\varphi}_{0,\alpha}\cdot\boldsymbol{T}_{,\beta} - \boldsymbol{\varphi}_{0,\beta}\cdot\boldsymbol{T}_{,\alpha}\right) = \boldsymbol{\varphi}_{,\alpha}\cdot\boldsymbol{t}_{,\beta} - \boldsymbol{\varphi}_{0,\alpha}\cdot\boldsymbol{T}_{,\beta}. \end{aligned} \tag{4.13}$$

For further use we will also express the components of $\boldsymbol{E}$ with respect to the orthonormal mid-surface basis $\widehat{\boldsymbol{e}}_i$, defined above in (4.2)

$$\boldsymbol{E} \approx \widehat{E}_{ij}\boldsymbol{A}^i \otimes \boldsymbol{A}^j = \widehat{\varepsilon}_{\alpha\beta}\widehat{\boldsymbol{e}}_\alpha \otimes \widehat{\boldsymbol{e}}_\beta + \xi\widehat{\kappa}_{\alpha\beta}\widehat{\boldsymbol{e}}_\alpha \otimes \widehat{\boldsymbol{e}}_\beta + \widehat{\varepsilon}_{\alpha 3}\left(\widehat{\boldsymbol{e}}_\alpha \otimes \boldsymbol{T} + \boldsymbol{T} \otimes \widehat{\boldsymbol{e}}_\alpha\right). \tag{4.14}$$

The transformations between the strains (4.12) and the strains (4.14) take the following rules

$$\widehat{\varepsilon}_{\gamma\delta} = \varepsilon_{\alpha\beta}\left(\widehat{\boldsymbol{e}}_\gamma\cdot\boldsymbol{A}^\alpha\right)\left(\widehat{\boldsymbol{e}}_\delta\cdot\boldsymbol{A}^\beta\right), \quad \widehat{\kappa}_{\gamma\delta} = \kappa_{\alpha\beta}\left(\widehat{\boldsymbol{e}}_\gamma\cdot\boldsymbol{A}^\alpha\right)\left(\widehat{\boldsymbol{e}}_\delta\cdot\boldsymbol{A}^\beta\right), \quad \widehat{\gamma}_\gamma = \gamma_\alpha\left(\widehat{\boldsymbol{e}}_\gamma\cdot\boldsymbol{A}^\alpha\right). \tag{4.15}$$

The stress resultants, which are energy-conjugated to the Green-Lagrange strains $\varepsilon_{\alpha\beta}$, $\kappa_{\alpha\beta}$ and γ_α, are the second Piola-Kirchhoff stress resultants $n^{\alpha\beta}$, q^α and $m^{\alpha\beta}$, respectively. The stress resultants $n^{\alpha\beta}$, $m^{\alpha\beta}$ and q^α are the classical (effective) shell membrane forces, the (symmetric) shell bending moments and the shell transverse shear forces. They are the components of the following second Piola-Kirchhoff stress resultant tensors resolved with respect to the $\boldsymbol{A}_i$ basis: the membrane force tensor $\boldsymbol{N}$, the transverse shear force tensor $\boldsymbol{Q}$ and the bending moment tensor $\boldsymbol{M}$

$$\boldsymbol{N} = n^{\alpha\beta}\boldsymbol{A}_\alpha \otimes \boldsymbol{A}_\beta, \qquad \boldsymbol{Q} = q^\alpha\left(\boldsymbol{A}_\alpha \otimes \boldsymbol{T} + \boldsymbol{T} \otimes \boldsymbol{A}_\alpha\right), \qquad \boldsymbol{M} = m^{\alpha\beta}\boldsymbol{A}_\alpha \otimes \boldsymbol{A}_\beta. \tag{4.16}$$

Those stress resultant tensors can be also expressed with respect to the midsurface orthonormal basis $\widehat{\boldsymbol{e}}_i$ as

$$\boldsymbol{N} = \widehat{n}^{\alpha\beta}\widehat{\boldsymbol{e}}_\alpha \otimes \widehat{\boldsymbol{e}}_\beta, \qquad \boldsymbol{Q} = \widehat{q}^{\alpha}\left(\widehat{\boldsymbol{e}}_\alpha \otimes \boldsymbol{T} + \boldsymbol{T} \otimes \widehat{\boldsymbol{e}}_\alpha\right), \qquad \boldsymbol{M} = \widehat{m}^{\alpha\beta}\widehat{\boldsymbol{e}}_\alpha \otimes \widehat{\boldsymbol{e}}_\beta. \tag{4.17}$$

The transformation of the stress resultants, defined with respect to $\boldsymbol{A}_i$ basis, to stress resultants, defined with respect to the midsurface orthonormal basis $\widehat{\boldsymbol{e}}_i$ is given as

$$\widehat{n}^{\gamma\delta} = n^{\alpha\beta}\left(\widehat{\boldsymbol{e}}_\gamma \cdot \boldsymbol{A}_\alpha\right)\left(\widehat{\boldsymbol{e}}_\delta \cdot \boldsymbol{A}_\beta\right), \quad \widehat{m}^{\gamma\delta} = m^{\alpha\beta}\left(\widehat{\boldsymbol{e}}_\gamma \cdot \boldsymbol{A}_\alpha\right)\left(\widehat{\boldsymbol{e}}_\delta \cdot \boldsymbol{A}_\beta\right), \quad \widehat{q}^{\gamma} = \gamma_\alpha\left(\widehat{\boldsymbol{e}}_\gamma \cdot \boldsymbol{A}_\alpha\right). \tag{4.18}$$

4.2.2 Variational formulation

To simplify the formulation, we will use in what follows the strains and the stress resultants resolved with respect to the local orthonormal basis $\widehat{\boldsymbol{e}}_i$. Those strains will be collected into the following vectors

$$\boldsymbol{\varepsilon} = \left[\boldsymbol{\epsilon}^T, \boldsymbol{\kappa}^T, \boldsymbol{\gamma}^T\right]^T, \quad \boldsymbol{\epsilon} = \left[\widehat{\varepsilon}_{11}, \widehat{\varepsilon}_{22}, 2\widehat{\varepsilon}_{12}\right]^T, \quad \boldsymbol{\kappa} = \left[\widehat{\kappa}_{11}, \widehat{\kappa}_{22}, 2\widehat{\kappa}_{12}\right]^T, \quad \boldsymbol{\gamma} = \left[\widehat{\gamma}_1, \widehat{\gamma}_2\right]^T, \tag{4.19}$$

and the stress resultants will be collected as

$$\boldsymbol{\sigma} = \left[\boldsymbol{n}^T, \boldsymbol{m}^T, \boldsymbol{q}^T\right]^T, \quad \boldsymbol{n} = \left[\widehat{n}_{11}, \widehat{n}_{22}, \widehat{n}_{12}\right]^T, \quad \boldsymbol{m} = \left[\widehat{m}_{11}, \widehat{m}_{22}, \widehat{m}_{12}\right]^T, \quad \boldsymbol{q} = \left[\widehat{q}_1, \widehat{q}_2\right]^T. \tag{4.20}$$

We will further define the virtual work equation (the weak form of the shell equilibrium equations), which will represent the starting point for the finite element discretization. However, before defining the virtual work principle, we need to express the virtual strains. Those are the strains that arise due to variation of displacement vector $\boldsymbol{u}$ for virtual displacement vector $\delta\boldsymbol{u}$, and due to variation of rotation vector $\boldsymbol{\vartheta}$ for virtual rotation vector $\delta\boldsymbol{\vartheta}$. By introducing the following displacements $\boldsymbol{u} \rightarrow \boldsymbol{u} + \omega\delta\boldsymbol{u}$ and the following rotation vector $\boldsymbol{\vartheta} \longrightarrow \boldsymbol{\vartheta} + \omega\delta\boldsymbol{\vartheta}$ into the expressions for strains that are collected in $\boldsymbol{\varepsilon}$ in (4.19), one can derive vector of virtual strains as

$$\delta\boldsymbol{\varepsilon} = \frac{d}{d\omega}\boldsymbol{\varepsilon}\left(\boldsymbol{u} + \omega\delta\boldsymbol{u}, \boldsymbol{\vartheta} + \omega\delta\boldsymbol{\vartheta}\right)|_{\omega=0} = \left[\delta\boldsymbol{\epsilon}^T, \delta\boldsymbol{\kappa}^T, \delta\boldsymbol{\gamma}^T\right]^T, \tag{4.21}$$

where

$$\delta\boldsymbol{\epsilon} = \left[\delta\widehat{\varepsilon}_{11}, \delta\widehat{\varepsilon}_{22}, 2\delta\widehat{\varepsilon}_{12}\right]^T, \quad \delta\boldsymbol{\kappa} = \left[\delta\widehat{\kappa}_{11}, \delta\widehat{\kappa}_{22}, 2\delta\widehat{\kappa}_{12}\right]^T, \quad \delta\boldsymbol{\gamma} = \left[\delta\widehat{\gamma}_1, \delta\widehat{\gamma}_2\right]^T. \tag{4.22}$$

Explicit expressions for virtual strains in (4.22) are (see (4.15))

$$\delta\widehat{\varepsilon}_{\gamma\delta} = \delta\varepsilon_{\alpha\beta}\left(\widehat{\boldsymbol{e}}_\gamma \cdot \boldsymbol{A}^\alpha\right)\left(\widehat{\boldsymbol{e}}_\delta \cdot \boldsymbol{A}^\beta\right), \quad \delta\widehat{\kappa}_{\gamma\delta} = \delta\kappa_{\alpha\beta}\left(\widehat{\boldsymbol{e}}_\gamma \cdot \boldsymbol{A}^\alpha\right)\left(\widehat{\boldsymbol{e}}_\delta \cdot \boldsymbol{A}^\beta\right), \quad \delta\widehat{\gamma}_{\gamma} = \delta\gamma_\alpha\left(\widehat{\boldsymbol{e}}_\gamma \cdot \boldsymbol{A}^\alpha\right), \tag{4.23}$$

where (see (4.13))

$$\begin{aligned}\delta\varepsilon_{\alpha\beta} &= \frac{1}{2}\left(\delta\boldsymbol{u}_{,\alpha}\cdot\boldsymbol{\varphi}_{,\beta}+\boldsymbol{\varphi}_{,\alpha}\cdot\delta\boldsymbol{u}_{,\beta}\right), \qquad \delta\gamma_\alpha=\delta\boldsymbol{u}_{,\alpha}\cdot\boldsymbol{t}+\boldsymbol{\varphi}_{,\alpha}\cdot\delta\boldsymbol{t}, \\ \delta\kappa_{\alpha\beta} &= \frac{1}{2}\left(\delta\boldsymbol{u}_{,\alpha}\cdot\boldsymbol{t}_{,\beta}+\boldsymbol{\varphi}_{,\alpha}\cdot\delta\boldsymbol{t}_{,\beta}+\delta\boldsymbol{u}_{,\beta}\cdot\boldsymbol{t}_{,\alpha}+\boldsymbol{u}_{,\beta}\cdot\delta\boldsymbol{t}_{,\alpha}\right)=\delta\boldsymbol{u}_{,\alpha}\cdot\boldsymbol{t}_{,\beta}+\boldsymbol{\varphi}_{,\alpha}\cdot\delta\boldsymbol{t}_{,\beta}.\end{aligned} \tag{4.24}$$

and $\delta\boldsymbol{t}=\frac{d}{d\omega}\boldsymbol{t}\left(\boldsymbol{\vartheta}+\omega\delta\boldsymbol{\vartheta}\right)|_{\omega=0}$.

The virtual work equation can now be written as

$$G\left(\boldsymbol{u},\boldsymbol{\vartheta};\delta\boldsymbol{u},\delta\boldsymbol{\vartheta};(\circ)\right)=\int_A\delta\boldsymbol{\varepsilon}^T\left(\boldsymbol{u},\boldsymbol{\vartheta};\delta\boldsymbol{u},\delta\boldsymbol{\vartheta}\right)\boldsymbol{\sigma}\left(\boldsymbol{u},\boldsymbol{\vartheta},(\circ)\right)dA-G_{ext}\left(\delta\boldsymbol{u},\delta\boldsymbol{\vartheta}\right)=0, \tag{4.25}$$

where the expression under the integral sign represents the virtual work of internal forces and G_{ext} represents the virtual work of external forces. An empty slot $(\circ)$ represents internal variables of chosen inelastic constitutive model. The stress resultants $\boldsymbol{\sigma}$ are functions of those variables. Since we consider here a shell model with inelastic constitutive relations, we assume dependency of the displacements $\boldsymbol{u}$, the rotation vector $\boldsymbol{\vartheta}$, the strains $\boldsymbol{\varepsilon}$ and the stress resultants $\boldsymbol{\sigma}$ on pseudo-time parameter $t\in[0,T]$.

The solution of the weak form of equilibrium equation (4.25) provides displacements of the shell midsurface and rotation of the shell director. It is obtained in the following manner. The weak form of equilibrium equations (4.25), is first discretized in space by using the finite element method. Then, the solution of the discretized weak form is searched for at discrete pseudo-time points $0<t_1<\ldots t_n<t_{n+1}\ldots<T$. The value of $(\Diamond)$ at the pseudo-time instant t_{n+1} will be denoted as $(\Diamond)_{n+1}$. The space discretization reveals that the solution of discretized form of (4.25) can be obtained by the operator split method. Namely, the solution search for displacements and rotation vector at discrete (nodal) points at, say, pseudo-time instant t_{n+1}, can be performed separately (but not independently) from the solution of inelastic constitutive equations to get stress resultants $\boldsymbol{\sigma}_{n+1}$ at the same pseudo-time instant.

Let us now shortly describe the solution search for displacements and rotation vector by assuming that the best guess for $\boldsymbol{\sigma}_{n+1}$ is known data. We use the superscript $(\odot)^h$ to denote the function $(\odot)$ has been approximated in space by using finite element interpolation functions. After spatial discretization the equation (4.25) turns to

$$\begin{aligned}&G^h\left(\boldsymbol{u}^h_{n+1},\boldsymbol{t}^h(\boldsymbol{\vartheta}_{n+1});\delta\boldsymbol{u}^h,\delta\boldsymbol{t}^h\left(\boldsymbol{\vartheta}_{n+1},\delta\boldsymbol{\vartheta}\right)\right)= \\ &=\int_{A^h}\delta\boldsymbol{\varepsilon}^{h,T}\left(\boldsymbol{u}^h_{n+1},\boldsymbol{\vartheta}_{n+1};\delta\boldsymbol{u}^h,\delta\boldsymbol{\vartheta}\right)\boldsymbol{\sigma}_{n+1}\left(\boldsymbol{u}^h_{n+1},\boldsymbol{\vartheta}_{n+1},(\circ)\right)dA-G^h_{ext}\left(\delta\boldsymbol{u}^h,\delta\boldsymbol{\vartheta}\right)=0.\end{aligned} \tag{4.26}$$

Eq. (4.26) provides a set of higly nonlinear equations with $\boldsymbol{u}^h_{n+1}$ and $\boldsymbol{\vartheta}_{n+1}$ as the unknowns. Linearization of (4.26) needs to be performed in order to get a solution by Newton-Raphson iterative method . One can derive linearized form of G^h by introducing

the following displacements $\boldsymbol{u}^h_{n+1} \rightarrow \boldsymbol{u}^h_{n+1} + \omega\Delta\boldsymbol{u}^h_{n+1}$ and the following rotation vector $\boldsymbol{\vartheta}_{n+1} \longrightarrow \boldsymbol{\vartheta}_{n+1} + \omega\Delta\boldsymbol{\vartheta}_{n+1}$ into G^h and by using

$$\Delta G^h = \frac{d}{d\omega} G^h \left(\boldsymbol{u}^h_{n+1} + \omega\Delta\boldsymbol{u}^h_{n+1}, \boldsymbol{\vartheta}_{n+1} + \omega\Delta\boldsymbol{\vartheta}_{n+1}\right) |_{\omega=0} \,. \tag{4.27}$$

It follows from (4.27) that

$$\begin{aligned} \Delta G^h \;=\; & \int_{A^h} \Delta\delta\boldsymbol{\varepsilon}^{h,T} \left(\Delta\boldsymbol{u}^h_{n+1}, \Delta\boldsymbol{\vartheta}_{n+1}; \delta\boldsymbol{u}^h, \delta\boldsymbol{\vartheta}\right) \boldsymbol{\sigma}_{n+1} \left(\boldsymbol{u}^h_{n+1}, \boldsymbol{\vartheta}_{n+1}, (\circ)\right) dA + \\ & \int_{A^h} \delta\boldsymbol{\varepsilon}^{h,T} \left(\boldsymbol{u}^h_{n+1}, \boldsymbol{\vartheta}_{n+1}; \delta\boldsymbol{u}^h, \delta\boldsymbol{\vartheta}\right) \frac{d\boldsymbol{\sigma}_{n+1}}{d\boldsymbol{\varepsilon}^h_{n+1}} \Delta\boldsymbol{\varepsilon}^{h,T}_{n+1} \left(\boldsymbol{u}^h_{n+1}, \boldsymbol{\vartheta}_{n+1}; \Delta\boldsymbol{u}^h_{n+1}, \Delta\boldsymbol{\vartheta}_{n+1}\right) dA. \end{aligned} \tag{4.28}$$

Eq. (4.28) shows that the linearization of the discrete weak form is split into two parts; the first one is called geometric and the second one material. The $d\boldsymbol{\sigma}_{n+1}/d\boldsymbol{\varepsilon}^h_{n+1}$ is called the consistent tangent modulus.

4.2.3 Stress-resultant constitutive equations for elastoplasticity

We will consider in this section the stress resultant elastoplasticity for shells. It will be based on Ilyushin-Shapiro multi-surface yield function, which is a stress resultant approximation of the classical von Mises yield function. The considered yield function takes into account both isotropic and kinematic hardening. The internal variables, describing the irreversible nature of the plastic process, are chosen as: the plastic strain $\boldsymbol{\varepsilon}^p = \left[\boldsymbol{\epsilon}^{p,T}, \boldsymbol{\kappa}^{p,T}, \boldsymbol{\gamma}^{p,T}\right]^T$, the scalar parameter ξ^I, which controls the isotropic hardening mechanism, and the strain-like parameters $\varkappa = [\varkappa^n_{11}, \varkappa^n_{22}, \varkappa^n_{12}, \varkappa^m_{11}, \varkappa^m_{22}, \varkappa^m_{12}, \varkappa^q_{13}, \varkappa^q_{23}]^T$, which control the kinematic hardening mechanism. Those variables, strains $\boldsymbol{\varepsilon}$ and stress resultants $\boldsymbol{\sigma}$ are functions of pseudo-time t, i.e. $\boldsymbol{\varepsilon}^p = \boldsymbol{\varepsilon}^p(t)$, $\xi^I = \xi^I(t)$, $\varkappa = \varkappa(t)$, $\boldsymbol{\varepsilon} = \boldsymbol{\varepsilon}(t)$ and $\boldsymbol{\sigma} = \boldsymbol{\sigma}(t)$.

A usual additive split of reversible (elastic) and irreversible (plastic) strains is assumed

$$\boldsymbol{\varepsilon} = \boldsymbol{\varepsilon}^e + \boldsymbol{\varepsilon}^p, \tag{4.29}$$

where $\boldsymbol{\varepsilon}^e = \left[\boldsymbol{\epsilon}^{e,T}, \boldsymbol{\kappa}^{e,T}, \boldsymbol{\gamma}^{e,T}\right]^T$. The strain energy function is assumed to be of the following (quadratic) form

$$\psi\left(\boldsymbol{\varepsilon}^e, \xi^I, \check{\varkappa}\right) = \frac{1}{2}\boldsymbol{\varepsilon}^{e,T}\boldsymbol{C}\boldsymbol{\varepsilon}^e + \Xi\left(\xi^I\right) + \frac{1}{2}\varkappa^T\boldsymbol{D}\varkappa. \tag{4.30}$$

By assuming isotropic elastic response, $\boldsymbol{C}$ is given as

$$\begin{aligned} \boldsymbol{C} &= diag[\boldsymbol{C}^n, \boldsymbol{C}^b, \boldsymbol{C}^s], \quad \boldsymbol{C}^n = h\overline{\boldsymbol{C}}, \quad \boldsymbol{C}^b = \frac{h^3}{12}\overline{\boldsymbol{C}}, \\ \overline{\boldsymbol{C}} &= \frac{E}{(1-\nu^2)} \begin{bmatrix} 1 & \nu & 0 \\ \nu & 1 & 0 \\ 0 & 0 & \frac{1-\nu}{2} \end{bmatrix}, \quad \boldsymbol{C}^s = k^s \begin{bmatrix} 1 & 0 \\ 0 & 1 \end{bmatrix}. \end{aligned} \tag{4.31}$$

The constants in (4.31) are: E is elastic modulus, ν is Poisson's ratio, h is shell thickness, $k^s = cGh$, $G = \frac{E}{2(1+\nu)}$ is shear modulus and c is shear correction factor, usually set to 5/6 for an isotropic material. Matrix $\boldsymbol{D}$ in (4.30) is $\boldsymbol{D} = \frac{2}{3}H_{kin}\boldsymbol{I}_8$, where $\boldsymbol{I}_8 = diag\,[1,1,1,1,1,1,1,1]$. In (4.30) we have assumed a general (nonlinear) form of isotropic hardening and a linear form of kinematic hardening with hardening modulus H_{kin}. We denote the stress-like internal variables, which correspond to the strain-like internal variables ξ^I and $\varkappa$, as q and $\boldsymbol{\alpha}$, respectively. These dual variables are used to define Ilyushin-Shapiro two-surface yield function $\phi = \phi(\phi_1, \phi_2) \leq 0$. A sketch of a two-surface yield function is presented in Figure 4.1. The elastic domain is defined with the intersection of $\phi_1 < 0 \cap \phi_2 < 0$, where $\phi < 0$, while the plastic domain is defined with $(\phi_1 < 0 \cap \phi_2 = 0) \cup (\phi_1 = 0 \cap \phi_2 < 0) \cup (\phi_1 = 0 \cap \phi_2 = 0)$, where $\phi = 0$. The non-dimensional

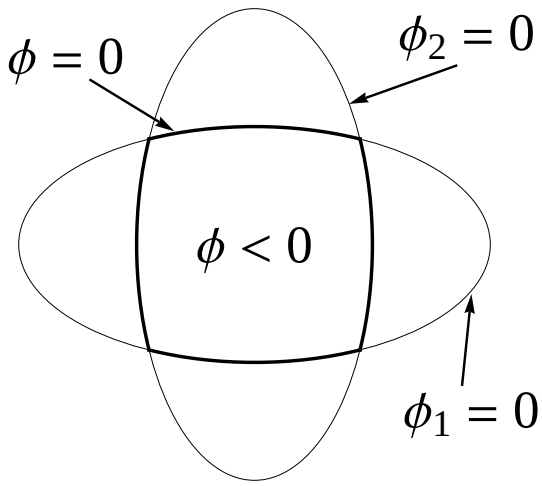

Figure 4.1: A sketch of a two-surface yield function

Slika 4.1: Skica funkcije tečenja določene z dvema ploskvama

forms ob ϕ_1 and ϕ_2 can be written as

$$\phi_\mu\left(\boldsymbol{\sigma}, q, \boldsymbol{\alpha}\right) = \left(\boldsymbol{\sigma} + \boldsymbol{\alpha}\right)^T \boldsymbol{A}_\mu \left(\boldsymbol{\sigma} + \boldsymbol{\alpha}\right) - \left(1 - \frac{q}{\sigma_y}\right)^2 \qquad \mu = 1, 2. \tag{4.32}$$

Here, $\boldsymbol{\sigma}$ is defined in (4.20), $\boldsymbol{\alpha}$ (the negative of the back stress resultants) is defined as $\boldsymbol{\alpha} = \left[\boldsymbol{\alpha}^{n,T}, \boldsymbol{\alpha}^{m,T}, \boldsymbol{\alpha}^{q,T}\right]^T$, where $\boldsymbol{\alpha}^{n,T} = [\alpha^n_{11}, \alpha^n_{22}, \alpha^n_{12}]^T$, $\boldsymbol{\alpha}^{m,T} = [\alpha^m_{11}, \alpha^m_{22}, \alpha^m_{12}]^T$, $\boldsymbol{\alpha}^{q,T} = [\alpha^q_{13}, \alpha^q_{23}]^T$ and σ_y is uniaxial yield stress. The matrix $\boldsymbol{A}_\mu$ for an isotropic plastic response

equals to

$$\boldsymbol{A}_\mu = \begin{bmatrix} \frac{1}{n_0^2}\boldsymbol{P} & \frac{sign(\mu)}{2\sqrt{3}n_0 m_0}\boldsymbol{P} & \boldsymbol{0} \\ \frac{sign(\mu)}{2\sqrt{3}n_0 m_0}\boldsymbol{P} & \frac{1}{m_0^2}\boldsymbol{P} & \boldsymbol{0} \\ \boldsymbol{0} & \boldsymbol{0} & \frac{1}{q_0^2}\boldsymbol{I}_2 \end{bmatrix}, \tag{4.33}$$

$$\boldsymbol{P} = \frac{1}{2}\begin{bmatrix} 2 & -1 & 0 \\ -1 & 2 & 0 \\ 0 & 0 & 6 \end{bmatrix}, \qquad sign\,(\mu) = \begin{cases} +1 \text{ if } \mu = 1 \\ -1 \text{ if } \mu = 2 \end{cases}.$$

Here, n_0, m_0 and q_0 are the yield parameters associated with membrane extension, bending and transverse shear, respectively. They are usually set to the fully plastic uniaxial membrane force $n_0 = \sigma_y h$, fully plastic uniaxial bending moment $m_0 = \frac{\sigma_y h^2}{4}$ and fully plastic uniaxial transverse shear force $q_0 = \frac{\sigma_y h}{\sqrt{3}}$. For further discussion on stress resultant yield functions for shells one could address [Crisfield and Peng, 1992], [Simo and Kennedy, 1992] and [Shi and Voyiadjis, 1992].

Having defined internal variables, strain energy function and yield function, we proceed with derivation of the remaining ingredients of the stress resultant elastoplasticity for shells. For the isothermal case we can write the following rate of material dissipation

$$\mathcal{D} = \boldsymbol{\sigma}^T\dot{\boldsymbol{\varepsilon}} - \frac{d}{dt}\psi\left(\boldsymbol{\varepsilon}^e, \xi^I, \varkappa\right) = \boldsymbol{\sigma}^T\dot{\boldsymbol{\varepsilon}} - \left(\frac{\partial\psi}{\partial\boldsymbol{\varepsilon}^e}\right)^T\left(\dot{\boldsymbol{\varepsilon}} - \dot{\boldsymbol{\varepsilon}}^p\right) - \frac{\partial\psi}{\partial\xi^I}\dot{\xi}^I - \left(\frac{\partial\psi}{\partial\varkappa}\right)^T\dot{\varkappa} \geqslant 0, \tag{4.34}$$

which is assumed to be non-negative. In (4.34) $(\dot{\circ}) = \frac{\partial(\circ)}{\partial t}$. Note that equation (4.34) can be derived from the second law of thermodynamics, see e.g. [Khan and Huang, 1995] or [Simo and Kennedy, 1992]. By assuming that the elastic process is non-dissipative (i.e. the state variables do not change during that process and $\mathcal{D} = 0$) one has

$$\boldsymbol{\sigma} = \frac{\partial\psi}{\partial\boldsymbol{\varepsilon}^e} = \boldsymbol{C}\boldsymbol{\varepsilon}^e. \tag{4.35}$$

By further consideration of (4.34) one can define the dual variables, i.e. the hardening variable q and the variables that control kinematic hardening $\boldsymbol{\alpha}$, as

$$q = -\frac{\partial\psi}{\partial\xi^I} = -\frac{d\Xi\left(\xi^I\right)}{d\xi^I} = -\Xi'\left(\xi^I\right), \qquad \boldsymbol{\alpha} = -\frac{\partial\psi}{\partial\varkappa} = -\boldsymbol{D}\varkappa. \tag{4.36}$$

If we consider the quadratic form of

$$\Xi = \frac{1}{2}K_h\xi^{I^2}, \tag{4.37}$$

we obtain the case of linear isotropic hardening

$$q = -K_h\xi^I, \tag{4.38}$$

where K_h is the isotropic hardening modulus. This type of hardening law was used to obtain the results of numerical simulations in Section 4.4. By using (4.35) and (4.36) in (4.34) we obtain the reduced material dissipation (i.e. the dissipation of the plastic process) as

$$\mathcal{D}^p = \boldsymbol{\sigma}^T \dot{\boldsymbol{\varepsilon}}^p + q\dot{\xi}^I + \boldsymbol{\alpha}^T \dot{\boldsymbol{\varkappa}} \geqslant 0. \tag{4.39}$$

The principle of maximum plastic dissipation states that among all the dual variables $(\boldsymbol{\sigma}, q, \boldsymbol{\alpha})$ that satisfy the yield criteria, one should choose those that maximize plastic dissipation. The problem can be written in the following form: Find minimum of $\mathcal{L}^p(\boldsymbol{\sigma}, q, \boldsymbol{\alpha}, \dot{\gamma}_1, \dot{\gamma}_2)$, where

$$\mathcal{L}^p(\boldsymbol{\sigma}, q, \boldsymbol{\alpha}, \dot{\gamma}_1, \dot{\gamma}_2) = -\mathcal{D}^p(\boldsymbol{\sigma}, q, \boldsymbol{\alpha}) + \sum_{\mu=1}^{p} \dot{\gamma}_\mu \phi_\mu(\boldsymbol{\sigma}, q, \boldsymbol{\alpha}), \tag{4.40}$$

$\dot{\gamma}_\mu \geqslant 0$ play the role of Lagrange multipliers and p is number of active yield surfaces. From the above minimization problem and (4.32) we obtain explicit forms of evolution equations for the internal variables

$$\begin{aligned}
\frac{\partial \mathcal{L}^p}{\partial \boldsymbol{\sigma}} &= -\dot{\boldsymbol{\varepsilon}}^p + \sum_{\mu=1}^{p} \dot{\gamma}_\mu \frac{\partial \phi_\mu}{\partial \boldsymbol{\sigma}} = 0 \Longrightarrow \dot{\boldsymbol{\varepsilon}}^p = \sum_{\mu=1}^{p} \dot{\gamma}_\mu \underbrace{2\boldsymbol{A}_\mu(\boldsymbol{\sigma} + \boldsymbol{\alpha})}_{\boldsymbol{\nu}_\mu}, \\
\frac{\partial \mathcal{L}^p}{\partial q} &= -\dot{\xi}^I + \sum_{\mu=1}^{p} \dot{\gamma}_\mu \frac{\partial \phi_\mu}{\partial q} = 0 \Longrightarrow \dot{\xi}^I = \sum_{\mu=1}^{p} \dot{\gamma}_\mu \underbrace{\frac{2}{\sigma_y}\left(1 - \frac{q}{\sigma_y}\right)}_{\beta}, \\
\frac{\partial \mathcal{L}^p}{\partial \boldsymbol{\alpha}} &= -\dot{\boldsymbol{\varkappa}} + \sum_{\mu=1}^{p} \dot{\gamma}_\mu \frac{\partial \phi_\mu}{\partial \boldsymbol{\alpha}} = 0 \Longrightarrow \dot{\boldsymbol{\varkappa}} = \sum_{\mu=1}^{p} \dot{\gamma}_\mu \underbrace{2\boldsymbol{A}_\mu(\boldsymbol{\sigma} + \boldsymbol{\alpha})}_{\boldsymbol{\nu}_\mu}.
\end{aligned} \tag{4.41}$$

Note that $\dot{\boldsymbol{\varkappa}} = \dot{\boldsymbol{\varepsilon}}^p$. The loading/unloading conditions follow from the demands that $\dot{\gamma}_\mu$ is non-negative, that ϕ_μ is non-positive, and that the plastic dissipation $\mathcal{D}^p$ equals zero for elastic process when $\phi_\mu < 0$

$$\dot{\gamma}_\mu \geqslant 0, \qquad \phi_\mu \leqslant 0, \qquad \dot{\gamma}_\mu \phi_\mu = 0. \tag{4.42}$$

In addition to (4.42) we have the condition $\dot{\phi}_\mu = 0$ if $\dot{\gamma}_\mu > 0$ (the consistency condition). It guarantees the admissibility of the subsequent state in the case of change of state variables.

4.3 Finite element formulation

4.3.1 Space-domain discretization

Let the initial shell midsurface A be discretized by n_{el} nonoverlaping elements with n_{en} nodes such that $A \approx \bigcup_{e=1}^{n_{el}} A_e = A^h$. Over the element domain A_e the initial shell

configuration (the midsurface and the shell director) are interpolated as

$$\boldsymbol{\varphi}_0^h\left(\xi^1,\xi^2\right)=\sum_{a=1}^{n_{en}} N_a\left(\xi^1,\xi^2\right)\boldsymbol{\varphi}_{0a}, \qquad \boldsymbol{T}^h\left(\xi^1,\xi^2\right)=\sum_{a=1}^{n_{en}} N_a\left(\xi^1,\xi^2\right)\boldsymbol{T}_a, \tag{4.43}$$

where $(\circ)_a$ are the corresponding nodal values. In this work we choose $n_{en}=4$ and the bi-linear shape functions $N_a\left(\xi^1,\xi^2\right)$, defined over the square domain $\mathcal{A}_e=[-1,1]\times[-1,1]$. Note, that $\boldsymbol{T}_a$ is chosen to coincide with the normal vector to a given shell midsurface at that nodal point. However, due to the bi-linear interpolation (4.43) $\boldsymbol{T}^h$ is only approximately perpendicular to the base vectors $\boldsymbol{A}_\alpha^h=\partial\boldsymbol{\varphi}_0^h/\partial\xi^\alpha$. The interpolation of the shell deformed configuration $\boldsymbol{\varphi}$, $\boldsymbol{t}$ is performed in a similar fashion as $\boldsymbol{\varphi}_0$, $\boldsymbol{T}$

$$\boldsymbol{u}^h\left(\xi^1,\xi^2\right)=\sum_{a=1}^{n_{en}} N_a\left(\xi^1,\xi^2\right)\boldsymbol{u}_a, \qquad \boldsymbol{\varphi}^h=\boldsymbol{\varphi}_0^h+\boldsymbol{u}^h, \qquad \boldsymbol{t}^h\left(\xi^1,\xi^2\right)=\sum_{a=1}^{n_{en}} N_a\left(\xi^1,\xi^2\right)\boldsymbol{t}_a\left(\boldsymbol{\vartheta}_a\right). \tag{4.44}$$

The virtual quantities $\delta\boldsymbol{\varphi}$ and $\delta\boldsymbol{t}$ are interpolated in the same manner as $\boldsymbol{\varphi}$ and $\boldsymbol{t}$

$$\delta\boldsymbol{\varphi}^h\left(\xi^1,\xi^2\right)=\sum_{a=1}^{n_{en}} N_a\left(\xi^1,\xi^2\right)\delta\boldsymbol{\varphi}_a, \qquad \delta\boldsymbol{t}^h\left(\xi^1,\xi^2\right)=\sum_{a=1}^{n_{en}} N_a\left(\xi^1,\xi^2\right)\delta\boldsymbol{t}_a. \tag{4.45}$$

Derivations of $\boldsymbol{\varphi}$, $\boldsymbol{t}$, $\delta\boldsymbol{\varphi}$ and $\delta\boldsymbol{t}$ with respect to ξ^α coordinates are obtained trivially. To avoid the transverse shear locking, the assumed natural strain (ANS) concept is chosen. The transverse shear strains are evaluated, using (4.13) and the interpolations (4.43) and (4.44), only at element edge mid-points A, B, C and D, where $\boldsymbol{\varphi}_0^I=\frac{1}{2}\left(\boldsymbol{\varphi}_{0J}+\boldsymbol{\varphi}_{0K}\right)$ and $I=A,B,C,D$, $J=1,2,3,4$ and $K=2,3,4,1$. The transverse shear strain field over the 4-node shell element is given by the interpolation suggested by [Bathe and Dvorkin, 1985]

$$\begin{aligned}\gamma_{13} &= \frac{1}{2}\left(1-\xi^2\right)\gamma_{13}^A+\frac{1}{2}\left(1+\xi^2\right)\gamma_{13}^C,\\ \gamma_{23} &= \frac{1}{2}\left(1-\xi^1\right)\gamma_{23}^D+\frac{1}{2}\left(1+\xi^1\right)\gamma_{23}^B.\end{aligned} \tag{4.46}$$

The transformation to $\widehat{\gamma}_{13}$ and $\widehat{\gamma}_{23}$ is given according to (4.15).

4.3.2 Computational issues for plasticity

The solution of the weak form of equilibrium equations (4.26), discretized in space is searched for at discrete pseudo-time points $0<t_1<\ldots t_n<t_{n+1}\ldots<T$. The value of $(\circ)$ at the pseudo-time instant t_{n+1} is denoted as $(\circ)_{n+1}$. In what follows a pseudo-time increment $\Delta t=t_{n+1}-t_n$ will be considered. As a result of space discretization, the evolution equations (4.41) become ordinary differential equations in pseudo-time that are related to each finite element integration point. This enables introduction of operator split method, see e.g. [Ibrahimbegovic, 2006]. This method consists of two sequential solution

procedures; one solution procedure (called global) searches for the values of nodal displacemens/rotations at pseudo-time instant t_{n+1} (at frozen values of internal variables), while the other solution procedure searches for the values of internal variables at integration points at t_{n+1} (while keeping frozen nodal displacements/rotations data). The later will be considered in this section.

For numerical integration of evolution equations (4.41) the backward Euler integration scheme will be used. At a pseudo-time increment $\Delta t = t_{n+1} - t_n$, the pseudo-time integration problem at an integration point located at $\boldsymbol{x}^h(\boldsymbol{\xi}_G) \in \Omega^h$ can be stated as: By knowing the values of the internal variables at t_n, i.e. $\boldsymbol{\varepsilon}_n^p, \xi_n^I, \varkappa_n$, find by integrating (4.41) such values of the internal variables at t_{n+1}, i.e. $\boldsymbol{\varepsilon}_{n+1}^p, \xi_{n+1}^I, \varkappa_{n+1}$, which will satisfy the yield criterion. The best guess for the strains at the end of the pseudo-time increment, $\boldsymbol{\varepsilon}_{n+1}^{(i)}$, is given data. Here (i) is an iteration counter of the global Newton-Raphson solution procedure that searches for nodal displacements/rotations at time t_{n+1}.

Prior the integration of evolution equations the following test is performed: (i) Assume that the pseudo-time step from t_n to t_{n+1} remains elastic and evaluate the trial (test) values of strain-like and stress-like internal variables

$$\boldsymbol{\sigma}_{n+1}^{trial} = \boldsymbol{C}\left(\boldsymbol{\varepsilon}_{n+1}^{(i)} - \underbrace{\boldsymbol{\varepsilon}_{n+1}^{p,trial}}_{\boldsymbol{\varepsilon}_n^p}\right), \; q_{n+1}^{trial} = -\Xi'\left(\underbrace{\xi_{n+1}^{I,trial}}_{\xi_n^I}\right), \; \boldsymbol{\alpha}_{n+1}^{trial} = -\frac{2}{3}H_{kin}\underbrace{\varkappa_{n+1}^{trial}}_{\varkappa_n}, \tag{4.47}$$

(ii) If both yield functions, evaluated with the trial values, $\phi_{\mu,n+1}^{tr} = \phi_\mu\left(\boldsymbol{\sigma}_{n+1}^{trial}, q_{n+1}^{trial}, \boldsymbol{\alpha}_{n+1}^{trial}\right) \leq 0$, then, see (4.42), $\gamma_{\mu,n+1} = \dot{\gamma}_\mu \Delta t = 0$. The final values at the end ofthe pseudo-time increment (marked with the bar) equal the trial values, i.e. $\overline{\boldsymbol{\varepsilon}}_{n+1}^p = \boldsymbol{\varepsilon}_{n+1}^{p,trial}$, $\overline{\xi}_{n+1}^I = \xi_{n+1}^{I,trial}$ and $\overline{\varkappa}_{n+1} = \varkappa_{n+1}^{trial}$. The pseudo-time step is indeed elastic. (iii) In the case that one or both yield functions for the trial values are violated, then $\gamma_{\mu,n+1} > 0$ and $\phi_{\mu,n+1} = 0$ for at least one $\mu = 1, 2$. The backward Euler integration of evolution equations needs to be performed, i.e.

$$\boldsymbol{\varepsilon}_{n+1}^p = \boldsymbol{\varepsilon}_n^p + \sum_{\mu=1}^{p} \gamma_{\mu,n+1}\boldsymbol{\nu}_{\mu,n+1}, \; \xi_{n+1}^I = \xi_n^I + \sum_{\mu=1}^{p} \gamma_{\mu,n+1}\beta_{n+1}, \; \varkappa_{n+1} = \varkappa_n + \sum_{\mu=1}^{p} \gamma_{\mu,n+1}\boldsymbol{\nu}_{\mu,n+1}, \tag{4.48}$$

to get final values of internal variables at the end of the pseudo-time step. Since equations (4.48) contain five unknowns, $\boldsymbol{\varepsilon}_{n+1}^p, \xi_{n+1}^I, \varkappa_{n+1}, \gamma_{1,n+1}$ and $\gamma_{2,n+1}$, one needs to solve those equations together with $\phi_{1,n+1} = 0$ and $\phi_{2,n+1} = 0$.

Remark 4.1. *When dealing with two-surface plasticity we have in general three different sets of equations, where $\phi_{1,n+1} = 0$ and $\phi_{2,n+1} = 0$ is only one of them. The remaining two occur when only one yield surface is active and then instead of solving the above equations*

we solve $\phi_{1,n+1} = 0$ *and* $\gamma_{2,n+1} = 0$ *or* $\gamma_{1,n+1} = 0$ *and* $\phi_{2,n+1} = 0$. *The procedures that produce the right set of equations and their solutions will be further addressed in Section 4.3.2, while for brevity we will here only consider the case when both functions are active.*

The rest of this section will be related to the solution of eqs. (4.48) constrained by $\phi_{1,n+1} = 0$ and $\phi_{2,n+1} = 0$. There are two ways of handeling this problem, where both of them have their benefits and drawbacks. One option is to reduce the number of unknowns by: (i) expressing stress resultants with eqs. (4.48), and (ii) use those stress resultants in $\phi_{1,n+1} = 0$ and $\phi_{2,n+1} = 0$, while the second option is to solve all the equations simultaneously.

We first consider the reduction of the unknowns. Let us consider the case when both yield surfaces are active. By using (4.48), one can express stress resultants at t_{n+1} as

$$\begin{aligned}
\boldsymbol{\sigma}_{n+1} &= \boldsymbol{C}\underbrace{\left(\boldsymbol{\varepsilon}^{(i)}_{n+1} - \boldsymbol{\varepsilon}^{p,trial}_{n+1}\right)}_{\boldsymbol{\varepsilon}^{(i)}_{n+1} - \boldsymbol{\varepsilon}^{p}_{n} - \underbrace{\Delta\boldsymbol{\varepsilon}^{p}_{n+1}}_{\Delta t\, \dot{\boldsymbol{\varepsilon}}^{p}_{n+1}}} = \boldsymbol{\sigma}^{trial}_{n+1} - \sum_{\mu=1}^{2} \gamma_{\mu,n+1}\boldsymbol{C}\boldsymbol{\nu}_{\mu,n+1}, \\
q_{n+1} &= -\Xi'\left(\xi^{I}_{n} + \sum_{\mu=1}^{2}\gamma_{\mu,n+1}\beta_{n+1}\right), \\
\boldsymbol{\alpha}_{n+1} &= -\frac{2}{3}H_{kin}\varkappa_{n+1} = \boldsymbol{\alpha}^{trial}_{n+1} - \frac{2}{3}H_{kin}\sum_{\mu=1}^{2}\gamma_{n+1}\boldsymbol{\nu}_{\mu,n+1}.
\end{aligned} \tag{4.49}$$

Since $\boldsymbol{\nu}_{\mu,n+1} = 2\boldsymbol{A}_{\mu}\left(\boldsymbol{\sigma}_{n+1} + \boldsymbol{\alpha}_{n+1}\right)$, one can conclude from (4.49) that

$$\left(\boldsymbol{\sigma}_{n+1} + \boldsymbol{\alpha}_{n+1}\right) = \left[\boldsymbol{I}_8 + \sum_{\mu=1}^{2}\gamma_{\mu,n+1}\left(2\boldsymbol{C}\boldsymbol{A}_{\mu} + \frac{4}{3}H_{kin}\boldsymbol{A}_{\mu}\right)\right]^{-1}\left(\boldsymbol{\sigma}^{trial}_{n+1} + \boldsymbol{\alpha}^{trial}_{n+1}\right), \tag{4.50}$$

$$q_{n+1} = q_{n+1}\left(\xi^{I}_{n} + \sum_{\mu=1}^{2}\gamma_{\mu,n+1}\beta_{n+1}\right), \tag{4.51}$$

where the matrix product $\boldsymbol{C}\boldsymbol{A}_{\mu}$ is

$$\boldsymbol{C}\boldsymbol{A}_{\mu} = \begin{bmatrix} \frac{1}{n_0^2}\boldsymbol{C}^{n}\boldsymbol{P} & \frac{sign(\mu)}{2\sqrt{3}n_0 m_0}\boldsymbol{C}^{n}\boldsymbol{P} & \boldsymbol{0} \\ \frac{sign(\mu)}{2\sqrt{3}n_0 m_0}\boldsymbol{C}^{b}\boldsymbol{P} & \frac{1}{m_0^2}\boldsymbol{C}^{b}\boldsymbol{P} & \boldsymbol{0} \\ \boldsymbol{0} & \boldsymbol{0} & \frac{1}{q_0^2}\boldsymbol{C}^{s}\boldsymbol{I}_2 \end{bmatrix}.$$

For the linear isotropic hardening case one can from (4.38), (4.41) and (4.51) easily obtain that

$$\beta_{n+1} = \frac{2(K_h\xi^{I}_{n} + \sigma_y)}{\sigma_y^2 - 2\sum_{\mu=1}^{2}\gamma_{\mu,n+1}K_h}. \tag{4.52}$$

It has been proven that the inverse in (4.50) can be obtained explicitly. Since the shear part of $(\boldsymbol{\sigma}_{n+1} + \boldsymbol{\alpha}_{n+1})$ is clearly uncoupled from the membrane and bending parts, one can use (4.50) to get the following expression for the shear stress resultants

$$\left(\boldsymbol{q}_{n+1} + \boldsymbol{\alpha}^q_{n+1}\right) = \frac{1}{\left(1 + \left(\gamma^1_{n+1} + \gamma^2_{n+1}\right)\frac{2}{q_0^2}\left(k^s + \frac{2}{3}H_{kin}\right)\right)}\left(\boldsymbol{q}^{trial}_{n+1} + \boldsymbol{\alpha}^{q,trial}_{n+1}\right).$$

The fact that $\boldsymbol{P}$ and $\overline{\boldsymbol{C}}$ have the same characteristic subspaces is further used, i.e.

$$\boldsymbol{P} = \boldsymbol{Q}\boldsymbol{\Lambda}_{\boldsymbol{P}}\boldsymbol{Q}^T, \quad \overline{\boldsymbol{C}} = \boldsymbol{Q}\boldsymbol{\Lambda}_{\overline{\boldsymbol{C}}}\boldsymbol{Q}^T, \quad \boldsymbol{Q} = \frac{1}{\sqrt{2}}\begin{bmatrix} 1 & 1 & 0 \\ -1 & 1 & 0 \\ 0 & 0 & \sqrt{2} \end{bmatrix}, \tag{4.53}$$

where $\boldsymbol{Q}^T = \boldsymbol{Q}^{-1}$ and

$$\boldsymbol{\Lambda}_{\boldsymbol{P}} = \begin{bmatrix} \frac{1}{2} & 0 & 0 \\ 0 & \frac{3}{2} & 0 \\ 0 & 0 & 3 \end{bmatrix}, \quad \boldsymbol{\Lambda}_{\overline{\boldsymbol{C}}} = \begin{bmatrix} \frac{E}{1-\nu} & 0 & 0 \\ 0 & \frac{E}{1+\nu} & 0 \\ 0 & 0 & \frac{E}{2(1+\nu)} \end{bmatrix}.$$

By defining $\hat{\boldsymbol{\sigma}}_{n+1} = \left[\boldsymbol{n}^T, \boldsymbol{m}^T\right]^T$, $\hat{\boldsymbol{\alpha}}_{n+1} = \left[\boldsymbol{\alpha}^{n,T}, \boldsymbol{\alpha}^{m,T}\right]^T$ and by using (4.53) one can get the following expression from (4.50)

$$\begin{aligned} & diag[\boldsymbol{Q}^T, \boldsymbol{Q}^T]\left(\hat{\boldsymbol{\sigma}}_{n+1} + \hat{\boldsymbol{\alpha}}_{n+1}\right) \\ = & \underbrace{\left[\boldsymbol{I}_6 + \sum_{\mu=1}^{2}\gamma_{\mu,n+1}\left(\begin{array}{c} 2\begin{bmatrix} \frac{h}{n_0^2}\boldsymbol{\Lambda}_{\overline{\boldsymbol{C}}}\boldsymbol{\Lambda}_{\boldsymbol{P}} & \frac{sign(\mu)h}{2\sqrt{3}n_0m_0}\boldsymbol{\Lambda}_{\overline{\boldsymbol{C}}}\boldsymbol{\Lambda}_{\boldsymbol{P}} \\ \frac{sign(\mu)h^3}{24\sqrt{3}n_0m_0}\boldsymbol{\Lambda}_{\overline{\boldsymbol{C}}}\boldsymbol{\Lambda}_{\boldsymbol{P}} & \frac{h^3}{12m_0^2}\boldsymbol{\Lambda}_{\overline{\boldsymbol{C}}}\boldsymbol{\Lambda}_{\boldsymbol{P}} \end{bmatrix} + \\ \frac{4}{3}H_{kin}\begin{bmatrix} \frac{1}{n_0^2}\boldsymbol{\Lambda}_{\boldsymbol{P}} & \frac{sign(\mu)}{2\sqrt{3}n_0m_0}\boldsymbol{\Lambda}_{\boldsymbol{P}} \\ \frac{sign(\mu)}{2\sqrt{3}n_0m_0}\boldsymbol{\Lambda}_{\boldsymbol{P}} & \frac{1}{m_0^2}\boldsymbol{\Lambda}_{\boldsymbol{P}} \end{bmatrix} \end{array}\right)\right]}_{\Theta}^{-1} \times \\ & diag[\boldsymbol{Q}^T, \boldsymbol{Q}^T]\left(\hat{\boldsymbol{\sigma}}^{trial}_{n+1} + \hat{\boldsymbol{\alpha}}^{trial}_{n+1}\right), \end{aligned} \tag{4.54}$$

where the matrix $\boldsymbol{\Theta}$ in (4.54) is of the following form

$$\boldsymbol{\Theta} = \begin{bmatrix} \widetilde{a} & 0 & 0 & \widetilde{g} & 0 & 0 \\ 0 & \widetilde{b} & 0 & 0 & \widetilde{h} & 0 \\ 0 & 0 & \widetilde{c} & 0 & 0 & \widetilde{i} \\ \widetilde{j} & 0 & 0 & \widetilde{d} & 0 & 0 \\ 0 & \widetilde{k} & 0 & 0 & \widetilde{e} & 0 \\ 0 & 0 & \widetilde{l} & 0 & 0 & \widetilde{f} \end{bmatrix}, \tag{4.55}$$

with

$$\begin{aligned} \widetilde{a} &= \frac{-(\gamma_{1,n+1}+\gamma_{2,n+1})(3Eh-2H_{kin}(\nu-1))}{3n_0^2(\nu-1)} + 1, \ \widetilde{b} = \frac{(\gamma_{1,n+1}+\gamma_{2,n+1})(3Eh+2H_{kin}(1+\nu))}{n_0^2(1+\nu)} + 1, \\ \widetilde{c} &= \frac{(\gamma_{1,n+1}+\gamma_{2,n+1})(3Eh+4H_{kin}(1+\nu))}{n_0^2(1+\nu)} + 1, \ \widetilde{d} = \frac{-(\gamma_{1,n+1}+\gamma_{2,n+1})(Eh^3-8H_{kin}(\nu-1))}{12m_0^2(\nu-1)} + 1, \\ \widetilde{e} &= \frac{(\gamma_{1,n+1}+\gamma_{2,n+1})(Eh^3+8H_{kin}(1+\nu))}{4m_0^2(1+\nu)} + 1, \ \widetilde{f} = \frac{(\gamma_{1,n+1}+\gamma_{2,n+1})(Eh^3+16H_{kin}(1+\nu))}{4m_0^2(1+\nu)} + 1, \end{aligned}$$

$$
\begin{aligned}
\widetilde{g} &= \frac{-(\gamma_{1,n+1}-\gamma_{2,n+1})(3Eh-2H_{kin}(\nu-1))}{6\sqrt{3}m_0n_0(\nu-1)},\ \widetilde{h} = \frac{(\gamma_{1,n+1}-\gamma_{2,n+1})(3Eh+2H_{kin}(1+\nu))}{2\sqrt{3}m_0n_0(1+\nu)},\\
\widetilde{i} &= \frac{(\gamma_{1,n+1}-\gamma_{2,n+1})(3Eh+4H_{kin}(1+\nu))}{2\sqrt{3}m_0n_0(1+\nu)},\ \widetilde{j} = \frac{-(\gamma_{1,n+1}-\gamma_{2,n+1})(Eh^3-8H_{kin}(\nu-1))}{24\sqrt{3}m_0n_0(\nu-1)},\\
\widetilde{k} &= \frac{(\gamma_{1,n+1}-\gamma_{2,n+1})(Eh^3+8H_{kin}(1+\nu))}{8\sqrt{3}m_0n_0(1+\nu)},\ \widetilde{l} = \frac{(\gamma_{1,n+1}-\gamma_{2,n+1})(Eh^3+16H_{kin}(1+\nu))}{8\sqrt{3}m_0n_0(1+\nu)}.
\end{aligned}
\tag{4.56}
$$

The form (4.55) allows inversion of $\boldsymbol{\Theta}$ leading to

$$
\boldsymbol{\Theta}^{-1} = \begin{bmatrix}
\frac{\widetilde{d}}{\widetilde{a}\widetilde{d}-\widetilde{g}\widetilde{j}} & 0 & 0 & \frac{\widetilde{g}}{-\widetilde{a}\widetilde{d}+\widetilde{g}\widetilde{j}} & 0 & 0\\
0 & \frac{\widetilde{e}}{\widetilde{b}\widetilde{e}-\widetilde{h}\widetilde{k}} & 0 & 0 & \frac{\widetilde{h}}{-\widetilde{b}\widetilde{e}+\widetilde{h}\widetilde{k}} & 0\\
0 & 0 & \frac{\widetilde{f}}{\widetilde{c}\widetilde{f}-\widetilde{i}\widetilde{l}} & 0 & 0 & \frac{\widetilde{i}}{-\widetilde{c}\widetilde{f}+\widetilde{i}\widetilde{l}}\\
\frac{\widetilde{j}}{-\widetilde{a}\widetilde{d}+\widetilde{g}\widetilde{j}} & 0 & 0 & \frac{\widetilde{a}}{\widetilde{a}\widetilde{d}-\widetilde{g}\widetilde{j}} & 0 & 0\\
0 & \frac{\widetilde{k}}{-\widetilde{b}\widetilde{e}+\widetilde{h}\widetilde{k}} & 0 & 0 & \frac{\widetilde{b}}{\widetilde{b}\widetilde{e}-\widetilde{h}\widetilde{k}} & 0\\
0 & 0 & \frac{\widetilde{l}}{-\widetilde{c}\widetilde{f}+\widetilde{i}\widetilde{l}} & 0 & 0 & \frac{\widetilde{c}}{\widetilde{c}\widetilde{f}-\widetilde{i}\widetilde{l}}
\end{bmatrix},
\tag{4.57}
$$

and

$$
(\hat{\boldsymbol{\sigma}}_{n+1} + \hat{\boldsymbol{\alpha}}_{n+1}) = diag[\boldsymbol{Q},\boldsymbol{Q}]\boldsymbol{\Theta}^{-1}diag[\boldsymbol{Q}^T,\boldsymbol{Q}^T]\left(\hat{\boldsymbol{\sigma}}^{trial}_{n+1} + \hat{\boldsymbol{\alpha}}^{trial}_{n+1}\right).
$$

One can now finally write eq. (4.50) as

$$
\begin{aligned}
&(\boldsymbol{\sigma}_{n+1} + \boldsymbol{\alpha}_{n+1}) =\\
&= \underbrace{\begin{bmatrix} diag[\boldsymbol{Q},\boldsymbol{Q}]\boldsymbol{\Theta}^{-1}diag[\boldsymbol{Q}^T,\boldsymbol{Q}^T] & \boldsymbol{0}\\ \boldsymbol{0} & \frac{1}{\left(1+\left(\gamma^1_{n+1}+\gamma^2_{n+1}\right)\frac{2}{q_0^2}(k^s+\frac{2}{3}H_{kin})\right)}\boldsymbol{I}_2 \end{bmatrix}}_{\boldsymbol{W}_{n+1}} \times\\
&\left(\boldsymbol{\sigma}^{trial}_{n+1} + \boldsymbol{\alpha}^{trial}_{n+1}\right),
\end{aligned}
\tag{4.58}
$$

with $\boldsymbol{Q}$ defined in (4.53) and $\boldsymbol{\Theta}^{-1}$ explicitly defined in (4.57). It can be clearly seen that the stress resultants $(\boldsymbol{\sigma}_{n+1} + \boldsymbol{\alpha}_{n+1})$ in (4.58) are only functions of $\gamma_{1,n+1}$ and $\gamma_{2,n+1}$.

Now, the yield functions can be rewritten by using (4.58) and (4.51) as

$$
\begin{aligned}
\phi_\mu(\gamma_{1,n+1},\gamma_{2,n+1}) &= (\boldsymbol{\sigma}_{n+1} + \boldsymbol{\alpha}_{n+1})^T \boldsymbol{A}_\mu (\boldsymbol{\sigma}_{n+1} + \boldsymbol{\alpha}_{n+1})\\
&\quad - \left(1 - \frac{q_{n+1}\left(\xi^I_n + \sum_{\mu=1}^2 \gamma_{\mu,n+1}\beta_{n+1}\right)}{\sigma_y}\right)^2 = 0, \qquad \mu = 1,2,
\end{aligned}
\tag{4.59}
$$

and further as

$$
\begin{aligned}
\phi_\mu(\gamma_{1,n+1},\gamma_{2,n+1}) &= \left(\boldsymbol{\sigma}^{trial}_{n+1} + \boldsymbol{\alpha}^{trial}_{n+1}\right)^T \boldsymbol{W}^T_{n+1}\boldsymbol{A}_\mu\boldsymbol{W}_{n+1}\left(\boldsymbol{\sigma}^{trial}_{n+1} + \boldsymbol{\alpha}^{trial}_{n+1}\right)\\
&\quad - \left(1 - \frac{q_{n+1}\left(\xi^I_n + \sum_{\mu=1}^2 \gamma_{\mu,n+1}\beta_{n+1}\right)}{\sigma_y}\right)^2 = 0, \qquad \mu = 1,2.
\end{aligned}
\tag{4.60}
$$

One finally gets only two equations for $\gamma_{1,n+1}$ and $\gamma_{2,n+1}$,

$$\boldsymbol{R}^p\left(\gamma_{1,n+1},\gamma_{2,n+1}\right)=\left[\begin{array}{c}\phi_1(\gamma_{1,n+1},\gamma_{2,n+1})\\ \phi_2(\gamma_{1,n+1},\gamma_{2,n+1})\end{array}\right]=\mathbf{0}, \tag{4.61}$$

that are highly nonlinear. Once (4.61) are solved for converged solutions $\overline{\gamma}_{1,n+1}$ and $\overline{\gamma}_{2,n+1}$, the strains (4.48) and stress-resultants (4.47) at the end of the time increment can be computed.

In the second case we simultaneously solve (4.48) along with $\phi_{1,n+1}=0$ and $\phi_{2,n+1}=0$ for five unknowns $\boldsymbol{\varepsilon}^p_{n+1},\xi^I_{n+1},\varkappa_{n+1},\gamma_{1,n+1}$ and $\gamma_{2,n+1}$. By considering the first and the last equation in (4.48) we can eliminate $\varkappa_{n+1}$ since $\varkappa_{n+1}=\boldsymbol{\varepsilon}^p_{n+1}$. In this situation, when all the internal variables are considered as the unknowns, we can obtain the values of stress and stress like variables

$$\boldsymbol{\sigma}_{n+1} = \boldsymbol{C}\left(\boldsymbol{\varepsilon}^{(i)}_{n+1}-\boldsymbol{\varepsilon}^p_{n+1}\right), \tag{4.62}$$

$$q_{n+1} = q_{n+1}\left(\xi^I_{n+1}\right), \tag{4.63}$$

$$\boldsymbol{\alpha}_{n+1} = -\frac{2}{3}H_{kin}\varkappa_{n+1}, \tag{4.64}$$

and with them express the yield functions

$$\phi_{\mu,n+1}=\left(\boldsymbol{\sigma}_{n+1}+\boldsymbol{\alpha}_{n+1}\right)^T\boldsymbol{A}_\mu\left(\boldsymbol{\sigma}_{n+1}+\boldsymbol{\alpha}_{n+1}\right)-\left(1-\frac{q_{n+1}}{\sigma_y}\right),\quad \mu=1,2. \tag{4.65}$$

The final system of equations that needs to be solved is then

$$\boldsymbol{R}^p\left(\boldsymbol{\varepsilon}^p_{n+1},\xi^I_{n+1}\gamma_{1,n+1},\gamma_{2,n+1}\right)=\left[\begin{array}{c}-\boldsymbol{\varepsilon}^p_{n+1}+\boldsymbol{\varepsilon}^p_n+\sum_{\mu=1}^2\gamma_{\mu,n+1}\boldsymbol{\nu}_{\mu,n+1}\\ -\xi^I_{n+1}+\xi^I_n+\sum_{\mu=1}^2\gamma_{\mu,n+1}\beta_{n+1}\\ \phi_{1,n+1}\\ \phi_{2,n+1}\end{array}\right]=\mathbf{0}. \tag{4.66}$$

Note that in this case all the expressions are rather simple. The drawback is that we need to solve a system of 11 equations (8 for plastic strains, 1 for isotropic hardening and 2 yield functions), which means we need to invert a matrix of size 11×11.

Solution algorithm

In the previous section we have presented the equations that one must solve in order to obtain the updated values of internal variables, i.e. (4.61) or (4.66). Both ways of handling the evolution of plastic variables and the yield functions produce completely the same results and for simlicity we will only consider the first case, i.e. (4.61).

As already mentioned in the previus section we have chosen the equations (4.61) by assuming that both yield surfaces $\mu=1,2$ are active

$$\boldsymbol{R}^p_{12}\left(\gamma_{1,n+1},\gamma_{2,n+1}\right)=\left[\begin{array}{c}\phi_1(\gamma_{1,n+1},\gamma_{2,n+1})\\ \phi_2(\gamma_{1,n+1},\gamma_{2,n+1})\end{array}\right]=\mathbf{0}. \tag{4.67}$$

The two other possibilities occur when only one yield surface is active. Let us first consider the option when only $\mu = 1$ is active. In this case we replace equations (4.67) with

$$\boldsymbol{R}_1^p\left(\gamma_{1,n+1}, \gamma_{2,n+1}\right) = \begin{bmatrix} \phi_1\left(\gamma_{1,n+1}, \gamma_{2,n+1}\right) \\ \gamma_{2,n+1} \end{bmatrix} = \mathbf{0}. \tag{4.68}$$

The last option is when only $\mu = 2$ is active and the equations that need to be solved are then

$$\boldsymbol{R}_2^p\left(\gamma_{1,n+1}, \gamma_{2,n+1}\right) = \begin{bmatrix} \gamma_{1,n+1} \\ \phi_2\left(\gamma_{1,n+1}, \gamma_{2,n+1}\right) \end{bmatrix} = \mathbf{0}. \tag{4.69}$$

Figure 4.2 depicts three different situations for the trial values of stress. For the trial

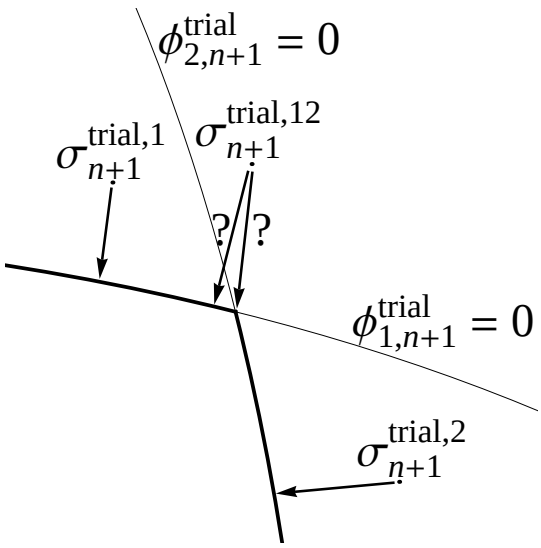

Figure 4.2: A sketch of a two-surface yield function and the closest point projection

Slika 4.2: Skica projekcije testnih vrednosti napetosti na funkcijo tečenja določeno z dvema ploskvama

value $\boldsymbol{\sigma}_{n+1}^{trial,1}$ we have $\phi_{1,n+1}^{trial} > 0$ and $\phi_{2,n+1}^{trial} < 0$. Here we know in advance that the solution of equations (4.68) gives us the closest point projection and the correct update of the internal variables. Similarly we know for $\boldsymbol{\sigma}_{n+1}^{trial,2}$ that we need to solve equations (4.69) since $\phi_{1,n+1}^{trial} < 0$ and $\phi_{2,n+1}^{trial} > 0$. But in the case of $\boldsymbol{\sigma}_{n+1}^{trial,12}$, when both trial values of yield functions are violated, we can not be sure in advance which set of equations is the right one.

In the last case, when we are not sure which equations to use, we have two alternative strategies:

- **Procedure 1.** In this method we look for solutions for all posible sets of equations and the admissibility of the solutions is checked by testing weather the Kuhn-Tucker conditions hold.

- **Procedure 2.** In this method we can change the set of equations during the iterative process by enforcing the admissibility constrain $\gamma_{\mu,n+1} \geq 0$ for all active surfaces.

A brief descriptions of the algorithms associated with Procedures 1 and 2 are given below.
Procedure 1: In this procedure we determine the solutions of three different sets of equations

$$\overline{\boldsymbol{\gamma}}_{a,n+1} = \left[\overline{\gamma}_{1,n+1,a}, \overline{\gamma}_{2,n+1,a}\right]^T, \quad \boldsymbol{R}_a^p\left(\overline{\boldsymbol{\gamma}}_{a,n+1}\right) = \mathbf{0} \quad \text{for} \quad a = 1, 2, 12, \tag{4.70}$$

where $(\overline{\circ})$ denotes the converged values of variables. Each solution is obtained with the following iterative procedure.

1. First we define the iteration counter k

$$k = 0,$$

and set the initial values of plastic multipliers to zero

$$\boldsymbol{\gamma}_{a,n+1}^{(k)} = [0, 0]^T.$$

2. Then we start an iterative loop in which we first determine the current values of $\boldsymbol{R}_a^p$

$$\boldsymbol{R}_a^{p,(k)} = \boldsymbol{R}_a^p\left(\boldsymbol{\gamma}_{a,n+1}^{(k)}\right),$$

and chech for convergence

$$||\boldsymbol{R}_a^{p,(k)}|| \overset{?}{<} \text{tol}..$$

3. If the convergence test is satisfied we are happy with the solution

$$\overline{\boldsymbol{\gamma}}_{a,n+1} = \boldsymbol{\gamma}_{a,n+1}^{(k)},$$

and we exit the iteration loop. Otherwise we move on to 4.

4. Here we compute the current value of matrix $\boldsymbol{K}^{\boldsymbol{R}_a^p} = \frac{\partial \boldsymbol{R}_a^p}{\partial \boldsymbol{\gamma}_a}$

$$\boldsymbol{K}^{\boldsymbol{R}^p,(k)} = \boldsymbol{K}^{\boldsymbol{R}_a^p}\left(\boldsymbol{\gamma}_{a,n+1}^{(k)}\right),$$

and compute the update for plastic multipliers

$$\Delta\boldsymbol{\gamma}_{a,n+1}^{(k)} = -(\boldsymbol{K}^{\boldsymbol{R}^p,(k)})^{-1}\boldsymbol{R}_a^{p,(k)}.$$

5. Then we set the iteration counter to

$$k = k + 1,$$

update the values of the plastic multipliers

$$\boldsymbol{\gamma}_{a,n+1}^{(k)} = \boldsymbol{\gamma}_{a,n+1}^{(k-1)} + \Delta\boldsymbol{\gamma}_{a,n+1}^{(k-1)},$$

and go to 2.

The admissibility of each solution is checked with the Kuhn-Tucker's loading/unloading conditions:

$$\underbrace{\overline{\gamma}_{1,n+1,a} \geq 0 \ \& \ \overline{\gamma}_{2,n+1,a} \geq 0 \ \& \ \phi_1\left(\overline{\boldsymbol{\gamma}}_{a,n+1}\right) \leq 0 \ \& \ \phi_2\left(\overline{\boldsymbol{\gamma}}_{a,n+1}\right) \leq 0}_{?}, \quad a = 1, 2, 12. \tag{4.71}$$

We denote the solution that satisfies all the conditions with $\overline{a}$

$$\overline{\boldsymbol{\gamma}}_{n+1} = \overline{\boldsymbol{\gamma}}_{\overline{a},n+1}. \tag{4.72}$$

Note that this procedure is robust and it always provides the solution but it is quite computationally expensive since three independent iteration procedures are performed.

Procedure 2: The below algorithm is a variation of a general multi-surface closest point projection iteration procedure, that is presented in [Simo and Kennedy, 1992] and [Simo and Hughes, 1998]. The difference is that in our work we deal with at most two active yield surfaces, whereas the original algorithm allows for an arbitrary number of active yield surfaces. The solution is obtained with the following iteration procedure.

1. First we define the iteration counter

$$k = 0,$$

set

$$a = 12,$$

to determine the starting set of equations and set the initial values of plastic multipliers to zero

$$\boldsymbol{\gamma}_{n+1}^{(k)} = [0, 0]^T.$$

2. Then we start an iterative loop in which we first determine the current values of $\boldsymbol{R}^p$

$$\boldsymbol{R}^{p,(k)} = \boldsymbol{R}_a^p\left(\boldsymbol{\gamma}_{n+1}^{(k)}\right),$$

and chech for convergence

$$||\boldsymbol{R}^{p,(k)}|| \overset{?}{<} \text{tol}..$$

3. If the convergence test is satisfied we are happy with the solution

$$\overline{\boldsymbol{\gamma}}_{n+1} = \boldsymbol{\gamma}_{n+1}^{(k)},$$

and we exit the iteration loop. Otherwise we move on to 4.

4. Here we compute the current value of matrix $\boldsymbol{K}^{\boldsymbol{R}^p} = \frac{\partial \boldsymbol{R}^p}{\partial \boldsymbol{\gamma}}$

$$\boldsymbol{K}^{\boldsymbol{R}^p,(k)} = \boldsymbol{K}^{\boldsymbol{R}^p}\left(\boldsymbol{\gamma}_{n+1}^{(k)}\right),$$

and compute the update for plastic multipliers

$$\Delta\boldsymbol{\gamma}_{n+1}^{(k)} = -(\boldsymbol{K}^{\boldsymbol{R}^p,(k)})^{-1}\boldsymbol{R}^{p,(k)}.$$

5. Then we set the iteration counter to

$$k = k + 1,$$

and if $a = 1$ or $a = 2$ update the values of the plastic multipliers

$$\boldsymbol{\gamma}_{n+1}^{(k)} = \boldsymbol{\gamma}_{n+1}^{(k-1)} + \Delta\boldsymbol{\gamma}_{n+1}^{(k-1)},$$

and go to 2. If $a = 12$ go to 6.

6. Here we compute the test values of plastic multipliers

$$\boldsymbol{\gamma}_{n+1}^{(k),test} = \boldsymbol{\gamma}_{n+1}^{(k-1)} + \Delta\boldsymbol{\gamma}_{n+1}^{(k-1)},$$

and check if those values are admissible

$$\gamma_{1,n+1}^{(k),test} \overset{?}{\geq} 0, \quad \gamma_{2,n+1}^{(k),test} \overset{?}{\geq} 0.$$

If both tests are satisfied we update the values of the plastic multipliers

$$\boldsymbol{\gamma}_{n+1}^{(k)} = \boldsymbol{\gamma}_{n+1}^{(k-1)} + \Delta\boldsymbol{\gamma}_{n+1}^{(k-1)},$$

and go to 2. If one of the tests fails, the values of plastic multipliers remain unchanged

$$\boldsymbol{\gamma}_{n+1}^{(k)} = \boldsymbol{\gamma}_{n+1}^{(k-1)},$$

we change the parameter a according to

$$\begin{array}{llll} \text{If} & \gamma_{1,n+1}^{(k)} < 0 & \text{then} & a = 2, \\ \text{If} & \gamma_{2,n+1}^{(k)} < 0 & \text{then} & a = 1, \end{array}$$

and go to 2.

This procedure is computationally much cheaper and is also rather robust. Theoretically, if the yield surface is convex, then the above algorithm is unconditionally convergent. Practically, it may occur that the above procedure does not produce the desired solution and in that case a step size adjustment is needed, see e.g. [Simo and Hughes, 1998] and references therein.

Consistent tanget modulus

In order to ensure the quadratic rate of convergence of the global iterative procedure we have to consistently linearize the global system of equations. This requires to compute the implicit dependencies among the state variables and the strain vector in order to obtain the consistent tangent modulus $d\boldsymbol{\sigma}_{n+1}/d\boldsymbol{\varepsilon}_{n+1}$. For that purpuse we assume the following functional dependencies

$$\boldsymbol{\sigma}\left(\boldsymbol{\varepsilon}_{n+1}\right) = \boldsymbol{C}\left(\boldsymbol{\varepsilon}_{n+1} - \boldsymbol{\varepsilon}^{p}_{n+1}\left(\overline{\boldsymbol{\gamma}}_{n+1}\left(\boldsymbol{\varepsilon}_{n+1}\right)\right)\right). \tag{4.73}$$

The challenging part is to obtain the derivatives of plastic strain with respect to the total strain. By applying the chain rule we have

$$\frac{d\boldsymbol{\varepsilon}^{p}_{n+1}}{d\boldsymbol{\varepsilon}_{n+1}} = \frac{d\boldsymbol{\varepsilon}^{p}_{n+1}}{d\overline{\boldsymbol{\gamma}}_{n+1}}\frac{d\overline{\boldsymbol{\gamma}}_{n+1}}{d\boldsymbol{\varepsilon}_{n+1}}, \tag{4.74}$$

and the only unknown derivative here is $\frac{d\overline{\boldsymbol{\gamma}}_{n+1}}{d\boldsymbol{\varepsilon}_{n+1}}$. The implicit dependencies are obtained from the consistency condition $\dot{\phi}_{\mu,n+1} = 0$. We assume that the yield surfaces (the plastic equations) are the functions of the total strain and the plastic multipliers

$$\phi_{\mu,n+1} = \phi_{\mu}\left(\boldsymbol{\varepsilon}_{n+1}, \overline{\boldsymbol{\gamma}}_{n+1}\left(\boldsymbol{\varepsilon}_{n+1}\right)\right) \;\Rightarrow\; \boldsymbol{R}^{p}\left(\boldsymbol{\varepsilon}_{n+1}, \overline{\boldsymbol{\gamma}}_{n+1}\left(\boldsymbol{\varepsilon}_{n+1}\right)\right). \tag{4.75}$$

By the chain rule derivation of the above equation we obtain

$$\begin{aligned}\dot{\boldsymbol{R}}^{p}{}_{\mu,n+1} &= \frac{d\boldsymbol{R}^{p}}{d\boldsymbol{\varepsilon}_{n+1}}\frac{d\boldsymbol{\varepsilon}_{n+1}}{dt} + \underbrace{\frac{d\boldsymbol{R}^{p}}{d\overline{\boldsymbol{\gamma}}_{n+1}}}_{\boldsymbol{K}^{\boldsymbol{R}^{p}}}\frac{d\overline{\boldsymbol{\gamma}}_{n+1}}{d\boldsymbol{\varepsilon}_{n+1}}\frac{d\boldsymbol{\varepsilon}_{n+1}}{dt} = \\ &= \underbrace{\left(\frac{d\boldsymbol{R}^{p}}{d\boldsymbol{\varepsilon}_{n+1}} + \boldsymbol{K}^{\boldsymbol{R}^{p}}\frac{d\overline{\boldsymbol{\gamma}}_{n+1}}{d\boldsymbol{\varepsilon}_{n+1}}\right)}_{=\mathbf{0}}\underbrace{\frac{d\boldsymbol{\varepsilon}_{n+1}}{dt}}_{\neq\mathbf{0}} = \mathbf{0},\end{aligned} \tag{4.76}$$

and the derivative that we are looking for is then

$$\frac{d\overline{\boldsymbol{\gamma}}_{n+1}}{d\boldsymbol{\varepsilon}_{n+1}} = -(\boldsymbol{K}^{\boldsymbol{R}^{p}})^{-1}\frac{d\boldsymbol{R}^{p}}{d\boldsymbol{\varepsilon}_{n+1}}, \tag{4.77}$$

where all the derivatives on the right hand side of (4.77) can be obtained by considering functional dependencies.

4.4 Numerical examples

In this section we present some numerical examples, computed by the above derived 4-node element. The computer implementation of the element is in complete accordance with the above derivation. The local Cartesian frames are introduced at the element integration points. The computer code was generated by using symbolic code manipulation program AceGen developed by Korelc [Korelc, 2007b], [Korelc, 1997]. The element codes were introduced into the finite element analysis program AceFEM, see [Korelc, 2007a].

4.4.1 Pinched cylinder with isotropic hardening

We consider a short cylinder bounded by two rigid diaphragms at its ends. The cylinder is loaded with two concentrated forces at the middle section. Due to symmetry, only one octant of the cylinder is modeled. The geometry, loading, boundary conditions and

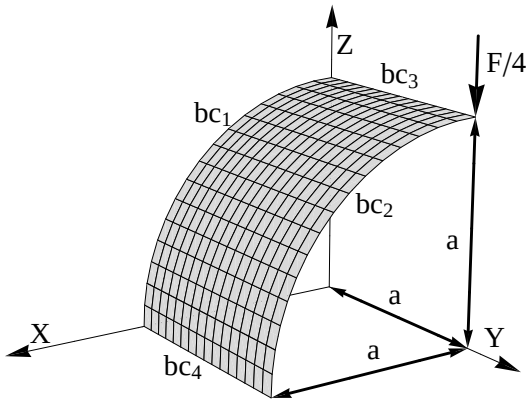

Figure 4.3: Geometry, loading and boundary conditions for pinched cylinder

Slika 4.3: Geometrija, obtežba in robni pogoji pri cilindru

the finite element mesh of the octant are presented in Figure 4.3, where $a = 300$ cm, bc_1 denotes the edge with the rigid diaphragm while bc_2, bc_3 and bc_4 denote the edges with the symmetry boundary conditions. The thickness of the cylinder wall is 3 cm and the material properties are: Young's modulus $E = 3000$ kN/cm^2, Poisson's ration $\nu = 0.3$ and yield stress $\sigma_y = 24.3$ kN/cm^2. The plastic behavior is characterized by linear isotropic hardening response with hardening modulus $K_h = 300$ kN/cm^2. The load versus displacement curves of our simulation along with the curves obtained in [Simo and Kennedy, 1992] and [Brank et al., 1997] are presented in Figure 4.4. One can see that all the formulations have similar responses at the low levels of loading while the differences grow with the increase of loading. Note that in this example Procedure 2 presented in Section 4.3.2 did not always produce the solution for internal variables. We believe this was caused by the relatively large steps in loading that occur due to local buckling of the cylinder. The robust Procedure 1 had no problems finding the solution. Figure 4.5 depicts the initial and the final deformed configuration of the cylinder.

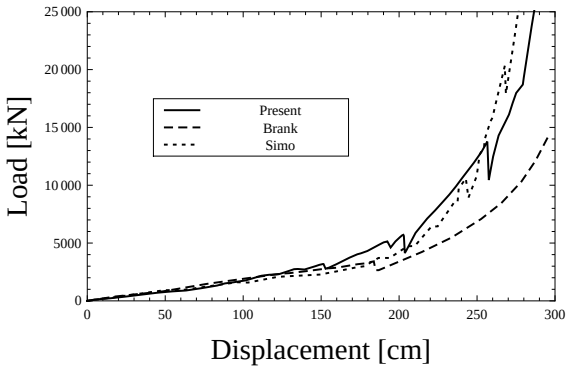

Figure 4.4: Load versus displacement curves for pinched cylinder

Slika 4.4: Diagram obtežba - pomik pri cilindru

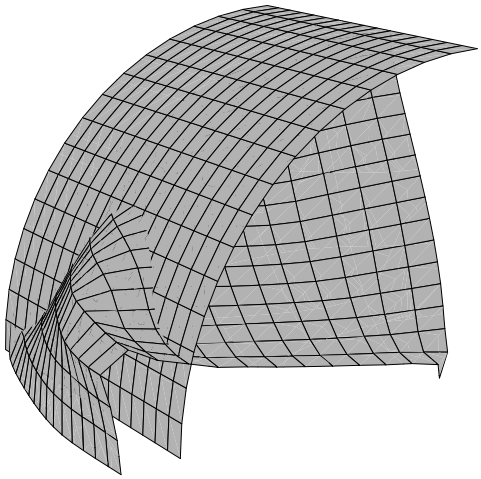

Figure 4.5: Initial and deformed configuration for pinched cylinder

Slika 4.5: Začetna in deformirana lega cilindra

4.4.2 Half of a sphere

We consider half of a sphere loaded with two inward and two outward forces. Due to symmetry, only one quadrant is modeled. The geometry, loading, boundary conditions

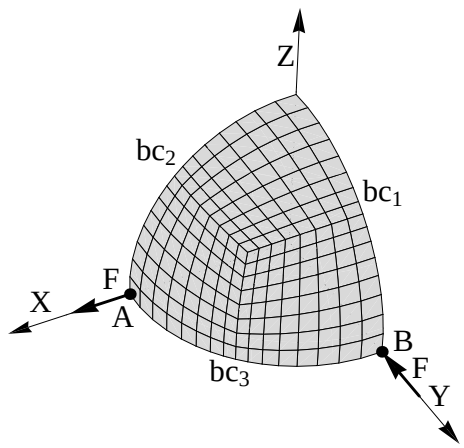

Figure 4.6: Geometry, loading and boundary conditions of half of a sphere

Slika 4.6: Geometrija, obtežba in robni pogoji pri polovici sfere

and the finite element mesh of the quadrant are presented in Figure 4.6, bc_1 and bc_2 denote the edges with the symmetry boundary conditions and the edge bc_3 is free. The radius of the sphere is 10 cm and the thickness is 0.5 cm. The material properties are: Young's modulus $E = 10$ kN/cm^2, Poisson's ration $\nu = 0.2$, yield stress $\sigma_y = 0.2$ kN/cm^2 and the linear hardening modulus $K_h = 3$ kN/cm^2. The load versus displacement curves of our simulation along with the curves obtained in [Simo and Kennedy, 1992] and [Basar and Itskov, 1999] are presented in Figure 4.7. We note that [Basar and Itskov, 1999] used stress-based plasticity for shells. In this example both procedures described in Section 4.3.2 did not exhibit any problems. Figure 4.8 depicts the initial configuration, the configuration under the maximum load and the final unloaded configuration, where irreversible nature of plastic deformation is evident.

4.4.3 Limit load analysis of a rectangular plate

A clamped (of hard type) rectangular plate of elastic-perfectly plastic material under uniformly distributed load in the Z direction is considered in this example. We consider

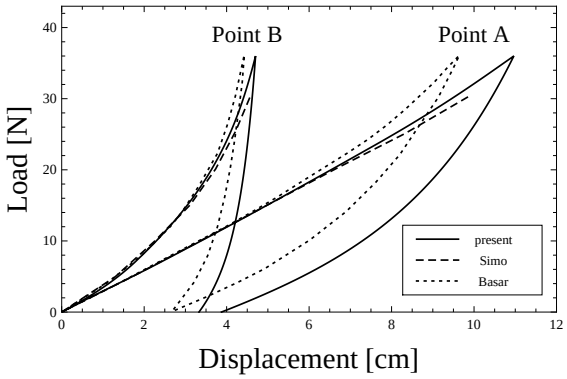

Figure 4.7: Load versus displacement curves for half of a sphere

Slika 4.7: Diagram obtežba - pomik pri polovici sfere

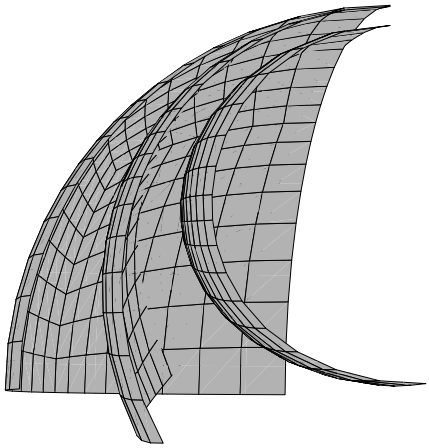

Figure 4.8: Initial, deformed fully loaded and deformed unloaded configuration for half of a sphere

Slika 4.8: Začetna, deformirana obremenjena in deformirana neobremenjena konfiguracija polovice sfere

two cases, a thin plate with thickness 0.5 cm and a thick plate with thickness 5 cm. The other geometry and material parameters are the same for both cases: length $a = 150$ cm, width $b = 100$ cm, Young's modulus $E = 21000$ kN/cm^2, Poisson's ration $\nu = 0.3$ and yield stress $\sigma_y = 40$ kN/cm^2. The geometry and the finite element mesh of the plate

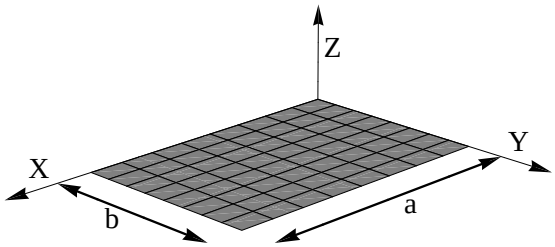

Figure 4.9: Geometry for rectangular plate

Slika 4.9: Geometrija pri pravokotni plošči

are presented in Figure 4.9. We compare the results of the geometrically nonlinear shell formulation with those obtained by the geometrically linear plate formulation presented in Chapter 3. Load-displacement curves for the thin plate are presented in Figure 4.10.

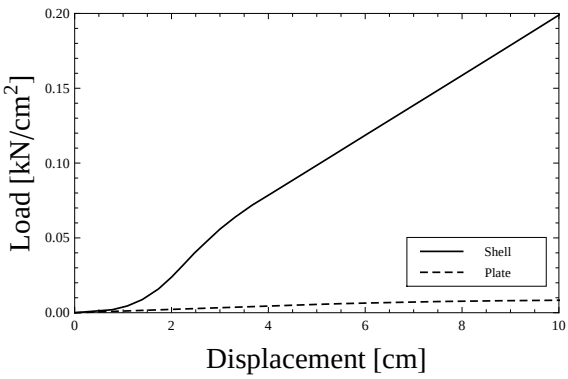

Figure 4.10: Load versus displacement curves for the thin plate

Slika 4.10: Krivulje obtežba pomik pri tanki plošči

There is a big difference in results of both formulations, since the plate is so thin, that the assumptions of the geometrically linear plate formulation are not valid. The influence of geometrical nonlinearity is negligable only when load is small. With the increase of load, the displacements also grow and the axial forces start to play a big role, thus giving a much stiffer response. We can see that limit load of the plate formulation is around

0.097 kN/cm^2, while the shell formulation at load level 2 kN/cm^2 is still in elastic regime. In Figure 4.11 we plot the load versus displacement curves for the thick plate. We can see

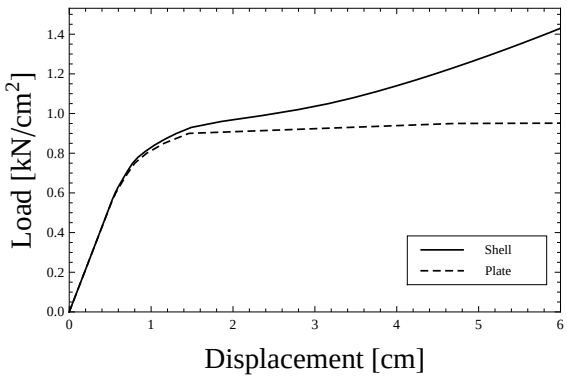

Figure 4.11: Load versus displacement curves of the thick plate

Slika 4.11: Krivulje obtežba pomik pri debeli plošči

that in this case we have a much better agreement in results. The limit load computed with the plate formulation is 0.95 kN/cm^2, while in the shell formulation axial stiffening occures, thus giving a greater resistance of the plate.

4.5 Concluding remarks and chapter summary

An inelastic geometrically exact shell finite element formulated entirely in terms of stress resultants has been presented in this chapter. The basic ingredients of the constitutive law are the usual additive split of elastic and plastic strains

$$\boldsymbol{\varepsilon} = \boldsymbol{\varepsilon}^e + \boldsymbol{\varepsilon}^p,$$

the strain energy function including isotropic and kinematic hardening

$$\psi\left(\boldsymbol{\varepsilon}^e, \xi^I, \check{\varkappa}\right) = \frac{1}{2}\boldsymbol{\varepsilon}^{e,T}\boldsymbol{C}\boldsymbol{\varepsilon}^e + \Xi\left(\xi^I\right) + \frac{1}{2}\varkappa^T\boldsymbol{D}\varkappa,$$

stress resultant yield function defined with two yield surfaces (see Figure 4.1)

$$\phi_\mu\left(\boldsymbol{\sigma}, q, \boldsymbol{\alpha}\right) = \left(\boldsymbol{\sigma} + \boldsymbol{\alpha}\right)^T \boldsymbol{A}_\mu\left(\boldsymbol{\sigma} + \boldsymbol{\alpha}\right) - \left(1 - \frac{q}{\sigma_y}\right)^2 \qquad \mu = 1, 2,$$

the plastic dissipation

$$\mathcal{D}^p = \boldsymbol{\sigma}^T\dot{\boldsymbol{\varepsilon}}^p + q\dot{\xi}^I + \boldsymbol{\alpha}^T\dot{\varkappa} \geqslant 0,$$

and the principle of maximum plastic dissipation

$$\mathcal{L}^p\left(\boldsymbol{\sigma}, q, \boldsymbol{\alpha}, \dot{\gamma}_1, \dot{\gamma}_2\right) = -\mathcal{D}^p\left(\boldsymbol{\sigma}, q, \boldsymbol{\alpha}\right) + \sum_{\mu=1}^{2} \dot{\gamma}_\mu \phi_\mu\left(\boldsymbol{\sigma}, q, \boldsymbol{\alpha}\right),$$

which here considers the multi-surface nature of the yield function. In Section 4.3.2 we first present two options of computing the updates of plastic variables. In the first approach we only solve the equations related to yield function

$$\boldsymbol{R}^p\left(\gamma_{1,n+1}, \gamma_{2,n+1}\right) = \begin{bmatrix} \phi_1(\gamma_{1,n+1}, \gamma_{2,n+1}) \\ \phi_2(\gamma_{1,n+1}, \gamma_{2,n+1}) \end{bmatrix} = \mathbf{0},$$

and with the newly computed values of plastic multipliers determine the updates of internal variables. In the second approach we determine the values of plastic variables directly, since evolution equations are included in the system of nonlinear equations

$$\boldsymbol{R}^p\left(\boldsymbol{\varepsilon}^p_{n+1}, \xi^I_{n+1}\gamma_{1,n+1}, \gamma_{2,n+1}\right) = \begin{bmatrix} -\boldsymbol{\varepsilon}^p_{n+1} + \boldsymbol{\varepsilon}^p_n + \sum_{\mu=1}^{2} \gamma_{\mu,n+1}\boldsymbol{\nu}_{\mu,n+1} \\ -\xi^I_{n+1} + \xi^I_n + \sum_{\mu=1}^{2} \gamma_{\mu,n+1}\beta_{n+1} \\ \phi_{1,n+1} \\ \phi_{2,n+1} \end{bmatrix} = \mathbf{0}.$$

When dealing with multi-surface plasticity we are in general not a priori sure which of the yield surfaces is active and in the case of two surfaces, we differ between three sets of equations

$$\boldsymbol{R}^p_{12} = \begin{bmatrix} \phi_{1,n+1} \\ \phi_{2,n+1} \end{bmatrix} = \mathbf{0}, \ \boldsymbol{R}^p_1 = \begin{bmatrix} \phi_{1,n+1} \\ \gamma_{2,n+1} \end{bmatrix} = \mathbf{0}, \ \boldsymbol{R}^p_2 = \begin{bmatrix} \gamma_{1,n+1} \\ \phi_{2,n+1} \end{bmatrix} = \mathbf{0},$$

which cover all the possible outcomes, i.e. $\boldsymbol{R}^p_{12}$ both yield surfaces are active, $\boldsymbol{R}^p_1$ only the first yield surface is active and $\boldsymbol{R}^p_2$ only the second yield surface is active. Two procedures for obtaining the proper solution have been presented. In Section 4.4 several numerical examples have been presented, which show a very satisfying performance of the presented approach compared to results from literature.

Chapter 5

Illustration of embedded discontinuity concept for failure analysis

5.1 Introduction

In this chapter we illustrate the embedded discontinuity concept for failure analysis of solids. The failure of a 1D solid contains all the significant features that are present in the failure of a more complex 2D and 3D solids yet it is simple enough to clearly illustrate the principle of the embedded discontinuity finite element method.

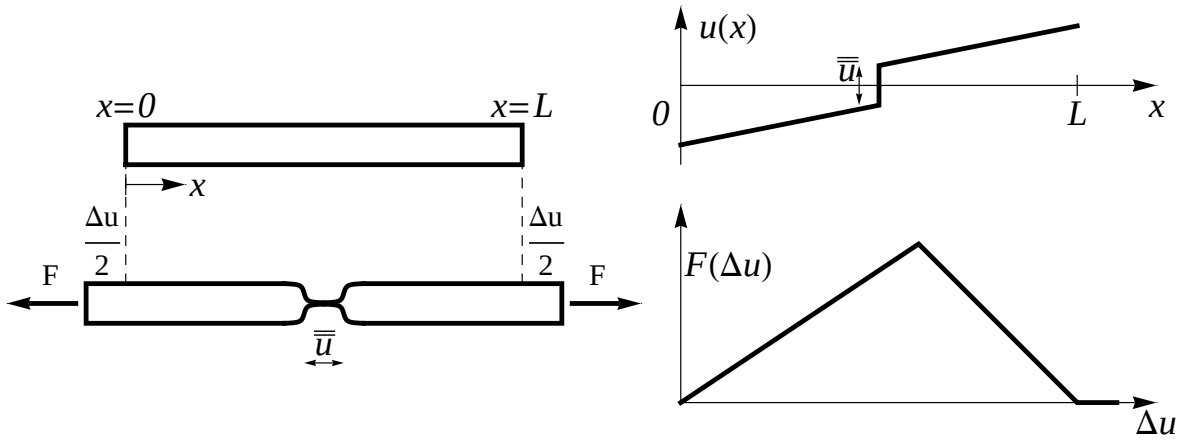

Figure 5.1: Tension test of an idealized bar

Slika 5.1: Natezni test idealizirane palice

We consider a tension test of an idealized bar presented in Figure 5.1. The response of the bar is linear elastic up to the point when the ultimate material stress is reached.

Then the resistance of the bar reduces linearly with the increasing imposed displacement, see bottom right part of Figure 5.1. The bottom left part of Figure 5.1 depicts one of the key features of the failure of the component, i.e. the resistance of the bar is reduced due to the localized failure that occurs in the small neighborhood of the bar's weakest point (we choose the midpoint of the bar). In the sketch we presented the failure by the necking effect that is common in the tension tests of metal bars. Note that except for the midpoint where irreversible (plastic) strains appeared the rest of the bar is elastic, thus the softening response of the bar is governed only by the behavior of the bar's midpoint. In the top right part of Figure 5.1 we present the distribution of displacements along the length of the bar for the bar that is in softening regime prior to complete failure. One can interpret the jump in displacements $\overline{\overline{u}}$ as the localized plastic strain at the position of the discontinuity.

The chapter is organized as follows: in Section 5.2 we present the kinematics, equilibrium equations and constitutive relations in a 1D solid finite element with embedded discontinuity. In Section 5.3 we present the computational procedure for failure analysis with the embedded discontinuity finite element method. Two numerical simulations are presented in Section 5.4. Finally in Section 5.5 concluding remarks and a short summary close the chapter.

5.2 1D finite element with embedded discontinuity

In this section we will present the formulation that is capable of modeling the failure of the idealized bar presented in the previous section.

Kinematics

As a starting point we consider a standard isoparametric 1D solid finite element of length L^e whose geometry is defined by

$$x^h(\xi) = \sum_{a=1}^{2} N_a(\xi) x_a, \quad x^h \in \Omega^e = [x_1, x_2], \tag{5.1}$$

where superscript h is used to denote the discretely approximated quantities, $\xi \in [-1, 1]$ is the element's local coordinate, x_a is the global coordinate of the node a, Ω^e is the element's domain and

$$N_a(\xi) = \frac{1}{2}(1 + \xi_a \xi), \qquad \begin{array}{ccc} a & 1 & 2 \\ \hline \xi_a & -1 & 1 \end{array}. \tag{5.2}$$

The element's displacement field is interpolated as

$$u^h_{\text{FEM}}(\xi) = \sum_{a=1}^{2} N_a(\xi) d_a, \tag{5.3}$$

where d_a is the displacement of the node a and subscript FEM is used to denote the displacement interpolation according to standard finite element method. Figure 5.2 depicts

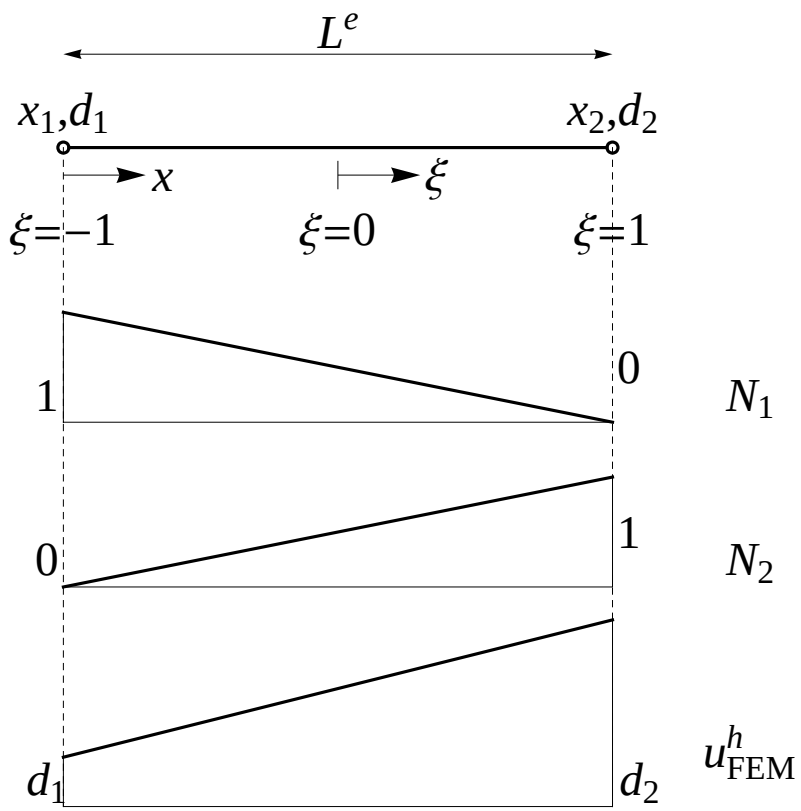

Figure 5.2: Standard isoparametric 1d solid finite element

Slika 5.2: Standardni izoparametrični končni element za palico

the finite element's geometry along with the graphic interpretation of shape functions and the displacement field. Clearly this finite element is not able to model the jump in displacement. In order to capture the discontinuity in the displacements we consider the same finite element as described above but now enriched with one additional kinematic parameter α, see Figure 5.3. The enriched displacement field can be then written as

$$u^h(\xi) = \underbrace{\sum_{a=1}^{2} N_a(\xi) d_a}_{u^h_{\text{FEM}}} + \underbrace{M_\alpha(\xi)\alpha}_{\text{enrichment}}, \tag{5.4}$$

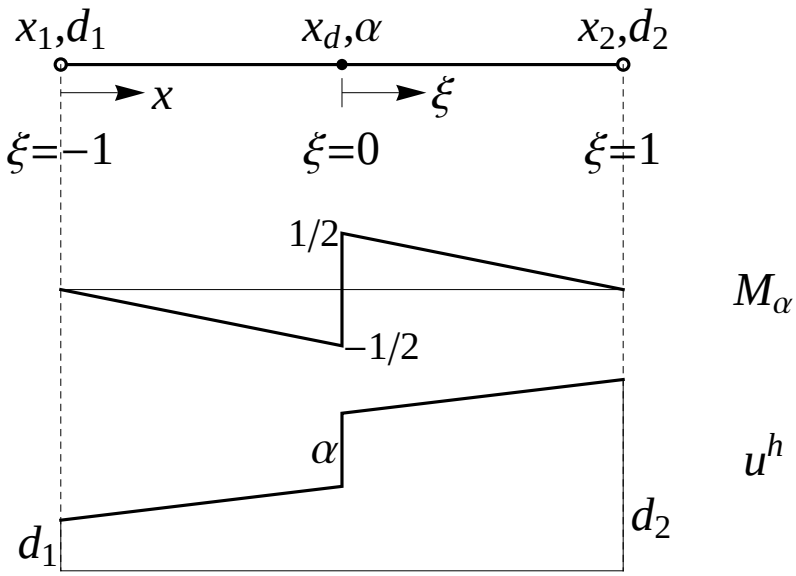

Figure 5.3: Isoparametric 1d solid finite element with embedded discontinuity

Slika 5.3: Izoparametrični končni element za palico z vgrajeno diskontinuiteto

where

$$M_\alpha(\xi) = H_{x_d}\left(x^h(\xi)\right) - N_2(\xi), \quad H_{x_d}\left(x^h(\xi)\right) = \begin{cases} 1 & \text{for } x^h > x_d \\ 0 & \text{otherwise} \end{cases}, \tag{5.5}$$

and x_d is the position of the discontinuity within the element (we choose the element's midpoint). The total strain field can be then computed as the space derivative of this displacement interpolation leading to

$$\epsilon = \frac{du^h}{dx} = \underbrace{\sum_{a=1}^{2} B_a(\xi) d_a}_{\epsilon_d} + \underbrace{G_\alpha(\xi)\alpha}_{\epsilon_\alpha}, \tag{5.6}$$

where

$$B_1(\xi) = -\frac{1}{L^e}, \quad B_2(\xi) = \frac{1}{L^e}, \quad G_\alpha = \underbrace{-B_2(\xi)}_{\overline{G}_\alpha} + \underbrace{\delta_{x_d}(\xi)}_{\overline{\overline{G}}_\alpha}. \tag{5.7}$$

In above expression we have used the following rule when deriving the Heaviside function

$$\frac{dH_{x_d}}{dx} = \delta_{x_d}(\xi) = \begin{cases} \infty & \text{for } x^h(\xi) = x_d \\ 0 & \text{otherwise} \end{cases}. \tag{5.8}$$

We further divide the strain field into a regular part $\overline{\epsilon}$ and singular part $\overline{\overline{\epsilon}}$

$$\epsilon = \overline{\epsilon} + \overline{\overline{\epsilon}} = \underbrace{\sum_{a=1}^{2} B_a(\xi) d_a + \overline{G}_\alpha \alpha}_{\overline{\epsilon}} + \underbrace{\overline{\overline{G}}_\alpha \alpha}_{\overline{\overline{\epsilon}}}. \tag{5.9}$$

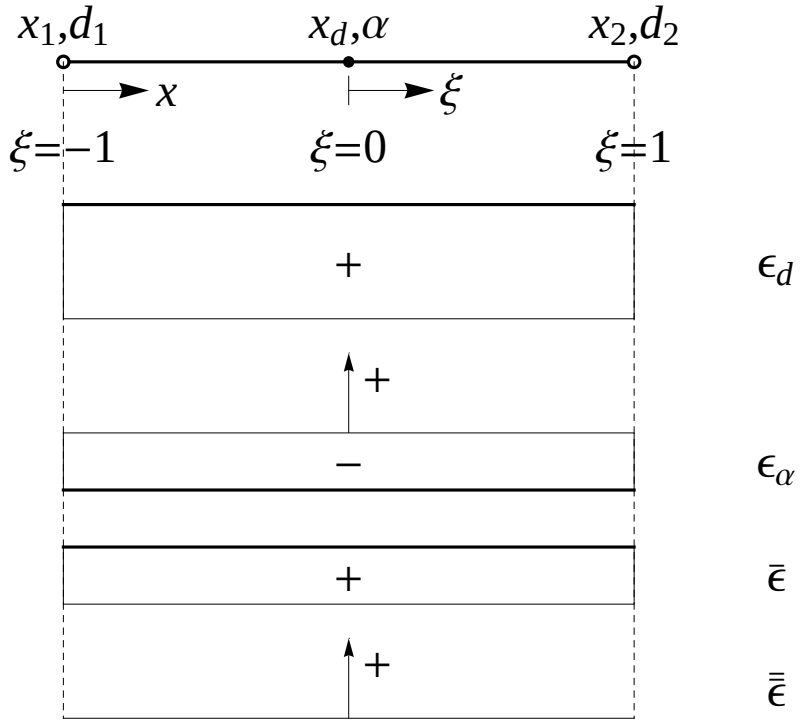

Figure 5.4: Strain distribution

Slika 5.4: Potek deformacij

In Figure 5.4 we present the contribution of the nodal displacements ϵ_d and the contribution of the discontinuity ϵ_α to the total strain field ϵ. Note that with the introduction of the discontinuity the element unloads, i.e. the regular part of the total strain is smaller in the whole domain of the element. All the irreversible deformations are concentrated at the position of the discontinuity, thus giving the infinite value of total deformation at that point.

Equilibrium

Virtual strains are interpolated according to

$$\hat{\epsilon} = \sum_{a=1}^{2} B_a(\xi)\hat{d}_a + \hat{G}_\alpha \hat{\alpha}, \tag{5.10}$$

where $\hat{d}_a$ are the virtual nodal displacements and $\hat{\alpha}$ is the virtual discontinuity parameter. The discontinuity parameter α can be viewed as additional (incompatible) degree of freedom and in that sense we use the following modification when computing the virtual strain

$$\begin{aligned} \hat{G}_\alpha &= G_\alpha - \frac{1}{L^e}\int_{\Omega^e} G_\alpha dx \\ &= \underbrace{\overline{G}_\alpha - \frac{1}{L^e}\int_{\Omega^e} \overline{G}_\alpha dx}_{=0} + \overline{\overline{G}}_\alpha - \frac{1}{L^e}\int_{\Omega^e} \overline{\overline{G}}_\alpha dx \\ &= \underbrace{-\frac{1}{L^e}\int_{\Omega^e} \delta_{x_d} dx}_{=-\frac{1}{L^e}=-B_2=\overline{G}_\alpha} + \underbrace{\delta_{x_d}}_{\overline{\overline{G}}_\alpha} = G_\alpha. \end{aligned} \tag{5.11}$$

In (5.11) we used the following rule to integrate the Dirac-delta function

$$\int_a^b \delta_{x_d} f(x) dx \stackrel{def}{=} f(x_d), \tag{5.12}$$

where $f(x)$ is an arbitrary scalar function. Note that in the general case operators G_α and $\hat{G}_\alpha$ are not necessary equal and that modification (5.11) ensures the convergence in the spirit of the patch test (see e.g. [Ibrahimbegovic and Wilson, 1991]).

The weak form of the equilibrium equations or the principle of virtual work for an element e, can be written as:

$$\delta\Pi^{int,(e)} - \delta\Pi^{ext,(e)} = 0. \tag{5.13}$$

By using (5.10) for the definition of the virtual strain, we can write the virtual work of

internal forces as:

$$\begin{aligned}\delta\Pi^{int,(e)} &= A^{(e)}\int_{\Omega^e}\hat{\epsilon}\sigma dx \\ &= \underbrace{\sum_{a=1}^{2}A^{(e)}\int_{\Omega^e}\hat{d}_a B_a\sigma dx}_{\text{standard FEM}} + \underbrace{A^{(e)}\int_{\Omega^e}\hat{\alpha}\hat{G}_\alpha\sigma dx}_{\text{additional}},\end{aligned} \tag{5.14}$$

where $A^{(e)}$ is the element's cross-section area and σ is the stress. From the term "standard FEM" in (5.14) we obtain the vector of internal nodal forces

$$\boldsymbol{f}^{int,(e)} = \left[f_1^{int,(e)}, f_2^{int,(e)}\right]^T, \quad f_a^{int,(e)} = A^{(e)}\int_{\Omega^e}B_a\sigma dx, \tag{5.15}$$

which is completely the same as in the standard finite element method formulation. From the virtual work of external forces $\delta\Pi^{ext,(e)}$ we can get the vector of element external nodal forces $\boldsymbol{f}^{ext,(e)}$, representing the external load applied to the element's nodes. The finite element assembly of vectors $\boldsymbol{f}^{int,(e)}$ and $\boldsymbol{f}^{ext,(e)}$, for all elements of the chosen mesh with N_{el} finite elements, leads to a set of global (i.e. mesh related) equations

$$A_{e=1}^{N_{el}}\left(\boldsymbol{f}^{int,(e)} - \boldsymbol{f}^{ext,(e)}\right) = \mathbf{0}, \tag{5.16}$$

where A is the assembly operator. Note that we have only used one part of the right side of equation (5.14) in (5.13) to get the set of global equations (5.16).

The other term in (5.14), denoted as "additional" (since it results from additional enriched kinematics due to embedded discontinuity), will also contribute to the weak form of the equilibrium. However, we will treat this contribution locally element by element. Then, in view of (5.13), the following equation is obtained for each element of the chosen mesh

$$\begin{aligned}h^{(e)} &= A^{(e)}\int_{\Omega^e}\hat{G}_\alpha\sigma dx = A^{(e)}\left(\int_{\Omega^e}\overline{G}_\alpha\sigma dx + \int_{\Omega^e}\overline{\overline{G}}_\alpha\sigma dx\right) \\ &= A^{(e)}\left(\int_{\Omega^e}\overline{G}_\alpha\sigma dx + \int_{\Omega^e}\delta_{x_d}\sigma dx\right) \\ &= A^{(e)}\left(\int_{\Omega^e}\overline{G}_\alpha\sigma dx + \sigma|_{x_d}\right) = 0.\end{aligned} \tag{5.17}$$

By defining the traction at the discontinuity as

$$t \overset{def}{=} \sigma|_{x_d}, \tag{5.18}$$

we write Eqn. (5.17) in its final form

$$h^{(e)} = A^{(e)}\left(\int_{\Omega^e}\overline{G}_\alpha\sigma dx + t\right) = 0. \tag{5.19}$$

One can interpret the above equation as weak form of the equilibrium equation between the stress in the bulk and the stress defined at discontinuity.

Constitutive relations

We chose to model the bulk material $\Omega^e \setminus x_d$ of the bar as linear elastic. The regular part of plastic strain is then equal to zero and the regular elastic strain is equal to the regular part of total strain

$$\overline{\epsilon}^p = 0, \quad \overline{\epsilon}^e = \overline{\epsilon}. \tag{5.20}$$

We assume that the free energy of the bulk material is equal to the strain energy function

$$\overline{\Psi}(\overline{\epsilon}^e) = \overline{W}\left(\overline{\epsilon}^e\right) = \frac{1}{2} E \overline{\epsilon}^{e2} \tag{5.21}$$

and express the stress as

$$\sigma = \frac{\partial \overline{\Psi}}{\partial \overline{\epsilon}^e} = E \overline{\epsilon}^e, \tag{5.22}$$

where E is the Young's modulus of the bar material. The response of the discontinuity x_d is considered to be rigid-plastic with linear softening. The basic ingredients of the chosen constitutive relation are built on classical plasticity (e.g. [Ibrahimbegovic et al., 1998]) and can be summarized as:

- The tensile traction t at the discontinuity x_d is related to jump in displacements α (see Figure 5.5)

$$t = t(\alpha). \tag{5.23}$$

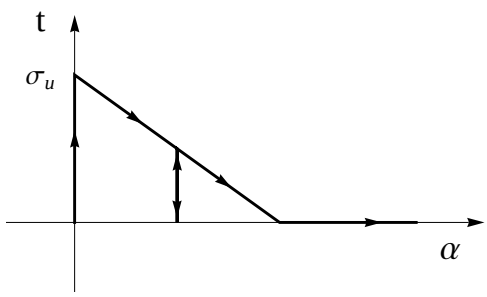

Figure 5.5: Cohesive law at the discontinuity

Slika 5.5: Kohezijski zakon na nezveznosti

- Cohesive law (5.23) can be rewritten in terms of localization criterion

$$\overline{\overline{\phi}}(t, \overline{\overline{q}}) = t - (\sigma_u - \overline{\overline{q}}) \leq 0, \tag{5.24}$$

where σ_u is the ultimate tensile strength, $\bar{\bar{q}}(\bar{\bar{\xi}})$ is the traction-like variable related to strain-like softening variable $\bar{\bar{\xi}}$. Note that localization criterion 5.24 does not allow the appearance of the discontinuity in compression.

- The softening potential is assumed to be

$$\bar{\bar{\Xi}}(\bar{\bar{\xi}}) = \frac{1}{2} K_s \bar{\bar{\xi}}^2, \tag{5.25}$$

where K_s is the linear softening modulus.

The remaining ingredients of the rigid-plastic response, describing softening at the discontinuity x_d, can be obtained from the consideration of thermodynamics of associative plasticity and the principle of maximum plastic dissipation (see e.g. [Ibrahimbegovic, 2009], [Lubliner, 1990], [Simo and Hughes, 1998]). We first define the strain energy function due to softening potential as $\bar{\bar{\Psi}} = \bar{\bar{\Xi}}$. The dissipation can be then written as:

$$0 \leq \bar{\bar{D}} \stackrel{def.}{=} t\dot{\alpha} - \dot{\bar{\bar{\Psi}}}(\bar{\bar{\xi}}) = t\dot{\alpha} - \frac{\partial \bar{\bar{\Psi}}}{\partial \bar{\bar{\xi}}} \dot{\bar{\bar{\xi}}}. \tag{5.26}$$

By defining

$$\bar{\bar{q}} = -\frac{\partial \bar{\bar{\Psi}}}{\partial \bar{\bar{\xi}}} = -\frac{\partial \bar{\bar{\Xi}}}{\partial \bar{\bar{\xi}}} = -K_s \bar{\bar{\xi}}, \tag{5.27}$$

the result in (5.26) can be rewritten as

$$\bar{\bar{D}} = \bar{\bar{D}}^p = t\dot{\alpha} + \bar{\bar{q}} \dot{\bar{\bar{\xi}}}, \tag{5.28}$$

where $\bar{\bar{D}}^p$ denotes the plastic dissipation. The principle of maximum plastic dissipation states that among all the variables $(t, \bar{\bar{q}})$ that satisfy the localization criteria $\bar{\bar{\phi}}\left(t, \bar{\bar{q}}\right) \leq 0$, one should choose those that maximize plastic dissipation. This can be written as a constrained optimization problem:

$$\min_{t, \bar{\bar{q}}} \max_{\dot{\bar{\bar{\gamma}}}} \left[\bar{\bar{L}}^p(t, \bar{\bar{q}}, \dot{\bar{\bar{\gamma}}}) = -\bar{\bar{D}}^p(t, \bar{\bar{q}}) + \dot{\bar{\bar{\gamma}}} \bar{\bar{\phi}}(t, \bar{\bar{q}}) \right], \tag{5.29}$$

where $\dot{\bar{\bar{\gamma}}} \geq 0$ is the Lagrange multiplier. By using (5.28) and (5.24), we get from (5.29) above the following evolution equations:

$$\frac{\partial \bar{\bar{L}}^p}{\partial t} = -\dot{\alpha} + \dot{\bar{\bar{\gamma}}} \frac{\partial \bar{\bar{\phi}}}{\partial t} = 0 \Longrightarrow \dot{\alpha} = \dot{\bar{\bar{\gamma}}}, \tag{5.30}$$

$$\frac{\partial \bar{\bar{L}}^p}{\partial \bar{\bar{q}}} = -\dot{\bar{\bar{\xi}}} + \dot{\bar{\bar{\gamma}}} \frac{\partial \bar{\bar{\phi}}}{\partial \bar{\bar{q}}} = 0 \Longrightarrow \dot{\bar{\bar{\xi}}} = \dot{\bar{\bar{\gamma}}}, \tag{5.31}$$

along with the Kuhn-Tucker loading/unloading conditions and the consistency condition

$$\dot{\bar{\bar{\gamma}}} \geq 0, \quad \bar{\bar{\phi}} \leq 0, \quad \dot{\bar{\bar{\gamma}}} \bar{\bar{\phi}} = 0, \quad \dot{\bar{\bar{\gamma}}} \dot{\bar{\bar{\phi}}} = 0. \tag{5.32}$$

5.3 Computational procedure for failure analysis

In this section we present a procedure for solving the set of global (mesh related) equations and the set of local (element related) equations generated by using the finite element with embedded discontinuity presented in Section 5.2.

The solution ought to be computed at discrete pseudo-time values $0, \tau_1, \tau_2, \ldots, \tau_{n-1}, \tau_n, \tau_{n+1}, \ldots, T$ by means of the incremental-iterative scheme. We will consider the solution in a typical pseudo-time incremental step from τ_n to τ_{n+1}. We assume that all the variables related to an element e are given at τ_n, i.e.

$$\text{given: } \boldsymbol{d}_n^{(e)} = [d_1, d_2]_n^{(e)^T}, \ \alpha_n^{(e)}, \ \bar{\bar{\xi}}_n^{(e)}. \tag{5.33}$$

We will then iterate in the pseudo-time step in order to compute the converged values of the variables at τ_{n+1}, i.e.

$$\text{find: } \boldsymbol{d}_{n+1}^{(e)} = [d_1, d_2]_{n+1}^{(e)^T}, \ \alpha_{n+1}^{(e)}, \ \bar{\bar{\xi}}_{n+1}^{(e)}. \tag{5.34}$$

The computation of solution (5.34) is split into two phases:

(a) In the global (mesh related) phase we compute the current iterative values of nodal displacements at τ_{n+1}, while keeping the other variables fixed

$$\text{global phase: } \boldsymbol{d}_{n+1}^{(e),(i)} = \boldsymbol{d}_{n+1}^{(e),(i-1)} + \Delta \boldsymbol{d}_{n+1}^{(e),(i-1)}, \tag{5.35}$$

where (i) is the iteration counter. The computation of iterative update $\Delta \boldsymbol{d}_{n+1}^{(e),(i-1)}$ will be explained further below.

(b) In the local (element) phase we compute the values of the variables $\alpha_{n+1}^{(e)}$, $\bar{\bar{\xi}}_{n+1}^{(e)}$ while keeping $\boldsymbol{d}_{n+1}^{(e),(i)}$ fixed.

In the rest of this section we will first describe in detail the phase (b). This will be followed by the description of the phase (a).

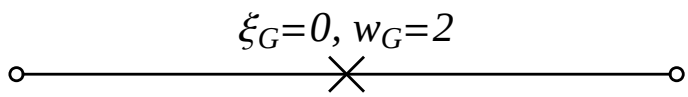

Figure 5.6: One point numerical integration scheme

Slika 5.6: Enotočkovna numerična integracijska shema

We first provide the trial value of stress in the integration point of the element (we use a 1 point Gauss integration scheme, see Figure 5.6)

$$\sigma_{n+1}^{G,trial} = \sigma(\overline{\epsilon}(\boldsymbol{d}_{n+1}^{(e)}, \alpha_n^{(e)}, \xi_G)), \tag{5.36}$$

where $\xi_G = 0$ is the coordinate of the integration point. Since we use the rigid plasticity law at the discontinuity, we are unable to determine the trial value of traction at the discontinuity by using the constitutive law. Instead we use the local equilibrium equation (5.19), i.e.

$$\begin{aligned} t_{n+1}^{trial} &= -\int_{\Omega^e} \overline{G}_\alpha \sigma_{n+1}^{trial} dx = \frac{1}{L^e}\int_{x_1}^{x_2} \sigma_{n+1}^{trial} dx \\ &\overset{num.integ.}{=} \frac{1}{L^e}\frac{1}{2}\underbrace{(x_2 - x_1)}_{=L^e}\underbrace{w_G}_{=2}\sigma_{n+1}^{G,trial} = \sigma_{n+1}^{G,trial}, \end{aligned} \tag{5.37}$$

where w_G is the Gauss quadrature point weight. Note that in the 1D setting, when using only one integration point, the traction at the discontinuity is equal to the stress in the integration point. Next we provide the trial value of the failure function at the discontinuity

$$\overline{\overline{\phi}}^{trial} = t_{n+1}^{trial} - (\sigma_u - \overline{\overline{q}}_{n+1}^{trial}) \overset{?}{\leq} 0, \tag{5.38}$$

where

$$\overline{\overline{q}}_{n+1}^{trial} = \min[-K_s \overline{\overline{\xi}}_n^{(e)}, \sigma_u]. \tag{5.39}$$

When computing the traction like softening variable in (5.39) we have to consider that the traction can never be less than zero therefore we set the upper value of this variable to the ultimate tensial strength of the material. If the trial failure criterion (5.38) is satisfied, the values of softening plasticity local variables remain unchanged

$$\overline{\overline{\phi}}^{trial} \leq 0 \implies \alpha_{n+1}^{(e)} = \alpha_n^{(e)}, \quad \overline{\overline{\xi}}_{n+1}^{(e)} = \overline{\overline{\xi}}_n^{(e)}. \tag{5.40}$$

In the case of violation of the criterion (5.38) the values of softening plasticity variables are updated by using the evolution equations (5.30) and (5.31) and the backward Euler integration scheme

$$\alpha_{n+1}^{(e)} = \alpha_n^{(e)} + \overline{\overline{\gamma}}_{n+1}, \quad \overline{\overline{\xi}}_{n+1}^{(e)} = \overline{\overline{\xi}}_n^{(e)} + \overline{\overline{\gamma}}_{n+1}^{(e)}, \tag{5.41}$$

where $\overline{\overline{\gamma}}_{n+1} = \dot{\overline{\overline{\gamma}}}_{n+1}(\tau_{n+1} - \tau_n)$ is the plastic multiplier. The value of the plastic multiplier $\overline{\overline{\gamma}}_{n+1}$ is determined from

$$\overline{\overline{\phi}} = t_{n+1}\left(\overline{\overline{\gamma}}_{n+1}\right) - \left(\sigma_u - \overline{\overline{q}}_{n+1}\left(\overline{\overline{\gamma}}_{n+1}\right)\right) = \overline{\overline{\phi}}\left(\overline{\overline{\gamma}}_{n+1}\right) = 0, \tag{5.42}$$

where we considered that the traction and the traction like softening variable are computed as

$$t_{n+1} = \sigma^G_{n+1} = E\left(\sum_{a=1}^{2} B_a d_{a,n+1} + \overline{G}_\alpha \alpha^{(e)}_{n+1}\left(\overline{\overline{\gamma}}_{n+1}\right)\right), \tag{5.43}$$

$$\overline{\overline{q}}_{n+1} = \min[-K_s \overline{\overline{\xi}}^{(e)}_{n+1}, \sigma_u]. \tag{5.44}$$

For the linear softening case one can determine by considering (5.36) to (5.39) and (5.41) to (5.44) the value of plastic multiplier explicitly as (see e.g. [Ibrahimbegovic, 2009] Section 8.3.4 for more details)

$$\overline{\overline{\gamma}}_{n+1} = -\frac{\overline{\overline{\phi}}^{trial}}{E\overline{G}_\alpha - \hat{K}_s}, \quad \hat{K}_s = \begin{cases} K_s & \text{for } \overline{\overline{q}}^{trial}_{n+1} < \sigma_u \\ 0 & \text{for } \overline{\overline{q}}^{trial}_{n+1} = \sigma_u \end{cases}, \tag{5.45}$$

whereas for a nonlinear softening case an iteration procedure has to be used.

Once the local variables are computed, we turn to the global phase (a) of the iterative loop in order to provide, if so needed, new iterative values of nodal displacements. First, the set of global equilibrium equations (5.16) is checked with newly computed σ^G_{n+1} from the local phase

$$\left\| A_{e=1}^{N_{el}} [\boldsymbol{f}^{int,(e)}_{n+1} - \boldsymbol{f}^{ext,(e),(i)}_{n+1}] \right\| \overset{?}{<} tol., \tag{5.46}$$

where we compute the internal nodal forces as

$$f^{int,(e)}_{a,n+1} = A^{(e)} \frac{L^e}{2} w_G B_a \sigma^G_{n+1}. \tag{5.47}$$

If the convergence criterion (5.46) is satisfied, we move on to the next pseudo-time incremental step. If the convergence criterion fails, we perform a new iterative sweep within the present pseudo-time incremental step. New iterative values of nodal generalized displacements of the finite element mesh are computed by accounting for each element contribution. A single element contribution can be written as

$$\begin{bmatrix} \boldsymbol{K}^{(e)} & \boldsymbol{K}^{f\alpha} \\ \boldsymbol{K}^{hd} & K^{h\alpha} \end{bmatrix}^{(i)}_{n+1} \begin{pmatrix} \Delta \boldsymbol{d}^{(e),(i)}_{n+1} \\ \Delta \alpha^{(e),(i)}_{n+1} \end{pmatrix} = \begin{pmatrix} \boldsymbol{f}^{ext,(e)}_{n+1} - \boldsymbol{f}^{int,(e),(i)}_{n+1} \\ 0 \ (= h^{(e),(i)}_{n+1}) \end{pmatrix}, \tag{5.48}$$

where the parts of the element stiffness matrix can be written as

$$\boldsymbol{K}_{n+1}^{(e),(i)} = \left(\frac{\partial \boldsymbol{f}^{int,(e)}}{\partial \boldsymbol{d}^{(e)}}\right)_{n+1}^{(i)} = \begin{bmatrix} K_{11} & K_{12} \\ K_{21} & K_{22} \end{bmatrix}_{n+1}^{(e),(i)}, \tag{5.49}$$

$$K_{ab} = A^{(e)}\frac{L^e}{2} w_G B_a E B_b, \quad a,b = 1,2, \tag{5.50}$$

$$\boldsymbol{K}_{n+1}^{f\alpha,(i)} = \left(\frac{\partial \boldsymbol{f}^{int,(e)}}{\partial \alpha^{(e)}}\right)_{n+1}^{(i)} = \begin{bmatrix} K_1^{f\alpha} \\ K_2^{f\alpha} \end{bmatrix}_{n+1}^{(i)}, \tag{5.51}$$

$$K_a^{f\alpha} = A^{(e)}\frac{L^e}{2} w_G B_a E \overline{G}_\alpha, \tag{5.52}$$

$$\boldsymbol{K}_{n+1}^{hd,(i)} = \left(\frac{\partial h^{(e)}}{\partial \boldsymbol{d}^{(e)}}\right)_{n+1}^{(i)} = \left[K_1^{hd}, K_2^{hd}\right]_{n+1}^{(i)}, \tag{5.53}$$

$$K_b^{hd} = A^{(e)}\frac{L^e}{2} w_G \overline{G}_\alpha E B_b, \tag{5.54}$$

$$K_{n+1}^{h\alpha,(i)} = \left(\frac{\partial h^{(e)}}{\partial \alpha^{(e)}}\right)_{n+1}^{(i)} = A^{(e)}\left(\frac{L^e}{2} w_G \overline{G}_\alpha E \overline{G}_\alpha + \hat{K}_s\right) \tag{5.55}$$

Note that by using equation (5.43) to compute the traction at the discontinuity we explicitly satisfy the local equilibrium equation $h_{n+1}^{(e),(i)} = 0$. In order to obtain all the components of the matrix in (5.48) we assumed the following term for the local equilibrium equation

$$h_{n+1}^{(e),(i)} = A^{(e)}\left(\frac{L^e}{2} w_G \overline{G}_\alpha \sigma_{n+1}^G(\boldsymbol{d}_{n+1}^{(e)}, \alpha_{n+1}^{(e)}) + t_{n+1}(\alpha_{n+1}^{(e)})\right), \tag{5.56}$$

$$t_{n+1}(\alpha_{n+1}^{(e)}) \overset{(5.42)}{=} \sigma_u - \overline{\overline{q}}_{n+1}(\underbrace{\overline{\overline{\xi}}_{n+1}^{(e)}}_{\overset{(5.41)}{=}\alpha_{n+1}^{(e)}}) \overset{(5.44)}{=} \sigma_u - \min[-K_s\alpha_{n+1}^{(e)}, \sigma_u]. \tag{5.57}$$

The static condensation of (5.48) allows us to form the standard form of the element stiffness matrix $\widehat{\boldsymbol{K}}_{n+1}^{(e),(i)}$ that contributes to the assembly

$$A_{e=1}^{N_{el}}\left(\widehat{\boldsymbol{K}}_{n+1}^{(e),(i)}\Delta \boldsymbol{d}_{n+1}^{(i)}\right) = A_{e=1}^{N_{el}}\left(\boldsymbol{f}_{n+1}^{ext,(e)} - \boldsymbol{f}_{n+1}^{int,(e),(i)}\right), \tag{5.58}$$

where

$$\widehat{\boldsymbol{K}}_{n+1}^{(e),(i)} = \boldsymbol{K}_{n+1}^{(e),(i)} - \boldsymbol{K}_{n+1}^{f\alpha,(i)}\left(K_{n+1}^{h\alpha,(i)}\right)^{-1}\boldsymbol{K}_{n+1}^{hd,(i)}. \tag{5.59}$$

Solution of (5.58) gives the values of iterative update $\Delta \boldsymbol{d}_{n+1}^{(e),(i)}$, which leads us back to (5.35).

5.4 Numerical examples

In this section we illustrate the performance of the above derived finite element. The code was generated by using symbolic manipulation code AceGen and the examples were computed by using finite element program AceFem, see [Korelc, 2007b] and [Korelc, 2007a].

5.4.1 Tension test of a bar

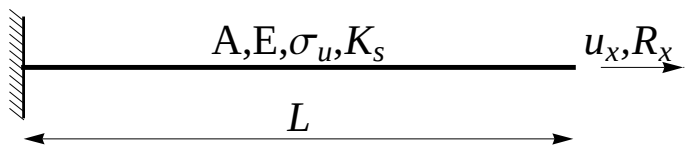

Figure 5.7: Tension test of one bar

Slika 5.7: Natezni preizkus ene palice

In the first example we consider a built-in bar subjected to tension, see Figure 5.7. The bar is made of material with Young's modulus $E = 1$, the ultimate tensile strength $\sigma_u = 0.3$ and the softening modulus $K_s = -0.2$. The length of the bar is $L = 1$ and we consider a unit cross-section area of the bar $A = 1$. We model the bar with one finite element, which is supported at the left side and pulled, by imposing the displacement, at the right side. In Figure 5.8 we present the reaction force versus imposed displacement

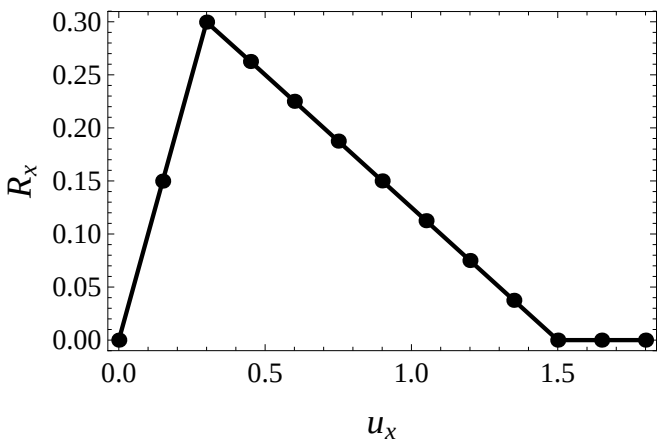

Figure 5.8: Reaction force versus imposed displacement curve

Slika 5.8: Krivulja reakcija - vsiljen pomik

diagrams where the dots denote the converged deformed configurations for the twelve load steps. The first and the second load step are elastic, in steps three through ten the element softens and in the last two steps the element failed completely thus giving zero resistance, see Figure 5.8. In Table 5.1 we present the convergence results where $||\Delta\boldsymbol{d}|| = \sqrt{\frac{\Delta\boldsymbol{d}\cdot\Delta\boldsymbol{d}}{\text{Num.Equations}}}$ is the modified Euclid's norm of the increment of the nodal displacements and $||\boldsymbol{f}|| = \sqrt{\frac{\boldsymbol{f}\cdot\boldsymbol{f}}{\text{Num.Equations}}}$ is the modified Euklid's norm of the residual vector, as given

Step	Iter.	$\|\|\Delta \boldsymbol{d}\|\|$	$\|\|\boldsymbol{f}\|\|$	Step	Iter.	$\|\|\Delta \boldsymbol{d}\|\|$	$\|\|\boldsymbol{f}\|\|$
1	1	$1.5 \cdot 10^{-1}$	$1.5 \cdot 10^{2}$	7	2	$1.9 \cdot 10^{-4}$	$1.9 \cdot 10^{-1}$
	2	$1.1 \cdot 10^{-17}$	$1.1 \cdot 10^{-14}$		3	$5.5 \cdot 10^{-17}$	$5.5 \cdot 10^{-14}$
2	1	$1.5 \cdot 10^{-1}$	$1.5 \cdot 10^{2}$	8	1	$1.5 \cdot 10^{-1}$	$1.5 \cdot 10^{2}$
	2	$2.1 \cdot 10^{-17}$	$2.1 \cdot 10^{-14}$		2	$1.9 \cdot 10^{-4}$	$1.9 \cdot 10^{-1}$
3	1	$1.5 \cdot 10^{-1}$	$1.5 \cdot 10^{2}$		3	$1.6 \cdot 10^{-16}$	$1.5 \cdot 10^{-13}$
	2	$1.9 \cdot 10^{-4}$	$1.9 \cdot 10^{-1}$	9	1	$1.5 \cdot 10^{-1}$	$1.5 \cdot 10^{2}$
	3	$8. \cdot 10^{-17}$	$8. \cdot 10^{-14}$		2	$1.9 \cdot 10^{-4}$	$1.9 \cdot 10^{-1}$
4	1	$1.5 \cdot 10^{-1}$	$1.5 \cdot 10^{2}$		3	$7.7 \cdot 10^{-17}$	$7.7 \cdot 10^{-14}$
	2	$1.9 \cdot 10^{-4}$	$1.9 \cdot 10^{-1}$	10	1	$1.5 \cdot 10^{-1}$	$1.5 \cdot 10^{2}$
	3	$2.1 \cdot 10^{-17}$	$2.1 \cdot 10^{-14}$		2	$1.9 \cdot 10^{-4}$	$1.9 \cdot 10^{-1}$
5	1	$1.5 \cdot 10^{-1}$	$1.5 \cdot 10^{2}$		3	0.	0.
	2	$1.9 \cdot 10^{-4}$	$1.9 \cdot 10^{-1}$	11	1	$1.5 \cdot 10^{-1}$	$1.5 \cdot 10^{2}$
	3	$3.2 \cdot 10^{-17}$	$3.2 \cdot 10^{-14}$		2	$1.5 \cdot 10^{-4}$	$1.5 \cdot 10^{-1}$
6	1	$1.5 \cdot 10^{-1}$	$1.5 \cdot 10^{2}$		3	0.	0.
	2	$1.9 \cdot 10^{-4}$	$1.9 \cdot 10^{-1}$	12	1	$1.5 \cdot 10^{-1}$	$1.5 \cdot 10^{2}$
	3	$4.6 \cdot 10^{-17}$	$4.6 \cdot 10^{-14}$		2	$1.5 \cdot 10^{-4}$	$1.5 \cdot 10^{-1}$
7	1	$1.5 \cdot 10^{-1}$	$1.5 \cdot 10^{2}$		3	0.	0.

Table 5.1: The convegrence results

Tabela 5.1: Rezultati konvergence

by the AceFem program [Korelc, 2007a]. Note that at most three iterations were needed in order to obtain the converged state.

5.4.2 Tension test of four parallel bars

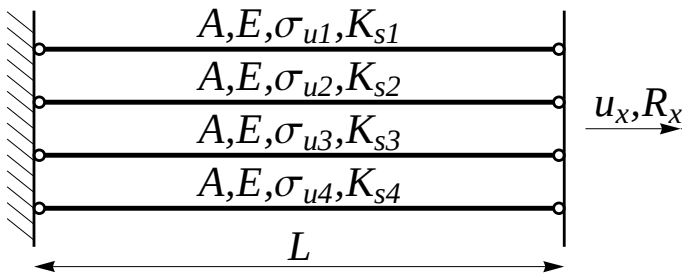

Figure 5.9: Tension test of four parallel bars

Slika 5.9: Natezni preizkus štirih vzporednih palic

In the second example we consider a simple structure composed of four parallel bars, see Figure 5.9. We consider that all the bars have the same Young's modulus $E = 1$ and the same cross-section area $A = 1$ but different material parameters that define the

softening response, i.e. $\sigma_{u1} = 0.6$, $K_{s1} = -0.21$, $\sigma_{u2} = 0.8$, $K_{s2} = -0.21$, $\sigma_{u3} = 1$, $K_{s3} = -0.22$, $\sigma_{u4} = 1.15$ and $K_{s4} = -0.20$. The length of the bars is $L = 1$. Each bar is moddeled with one finite element, which is supported at the left side and pulled at the right side, by imposing the displacement. Note that we considered that both of the nodes are common to all the elements, i.e. the actual vertical distance between the elements is zero. In the left hand side of Figure 5.10 we present the reaction versus

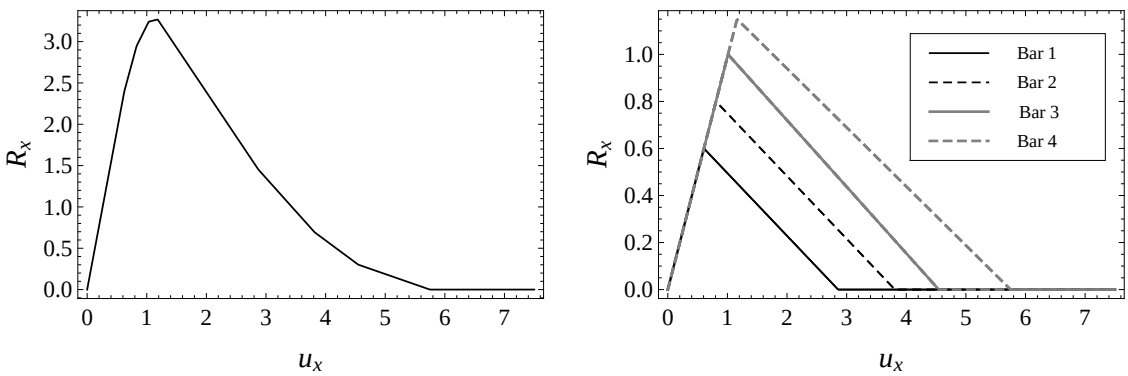

Figure 5.10: Reaction versus imposed displacement of structure (left) and structural components (right)

Slika 5.10: Krivulje reakcija - vsiljen pomik za celotno konstrukcijo (levo) in za njene posamezne dele (desno)

imposed displacement curve for the structure and in the right hand side of the same figure we plot the reaction versus imposed displacement curves for each bar separately. Even though some of the components are in the softening regime the structure still exhibits the hardening like response. The ultimate load of the structure is reached at the moment when the last bar, i.e. Bar 4, reaches its maximum resistance and afterwards the resistance of the structure reduces with the increase of the displacement.

5.5 Concluding remarks and chapter summary

In this chapter we have presented the embedded discontinuity concept on a 1D solid finite element. With the introduction of one additional parameter into the standard isoparametric 1d solid finite element we obtained the enriched displacement field

$$u^h(\xi) = \underbrace{\sum_{a=1}^{2} N_a(\xi) d_a}_{u^h_{\mathrm{FEM}}} + \underbrace{M_\alpha(\xi)\alpha}_{\text{enrichment}},$$

and the space derivative of this field gives us the enriched strain field

$$\epsilon = \frac{du^h}{dx} = \underbrace{\sum_{a=1}^{2} B_a(\xi) d_a}_{\epsilon_d} + \underbrace{G_\alpha(\xi)\alpha}_{\epsilon_\alpha}.$$

We considered that the virtual strains are interpolated according to

$$\hat{\epsilon} = \sum_{a=1}^{2} B_a(\xi)\hat{d}_a + \hat{G}_\alpha \hat{\alpha},$$

where the following modification ensures the convergence in the spirit of the patch test

$$\hat{G}_\alpha = G_\alpha - \frac{1}{L^e}\int_{\Omega^e} G_\alpha dx.$$

We introduced the virtual strains into the principle of virtual work and obtained the virtual work of internal forces as

$$\delta\Pi^{int,(e)} = \underbrace{\sum_{a=1}^{2} A^{(e)} \int_{\Omega^e} \hat{d}_a B_a \sigma dx}_{\text{standard FEM}} + \underbrace{A^{(e)} \int_{\Omega^e} \hat{\alpha}\hat{\boldsymbol{G}}_\alpha \sigma dx}_{\text{additional}}.$$

From the term "additional" we obtained one additional equation per finite element

$$h^{(e)} = A^{(e)}\left(\int_{\Omega^e} \overline{G}_\alpha \sigma dx + t\right),$$

which ensures that the traction at the discontinuity is in equilibrium with the stress field in the element. We built the rigid plastic cohesive law (see Figure 5.5) by considering the localization criterion

$$\overline{\overline{\phi}}(t, \overline{\overline{q}}) = t - (\sigma_u - \overline{\overline{q}}) \leq 0,$$

and the softening potential

$$\overline{\overline{\Xi}}(\overline{\overline{\xi}}) = \frac{1}{2} K_s \overline{\overline{\xi}}^2.$$

The remaining ingredients of the rigid-plastic response were obtained by defining the plastic dissipation

$$\overline{\overline{D}}^p = t\dot{\alpha} + \overline{\overline{q}}\dot{\overline{\overline{\xi}}},$$

and by considering the principle of maximum plastic dissipation

$$\min_{t,\overline{\overline{q}}} \max_{\dot{\overline{\overline{\gamma}}}} \left[\overline{\overline{L}}^p(t, \overline{\overline{q}}, \dot{\overline{\overline{\gamma}}}) = -\overline{\overline{D}}^p(t, \overline{\overline{q}}) + \dot{\overline{\overline{\gamma}}}\overline{\overline{\phi}}(t, \overline{\overline{q}})\right].$$

The computational procedure presented in Section 5.3 is split into the local and global phase. In the local phase we determine the updates for the variables related to rigid plasticity by solving the following equation

$$\overline{\overline{\phi}} = t_{n+1}\left(\overline{\overline{\gamma}}_{n+1}\right) - \left(\sigma_u - \overline{\overline{q}}_{n+1}\left(\overline{\overline{\gamma}}_{n+1}\right)\right) = \overline{\overline{\phi}}\left(\overline{\overline{\gamma}}_{n+1}\right) = 0,$$

where we explicitly use the additional equilibrium equation to compute the traction at the discontinuity

$$t_{n+1} = -\int_{\Omega^e} \overline{G}_\alpha \sigma_{n+1} dx = \sigma^G_{n+1}.$$

In the global phase, where the single element contribution to the system of global equations is

$$\begin{bmatrix} \boldsymbol{K}^{(e)} & \boldsymbol{K}^{f\alpha} \\ \boldsymbol{K}^{hd} & K^{h\alpha} \end{bmatrix}^{(i)}_{n+1} \begin{pmatrix} \Delta \boldsymbol{d}^{(e),(i)}_{n+1} \\ \Delta \alpha^{(e),(i)}_{n+1} \end{pmatrix} = \begin{pmatrix} \boldsymbol{f}^{ext,(e)}_{n+1} - \boldsymbol{f}^{int,(e),(i)}_{n+1} \\ 0 \ (= h^{(e),(i)}_{n+1}) \end{pmatrix},$$

we determine the updates for the current iterative values of nodal displacements

$$\boldsymbol{d}^{(e),(i)}_{n+1} = \boldsymbol{d}^{(e),(i-1)}_{n+1} + \Delta \boldsymbol{d}^{(e),(i-1)}_{n+1}.$$

The static condensation allowed us to form the standard form of the element stiffness matrix

$$\widehat{\boldsymbol{K}}^{(e),(i)}_{n+1} = \boldsymbol{K}^{(e),(i)}_{n+1} - \boldsymbol{K}^{f\alpha,(i)}_{n+1} \left(K^{h\alpha,(i)}_{n+1}\right)^{-1} \boldsymbol{K}^{hd,(i)}_{n+1},$$

thus the global solution procedure is completely the same as in the standard finite element formulation. In the first numerical simulation in Section 5.4 we presented the convergence result for a test with one finite element, while in the second simulation we show the results for a structure composed of four parallel bars.

Chapter 6

Failure analysis of metal beams and frames

6.1 Introduction

A typical example of a failure (collapse) analysis is the the push-over analysis in earthquake engineering. This is a non-linear static analysis of a building structure, subjected to an equivalent static loading that is pushing a structure over its limit capacity (e.g. [Fajfar et al., 2006]).

It has been observed from failure modes, produced by seismic activities and experimental tests, that practical frame structures, composed of columns and beams, fail by exhibiting localized failures in a limited number of critical zones. Those critical zones are usually described as plastic (inelastic) hinges. A usual approach to compute the limit load of a structural frame, or to compute its complete failure, is to model plastic hinges with nonlinear inelastic spring finite elements. Inelastic springs are introduced at predefined critical locations in a mesh of conventional elastic beam finite elements (e.g. [Wilson, 2002]), or, alternatively (e.g. [Powell, 1986]), elastic beam elements with lumped nonlinear spring at both ends are used. In this chapter we present another option, i.e. a nonlinear analysis using the embedded discontinuity finite element method.

In the first part of this chapter, we carry on with the developments related to numerical treatment of localized failure in beams in order to study failure of elastoplastic metal frames. To this end, we derive a planar straight stress-resultant beam finite element with the following features: (i) Euler-Bernoulli kinematics, (ii) an elastoplastic stress-resultant constitutive model with isotropic hardening, (iii) a localized softening plastic hinge related to the strong discontinuity in generalized displacements, and (iv) an approximation of the geometrically nonlinear effects by using the von Karman strains for the virtual axial deformations.

The derived finite element can be effectively used for the limit load analysis, the push-

over analysis and the complete failure analysis of planar metal frames. Localized softening, introduced by embedded discontinuity approach, solves the problem of mesh-dependency. Moreover, the spreading of plasticity over the entire frame and the appearance of the softening plastic hinges in the frame is consistently accounted for in the course of the nonlinear analysis. With respect to the existing embedded discontinuity beam finite elements, see [Ehrlich and Armero, 2005], [Armero and Ehrlich, 2006b], [Armero and Ehrlich, 2004], and [Wackerfuss, 2008], we use more complex material models: stress-resultant elastoplasticity with hardening to describe beam material behavior and stress-resultant rigid-plastic softening to describe material behavior at the discontinuity.

The second part of this chapter pertains to a procedure that provides characteristic values of material parameters, used by chosen inelastic models. Those values are the yield and the failure (ultimate resistance) moments of the beam cross-section, the hardening modulus for the stress-resultant beam plasticity, and the softening modulus for the softening plastic hinge. Ideally, one should for any geometry of beam cross-section, any material type and any type of beam stress state seek the appropriate experimental results and fit to them the beam model material parameters with respect to significant quantities (e.g. forces, displacements, energy, dissipation), see e.g. [Kučerova et al., 2009]. In the absence of experimental results for metal beams to make any definitive conclusions, we turn to another approach that belongs under multi-scale label.

The material parameters are obtained by numerical simulations on representative part of a beam by using a refined model, which is superior to the beam model in a sense that it is able to describe in more detail the beam response. We focus on rather typical metal frames with thin-walled cross-sections. For this kind of frames, the refined model can be chosen as the nonlinear shell model (e.g. [Brank et al., 1997], [Brank, 2005]). The shell model is superior to the beam model in providing a proper local description of the strain/stress fields and the overall spread of plasticity. It is also capable of describing local buckling of the flanges and the web, which is, in bending dominated conditions, very often the reason for the localized beam failure. Considering the above, the shell model can be seen as the meso-scale model and the beam model as the macro-scale model.

The outline of the chapter is as follows. In Section 6.2, we derive an elastoplastic Euler-Bernoulli beam finite element with embedded discontinuity. In Section 6.3, we discuss computation of the beam plasticity parameters and the softening plastic hinge parameters by using the shell model. In Section 6.4, we present details of the computational procedure. Numerical examples are presented in Section 6.5 and concluding remarks in Section 6.6.

6.2 Beam element with embedded discontinuity

We consider in this section a planar Euler-Bernoulli beam finite element. The element can represent an elastoplastic bending, including the localized softening effects, which are associated with the strong discontinuity in rotation. The geometrical nonlinearity is approximately taken into account by virtual axial strains of von Karman type, which allows this element to capture the global buckling modes.

6.2.1 Kinematics

We consider a straight planar frame member, which middle axis occupies domain $\Omega \in \mathbb{R}$. Spatial discretization of Ω leads to N_{el} ($\Omega = [0, L] = \cup_{e=1}^{N_{el}} L^{(e)}$) finite elements. A typical

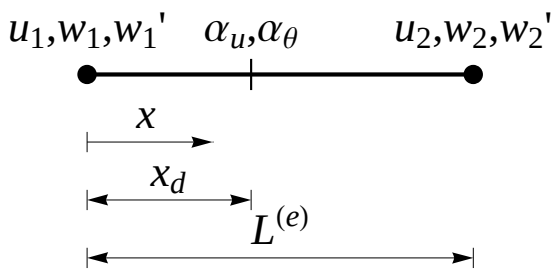

Figure 6.1: Beam finite element with embedded discontinuity

Slika 6.1: Končni element za nosilce z vgrajeno nezveznostjo

2-node finite element is presented in Figure 6.1. The following notation is used: u_i are nodal axial displacements, w_i are nodal transverse displacements, w_i' are nodal values of the beam axis rotation (derivative of transverse displacement with respect to the beam axial coordinate $x \in [0, L^{(e)}]$), and $i = 1, 2$ is node number. In addition to the standard degrees of freedom at the two nodes, we assume strong discontinuity in axial displacement α_u and beam axis rotation α_θ at $x_d \in L^{(e)}$. We also assume that the domain of the discontinuity influence corresponds to a single element. The axial displacement is thus defined as:

$$u^h(x, x_d) = \boldsymbol{N}^u(x)\boldsymbol{u} + M^u(x, x_d)\alpha_u, \tag{6.1}$$

where $\boldsymbol{N}^u(x) = [1 - x/L^{(e)}, x/L^{(e)}]$, $\boldsymbol{u} = [u_1, u_2]^T$, and $M^u(x, x_d)$ is a function with zero values at the nodes and a unit jump at x_d, i.e. $M^u(0, x_d) = M^u(L^{(e)}, x_d) = 0$ and $M^u(x_d^+, x_d) = M^u(x_d^-, x_d) + 1$. Similarly, we can write the transverse displacement as

$$w^h(x, x_d) = \boldsymbol{N}^w(x)\boldsymbol{w} + \boldsymbol{N}^{w'}(x)\boldsymbol{w}' + M^\theta(x, x_d)\alpha_\theta, \tag{6.2}$$

where

$$\boldsymbol{N}^w(x) = [2(\frac{x}{L^{(e)}})^3 - 3(\frac{x}{L^{(e)}})^2 + 1, -2(\frac{x}{L^{(e)}})^3 + 3(\frac{x}{L^{(e)}})^2],\ \boldsymbol{w} = [w_1, w_2]^T, \tag{6.3}$$

$$\boldsymbol{N}^{w'}(x) = L^{(e)}[(\frac{x}{L^{(e)}})^3 - 2(\frac{x}{L^{(e)}})^2 + (\frac{x}{L^{(e)}}), (\frac{x}{L^{(e)}})^3 - (\frac{x}{L^{(e)}})^2],\ \boldsymbol{w}' = [w_1', w_2']^T, \tag{6.4}$$

and $M^\theta(x, x_d)$ is a function with zero values at the nodes and a unit jump of its first derivative at x_d, i.e. $M^\theta(0, x_d) = M^\theta(L^{(e)}, x_d) = 0$ and $M^{\theta'}(x_d^+, x_d) = M^{\theta'}(x_d^-, x_d) + 1$.

The beam axial strain can then be written as:

$$\varepsilon(x, x_d) = \frac{\partial u^h}{\partial x} = \underbrace{\boldsymbol{B}^u(x)\boldsymbol{u} + G^u(x, x_d)\alpha_u}_{\overline{\varepsilon}} + \underbrace{\delta_{x_d}\alpha_u}_{\overline{\overline{\varepsilon}}}, \tag{6.5}$$

where $\boldsymbol{B}^u(x) = [-1/L^{(e)}, 1/L^{(e)}]$, $G^u(x, x_d) = \partial M^u/\partial x$, and δ_{x_d} is the Dirac-delta, which appears due to discontinuous nature of axial displacement at x_d. We further divide the axial strain into a regular part $\overline{\varepsilon}$ and a singular part $\overline{\overline{\varepsilon}}$. The later can be interpreted as a localized plastic axial strain. The beam curvature is computed as:

$$\kappa(x, x_d) = \frac{\partial^2 w^h}{\partial x^2} = \underbrace{\boldsymbol{B}^w(x)\boldsymbol{w} + \boldsymbol{B}^{w'}(x)\boldsymbol{w}' + G^\theta(x, x_d)\alpha_\theta}_{\overline{\kappa}} + \underbrace{\delta_{x_d}\alpha_\theta}_{\overline{\overline{\kappa}}}, \tag{6.6}$$

where

$$\boldsymbol{B}^w(x) = [-\frac{6}{L^{(e)^2}}(1 - \frac{2x}{L^{(e)}}), \frac{6}{L^{(e)^2}}(1 - \frac{2x}{L^{(e)}})], \tag{6.7}$$

$$\boldsymbol{B}^{w'}(x) = [-\frac{2}{L^{(e)}}(2 - \frac{3x}{L^{(e)}}), -\frac{2}{L^{(e)}}(1 - \frac{3x}{L^{(e)}})], \tag{6.8}$$

and $G^\theta(x, x_d) = \partial^2 M^\theta/\partial x^2$. The curvature κ is divided into a regular part $\overline{\kappa}$ and a singular part $\overline{\overline{\kappa}}$. The later can be interpreted as a localized plastic curvature. The beam strains can be rewritten in a matrix notation as

$$\boldsymbol{\epsilon} = \overline{\boldsymbol{\epsilon}} + \overline{\overline{\boldsymbol{\epsilon}}}, \tag{6.9}$$

$$\overline{\boldsymbol{\epsilon}} = \underbrace{\boldsymbol{B}\boldsymbol{d}}_{\overline{\overline{\boldsymbol{\epsilon}}}} + \boldsymbol{G}\boldsymbol{\alpha}, \quad \overline{\overline{\boldsymbol{\epsilon}}} = \delta_{x_d}\boldsymbol{\alpha}, \tag{6.10}$$

where $\boldsymbol{\epsilon} = [\varepsilon, \kappa]^T$, $\overline{\boldsymbol{\epsilon}} = [\overline{\varepsilon}, \overline{\kappa}]^T$, $\widetilde{\overline{\boldsymbol{\epsilon}}} = \left[\widetilde{\overline{\varepsilon}}, \widetilde{\overline{\kappa}}\right]^T$, $\overline{\overline{\boldsymbol{\epsilon}}} = \left[\overline{\overline{\varepsilon}}, \overline{\overline{\kappa}}\right]^T$ and

$$\boldsymbol{B} = \begin{bmatrix} \boldsymbol{B}^u & \boldsymbol{0} & \boldsymbol{0} \\ \boldsymbol{0} & \boldsymbol{B}^w & \boldsymbol{B}^{w'} \end{bmatrix}, \quad \boldsymbol{d} = [\boldsymbol{u}^T, \boldsymbol{w}^T, \boldsymbol{w}'^T]^T, \tag{6.11}$$

$$\boldsymbol{G} = DIAG\left[G^u, G^\theta\right], \quad \boldsymbol{\alpha} = [\alpha_u, \alpha_\theta]^T. \tag{6.12}$$

Kinematic description of the element is concluded by derivation of $\boldsymbol{G}$ operator. It may be derived indirectly (i.e. without defining M^u and M^θ) through requirement that

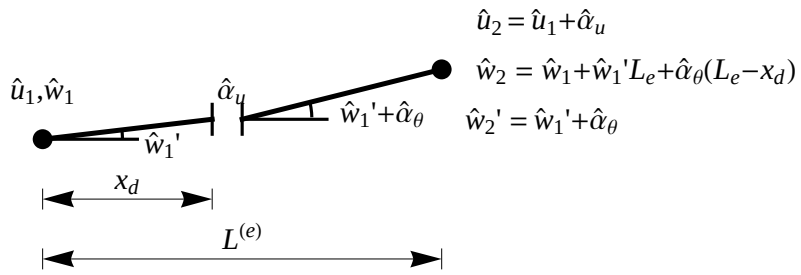

Figure 6.2: Strain-free mode of the element

Slika 6.2: Element v brezdeformacijskem stanju

an element has to be able to describe strain-free mode at some non-zero values of $\hat{\alpha}_u$ and $\hat{\alpha}_\theta$, see [Armero and Ehrlich, 2006b]. According to Fig. 6.2, the generalized nodal displacements $\hat{\boldsymbol{d}}_{hinge} = [\hat{u}_1, \hat{u}_2, \hat{w}_1, \hat{w}_2, \hat{w}_1', \hat{w}_2']^T$ of such strain-free mode are composed as

$$\hat{\boldsymbol{d}}_{hinge} = \hat{\boldsymbol{d}}_{rigid} + \boldsymbol{D}_{hinge}\hat{\boldsymbol{\alpha}}, \quad \boldsymbol{D}_{hinge} = \begin{bmatrix} 0 & 1 & 0 & 0 & 0 & 0 \\ 0 & 0 & 0 & L^{(e)} - x_d & 0 & 1 \end{bmatrix}^T \tag{6.13}$$

where $\hat{\boldsymbol{d}}_{rigid} = \left[\hat{u}_1, \hat{u}_1, \hat{w}_1, \hat{w}_1 + \hat{w}_1' L^{(e)}, \hat{w}_1', \hat{w}_1'\right]^T$ are generalized nodal displacements due to rigid-body motion of a complete beam, and $\boldsymbol{D}_{hinge}\hat{\boldsymbol{\alpha}}$ are generalized nodal displacements due to rigid-body motion of one part of the beam due to imposed strong discontinuity $\hat{\boldsymbol{\alpha}} = [\hat{\alpha}_u, \hat{\alpha}_\theta]^T$. If we now set strains (6.9) to zero for $\hat{\boldsymbol{d}}_{hinge}$, we have

$$\mathbf{0} = \boldsymbol{B}\hat{\boldsymbol{d}}_{hinge} + \boldsymbol{G}\hat{\boldsymbol{\alpha}} = \underbrace{\boldsymbol{B}\hat{\boldsymbol{d}}_{rigid}}_{=\mathbf{0}} + (\boldsymbol{G} + \boldsymbol{B}\boldsymbol{D}_{hinge})\hat{\boldsymbol{\alpha}}. \tag{6.14}$$

Since the above equation should hold for any $\hat{\boldsymbol{\alpha}}$, we get the $\boldsymbol{G}$ operator as

$$\boldsymbol{G} = -\boldsymbol{B}\boldsymbol{D}_{hinge}, \tag{6.15}$$

which leads to

$$G^u(x, x_d) = -\frac{1}{L^{(e)}}, \tag{6.16}$$

$$G^\theta(x, x_d) = -\frac{1 + 3(1 - \frac{2x_d}{L^{(e)}})(1 - \frac{2x}{L^{(e)}})}{L^{(e)}}. \tag{6.17}$$

The above definition of $\boldsymbol{G}$ matrix concludes kinematic description of the geometrically linear element.

Remark 6.1. *By using (6.1) and (6.2) to describe strain-free mode of Fig. 6.2, one can also derive interpolation functions M^u and M^θ. By setting in (6.1) $u_1 = \hat{u}_1 = 0$,*

$u_2 = \hat{u}_2 = \hat{\alpha}_u$, $u^h = 0$ for $x < x_d$, and $u^h = 0$ for $x \geq x_d$, one can conclude that $M^u = H(x - x_d) - \boldsymbol{N}^u \cdot [0, 1]$. Here, $H(x - x_d)$ is unit-step function, which is 0 for $x < x_d$ and 1 for $x \geq x_d$. Derivation $\partial M^u/\partial x$ gives G^u in (6.16). By using similar procedure for bending in (6.2), one can obtain $M^\theta = (H(x - x_d))\,(x - x_d) - \boldsymbol{N}^w \cdot \left[0, L^{(e)} - x_d\right] - \boldsymbol{N}^{w'} \cdot [0, 1]$. Derivation $\partial^2 M^u/\partial x^2$ gives G^θ in (6.17).

In order to account for the geometrically nonlinear effects, and related global buckling, we will use the von Karman axial strain when computing the virtual axial strain. The real axial strain, used for computing the internal forces, will still be assumed as linear, as given in eq. (6.5). The von Karman axial strain is defined as $\varepsilon^{VK} = \frac{\partial u^h}{\partial x} + \frac{1}{2}(\frac{\partial w^h}{\partial x})^2$. The corresponding virtual axial strain is thus:

$$\delta\varepsilon^{VK} = \frac{\partial \delta u^h}{\partial x} + \frac{\partial w^h}{\partial x}\frac{\partial \delta w^h}{\partial x}. \tag{6.18}$$

If we choose to interpolate δu^h, w^h and δw^h in (6.18) as $\delta u^h = \boldsymbol{N}^u(x)\delta\boldsymbol{u} + M^u(x, x_d)\delta\alpha_u$, $w^h = \boldsymbol{N}^w(x)\boldsymbol{w} + \boldsymbol{N}^{w'}(x)\boldsymbol{w'}$ and $\delta w^h = \boldsymbol{N}^w(x)\delta\boldsymbol{w} + \boldsymbol{N}^{w'}(x)\delta\boldsymbol{w'}$, where $\delta\boldsymbol{u} = [\delta u_1, \delta u_2]^T$ is vector of virtual nodal axial displacements, $\delta\boldsymbol{w} = [\delta w_1, \delta w_2]^T$ and $\delta\boldsymbol{w'} = [\delta w_1', \delta w_2']^T$ are vectors of virtual nodal transverse displacements and rotations, and $\delta\alpha_u$ is virtual discontinuity in axial displacement at x_d, the chosen interpolations lead to

$$\delta\varepsilon^{VK} = \underbrace{\boldsymbol{B}^u(x)\,\delta\boldsymbol{u} + \boldsymbol{B}^{u,w}(x)\,\delta\boldsymbol{w} + \boldsymbol{B}^{u,w'}(x)\,\delta\boldsymbol{w'} + G^u(x, x_d)\delta\alpha_u}_{\delta\overline{\varepsilon}^{VK}} + \underbrace{\delta_{x_d}\delta\alpha_u}_{\delta\overline{\overline{\varepsilon}}} \tag{6.19}$$

where

$$\boldsymbol{B}^{u,w}(x) = C\frac{d\boldsymbol{N}^w}{dx}, \quad \boldsymbol{B}^{u,w'}(x) = C\frac{d\boldsymbol{N}^{w'}}{dx}, \quad C = \left(\frac{d\boldsymbol{N}^w}{dx}\cdot\boldsymbol{w} + \frac{d\boldsymbol{N}^{w'}}{dx}\cdot\boldsymbol{w'}\right). \tag{6.20}$$

The linear matrix operator $\boldsymbol{B}$ from (6.11) should be thus replaced with the nonlinear matrix operator $\boldsymbol{B}^{VK}$ when computing virtual strains $\delta\overline{\boldsymbol{\epsilon}} = [\delta\overline{\varepsilon}, \delta\overline{\kappa}]^T$, i.e.

$$\begin{bmatrix} \delta\overline{\varepsilon} = \delta\overline{\varepsilon}^{VK} \\ \delta\overline{\kappa} \end{bmatrix} = \underbrace{\begin{bmatrix} \boldsymbol{B}^u & \boldsymbol{B}^{u,w} & \boldsymbol{B}^{u,w'} \\ \boldsymbol{0} & \boldsymbol{B}^w & \boldsymbol{B}^{w'} \end{bmatrix}}_{\boldsymbol{B}^{VK}}\delta\boldsymbol{d} + \boldsymbol{G}\delta\boldsymbol{\alpha}. \tag{6.21}$$

In (6.21) above, we denote with $\delta\boldsymbol{d} = [\delta\boldsymbol{u}^T, \delta\boldsymbol{w}^T, \delta\boldsymbol{w'}^T]^T$ the generalized virtual nodal displacements and with $\delta\boldsymbol{\alpha} = [\delta\alpha_u, \delta\alpha_\theta]^T$ virtual jumps at x_d.

Remark 6.2. *The tangent stiffness matrix of the beam finite element with von Karman virtual axial strain has symmetric geometric part and non-symmetric material part. The matrix can be symmetrized by using $\boldsymbol{B}$ instead of $\boldsymbol{B}^{VK}$ when computing its material part. Such an approach would lead (for elastic beams) to the element presented in [Wilson, 2002], section 11. In this work we use non-symmetric tangent stiffness matrix.*

Remark 6.3. ***(b)*** *If one uses von Karman definition of axial strains for both real and virtual strains, see [Reddy, 2004], section 4.2, the element exhibits severe locking.*

6.2.2 Equilibrium equations

The weak form of the equilibrium equations (the principle of virtual work) for an element e of a chosen finite element mesh with N_{el} finite elements, can be written as:

$$\delta\Pi^{int,(e)} - \delta\Pi^{ext,(e)} = 0. \tag{6.22}$$

By denoting the virtual strains as $\delta\boldsymbol{\epsilon} = \left[\delta\varepsilon^{VK}, \delta\kappa\right]^T$, where virtual curvatures $\delta\kappa = \delta\overline{\kappa} + \delta\overline{\overline{\kappa}}$ are of the same form as real curvatures κ in (6.6), we can write a single element contribution to the virtual work of internal forces as:

$$\begin{aligned} \delta\Pi^{int,(e)} &= \int_0^{L^{(e)}} (\delta\boldsymbol{\epsilon})^T \boldsymbol{\sigma} dx \\ &= \underbrace{\int_0^{L^{(e)}} \delta\boldsymbol{d}^T \left(\boldsymbol{B}^{VK}\right)^T \boldsymbol{\sigma} dx}_{\text{standard}} + \underbrace{\int_0^{L^{(e)}} \delta\boldsymbol{\alpha}^T (\boldsymbol{G}^T\boldsymbol{\sigma} + \delta_{x_d}\boldsymbol{\sigma}) dx}_{\text{additional}}, \end{aligned} \tag{6.23}$$

The matrices $\boldsymbol{B}^{VK}$ and $\boldsymbol{G}$ are defined in (6.21) and (6.15), and

$$\boldsymbol{\sigma} = [N, M]^T \tag{6.24}$$

is the vector of beam internal forces that contains axial force N and bending moment M. From the term "standard" in (6.23) we obtain the vector of element internal nodal forces

$$\boldsymbol{f}^{int,(e)} = \int_0^{L^{(e)}} \left(\boldsymbol{B}^{VK}\right)^T \boldsymbol{\sigma} dx. \tag{6.25}$$

From the virtual work of external forces $\delta\Pi^{ext,(e)}$ we can get the vector of element external nodal forces $\boldsymbol{f}^{ext,(e)}$, representing the external load applied to the element. The finite element assembly of vectors $\boldsymbol{f}^{int,(e)}$ and $\boldsymbol{f}^{ext,(e)}$, for all elements of the chosen mesh, leads to a set of global (i.e. mesh related) equations

$$A_{e=1}^{N_{el}} \left(\boldsymbol{f}^{int,(e)} - \boldsymbol{f}^{ext,(e)}\right) = \boldsymbol{0}, \tag{6.26}$$

where A is the assembling operator.

We have only used one part of the right side of equation (6.23) in (6.22) when getting the set of global equations (6.26). The other term in (6.23), denoted as "additional" (since it results from additional enriched kinematics due to embedded discontinuity), will also contribute to the weak form of the equilibrium. However, we will treat this contribution

locally element by element. Then, in view of (6.22), the following two equations are obtained for each element of the chosen mesh

$$\begin{aligned} \boldsymbol{h}^{(e)} &= \left[h_N^{(e)}, h_M^{(e)}\right]^T = \int_0^{L^{(e)}} (\boldsymbol{G}^T\boldsymbol{\sigma} + \delta_{x_d}\boldsymbol{\sigma})dx \\ &= \int_0^{L^{(e)}} \boldsymbol{G}^T\boldsymbol{\sigma}dx + \underbrace{\boldsymbol{\sigma}|_{x_d}}_{=\boldsymbol{t}} = \int_0^{L^{(e)}} \boldsymbol{G}^T\boldsymbol{\sigma}dx + \boldsymbol{t} = \boldsymbol{0}, \quad \forall e \in [1, N_{el}]\,. \end{aligned} \tag{6.27}$$

We have defined in (6.27) vector $\boldsymbol{t} = \boldsymbol{\sigma}|_{x_d} = [t_N, t_M]^T$ with components t_N and t_M that represent axial traction and moment (bending) traction at the discontinuity. By using (6.17) and (6.24), one can obtain the component form of (6.27)

$$\begin{aligned} h_N^{(e)} &= \int_0^{L^{(e)}} G^u N dx + t_N = 0, \\ h_M^{(e)} &= \int_0^{L^{(e)}} G^\theta M dx + t_M = 0, \quad \forall e \in [1, N_{el}]\,. \end{aligned} \tag{6.28}$$

The problem of solving a set of global equations (6.26) together with a set of local (element) equations (6.27) will be further addressed in Section 4.

6.2.3 Constitutive relations

We assume that the axial response of the beam material remains always elastic, thus discarding the failure by necking, for example. For the bending behavior of the beam material we choose the following constitutive models: (i) stress-resultant elastoplastic constitutive model with linear isotropic hardening, (ii) stress-resultant rigid-plasticity model with linear softening at the softening plastic hinge. The basic ingredients of the chosen constitutive relations are built on classical plasticity (e.g. [Ibrahimbegovic et al., 1998]) and can be summarized as:

- The regular strains $\overline{\boldsymbol{\epsilon}}$ (6.10) can be additively decomposed into elastic part $\overline{\boldsymbol{\epsilon}}^e$ and plastic part $\overline{\boldsymbol{\epsilon}}^p$

$$\overline{\boldsymbol{\epsilon}} = \overline{\boldsymbol{\epsilon}}^e + \overline{\boldsymbol{\epsilon}}^p, \quad \overline{\boldsymbol{\epsilon}}^e = [\overline{\varepsilon}^e, \overline{\kappa}^e]^T, \quad \overline{\boldsymbol{\epsilon}}^p = [\overline{\varepsilon}^p, \overline{\kappa}^p]^T. \tag{6.29}$$

- The axial strain of the beam (6.5) remains always elastic, thus

$$\varepsilon = \overline{\varepsilon} = \overline{\varepsilon}^e, \quad \overline{\overline{\varepsilon}} = 0 \quad \Longleftrightarrow \quad \overline{\varepsilon}^p = 0, \quad \alpha_u = 0. \tag{6.30}$$

- The free energy for the beam material (before localized softening is activated) is assumed to be the sum of the strain energy function $\overline{W}$ and the hardening potential $\overline{\Xi}$

$$\overline{\Psi}(\overline{\boldsymbol{\epsilon}}^e, \overline{\xi}) := \overline{W}\,(\overline{\boldsymbol{\epsilon}}^e) + \overline{\Xi}(\overline{\xi}) = \frac{1}{2}\overline{\boldsymbol{\epsilon}}^{eT}\boldsymbol{C}\overline{\boldsymbol{\epsilon}}^e + \frac{1}{2}K_h\overline{\xi}^2, \tag{6.31}$$

where $\boldsymbol{C} = DIAG\left[EA, EI\right]$, E is elastic modulus, A and I are area and moment of inertia of cross-section, $\overline{\xi} \geq 0$ is strain-like bending hardening variable, and $K_h \geq 0$ is linear bending hardening modulus.

- The yield criterion for the beam material is defined in terms of the bending moment. The admissible values of the bending moment and the stress-like bending hardening variable $\overline{q}(\overline{\xi})$ are governed by the function

$$\overline{\phi}(M, \overline{q}) = |M| - (M_y - \overline{q}) \leq 0, \tag{6.32}$$

where $M_y > 0$ denotes the positive yield moment of the cross-section. Influence of the axial force N on the cross-section yielding is taken into account by defining M_y and $\overline{q}$ as functions of N, as shown subsequently.

- The bending traction t_M at the discontinuity x_d is related to the rotation jump as shown in Fig. 6.3

$$t_M = t_M(\alpha_\theta). \tag{6.33}$$

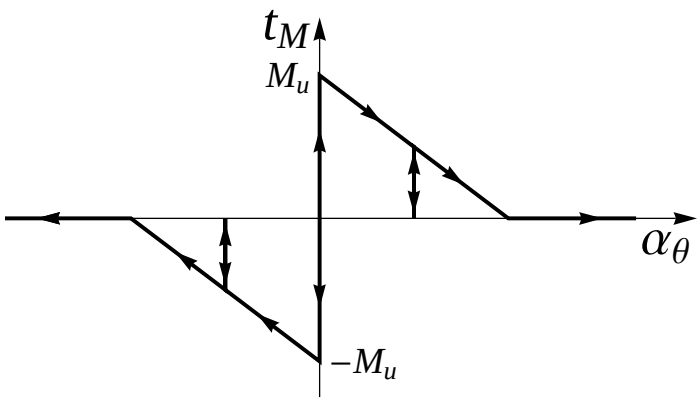

Figure 6.3: Rigid-plastic cohesive law at discontinuity

Slika 6.3: Kohezijski zakon (toga plastičnost) v nezveznosti

- Cohesive law (6.33) can be written in terms of localization (failure) criterion that activates softening at discontinuity at x_d and is defined in terms of the bending traction t_M and the stress-like softening bending variable $\overline{\overline{q}}(\overline{\overline{\xi}})$ (the later is defined in terms of the bending strain-like softening variable $\overline{\overline{\xi}} \geq 0$)

$$\overline{\overline{\phi}}(t_M, \overline{\overline{q}}) = |t_M| - (M_u - \overline{\overline{q}}) \leq 0, \tag{6.34}$$

where $M_u > M_y > 0$ denotes the positive ultimate (failure) moment of the cross-section. Influence of axial force N on the cross-section failure is taken into account by defining M_u and $\overline{\overline{q}}$ as functions of N, as shown below.

- The softening potential is assumed to be

$$\overline{\overline{\Xi}}(\overline{\overline{\xi}}) = \frac{1}{2} K_s \overline{\overline{\xi}}^2, \tag{6.35}$$

where $K_s \leq 0$ is the linear (bending) softening modulus.

The remaining ingredients of the elastoplasticity with hardening can be obtained from the consideration of thermodynamics of associative plasticity and the principle of maximum plastic dissipation (see e.g. [Ibrahimbegovic, 2009], [Lubliner, 1990], [Simo and Hughes, 1998]). In the present beam model the elastoplasticity with hardening happens for $\boldsymbol{\alpha} = \mathbf{0}$, which leads to $\overline{\boldsymbol{\epsilon}} = \widetilde{\overline{\boldsymbol{\epsilon}}}$ and $\overline{\overline{\boldsymbol{\epsilon}}} = \mathbf{0}$, see (6.10). By using (6.29) and (6.31) the mechanical dissipation can be written as

$$0 \leq \overline{D} \overset{def.}{=} \boldsymbol{\sigma}^T \dot{\overline{\boldsymbol{\epsilon}}} - \dot{\overline{\Psi}}(\overline{\boldsymbol{\epsilon}}^e, \overline{\xi}) = (\boldsymbol{\sigma} - \frac{\partial \overline{\Psi}}{\partial \overline{\boldsymbol{\epsilon}}^e})^T \dot{\overline{\boldsymbol{\epsilon}}}^e + \boldsymbol{\sigma}^T \dot{\overline{\boldsymbol{\epsilon}}}^p - \frac{\partial \overline{\Psi}}{\partial \overline{\xi}} \dot{\overline{\xi}}, \tag{6.36}$$

where $(\dot{o}) = \partial (o) / \partial t$ and $t \in [0, T]$ is pseudo-time. By assuming that the elastic process is non-dissipative (i.e. $\overline{D} = 0$), and that the plastic state variables do not change, we obtain from (6.36)

$$\boldsymbol{\sigma} = \frac{\partial \overline{\Psi}}{\partial \overline{\boldsymbol{\epsilon}}^e} = \boldsymbol{C} \overline{\boldsymbol{\epsilon}}^e \Longrightarrow N = EA\overline{\varepsilon},\ M = EI\left(\overline{\kappa} - \overline{\kappa}^p\right). \tag{6.37}$$

We can define the hardening variable $\overline{q}$ by further considering (6.36) and (6.31)

$$\overline{q} = -\frac{\partial \overline{\Psi}}{\partial \overline{\xi}} = -\frac{\partial \overline{\Xi}}{\partial \overline{\xi}} = -K_h \overline{\xi}. \tag{6.38}$$

By replacing (6.37) and (6.38) in (6.36), the plastic dissipation can be obtained as

$$\overline{D}^p = \boldsymbol{\sigma}^T \dot{\overline{\boldsymbol{\epsilon}}}^p + \overline{q} \dot{\overline{\xi}} \overset{(6.24),\ (6.29),\ (6.30)}{\Longrightarrow} \overline{D}^p = M \dot{\overline{\kappa}}^p + \overline{q} \dot{\overline{\xi}}. \tag{6.39}$$

The principle of maximum plastic dissipation states that among all the variables $(M,\ \overline{q})$ that satisfy the yield criteria $\overline{\phi}\,(M, \overline{q}) \leq 0$, one should choose those that maximize plastic dissipation (at frozen rates $\dot{\overline{\kappa}}^p$ and $\dot{\overline{\xi}}$). This can be written as a constrained optimization problem:

$$\min_{M, \overline{q}} \max_{\dot{\overline{\gamma}}} \left[\overline{L}^p(M, \overline{q}, \dot{\overline{\gamma}}) = -\overline{D}^p(M, \overline{q}) + \dot{\overline{\gamma}} \overline{\phi}(M, \overline{q}) \right], \tag{6.40}$$

where $\dot{\overline{\gamma}} \geq 0$ plays the role of Lagrange multiplier. By using (6.39) and (6.32), the last result can provide the evolution equations for internal variables

$$\frac{\partial \overline{L}^p}{\partial M} = -\dot{\overline{\kappa}}^p + \dot{\overline{\gamma}}\frac{\partial \overline{\phi}}{\partial M} = 0 \implies \dot{\overline{\kappa}}^p = \text{sign}(M)\dot{\overline{\gamma}}, \tag{6.41}$$

$$\frac{\partial \overline{L}^p}{\partial \overline{q}} = -\dot{\overline{\xi}} + \dot{\overline{\gamma}}\frac{\partial \overline{\phi}}{\partial \overline{q}} = 0 \implies \dot{\overline{\xi}} = \dot{\overline{\gamma}}, \tag{6.42}$$

along with the Kuhn-Tucker loading/unloading conditions and the consistency condition

$$\dot{\overline{\gamma}} \geq 0, \quad \overline{\phi} \leq 0, \quad \dot{\overline{\gamma}}\overline{\phi} = 0, \quad \dot{\overline{\gamma}}\dot{\overline{\phi}} = 0. \tag{6.43}$$

To obtain the remaining ingredients of the rigid-plastic response describing softening at the discontinuity x_d, let us isolate the softening plastic hinge. We first define the strain energy function due to softening potential as $\overline{\overline{\Psi}} = \overline{\overline{\Xi}}$. The dissipation at x_d can be then written as:

$$0 \leq \overline{\overline{D}} \overset{def.}{=} t_M\dot{\alpha}_\theta - \dot{\overline{\overline{\Psi}}}(\overline{\overline{\xi}}) = t_M\dot{\alpha}_\theta - \frac{\partial \overline{\overline{\Psi}}}{\partial \overline{\overline{\xi}}}\dot{\overline{\overline{\xi}}}. \tag{6.44}$$

where t_M is the discontinuity bending traction given by (6.33). By defining

$$\overline{\overline{q}} = -\frac{\partial \overline{\overline{\Psi}}}{\partial \overline{\overline{\xi}}} = -\frac{\partial \overline{\overline{\Xi}}}{\partial \overline{\overline{\xi}}} = -K_s\overline{\overline{\xi}} = |K_s|\,\overline{\overline{\xi}}, \tag{6.45}$$

the result in (6.44) can be rewritten as

$$\overline{\overline{D}} = \overline{\overline{D}}^p = t_M\dot{\alpha}_\theta + \overline{\overline{q}}\dot{\overline{\overline{\xi}}}. \tag{6.46}$$

The principle of maximum plastic dissipation at the rigid-plastic discontinuity can then be defined as:

$$\min_{t_M,\overline{\overline{q}}} \max_{\dot{\overline{\overline{\gamma}}}} \left[\overline{\overline{L}}^p(t_M,\overline{\overline{q}},\dot{\overline{\overline{\gamma}}}) = -\overline{\overline{D}}^p(t_M,\overline{\overline{q}}) + \dot{\overline{\overline{\gamma}}}\overline{\overline{\phi}}(t_M,\overline{\overline{q}})\right], \tag{6.47}$$

where $\dot{\overline{\overline{\gamma}}} \geq 0$ is the Lagrange multiplier. By using (6.46) and (6.34), we get from (6.47) above the following evolution equations:

$$\frac{\partial \overline{\overline{L}}^p}{\partial t_M} = -\dot{\alpha}_\theta + \dot{\overline{\overline{\gamma}}}\frac{\partial \overline{\overline{\phi}}}{\partial t_M} = 0 \Longrightarrow \dot{\alpha}_\theta = \text{sign}(t_M)\dot{\overline{\overline{\gamma}}}, \tag{6.48}$$

$$\frac{\partial \overline{\overline{L}}^p}{\partial \overline{\overline{q}}} = -\dot{\overline{\overline{\xi}}} + \dot{\overline{\overline{\gamma}}}\frac{\partial \overline{\overline{\phi}}}{\partial \overline{\overline{q}}} = 0 \Longrightarrow \dot{\overline{\overline{\xi}}} = \dot{\overline{\overline{\gamma}}}. \tag{6.49}$$

By observing that $\text{sign}(t_M) = \text{sign}(\alpha_\theta)$ (see (6.33) and Fig. 6.3), it follows from (6.48) that

$$\text{sign}(\alpha_\theta)\dot{\alpha}_\theta = \dot{\overline{\overline{\xi}}} \Rightarrow |\alpha_\theta| = \overline{\overline{\xi}}. \tag{6.50}$$

The Kuhn-Tucker loading/unloading conditions and the consistency condition also apply:

$$\dot{\overline{\overline{\gamma}}} \geq 0, \quad \overline{\overline{\phi}} \leq 0, \quad \dot{\overline{\overline{\gamma}}}\overline{\overline{\phi}} = 0, \quad \dot{\overline{\overline{\gamma}}}\dot{\overline{\overline{\phi}}} = 0. \tag{6.51}$$

With the above results, we are in position to write the total dissipation of the beam finite element when the element is in the softening regime. Namely, by accounting for the proper definition of strain energy terms for the beam finite element according to $\Psi = \int_0^{L^{(e)}} \overline{\Psi} dx + \overline{\overline{\Psi}}$, the total dissipation in the softening regime can be written as

$$\begin{aligned}
\overline{\overline{D}}^{tot}_{L^{(e)}} &= \int_0^{L^{(e)}} \left(\boldsymbol{\sigma}^T \dot{\overline{\boldsymbol{\epsilon}}} - \dot{\overline{\Psi}}(\overline{\boldsymbol{\epsilon}}^e, \overline{\xi}) \right) dx + \left(t_M \dot{\alpha}_\theta - \dot{\overline{\overline{\Psi}}}(\overline{\overline{\xi}}) \right) \\
&= \int_0^{L^{(e)}} \left(\boldsymbol{\sigma}^T \dot{\widetilde{\boldsymbol{\epsilon}}} + \boldsymbol{\sigma}^T \boldsymbol{G} \dot{\boldsymbol{\alpha}} - \boldsymbol{\sigma}^T \underbrace{\dot{\overline{\boldsymbol{\epsilon}}}^e}_{\dot{\widetilde{\boldsymbol{\epsilon}}}^e} + \overline{q}\dot{\overline{\xi}} \right) dx + \left(t_M \dot{\alpha}_\theta + \overline{\overline{q}}\dot{\overline{\overline{\xi}}} \right) \\
&= \int_0^{L^{(e)}} \underbrace{\left(M\dot{\overline{\kappa}}^p + \overline{q}\dot{\overline{\xi}} \right)}_{\overline{D}^p, \text{ see (6.39)}} dx + \underbrace{\left(\int_0^{L^{(e)}} G^\theta M dx + t_M \right)}_{=0, \text{ see (6.28)}} \dot{\alpha}_\theta + \underbrace{\overline{\overline{q}}}_{|K_s|\overline{\overline{\xi}}} \dot{\overline{\overline{\xi}}}.
\end{aligned} \tag{6.52}$$

It can be seen from (6.52) that enforcing eq. (6.28) will decouple dissipation in the softening plastic hinge from the dissipation in the rest of the beam. Therefore, eq. (6.28) is further used to compute t_M.

We conclude description of constitutive relations by defining plastic work of the beam cross-section in the hardening regime

$$\overline{W}^p = M\dot{\overline{\kappa}}^p = |M|\,\dot{\overline{\xi}} = \left(M_y + K_h \overline{\xi} \right) \dot{\overline{\xi}}, \tag{6.53}$$

and plastic work for the beam finite element in the softening regime as

$$\overline{\overline{W}}^p = t_M \dot{\alpha}_\theta = |t_M|\,\dot{\overline{\overline{\xi}}} = \left(M_u + K_s \overline{\overline{\xi}} \right) \dot{\overline{\overline{\xi}}}. \tag{6.54}$$

6.3 Computation of beam plasticity material parameters

In the previous section, we have built the framework for stress-resultant plasticity for beam finite element with embedded discontinuity. The material parameters that need to be known for chosen material models are: (i) M_y and K_h for the plasticity with hardening, and (ii) M_u and K_s for the softening plastic hinge. In this section we will elaborate on determination of the above parameters.

The yield moment M_y can be determined by considering the uniaxial yield stress of the material σ_y, the bending resistance modulus of cross-section W, the cross-section area

A, and the level of axial force N. One can associate the yield moment of the cross-section with the yielding of the most-stressed material fiber to get

$$M_y\left(N\right) = W\sigma_y(1 - \frac{|N|}{A\sigma_y}). \tag{6.55}$$

The ultimate bending moment M_u can be derived in a closed form by assuming elastic-perfectly-plastic response of material fibers, e.g. [Lubliner, 1990]. However, one may try to determine a better estimate for M_u, which takes into consideration material hardening, as well as possibility of local buckling (e.g. buckling of the flanges and/or the web of the I-beam). This task is addressed in the present work by performing computations with refined finite element model based on geometrically and materially nonlinear shell element, which is able to capture local buckling and gradual spreading of plasticity over the cross-section. The ultimate bending resistance M_u can be obtained by using results of such a shell model computations, as can be moduli K_h and K_s.

To obtain desired results, a part of the frame member with a reference length $L^{ref} < L^{tot}$ (L^{tot} is the total length of the frame member under consideration) is: (i) modeled with shell finite elements, (ii) subjected to an external axial force $\widehat{N}$ in the first loading step, and (iii) subjected to a varying external bending moment at the end cross-sections in the second loading step, while keeping $\widehat{N}$ fixed, see Fig. 6.4 (b). It is assumed that such a loading pattern would produce approximately constant internal axial force $N = \widehat{N}$ during the analysis. The computation with shell model takes into account geometrical and material nonlinearity that include: plasticity with hardening and strain-softening, strain-softening regularization, and local buckling effects. The results of shell analysis are cast in terms of diagrams presented in Figs. 6.4 (d) and (g). One can associate the ultimate bending moment M_u with the peak point in the diagram at Fig. 6.4 (d), where applied end moment is plotted versus the end rotation, i.e.

$$M_u\left(N\right) = M_u^{ref}(N). \tag{6.56}$$

One can also use this point as a border-point between the hardening regime and the softening regime, where the softening can be due to material and/or geometric effects. To determine the values of the beam model hardening and softening parameters, we make an assumption that the plastic work at failure should be equal for both the beam and the shell model. In other words, we want the internal forces of the beam model to produce the same amount of the plastic work as the internal forces of the shell model, when considering the full failure of the part of the frame member of length L^{ref}.

Since the plastic work is done in two regimes (hardening and softening), we have to assure that the amount of plastic work in each regime matches for both models, i.e.

$$E^{\overline{W}^p}\left(N\right) = E^{\overline{W}^{p,ref}}\left(N\right), \quad E^{\overline{\overline{W}}^p}\left(N\right) = E^{\overline{\overline{W}}^{p,ref}}\left(N\right). \tag{6.57}$$

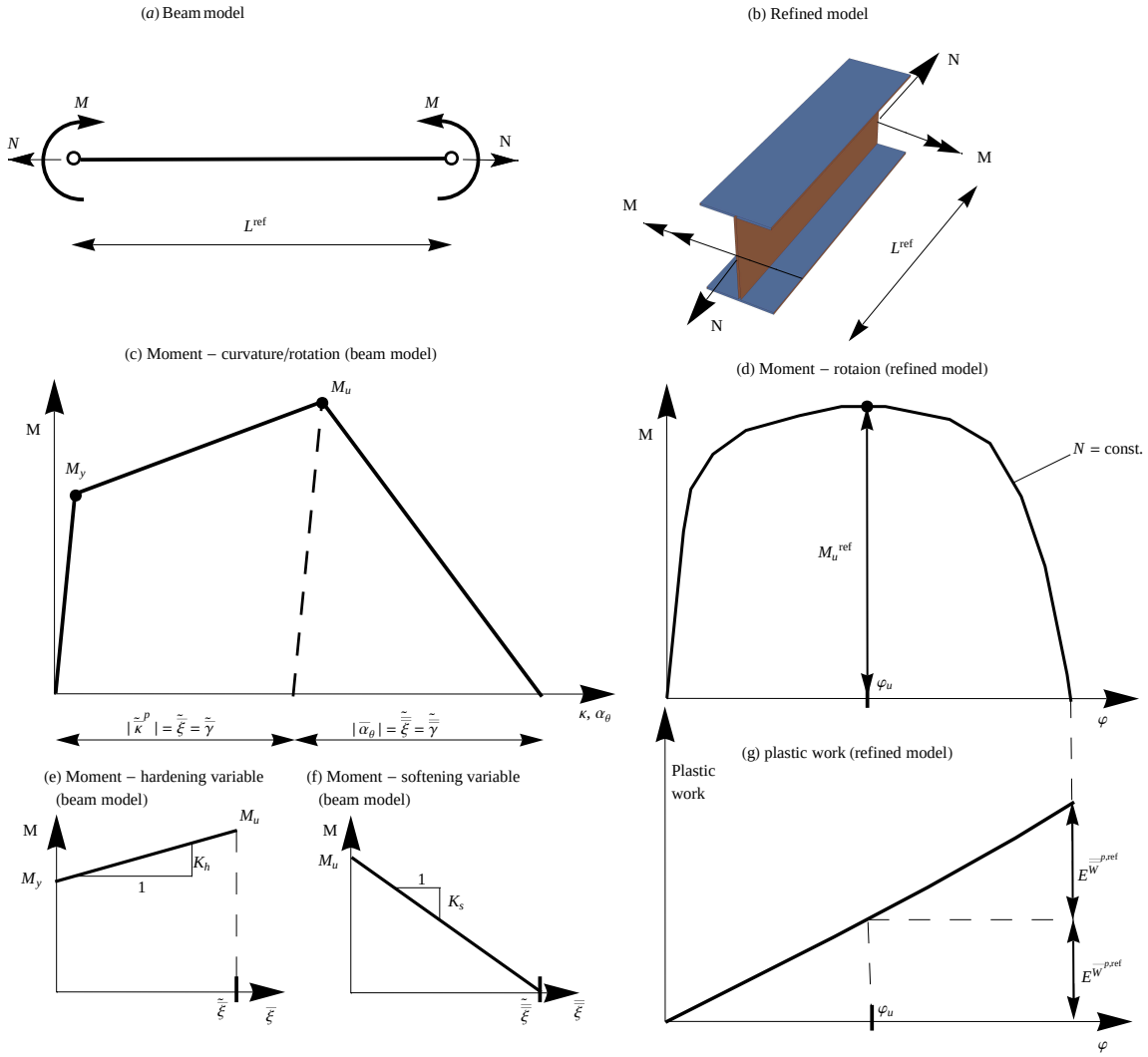

Figure 6.4: Evaluation of beam material parameters by using results of refined analysis

Slika 6.4: Določitev parametrov za nosilce z uporabo rezultatov podrobnejše analize

The plastic work in the hardening regime, $E^{\overline{W}^{p,ref}}$, and the plastic work in the softening regime, $E^{\overline{\overline{W}}^{p,ref}}$, are obtained from the shell model analysis, Fig. 6.4 (g).

The plastic work of the beam model in the hardening regime, $E^{\overline{W}^{p}}$, can be determined by observing that each cross-section in the frame member of length L^{ref} is approximately under the same force-moment state during the hardening regime. Integration of (6.53) allows us to write

$$E^{\overline{W}^{p}} = \int_0^{L^{ref}} \int_0^{t \text{ at } M_u} \overline{W}^{p} d\tau dl = L^{ref}(M_y \tilde{\bar{\xi}} + \frac{1}{2} K_h \tilde{\bar{\xi}}^2). \tag{6.58}$$

In (6.58) above $\tilde{\bar{\xi}}$ is the value of hardening variable that corresponds to the bending moment M_u, Fig. 6.4 (e). Since we have assumed linear hardening in the beam model (6.38), we get

$$\tilde{\bar{\xi}} = \frac{M_u - M_y}{K_h}. \tag{6.59}$$

By using (6.59), (6.58) and (6.57), one can obtain an expression for hardening modulus as

$$K_h(N) = \frac{(M_u^2(N) - M_y^2(N))L^{ref}}{2E^{\overline{W}^{p,ref}}(N)}. \tag{6.60}$$

The plastic work of beam model in the softening regime, $E^{\overline{\overline{W}}^{p}}$, can be determined by assuming that the softening part of $M - \varphi$ curve in Fig. 6.4 (d), obtained from the shell model analysis, is produced by a very localized phenomenon (in a single cross-section) related to the local buckling and/or to the localized strain-softening. By using (6.54), one can compute the plastic work in the softening regime for the beam model as

$$E^{\overline{\overline{W}}^{p}} = \int_0^{t} \overline{\overline{W}}^{p} d\tau = \int_0^{\bar{\bar{\xi}} \text{ at } t_M=0} \left(M_u + K_s \bar{\bar{\xi}}\right) d\bar{\bar{\xi}} = \frac{1}{2} |K_s| \tilde{\bar{\bar{\xi}}}^2. \tag{6.61}$$

In (6.61) $\tilde{\bar{\bar{\xi}}}$ is the value of the softening variable that corresponds to the total cross-section failure, Fig. 6.4 (f). Since we have assumed linear softening in the beam model, we obtain

$$\tilde{\bar{\bar{\xi}}} = \frac{M_u}{|K_s|}. \tag{6.62}$$

By using (6.62), (6.61) and (6.57), one can obtain an expression for softening modulus as

$$|K_s(N)| = \frac{M_u^2(N)}{2E^{\overline{\overline{W}}^{p,ref}}(N)}, \quad K_s \leq 0. \tag{6.63}$$

We note, that the choice of the reference length L^{ref} should have very small influence on the values of the searched material parameters. The influence on the value of K_h

should be small, since each cross-section is approximately under the same force-moment state during the hardening regime. The influence on the value of K_s should not be too big neither, since the softening effect is localized. However, one should perform large displacement correction of M_u, if the chosen length of L^{ref} enables large deflections, as shown in example 5.4.

6.4 Computational procedure

In this section we will present a procedure for solving the set of global (mesh related) and the set of local (element related) nonlinear equations generated by using the stress-resultant plasticity beam finite element with embedded discontinuity presented in section 2.

The solution of the set of global nonlinear equations (6.26), along with the set of local nonlinear equations (6.27) (note that (6.27) is reduced to (6.28) due to assumption (6.30)), ought to be computed at discrete pseudo-time values $0, t_1, t_2, \ldots, t_{n-1}, t_n, t_{n+1}, \ldots, T$ by means of the incremental-iterative scheme. We will consider the solution in a typical pseudo-time incremental step from t_n to t_{n+1}. Let us assume that all the variables, related to an element e and its integration points $ip = 1, 2, 3$ (a 3-point Lobatto integration scheme is used) are given at t_n, i.e.

$$\text{given: } \boldsymbol{d}_n^{(e)},\ \overline{\kappa}_n^{p,ip},\ \overline{\xi}_n^{ip},\ \alpha_{\theta,n}^{(e)},\ \overline{\overline{\xi}}_n^{(e)} \quad \text{and} \quad M_y^{ip},\ x_d^{(e)},\ M_u^{(e)}. \tag{6.64}$$

We have also added in (6.64): (i) the yield moment at integration point M_y^{ip} (which is only true if hardening plasticity has been activated so far) and (ii) position of the discontinuity $x_d^{(e)}$ and the ultimate bending moment $M_u^{(e)}$ (which is only true if softening plastic hinge has been activated so far). We will then iterate in the pseudo-time step in order to compute the converged values of the variables at t_{n+1}, i.e.

$$\text{find: } \boldsymbol{d}_{n+1}^{(e)},\ \overline{\kappa}_{n+1}^{p,ip},\ \overline{\xi}_{n+1}^{ip},\ \alpha_{\theta,n+1}^{(e)},\ \overline{\overline{\xi}}_{n+1}^{(e)} \quad \text{and (if not given already)} \quad M_y^{ip},\ x_d^{(e)},\ M_u^{(e)}. \tag{6.65}$$

The moments M_y^{ip} and $M_u^{(e)}$ are computed by using (6.55) and (6.56). Although they depend on axial force N, we keep them fixed once determined.

The computation of solution (6.65) is split into two phases:

(a) The global (mesh related) phase computes the current iterative values (with (i) as the iteration counter) of nodal generalized displacements at t_{n+1} while keeping the other variables fixed, i.e.

$$\text{global phase: } \boldsymbol{d}_{n+1}^{(e),(i)} = \boldsymbol{d}_{n+1}^{(e),(i-1)} + \Delta\boldsymbol{d}_{n+1}^{(e),(i-1)}. \tag{6.66}$$

The computation of iterative update $\Delta \boldsymbol{d}_{n+1}^{(e),(i-1)}$ will be explained below.

(b) The local (element and integration point related) phase computes the values of variables $\overline{\kappa}_{n+1}^{p,ip}$, $\overline{\xi}_n^{ip}$, $\alpha_{\theta,n+1}^{(e)}$, $\overline{\overline{\xi}}_{n+1}^{(e)}$ while keeping $\boldsymbol{d}_{n+1}^{(e),(i)}$ fixed. The computation procedure depends on weather the softening plastic hinge has been activated in the considered element or not. Therefore, the local computation procedure on the level of a single element can be based either on hardening plasticity procedure or on softening plasticity procedure (excluding each other).

In the rest of this section we will first describe the local phase, which will be followed by the description of the global phase. The hardening plasticity procedure is carried out at each integration point ip (e.g. [Dujc and Brank, 2008]). We first provide the trial value of the bending moment

$$M_{n+1}^{trial,ip} = EI(\overline{\kappa}(\boldsymbol{d}_{n+1}^{(e),(i)}, \alpha_{\theta,n}^{(e)}) - \overline{\kappa}_n^{p,ip}), \tag{6.67}$$

and the trial value of the yield function $\overline{\phi}^{trial,ip}$. If the trial yield criterion

$$\overline{\phi}^{trial,ip}(M_{n+1}^{trial,ip}, \overline{q}(\overline{\xi}_n^{ip})) \overset{?}{\leq} 0 \tag{6.68}$$

is satisfied, the values of hardening plasticity local variables remain unchanged (the step is elastic)

$$\overline{\phi}^{trial,ip} \leq 0 \quad \Longrightarrow \quad \overline{\kappa}_{n+1}^{p,ip} = \overline{\kappa}_n^{p,ip}, \quad \overline{\xi}_{n+1}^{ip} = \overline{\xi}_n^{ip}. \tag{6.69}$$

In the case of violation of the trial yield criterion (6.68), the values of local variables are updated by backward Euler integration scheme

$$\overline{\kappa}_{n+1}^{p,ip} = \overline{\kappa}_n^{p,ip} + \mathrm{sign}(M_{n+1}^{trial,ip})\overline{\gamma}_{n+1}^{ip}, \quad \overline{\xi}_{n+1}^{ip} = \overline{\xi}_n^{ip} + \overline{\gamma}_{n+1}^{ip}, \tag{6.70}$$

where $\overline{\gamma}_{n+1}^{ip} = \dot{\overline{\gamma}}_{n+1}^{ip}(t_{n+1} - t_n)$. The value of the plastic multiplier $\overline{\gamma}_{n+1}^{ip}$ is determined from

$$\overline{\phi}^{ip}(M_{n+1}^{ip}(\boldsymbol{d}_{n+1}^{(e),(i)}, \overline{\kappa}_{n+1}^{p,ip}(\overline{\gamma}_{n+1}^{ip})), \overline{q}(\overline{\xi}_{n+1}^{ip}(\overline{\gamma}_{n+1}^{ip}))) = \overline{\phi}^{ip}(\overline{\gamma}_{n+1}^{ip}) = 0. \tag{6.71}$$

For the linear hardening one can determine $\overline{\gamma}_{n+1}^{ip}$ explicitly. For a nonlinear hardening an iteration procedure has to be used. The main result of the above described hardening plasticity procedure is the new values of the bending moment M_{n+1}^{ip}, computed as

$$M_{n+1}^{ip} = EI(\overline{\kappa}(\boldsymbol{d}_{n+1}^{(e),(i)}, \alpha_{\theta,n}^{(e)}) - \overline{\kappa}_{n+1}^{p,ip}), \tag{6.72}$$

and the elastoplastic tangent operator $\partial M_{n+1}^{ip}/\partial \kappa_{n+1}^{ip,(i)}$. The updated value of the rotation jump is $\alpha_{\theta,n+1}^{(e)} = \alpha_{\theta,n}^{(e)}$.

The softening plasticity procedure is carried out at each finite element e. The discontinuity $x_d^{(e)}$ can only appear at the position of the integration point with the largest absolute value of the bending moment. We first provide the trial value of the bending traction at the discontinuity

$$t_{M,n+1}^{trial,(e)} = -\int_0^{L^{(e)}} G^\theta(x_d^{(e)}, x) M(\boldsymbol{d}_{n+1}^{(e),(i)}, \overline{\kappa}_n^{p,ip}, \alpha_{\theta,n}^{(e)}) dx. \tag{6.73}$$

and the trial value of the failure function

$$\overline{\overline{\phi}}^{trial,(e)}(t_{M,n+1}^{trial,(e)}, \overline{\overline{q}}(\overline{\overline{\xi}}_n^{(e)})) \overset{?}{\leq} 0. \tag{6.74}$$

If the trial failure criterion (6.74) is satisfied, the values of softening plasticity local variables remain unchanged

$$\overline{\overline{\phi}}^{trial,(e)} \leq 0 \quad \Longrightarrow \quad \alpha_{\theta,n+1}^{(e)} = \alpha_{\theta,n}^{(e)}, \quad \overline{\overline{\xi}}_{n+1}^{(e)} = \overline{\overline{\xi}}_n^{(e)}. \tag{6.75}$$

In the case of violation of the trial yield criterion (6.74), the values of local variables are updated by backward Euler integration scheme

$$\alpha_{\theta,n+1}^{(e)} = \alpha_{\theta,n}^{(e)} + \text{sign}(t_{M,n+1}^{trial,(e)}) \overline{\overline{\gamma}}_{n+1}^{(e)}, \quad \overline{\overline{\xi}}_{n+1}^{(e)} = \overline{\overline{\xi}}_n^{(e)} + \overline{\overline{\gamma}}_{n+1}^{(e)}, \tag{6.76}$$

where $\overline{\overline{\gamma}}_{n+1}^{(e)} = \dot{\overline{\overline{\gamma}}}_{n+1}^{(e)}(t_{n+1} - t_n)$. The value of the plastic multiplier $\overline{\overline{\gamma}}_{n+1}^{(e)}$ is determined from condition

$$\overline{\overline{\phi}}^{(e)}(t_{M,n+1}^{(e)}(\alpha_{\theta,n+1}^{(e)}(\overline{\overline{\gamma}}_{n+1}^{(e)})), \overline{\overline{q}}(\overline{\overline{\xi}}_{n+1}^{(e)}(\overline{\overline{\gamma}}_{n+1}^{(e)}))) = \overline{\overline{\phi}}^{(e)}(\overline{\overline{\gamma}}_{n+1}^{(e)}) = 0. \tag{6.77}$$

For the linear softening one can determine the plastic multiplier explicitly, whereas for nonlinear softening an iterative solution procedure is needed. Note, that we compute the bending traction in (6.77) as

$$t_{M,n+1}^{(e)} = -\int_{\Omega^e} G^\theta(x_d^{(e)}, x) M(\boldsymbol{d}_{n+1}^{(e),(i)}, \overline{\kappa}_n^{p,ip}, \alpha_{\theta,n+1}^{(e)}) dx. \tag{6.78}$$

The main result of the above described softening plasticity procedure is the new value of softening variable $\alpha_{\theta,n+1}^{(e)}$, which influences the stress state of the whole element by giving the new values of the bending moment M_{n+1}^{ip} as

$$M_{n+1}^{ip} = EI(\overline{\kappa}(\boldsymbol{d}_{n+1}^{(e),(i)}, \alpha_{\theta,n+1}^{(e)}) - \overline{\kappa}_n^{p,ip}). \tag{6.79}$$

The updated value of the plastic curvature is $\overline{\kappa}_{n+1}^{p,ip} = \overline{\kappa}_n^{p,ip}$.

Once the local variables are computed, we turn to the global phase of the iterative loop in order to provide, if so needed, new iterative values of nodal displacements. First,

the set of global equilibrium equations (6.26) is checked with newly computed M^{ip}_{n+1} from the local phase

$$\left\| A_{e=1}^{N_{el}} [\boldsymbol{f}^{int,(e)}_{n+1} - \boldsymbol{f}^{ext,(e),(i)}_{n+1}] \right\| \overset{?}{<} tol. \tag{6.80}$$

If the convergence criterion (6.80) is satisfied, we move on to the next pseudo-time incremental step. If the convergence criterion fails, we perform a new iterative sweep within the present pseudo-time incremental step. New iterative values of nodal generalized displacements of the finite element mesh are computed by accounting for each element contribution. A single element contribution can be written as

$$\begin{bmatrix} \boldsymbol{K}^{(e)} & \boldsymbol{K}^{f\alpha} \\ \boldsymbol{K}^{hd} & K^{h\alpha} \end{bmatrix}^{(i)}_{n+1} \begin{pmatrix} \Delta \boldsymbol{d}^{(e),(i)}_{n+1} \\ \Delta \alpha^{(e),(i)}_{\theta,n+1} \end{pmatrix} = \begin{pmatrix} \boldsymbol{f}^{ext,(e)}_{n+1} - \boldsymbol{f}^{int,(e),(i)}_{n+1} \\ 0 \end{pmatrix}, \tag{6.81}$$

where the parts of the element stiffness matrix can be formally written as

$$\begin{aligned} \boldsymbol{K}^{(e),(i)}_{n+1} &= \left(\frac{\partial \boldsymbol{f}^{int,(e)}}{\partial \boldsymbol{d}^{(e)}} \right)^{(i)}_{n+1}, \quad \boldsymbol{K}^{f\alpha,(i)}_{n+1} = \left(\frac{\partial \boldsymbol{f}^{int,(e)}}{\partial \alpha^{(e)}_{\theta}} \right)^{(i)}_{n+1}, \\ \boldsymbol{K}^{hd,(i)}_{n+1} &= \left(\frac{\partial h^{(e)}_{M}}{\partial \boldsymbol{d}^{(e)}} \right)^{(i)}_{n+1}, \qquad K^{h\alpha,(i)}_{n+1} = \left(\frac{\partial h^{(e)}_{M}}{\partial \alpha^{(e)}_{\theta}} \right)^{(i)}_{n+1}. \end{aligned} \tag{6.82}$$

The static condensation of (6.81) allows us to form the element stiffness matrix $\widehat{\boldsymbol{K}}^{(e),(i)}_{n+1}$ that contributes to the assembly

$$A_{e=1}^{N_{el}} \left(\widehat{\boldsymbol{K}}^{(e),(i)}_{n+1} \Delta \boldsymbol{d}^{(i)}_{n+1} \right) = A_{e=1}^{N_{el}} \left(\boldsymbol{f}^{ext,(e)}_{n+1} - \boldsymbol{f}^{int,(e),(i)}_{n+1} \right), \tag{6.83}$$

where

$$\widehat{\boldsymbol{K}}^{(e),(i)}_{n+1} = \boldsymbol{K}^{(e),(i)}_{n+1} - \boldsymbol{K}^{f\alpha,(i)}_{n+1} \left(K^{h\alpha,(i)}_{n+1} \right)^{-1} \boldsymbol{K}^{hd,(i)}_{n+1}. \tag{6.84}$$

Solution of (6.83) gives the values of iterative update $\Delta \boldsymbol{d}^{(e),(i)}_{n+1}$, which leads us back to (6.66).

6.5 Examples

In this section we illustrate performance of the above derived beam element when analyzing push-over and collapse of steel frames. We also illustrate the procedure, presented in Section 6.3, for computing the beam model plasticity material parameters by using the shell finite element model. The beam model computer code was generated by using symbolic manipulation code AceGen and the examples were computed by using finite element program AceFem, see [Korelc, 2007b] and [Korelc, 2007a].

6.5.1 Computation of beam plasticity material parameters

With this example we illustrate computation of beam plasticity material parameters M_u, K_h and K_s as suggested in Section 6.3. We consider a frame member with an I-cross-section with flange width $b_f = 30$ cm, flange thickness $t_f = 1.5$ cm, web height $b_w = 40$ cm and web thickness $t_w = 0.8$ cm. The cross-section area is $A = 122$ cm^2 and the bending resistance modulus is $I = 43034.2$ cm^4. We model a part of the frame member of length $L^{ref} = 2L = 300$ cm, which is 7 times the height of the section. This length should be sufficient to capture the local softening effects due to local buckling and/or strain softening. The frame member is made of an elastoplastic material (steel), whose uniaxial response is plotted in Fig. 6.5. Young's modulus is $E = 21000$ kN/cm^2, yield stress is $\sigma_y = 24$ kN/cm^2, ultimate stress is $\sigma_u = 36$ kN/cm^2, yield strain is $\varepsilon_y = \sigma_y/E$, strain at ultimate stress is $\varepsilon_u = 0.1$ and strain at failure is $\varepsilon_f = 0.12778$.

The example has been computed with the finite element code ABAQUS [Hobbit et al., 2007] by using shell finite element S4R with 5 integration points through the thickness. Only one half of the considered geometry was discretized, see Figs. 6.6 and 6.7. The symmetry conditions $u_z = \varphi_x = \varphi_y = 0$ were used in the symmetry plane. The mesh consists of equal squared elements. The free-end cross-section of the model was made rigid by coupling the degrees of freedom of that cross-section.

The plasticity models with strain softening are mesh-dependent. In order to minimize that effect, we have adjusted the post peak uniaxial stress-strain relation to fit the mesh size, as suggested in [Ibrahimbegovic, 2009]. According to [Ibrahimbegovic, 2009] the linear softening modulus is computed as

$$K_s^{l_e} = -\frac{l_e \sigma_u^2}{2 g_s}, \tag{6.85}$$

where l_e is a characteristic dimension of the element (in the present case $l_e = 5$ cm is the side-length of the elements) and g_s is the plastic work density (plastic work per unit volume) in the softening regime of the shell material that corresponds to the gray-colored area in Figure 6.5 (in the present case $g_s = 0.5$ kN/cm^2). The strain at failure, adjusted to the mesh, is then

$$\varepsilon_f^{l_e} = \varepsilon_u + \frac{\sigma_u}{\frac{E K_s^{l_e}}{E + K_s^{l_e}}} = 0.10727. \tag{6.86}$$

The load was applied in two steps. In the first step we applied a desired level of axial force N at the mid-point MP of the rigid cross-section, see Fig. 6.6. In the second step we applied bending moment M at the point MP and performed nonlinear analysis with the path-following method. Several analyses were carried out with different values

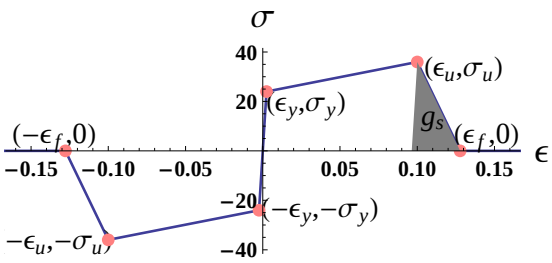

Figure 6.5: Uniaxial stress - strain curve

Slika 6.5: Enoosna krivulja napetost - deformacija

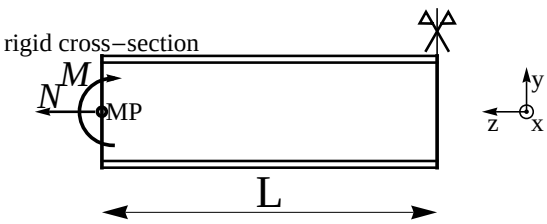

Figure 6.6: Boundary conditions for the shell model analysis

Slika 6.6: Robni pogoji pri analizi s končnimi elementi za lupine

of the axial force (from $N = -0.3N_y$ to $N = 0.3N_y$, where $N_y = A\sigma_y$). For each case we monitored the response until the bending resistance dropped to zero (or the analysis ran into convergence problems).

The results of analyses are presented in Figs. 6.7 to 6.9. Final deformed configuration of the shell model and distribution of the equivalent plastic strain are presented in Fig. 6.7 for pure bending case ($N = 0$). We can see that the considered part of the frame member failed by localized buckling of the bottom flange. We also note strong localized yielding of the flange which is concentrated in the neighborhood of the web. Such failure mode was observed also for all other cases. In Figure 6.8, we show the corresponding moment-rotation curves. We can see that the level of axial force has a significant influence on the peak bending resistance and on the overall response. In Figure 6.9 we present the plastic work versus rotation curves. Here, the value of the axial force does not influence much the shape of the curve. The relation between rotation and plastic work is almost linear. In figures 6.8 and 6.9, we marked the points with the maximum bending moment. We assume that those points separate hardening regime from softening regime.

The obtained results by the shell model are now used for evaluation of the beam model material parameters. In Table 6.1 we summarized the following shell model results: the

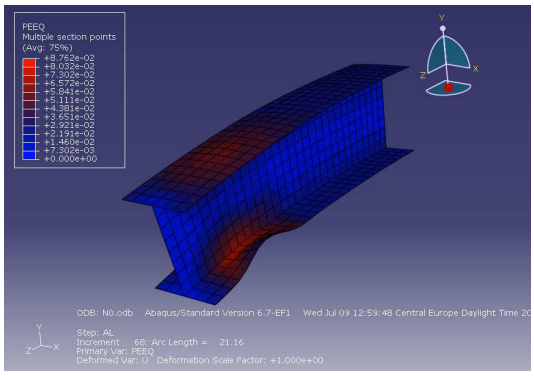

Figure 6.7: Failure mode of the representative part of the frame member as computed by the shell model

Slika 6.7: Porušitev dela nosilca pri simulaciji s končnimi elementi za lupine

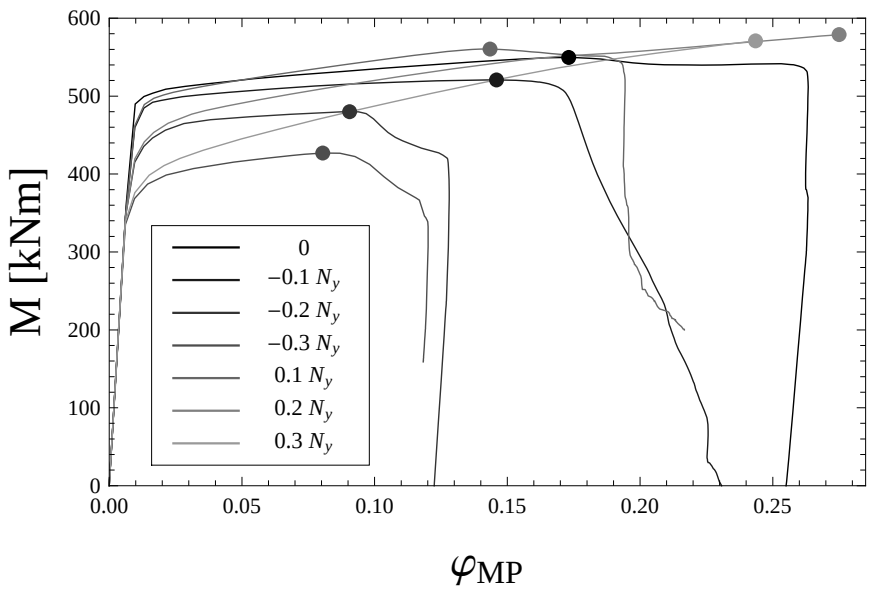

Figure 6.8: Bending moment versus rotation curves for the end cross-section

Slika 6.8: Krivulje moment - rotacija za prerez na koncu nosilca

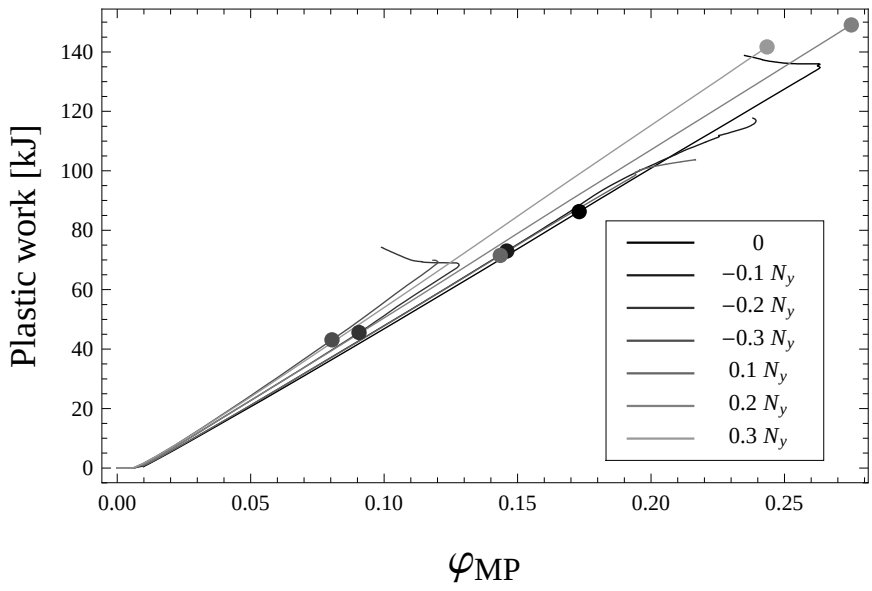

Figure 6.9: Plastic work versus end cross-section rotation curves

Slika 6.9: Krivulje plastično delo - rotacija na koncu nosilca

maximum bending moment M_u^{ref}, the plastic work in hardening regime $E^{\overline{W}^{p,ref}}$, and the plastic work in softening regime $E^{\overline{\overline{W}}^{p,ref}}$ for different values of axial force N. We can see that M_u^{ref} decreases if N is compressive, whereas the tensile axial force has only slight effect on M_u^{ref}.

N/N_y	$M_u^{ref.}$ [kNm]	$E^{\overline{W}^{p,ref.}}$ [kJ]	$E^{\overline{\overline{W}}^{p,ref.}}$ [kJ]
0	550	86	53
-0.1	521	73	45
-0.2	480	46	29
-0.3	427	43	27
0.1	560	72	32
0.2	579	149	0
0.3	571	142	0

Table 6.1: Summary of results of the shell model analyses

Tabela 6.1: Povzetek rezultatov analize s končnimi elementi za lupine

By using Table 6.1, we determined a bilinear approximation function for M_u^{ref} as

$$\widetilde{M}_u^{ref}(N) = \begin{cases} M_u^{ref,0}(1.03 + 0.85\frac{N}{N_y}) & \text{if } N < -0.035N_y \\ M_u^{ref,0} & \text{if } N \geq -0.035N_y \end{cases}, \tag{6.87}$$

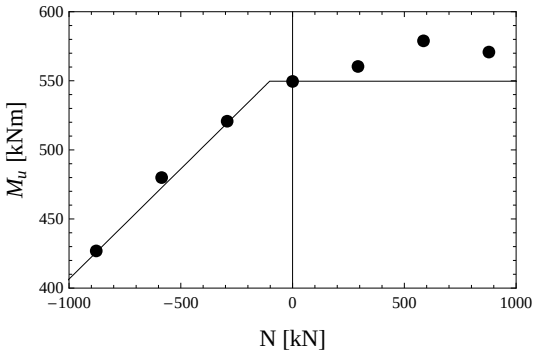

Figure 6.10: Approximation of the ultimate bending moment of the cross-section

Slika 6.10: Aproksimacija mejnega upogibnega momenta prereza

where $M_u^{ref,0} = M_u^{ref}(N = 0)$. We assume that $\widetilde{M}_u^{ref}(N)$ can be used to evaluate the ultimate bending moment of the beam model M_u, i.e.

$$M_u\,(N) = \widetilde{M}_u^{ref}(N), \tag{6.88}$$

see Fig. 6.10. The values for the ultimate resistance obtained with the shell analyses are marked with dots in Fig. 6.10.

The beam model hardening modulus K_h can be evaluated point-wise by using (6.60), (6.55), (6.88) and third column of Table 6.1. We get K_h ranging from $6.26 \cdot 10^6$ kN/cm^2 to $1.35 \cdot 10^7$ kN/cm^2 with an average value of $1.06 \cdot 10^7$ kN/cm^2. Although one could easily find a higher-order function that fits these results, we assume for simplicity that the axial force has no influence on the hardening modulus and adopt

$$K_h(N) = 1.06 \cdot 10^7 \text{ kN/cm}^2. \tag{6.89}$$

The beam model softening modulus K_s can be evaluated point-wise by using (6.63), (6.88) and the last column of Table 6.1. The gray-colored fields in Table 6.1 present unreliable results for $E^{\overline{\overline{W}}^{p,ref}}$, since for those cases the shell analysis did not converge. Softening modulus for the first three analyses ranges from $-2.85 \cdot 10^5$ kN/cm^2 to $-3.97 \cdot 10^5$ kN/cm^2. We assume that the axial force has no influence on softening modulus and adopt the average value

$$K_s(N) = -3.28 \cdot 10^5 \text{ kN/cm}^2. \tag{6.90}$$

In Table 6.2 we make a point-wise comparison between the shell analysis results M_u^{ref}, $E^{\overline{W}^{p,ref}}$ and $E^{\overline{\overline{W}}^{p,ref}}$ and the corresponding beam model results M_u, $E^{\overline{W}^p}$ and $E^{\overline{\overline{W}}^p}$, computed by using approximations (6.88), (6.89), (6.90) and expressions (6.58), (6.61) and

(6.53). We can see that the error in ultimate bending moment is small, while the error in dissipated plastic work can be quite large.

N/N_y	M_u [kNm]	$\lvert\frac{M_u-M_u^{ref.}}{M_u^{ref.}}\rvert$ [%]	$E^{\overline{W}^p}$ [kJ]	$\lvert\frac{E^{\overline{W}^p}-E^{\overline{W}^{p,ref.}}}{E^{\overline{W}^{p,ref.}}}\rvert$ [%]	$E^{\overline{\overline{W}}^p}$ [kJ]	$\lvert\frac{E^{\overline{\overline{W}}^p}-E^{\overline{\overline{W}}^{p,ref.}}}{E^{\overline{\overline{W}}^{p,ref.}}}\rvert$ [%]
0	550	0.00	50	42	46	12
−0.1	519	0.26	59	20	41	8
−0.2	473	1.54	54	17	34	19
−0.3	426	0.22	48	12	28	?
0.1	550	1.94	81	14	46	?
0.2	550	5.07	109	27	46	?
0.3	550	3.72	134	6	46	?

Table 6.2: Comparison between approximations and shell analyses results

Tabela 6.2: Primerjava med aproksimacijami in rezultati analiz z uporabo končnih elementov za lupine

6.5.2 Push-over of a symmetric frame

In this example we present a push-over analysis of a symmetric frame. The geometry is given in Fig. 6.11, where $L_B = 500$ and $H_C = 250$ cm. The material and cross-section properties of all frame members are equal. They are the same as those presented in Section 5.1. The vertical load is constant and equals $q_v = 0.05$ kN/cm. The lateral loading is presented in Figure 6.11, where $F_0 = 1$ kN is a concentrated force and λ is load multiplier. The mesh consists of eight beam finite elements per each frame member.

We performed two analyses, one by using the geometrically linear and the other by using the geometrically nonlinear beam finite elements. The results are presented in Figures 6.12 and 6.13, where u_{top} is horizontal displacement of the top right corner of the frame. In the left part of the Fig. 6.12 we present the total lateral load versus u_{top} curves. The points on those curves mark configurations where the softening hinge was activated in one of the elements of the mesh. We can see that, even though some parts of the frame are failing, the total resistance of the structure is still growing until the maximum load is reached at 1527.3 kN for geometrically linear case, and at 1522.3 kN for geometrically nonlinear case.

In the right part of Fig. 6.12 we present the plastic work versus u_{top} displacement curves. The results of the geometrically linear and the geometrically nonlinear elements are completely the same. At the beginning of the analysis there is no energy dissipation since the material response is elastic. The non-dissipative period is followed by a short period with dissipation due to material hardening only, which ends with the first activation

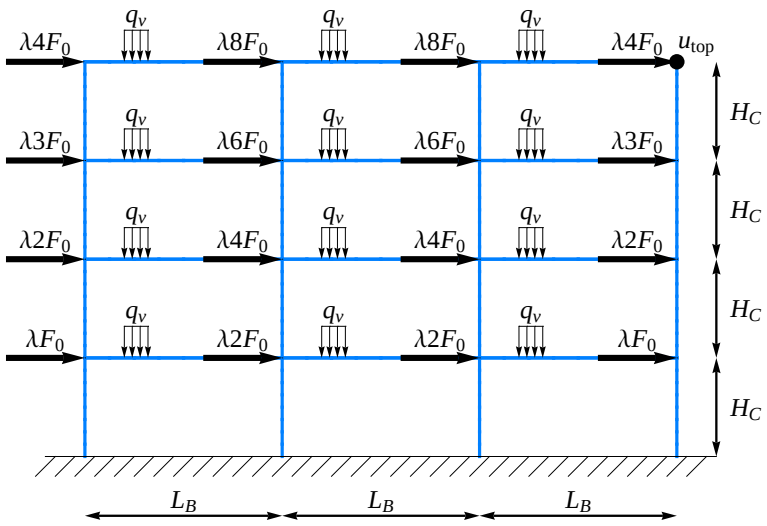

Figure 6.11: Symmetric frame: geometry and loading

Slika 6.11: Simetrični okvir: geometrija in obtežba

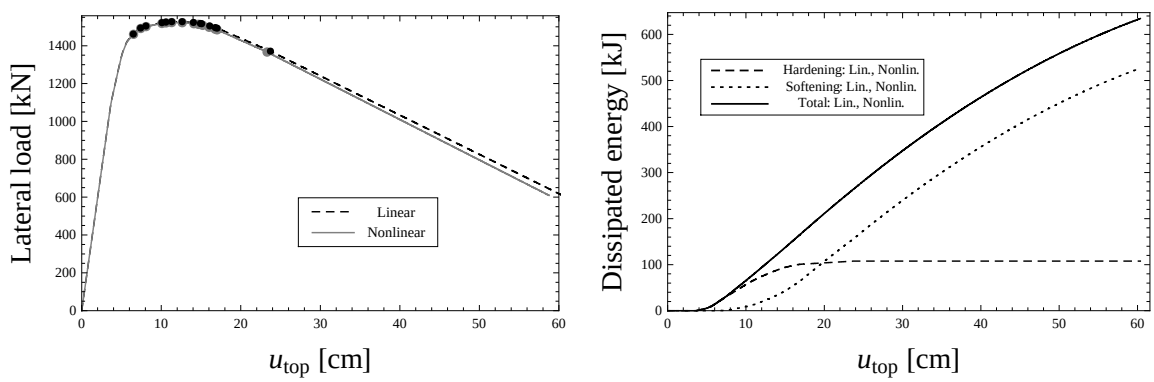

Figure 6.12: Load versus displacement and dissipated energy versus displacement curves for symmetric frame

Slika 6.12: Krivulje obtežba - pomik in disipirana energija - pomik pri simetričnem okvirju

of softening plastic hinge in one of the beam finite elements. For a while we have a combined hardening and softening energy dissipation, which is finally followed by a period when the structure is dissipating energy only due to softening. On the left part of Fig.

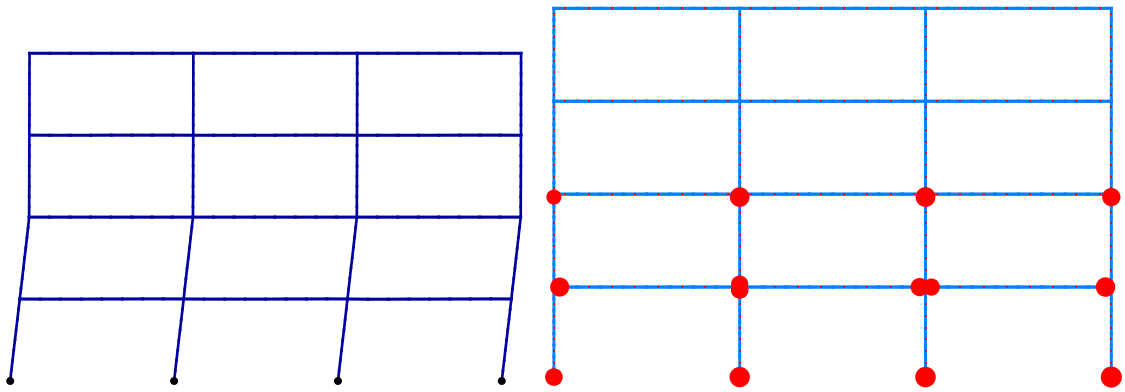

Figure 6.13: Symmetric frame: deformed shape and locations of softening plastic hinges at $u_{top} \approx 60$ cm

Slika 6.13: Simetričen okvir: deformirana lega in mesta plastičnih členkov pri pomiku gornje eteže $u_{top} \approx 60$ cm

6.13 we present the final deformed configuration of the frame. In the right part of Fig. 6.13 we present locations where the softening plastic hinges appeared during the analysis.

6.5.3 Push-over of an asymmetric frame

In this example we analyze an asymmetric frame presented in Fig. 6.14, where $L_{B1} = 600$ cm, $L_{B2} = 500$ cm, $L_{B3} = 400$ cm and $H_C = 250$ cm. All the other geometrical, material and loading parameters are the same as in the previous example.

The results are presented in Figs. 6.15 to 6.16. The total lateral load versus u_{top} curves, where u_{top} is horizontal displacement at the top-left corner of the frame, are presented on the left part of Fig. 6.15. The results of geometrically linear and geometrically nonlinear analyses are nearly the same before the ultimate resistance is reached at 1581.8 kN for geometrically linear case and at 1578.4 kN for geometrically nonlinear case. After that point the difference between those two analyses is bigger. The final computed equilibrium configuration for the geometrically nonlinear case is at $u_{top} = 26.52$ cm. In the next load step one additional softening plastic hinge is activated, which results in the global failure mechanism. Since our path-following algorithm is only governed by the the increase of u_{top}, we are unable to capture the remaining part of the load-displacement curve.

In the right part of Fig. 6.15 we present the dissipated energy versus u_{top} curves. The shapes of the curves are very similar to those from the symmetric frame case. Namely, first

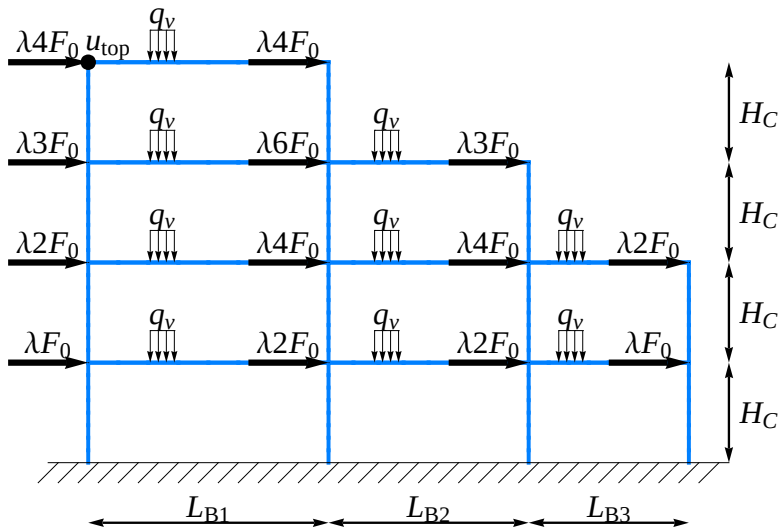

Figure 6.14: Asymmetric frame: geometry and loading

Slika 6.14: Nesimetrični okvir: geometrija in obtežba

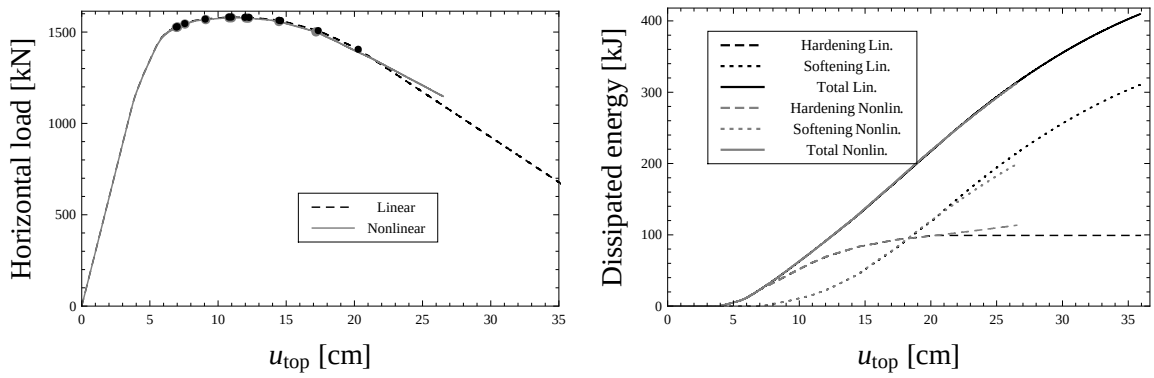

Figure 6.15: Load versus displacement and dissipated energy versus displacement curves for asymmetric frame

Slika 6.15: Krivulje obtežba - pomik in disipirana energija - pomik pri nesimetričnem okvirju

there is the elastic non-dissipative phase, followed by the pure hardening dissipation phase, followed by the combined hardening and softening dissipation phase and finally the pure softening dissipation phase. In the geometrically nonlinear case we do not have the final pure softening dissipation phase due to activation of global failure mechanism. On the left part of Fig. 6.16 we present the deformed configuration of the frame at $u_{top} = 26.52$ cm. Locations, where softening plastic hinges were activated at $u_{top} \approx 26.52$ cm, are presented in the middle part of Fig. 6.16 for the geometrically linear case and in the right part of the same figure for the geometrically nonlinear case.

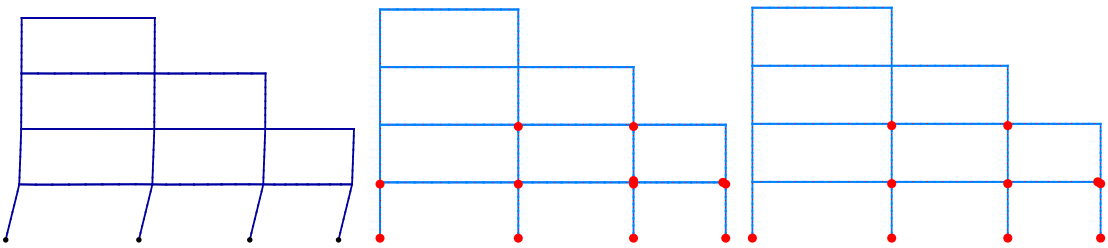

Figure 6.16: Asymmetric frame: Deformed shape and locations of softening plastic hinges

Slika 6.16: Nesimetričen okvir: deformirana lega in mesta plastičnih členkov

6.5.4 Bending of beam under constant axial force

In this example we compare results of the beam model with results obtained by using the shell finite element model from ABAQUS. For the comparison we choose the problem of the bending of the beam of length L^{ref} under a constant axial force, presented in Section 5.1. For that reason, the geometric and material properties are the same as those in the Section 5.1. The beam model analyses are performed with two sets of material parameters, where the first set (SET1) is given by (6.88) to (6.90). In the second set (SET2) we replace the expression (6.88) with

$$M_u^* = M_u^{(6.88)} - N\,|\Delta u_y|\,, \tag{6.91}$$

where M_u is the maximum concentrated moment applied at the end cross-section (point MP, see Fig. 6.6), N is the applied axial force (positive when producing tension) and Δu_y is the relative displacement in the y direction between the point MP and the position of the local failure. The difference between the applied concentrated moment at the point MP (see Fig. 6.6) and M_u^* thus arises due to large displacements correction. When the yielding and local buckling of the beam are significant and the displacements in the y direction are no longer negligible, the contribution of the axial force N to the bending

moment must be taken into account. In this particular case we have $N = -0.1Ny$, $M_u = 521$ kNm and $\Delta u_y = 0.15$ m, which leads to $M_u^* = 565$ kNm.

Five beam finite elements are used to model one-half of the beam under consideration, since the symmetry is taken into account. The symmetry conditions at the symmetry plane are $u = w = w' = 0$. The load was applied in two steps. In the first step the beam was loaded with compressive axial force $N = -0.1N_y$. In the second step the moment M was applied at the free-end of the beam. In order to ensure the proper activation of softening in the geometrically linear analyses the ultimate bending moment of the finite element near the symmetry plane was slightly weakened.

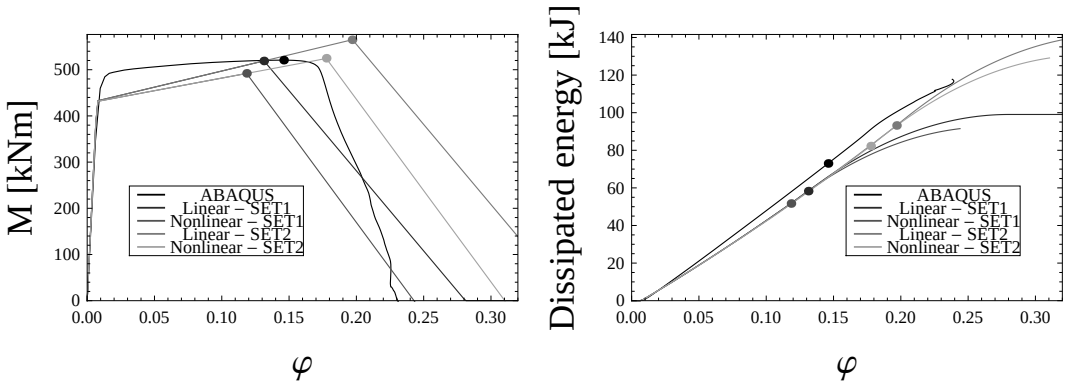

Figure 6.17: Comparison of results for the bending of the beam under compressive axial force

Slika 6.17: Primerjava rezultatov pri upogibu nosilca pod vplivom tlačne osne sile

In Fig. 6.17 the results for geometrically linear and geometrically nonlinear cases are compared with the results of the shell model from ABAQUS. On the left part of Fig. 6.17 we present curves relating applied moment to free-end rotation. The ultimate bending moments of the shell model, the geometrically linear SET1 beam model and the geometrically nonlinear SET2 beam model are very close, whereas the geometrically linear SET2 beam model gives slightly bigger and the geometrically nonlinear SET1 beam model gives slightly lower value for ultimate bending moment.

On the right part of Figure 6.17 we present the plastic work versus rotation of the end cross-section curves. There is hardly any difference between the beam model results when φ is smaller than 0.15. After that point the difference becomes bigger. The prediction of the beam model for plastic work in hardening regime is in the case of geometrically

linear analysis with SET1 material parameters 80% of the shell model prediction, and the prediction for plastic work in softening regime is 92% of the shell model prediction. This is in agreement with the results of Table 6.2. The predictions for plastic work of other beam analyses give bigger differences compared to the shell model. We note that one could get better agreements in plastic work by using better approximations for hardening and softening moduli in place of simplifications (6.89) and (6.90).

6.5.5 Collapse of a simple frame

In this example we compare results of the nonlinear beam model with the results of the shell model. We consider a simple frame presented in Fig. 6.18. The geometry of the beam model (middle axes of the beam model correspond to the middle axes of the shell model) is presented on the left part of Fig. 6.18. The geometry and the finite element mesh of the shell model is presented on the right side of Fig. 6.18. The cross-section and the material properties of the shell model are the same as those in the section 5.1. In the shell model we made connections between the beam and the columns rigid by coupling the degrees of freedom of the corresponding end cross-sections. The beam model mesh consists of eight finite elements per each frame member. Two different sets of material parameters are used for the beam model analysis. The first set (SET1) is given by (6.55) and (6.88) to (6.90) and the second set (SET2) by

$$M_y = 1.2M_y^{(6.55)}, \quad M_u = 1.2M_u^{(6.88)}, \quad K_h = 0.6K_h^{(6.89)}, \quad K_s = K_s^{(6.90)}. \tag{6.92}$$

Support conditions are ($u = w = w' = 0$ for the beam model and $u_x = u_y = u_z = \varphi_x = \varphi_y = \varphi_z = 0$ for the shell model).

The load applied to the frame is presented in Fig. 6.18. The vertical load is constant and equal to $Q = 500$ kN, while the horizontal load multiplier λ ($F_0 = 1$ kN) is controlled with the path-following method.

The results are presented in Figs. 6.19 to 6.21. The total lateral load versus u_{top} curves (u_{top} is horizontal displacement of the top-right corner of the frame) are presented on the left part of Fig. 6.19. The dissipated energy versus u_{top} curves are presented on the right part of Fig. 6.19. On the left part of Fig. 6.20 we present the equivalent plastic deformation on the deformed configuration of the shell model. The deformed configuration of the beam model, along with positions where the softening response was activated, is presented on the right part of Fig. 6.20. Note, that in both models the localized failure appears at the ends of the columns. In Fig. 6.21 we present the internal forces at the right support of the shell model. Note that the axial force is not constant at the beginning of the loading, but once the response becomes nonlinear it hardly changes.

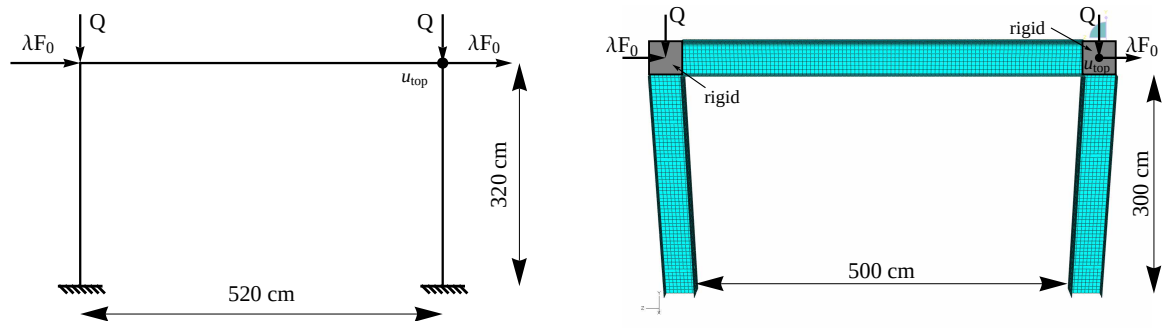

Figure 6.18: Simple frame: the beam and the shell model

Slika 6.18: Preprost okvir: računski model z elementi za nosilce in računski model z elementi za lupine

The lateral load versus u_{top} curve (left part of Fig. 6.19) of the beam model with SET1 material parameters has a similar shape as the shell model curve, but the prediction of the maximum resistance of the beam model is around 84% of the shell model's resistance. We have a similar situation as in the previous example, where the resistance of the cross-section was greater than the one obtained by analysis in Section 5.1. On the bottom-right part of Fig. 6.21 one can see that the axial force that corresponds to the maximum bending moment $M_{max} = 523$ kNm is around $N(M_{max}) = -720$ kN $\approx -0.25N_y$. If we compare M_{max} to $M_u(-0.2Ny) = 473$ kNm from Table 6.2, we can see that we have more than 10% bigger bending resistance. One must also consider that plasticity (hardening and softening) in the beam model is triggered at positions where we have rigid connections in the shell model, which also decreases the resistance of the beam model compared to the shell model.

The dissipated energy versus u_{top} curve (right part of Fig. 6.19) of the beam model with SET1 material parameters has a similar shape to the shell model's curve. The prediction of the SET1 beam model for the value of the dissipated energy that corresponds to $u_{top} = 20$ cm is around 71% of the shell model prediction.

These results are significantly improved, and we obtain much better fit to the shell model, when SET2 beam parameters are used; see Fig. 6.19. We recall that the latter accounts for the large displacement correction of ultimate resistance.

6.5.6 Darvall-Mendis frame

We consider the clamped portal frame under vertical loading first studied by [Darvall and Mendis, 1985] and later examined by [Armero and Ehrlich, 2006b] and [Wackerfuss,

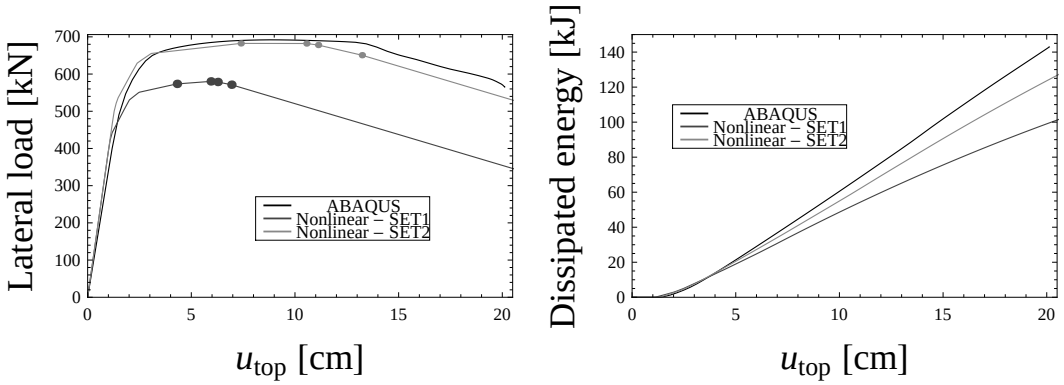

Figure 6.19: Comparison of results for simple frame example

Slika 6.19: Primerjava rezultatov pri preprostem okvirju

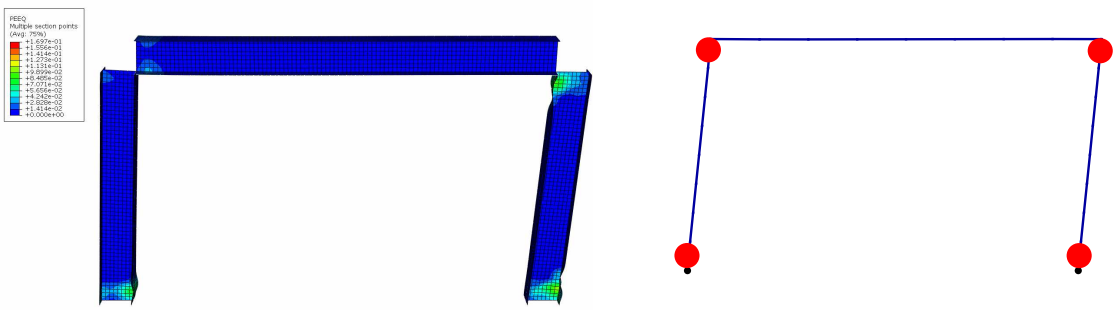

Figure 6.20: Deformed shapes of the simple frame

Slika 6.20: Deformirani legi preprostega okvirja

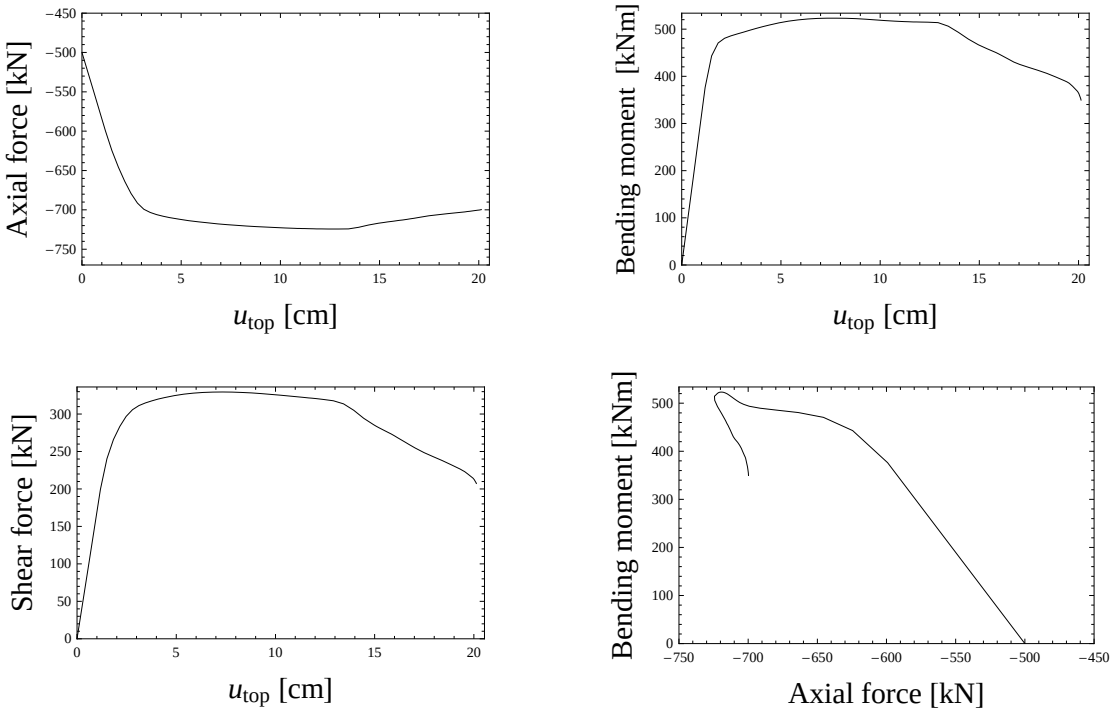

Figure 6.21: Internal forces at the right support of the shell model

Slika 6.21: Notranje sile pri desni podpori pri analizi z elementi za lupine

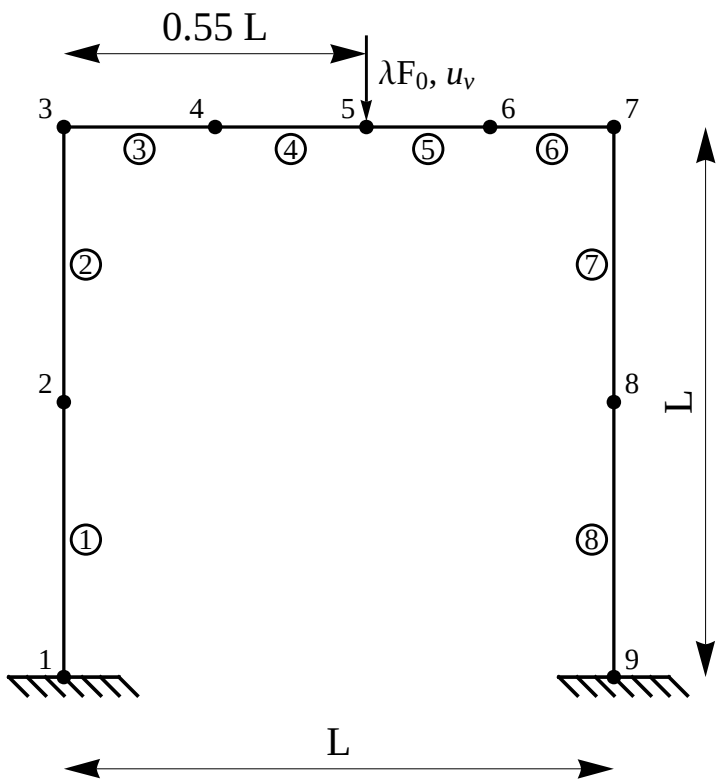

Figure 6.22: Geometry and loading of the portal frame.

Slika 6.22: Geometrija in obtežba portalnega okvirja

2008]. The geometry of the frame is presented in Figure 6.22. The length of the columns and the beam is $L = 3.048$ m, cross-section area of all the members is $A = 0.103$ m^2 and their moment of inertia is $I = 0.001$ m^4. The elastic material response is defined by the Young's modulus $E = 2.068 \times 10^7$ kN/m^2. The inelastic response is defined by the ultimate bending moment $M_{u,C} = 158.18$ kNm for the columns, the ultimate bending moment $M_{u,B} = 169.48$ kNm for the beam, and the softening modulus $K_s = \frac{aEI}{10L}$, where the values $a = 0$, -0.04, -0.06, -0.0718 are considered. Note, that in this example the inelastic response does not include any material hardening. We also consider that the axial force has no influence on the ultimate bending resistance of the frame members. The mesh consists of eight geometrically linear beam finite elements, see Figure 6.22. The frame is loaded with a vertical load λF_0 ($F_0 = 1$ kN) applied at the node 5, see Figure 6.22. In the numerical simulations we control the load multiplier λ and the vertical displacement u_v at the node 5 by the path-following method.

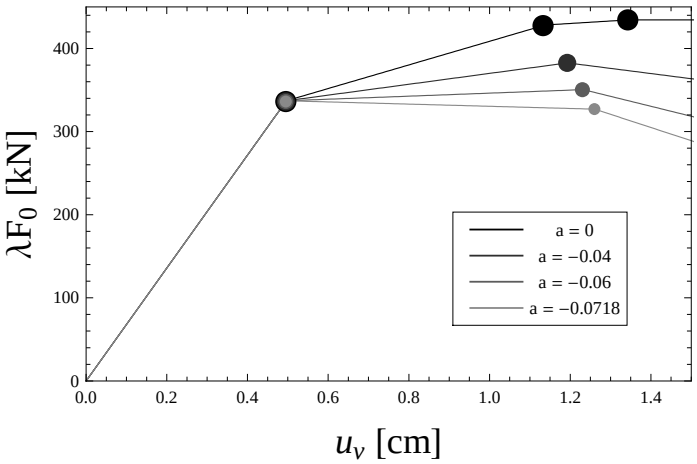

Figure 6.23: Vertical load versus vertical deflection curves

Slika 6.23: Krivulje vertikalna obtežba - vertikalni pomik

The vertical load versus vertical deflection curves are presented in Figure 6.23, where the points on the curves mark configurations where the softening plastic hinge was activated in one of the elements of the mesh. In all cases hinges form at the same locations. The first hinge forms in elements 4 and 5 at node 5, the second hinge forms in element 7 at node 7 and the third hinge forms in element 2 at node 3. This example shows the significant influence of the softening modulus on the ultimate load of the structure. The ultimate load in the case of perfectly plastic response of the hinges ($a = 0$) is 434 kN when the third hinge forms. In cases $a = -0.04$ and $a = -0.06$ the structure fails when the

second hinge forms when the vertical load reaches 383 kN and 350 kN, respectively. In the case of $a = -0.0718$ the structure fails when the first hinge forms at 336 kN. In Table 6.3 we compare our results with the results obtained by [Darvall and Mendis, 1985], [Armero and Ehrlich, 2006b] and [Wackerfuss, 2008].

		[Darvall and Mendis, 1985]		[Armero and Ehrlich, 2006b]		[Wackerfuss, 2008]		Present	
a	Hinge	u_v [cm]	λF_0 [kN]	u_v [cm]	λF_0 [kN]	u_v [cm]	λF_0 [kN]	u_v [cm]	λF_0 [kN]
0	1	0.50	336	0.50	337	0.53	342	0.50	336
	2	1.14	427	1.14	428	1.13	435	1.13	427
	3	1.34	433	1.34	434	1.33	440	1.34	434
-0.04	1	0.50	336	0.50	337	0.53	349	0.50	336
	2	1.14	387	1.18	388	1.16	401	1.19	383
-0.06	1	0.50	336	0.50	337	0.52	348	0.50	336
	2	1.19	336	1.29	337	1.23	349	1.23	350
-0.0718	1	0.50	336	0.50	337			0.50	336

Table 6.3: Comparison of the presented formulation with the literature

Tabela 6.3: Primerjava rezultatov, dobljenih s predstavljeno formulacijo, z rezultati iz literature

6.6 Concluding remarks and chapter summary

In this chapter we presented the multi-scale model for computing the limit load of planar metal frames under the push-over and the full collapse analysis. This approach combines the best of two worlds: on one side the effectiveness and robustness of the macro-scale beam model for the entire structure, and on another side, a refined representation of localized instability effects (both geometric and material) by meso-scale effects based upon the geometrically nonlinear elastoplastic shell formulation. The latter is captured and stored within the macro-scale beam model in the manner which is compatible with enhanced beam kinematics with embedded discontinuity. With the introduction of additional parameters related to plastic hinge into the Euler-Bernoulli kinematics we obtained the equation for the enriched strain field

$$\boldsymbol{\epsilon} = \overline{\boldsymbol{\epsilon}} + \overline{\overline{\boldsymbol{\epsilon}}},\ \overline{\boldsymbol{\epsilon}} = \boldsymbol{B}\boldsymbol{d} + \boldsymbol{G}\boldsymbol{\alpha},\ \overline{\overline{\boldsymbol{\epsilon}}} = \delta_{x_d}\boldsymbol{\alpha},$$

where the strain operator related to additional parameters is obtained by enforcing the strain free mode of the beam element and is finally computed as

$$\boldsymbol{G} = -\boldsymbol{B}\boldsymbol{D}_{hinge}.$$

In order to account for the geometrically nonlinear effects, and related global buckling, we used the von Karman axial strain when computing the virtual axial strain

$$\begin{bmatrix} \delta\overline{\varepsilon} = \delta\overline{\varepsilon}^{VK} \\ \delta\overline{\kappa} \end{bmatrix} = \underbrace{\begin{bmatrix} \boldsymbol{B}^{u} & \boldsymbol{B}^{u,w} & \boldsymbol{B}^{u,w'} \\ \boldsymbol{0} & \boldsymbol{B}^{w} & \boldsymbol{B}^{w'} \end{bmatrix}}_{\boldsymbol{B}^{VK}} \delta\boldsymbol{d} + \boldsymbol{G}\delta\boldsymbol{\alpha}.$$

We introduced the virtual strains into the principle of virtual work and obtained the virtual work of internal forces as

$$\delta\Pi^{int,(e)} = \underbrace{\int_0^{L^{(e)}} \delta\boldsymbol{d}^T \left(\boldsymbol{B}^{VK}\right)^T \boldsymbol{\sigma} dx}_{\text{standard}} + \underbrace{\int_0^{L^{(e)}} \delta\boldsymbol{\alpha}^T (\boldsymbol{G}^T\boldsymbol{\sigma} + \delta_{x_d}\boldsymbol{\sigma}) dx}_{\text{additional}},$$

and from the term "additional" we obtained two additional equations per finite element

$$h_N^{(e)} = \int_0^{L^{(e)}} G^u N dx + t_N = 0, \; h_M^{(e)} = \int_0^{L^{(e)}} G^\theta M dx + t_M = 0,$$

which ensure that axial traction and moment (bending) traction at the discontinuity are in equilibrium with the stress field in the element. The basic ingredients of the chosen constitutive relations for the bulk material and the discontinuity are the usual additive decomposition of regular strains into elastic and plastic part

$$\overline{\boldsymbol{\epsilon}} = \overline{\boldsymbol{\epsilon}}^e + \overline{\boldsymbol{\epsilon}}^p, \quad \overline{\boldsymbol{\epsilon}}^e = [\overline{\varepsilon}^e, \overline{\kappa}^e]^T, \quad \overline{\boldsymbol{\epsilon}}^p = [\overline{\varepsilon}^p, \overline{\kappa}^p]^T,$$

limiting the plastic response to bending only

$$\varepsilon = \overline{\varepsilon} = \overline{\varepsilon}^e, \quad \overline{\overline{\varepsilon}} = 0 \quad \Longleftrightarrow \quad \overline{\varepsilon}^p = 0, \quad \alpha_u = 0,$$

the free energy of the bulk material considering isotropic hardening

$$\overline{\Psi}(\overline{\boldsymbol{\epsilon}}^e, \overline{\xi}) := \overline{W}\left(\overline{\boldsymbol{\epsilon}}^e\right) + \overline{\Xi}(\overline{\xi}) = \frac{1}{2}\overline{\boldsymbol{\epsilon}}^{eT}\boldsymbol{C}\overline{\boldsymbol{\epsilon}}^e + \frac{1}{2}K_h\overline{\xi}^2,$$

the yield criterion for the bulk material

$$\overline{\phi}(M, \overline{q}) = |M| - (M_y - \overline{q}) \leq 0,$$

the localization criterion

$$\overline{\overline{\phi}}(t_M, \overline{\overline{q}}) = |t_M| - (M_u - \overline{\overline{q}}) \leq 0,$$

and the softening potential

$$\overline{\overline{\Xi}}(\overline{\overline{\xi}}) = \frac{1}{2}K_s\overline{\overline{\xi}}^2.$$

The remaining ingredients of beam elastoplasticity were obtained by defining the plastic dissipation

$$\overline{D}^p = M\dot{\overline{\kappa}}^p + \overline{q}\dot{\overline{\xi}},$$

and by considering the principle of maximum plastic dissipation

$$\min_{M,\overline{q}} \max_{\dot{\overline{\gamma}}} \left[\overline{L}^p(M,\overline{q},\dot{\overline{\gamma}}) = -\overline{D}^p(M,\overline{q}) + \dot{\overline{\gamma}}\overline{\phi}(M,\overline{q})\right].$$

Similarly, we also defined the plastic dissipation at the discontinuity

$$\overline{\overline{D}} = \overline{\overline{D}}^p = t_M\dot{\alpha}_\theta + \overline{\overline{q}}\dot{\overline{\overline{\xi}}},$$

and considered the principle of maximum plastic dissipation

$$\min_{t_M,\overline{\overline{q}}} \max_{\dot{\overline{\overline{\gamma}}}} \left[\overline{\overline{L}}^p(t_M,\overline{\overline{q}},\dot{\overline{\overline{\gamma}}}) = -\overline{\overline{D}}^p(t_M,\overline{\overline{q}}) + \dot{\overline{\overline{\gamma}}}\overline{\overline{\phi}}(t_M,\overline{\overline{q}})\right],$$

which is here limited to discontinuity only. Next we elaborated on determination of the following four parameters: M_y, K_h, M_u and K_s, which determine the beam constitutive behavior. We associate the yield moment of the cross-section with the yielding of the most-stressed material fiber

$$M_y(N) = W\sigma_y(1 - \frac{|N|}{A\sigma_y}).$$

In order to obtain a good estimate for the remaining three parameters we consider modeling a part of a frame member by using a refined finite element model which was in the present work based on geometrically and materially nonlinear shell element. We associate the ultimate bending moment M_u of the beam model with the peak moment computed with the refined shell model

$$M_u(N) = M_u^{ref}(N).$$

We also used that point as a border-point between the hardening regime and the softening regime, where the softening can be due to material and/or geometric effects. To determine the values of the beam model hardening and softening parameters, we made an assumption that the plastic work at failure should be equal for both the beam and the shell model and since the plastic work is done in two regimes, i.e. hardening and softening, we had to assure that the amount of plastic work in each regime matches for both models

$$E^{\overline{W}^p}(N) = E^{\overline{W}^{p,ref}}(N), \quad E^{\overline{\overline{W}}^p}(N) = E^{\overline{\overline{W}}^{p,ref}}(N).$$

By assuming that each cross-section in the frame member of length L^{ref} is approximately under the same force-moment state during the hardening regime we obtained the following expression for hardening modulus

$$K_h(N) = \frac{(M_u^2(N) - M_y^2(N))L^{ref}}{2E^{\overline{W}^{p,ref}}(N)}.$$

Contraty, we assumed that all the softening effects are very local and limited to only one cross-section and the softening modulus is then

$$|K_s(N)| = \frac{M_u^2(N)}{2E^{\overline{\overline{W}}^{p,ref}}(N)}, \quad K_s \leq 0.$$

The computational procedure presented in Section 6.4 is split into the local and global phase. In the local phase we determine the updates for the hardening variables related to element integration points by solving the following equation

$$\overline{\phi}^{ip}(M_{n+1}^{ip}(\boldsymbol{d}_{n+1}^{(e),(i)}, \overline{\kappa}_{n+1}^{p,ip}(\overline{\gamma}_{n+1}^{ip})), \overline{q}(\overline{\xi}_{n+1}^{ip}(\overline{\gamma}_{n+1}^{ip}))) = \overline{\phi}^{ip}(\overline{\gamma}_{n+1}^{ip}) = 0.$$

The softening variables are determined by considering that the localization criterion is zero in the softening step

$$\overline{\overline{\phi}}^{(e)}(t_{M,n+1}^{(e)}(\alpha_{\theta,n+1}^{(e)}(\overline{\overline{\gamma}}_{n+1}^{(e)})), \overline{\overline{q}}(\overline{\overline{\xi}}_{n+1}^{(e)}(\overline{\overline{\gamma}}_{n+1}^{(e)}))) = \overline{\overline{\phi}}^{(e)}(\overline{\overline{\gamma}}_{n+1}^{(e)}) = 0,$$

where we explicitly use the additional equilibrium equation to compute the bending traction at the discontinuity

$$t_{M,n+1}^{(e)} = -\int_{\Omega^e} G^{\theta}(x_d^{(e)}, x) M(\boldsymbol{d}_{n+1}^{(e),(i)}, \overline{\kappa}_n^{p,ip}, \alpha_{\theta,n+1}^{(e)}) dx.$$

In the global phase, where the single element contribution to the system of global equations is

$$\begin{bmatrix} \boldsymbol{K}^{(e)} & \boldsymbol{K}^{f\alpha} \\ \boldsymbol{K}^{hd} & K^{h\alpha} \end{bmatrix}_{n+1}^{(i)} \begin{pmatrix} \Delta \boldsymbol{d}_{n+1}^{(e),(i)} \\ \Delta \alpha_{\theta,n+1}^{(e),(i)} \end{pmatrix} = \begin{pmatrix} \boldsymbol{f}_{n+1}^{ext,(e)} - \boldsymbol{f}_{n+1}^{int,(e),(i)} \\ 0 \end{pmatrix},$$

we determine the updates for the current iterative values of nodal displacements

$$\boldsymbol{d}_{n+1}^{(e),(i)} = \boldsymbol{d}_{n+1}^{(e),(i-1)} + \Delta \boldsymbol{d}_{n+1}^{(e),(i-1)}.$$

The static condensation allowed us to form the standard form of the element stiffness matrix

$$\widehat{\boldsymbol{K}}_{n+1}^{(e),(i)} = \boldsymbol{K}_{n+1}^{(e),(i)} - \boldsymbol{K}_{n+1}^{f\alpha,(i)} \left(K_{n+1}^{h\alpha,(i)}\right)^{-1} \boldsymbol{K}_{n+1}^{hd,(i)},$$

thus the global solution procedure is completely the same as in the standard finite element formulation. In the first numerical example in Section 6.5 we presented the shell model computation and by using its results we determined a bilinear approximation function for

$$M_u(N) = \widetilde{M}_u^{ref}(N) = \begin{cases} M_u^{ref,0}(1.03 + 0.85\frac{N}{N_y}) & \text{if } N < -0.035N_y \\ M_u^{ref,0} & \text{if } N \geq -0.035N_y \end{cases},$$

and we also assumed a constant values for hardening and softening modulus

$$K_h(N) = 1.06 \cdot 10^7 \text{ kN/cm}^2, \; K_s(N) = -3.28 \cdot 10^5 \text{ kN/cm}^2.$$

These values were used in the rest of numerical simulations.

The multi-scale procedure proposed in this chapter belongs to the class of weak coupling methods, where we carry out the sequential computations. The results of the shell model computations, accounting for material and geometric localized instability, are stored to be used within the beam model softening response. As presented by numerical simulations, performance of the proposed multi-scale computational approach is very satisfying. One of its main features is that detection and development of the softening plastic hinges in the frame is fully automatic, and spreads gradually in accordance with stress redistribution in the course of the nonlinear analysis. This is in contrast with many standard computational approaches to the limit load, under the push-over and the full collapse analysis of frames, which rely on predefined locations of plastic hinges and the corresponding inelastic deformations.

Chapter 7

Failure analysis of 2D solids

7.1 Introduction

In this chapter we present a quadrilateral two-dimensional elastoplastic finite element with embedded strong discontinuity. The effective locking-free design of quadrilateral finite element with embedded discontinuity is much more demanding, e.g. [Linder and Armero, 2007], [Manzoli and Shing, 2006], than that of the constant strain triangle. This might be one of the reasons that the constant strain triangle has been used in majority of works related to embedded discontinuity finite element modeling of failure in two-dimensional solids, e.g. [Sancho et al., 2007], [Ibrahimbegovic and Brancherie, 2003], [Brancherie and Ibrahimbegovic, 2008], [Mosler, 2005], [Jirasek and Zimmermann, 2001]. The derived quadrilateral element does not show any locking problems. Its kinematics can model linear jumps in both normal and tangential displacements along the discontinuity line.

We use the derived quadrilateral element to describe tensile fracture process in plain concrete two-dimensional solids and to model the crack growth. The same formulation is also suitable for failure analysis of ductile materials where localized shear bands form.

The outline of the chapter is as follows. In Section 7.2, we derive an elastoplastic quadrilateral two-dimensional finite element with embedded discontinuity. In Section 7.3 we present details of the computational procedure. Numerical examples are presented in Section 7.4 and concluding remarks and a short summary are given in Section 7.5.

7.2 Family of ED elements for planar problems

In this section we present a family of quadrilateral elements in the two-dimensional setting. The finite elements of this kind can represent the elasto-plastic response, including both hardening and the localized softening effects, the latter being associated with the strong discontinuity in displacements.

7.2.1 Kinematics

We consider a quadrilateral finite element occupying domain Ω^e (see Figure 7.1), divided with the discontinuity line Γ^e into two sub-domains, Ω^{e+} and Ω^{e-} ($\Omega^e = \Omega^{e+} \cup \Omega^{e-}$). Element's geometry is defined by the bilinear mapping $\boldsymbol{\xi} \mapsto \boldsymbol{x}^h$ ($\boldsymbol{\xi} \in [-1,1]\times[-1,1]$; $\boldsymbol{x}^h \in$

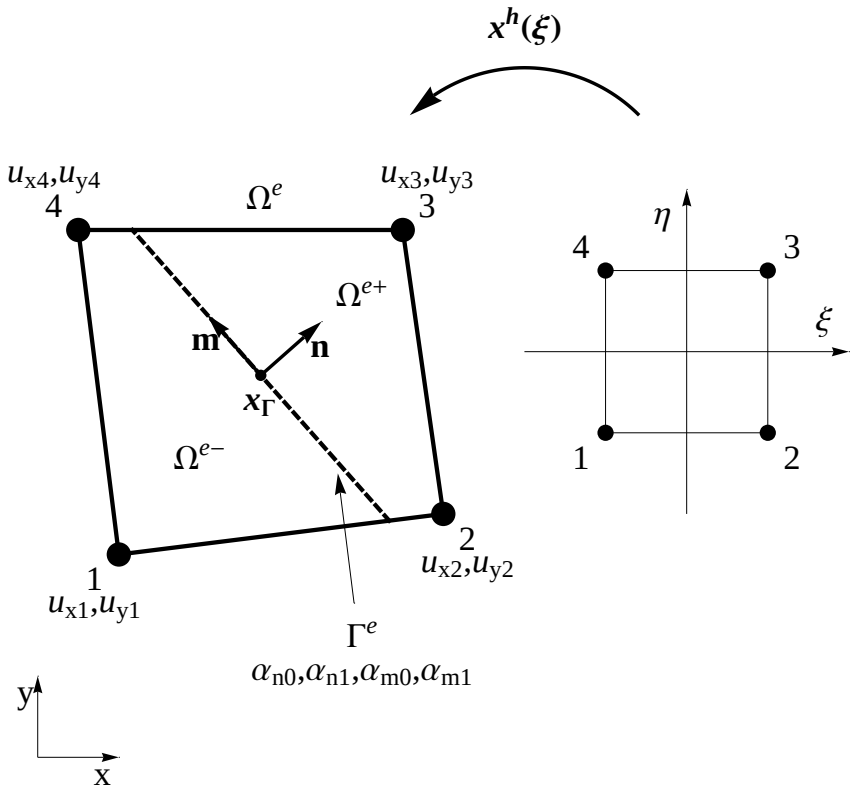

Figure 7.1: Quadrilateral finite element with embedded discontinuity

Slika 7.1: Štirivozliščni končni element z vgrajeno nezveznostjo

Ω^e) with

$$\boldsymbol{x}^h(\boldsymbol{\xi})\,|_{\Omega^e} = \sum_{a=1}^{4} N_a(\boldsymbol{\xi})\,\boldsymbol{x}_a, \qquad \boldsymbol{x}_a = [x_a, y_a]^T, \qquad \boldsymbol{\xi} = [\xi, \eta]^T, \tag{7.1}$$

where $\boldsymbol{x}_a$ are coordinates of the finite element node a and

$$N_a(\boldsymbol{\xi}) = \frac{1}{4}(1+\xi_a\xi)(1+\eta_a\eta), \qquad \begin{array}{cccc} a & 1 & 2 & 3 & 4 \\ \hline \xi_a & -1 & 1 & 1 & -1 \\ \hline \eta_a & -1 & -1 & 1 & 1 \end{array}. \tag{7.2}$$

The superscript h is used to denote the discrete approximation of different fields. In Figure 7.1, u_{xa} and u_{ya} are the nodal displacements in x and y direction of the node a. In addition to (standard) nodal degrees of freedom we use strong discontinuity interpolation parameters α_{n0} and α_{n1} for the normal direction and α_{m0} and α_{m1} for the tangential

direction, along with the unit normal vector $\boldsymbol{n}$ and the unit tangent vector $\boldsymbol{m}$ (see Figure 7.1). The mid-point of the discontinuity line is denoted with $\boldsymbol{x}_\Gamma$, see Figure 7.1. We assume that the domain of the discontinuity influence corresponds to a single element and write the displacement field as:

$$[u_x^h, u_y^h]^T = \boldsymbol{u}^h(\boldsymbol{\xi}, \Gamma^e) = \underbrace{\sum_{a=1}^{4} N_a(\boldsymbol{\xi})\boldsymbol{d}_a}_{\boldsymbol{u}_d^h} +$$
$$+ \underbrace{\boldsymbol{M}_{n0}(\boldsymbol{\xi}, \Gamma^e)\alpha_{n0} + \boldsymbol{M}_{n1}(\boldsymbol{\xi}, \Gamma^e)\alpha_{n1} + \boldsymbol{M}_{m0}(\boldsymbol{\xi}, \Gamma^e)\alpha_{m0} + \boldsymbol{M}_{m1}(\boldsymbol{\xi}, \Gamma^e)\alpha_{m1}}_{\boldsymbol{u}_\alpha^h}, \tag{7.3}$$

where $\boldsymbol{d}_a = [u_{xa}, u_{ya}]^T$ are the nodal values of $\boldsymbol{u}_d^h$, the part of the displacement field arising from standard isoparametric interpolation of nodal displacements. Similarly, $\boldsymbol{u}_\alpha^h$ is the part which arises with the introduction of strong discontinuity and $\boldsymbol{M}_{n0}(\boldsymbol{\xi}, \Gamma^e)$, $\boldsymbol{M}_{n1}(\boldsymbol{\xi}, \Gamma^e)$, $\boldsymbol{M}_{m0}(\boldsymbol{\xi}, \Gamma^e)$ and $\boldsymbol{M}_{m1}(\boldsymbol{\xi}, \Gamma^e)$ are the interpolation matrices related to discontinuity parameters that will be derived below. With four discontinuity parameters we model four modes of element separation along Γ^e (see Figure 7.2):

1. "n0" - the constant mode of separation in the normal direction,

2. "n1" - the linear mode of separation in the normal direction,

3. "m0" - the constant mode of separation in the tangential direction and

4. "m1" - the linear mode of separation in the tangential direction.

We investigate the motion of two rigid bodies, Ω^{e-} and Ω^{e+}, due to the particular separation mode(Figure 7.2). From (7.3) we can obtain the displacements for a mode, $mode \in (n0, n1, m0, m1)$,

$$\overline{\boldsymbol{u}}_{mode}^h = \overline{\boldsymbol{u}}_{d,mode}^h + \overline{\boldsymbol{u}}_{\alpha,mode}^h, \quad \overline{\boldsymbol{u}}_{\alpha,mode}^h = \boldsymbol{M}_{mode}\overline{\alpha}_{mode}. \tag{7.4}$$

From this equation we can then determine the interpolation matrix

$$\boldsymbol{M}_{mode} = \frac{\overline{\boldsymbol{u}}_{mode}^h - \overline{\boldsymbol{u}}_{d,mode}^h}{\overline{\alpha}_{mode}}. \tag{7.5}$$

By examining Figure 7.2 we can determine $\overline{u}_{mode}^h$ and $\overline{u}_{d,mode}^h$ for each mode. By using (7.5) we can then derive the interpolation matrices as follows:

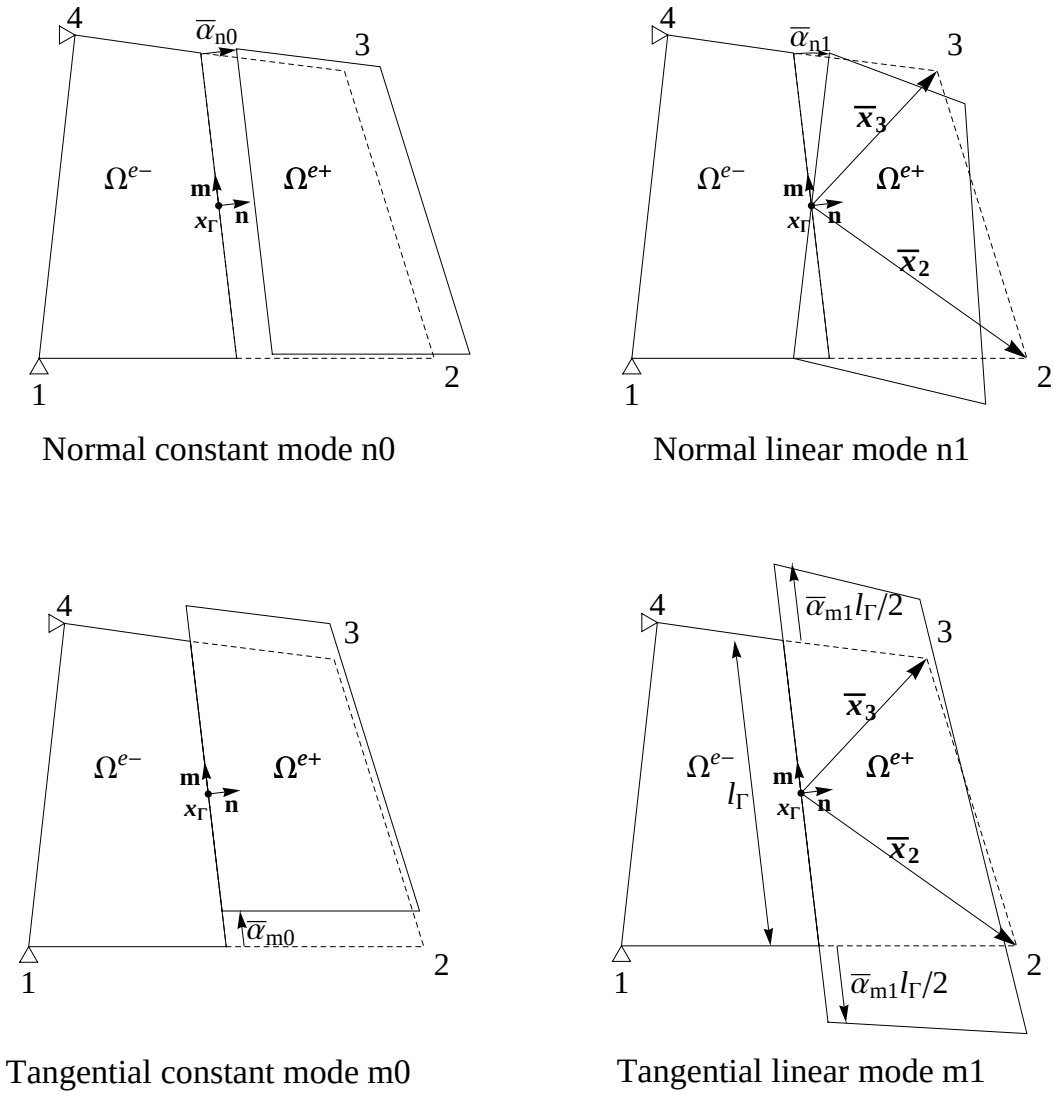

Figure 7.2: Different element separation modes

Slika 7.2: Različni načini ločevanja končnega elementa

- Constant normal separation mode - "$n0$"

$$\overline{\boldsymbol{d}}_{a,n0} = \begin{cases} \boldsymbol{n}\overline{\alpha}_{n0} & \text{for } a \in \Omega^{e+} \\ \boldsymbol{0} & \text{otherwise} \end{cases} \tag{7.6}$$

$$\overline{\boldsymbol{u}}^h_{n0} = H_\Gamma(\boldsymbol{x})\boldsymbol{n}\overline{\alpha}_{n0}\ ; \quad H_\Gamma(\boldsymbol{x}) = \begin{cases} 1 & \text{for } \boldsymbol{x} \in \Omega^{e+} \\ 0 & \text{otherwise} \end{cases} \tag{7.7}$$

$$\overline{\boldsymbol{u}}^h_{d,n0} = \sum_{a\in\Omega^{e+}} N_a \overline{\boldsymbol{d}}_{a,n0} \tag{7.8}$$

$$\boldsymbol{M}_{n0} = \frac{\overline{\boldsymbol{u}}^h_{n0} - \overline{\boldsymbol{u}}^h_{d,n0}}{\overline{\alpha}_{n0}} = \left(H_\Gamma(\boldsymbol{x}) - \sum_{a\in\Omega^{e+}} N_a \right) \boldsymbol{n} \tag{7.9}$$

- Linear normal separation mode - "$n1$"

$$\overline{\boldsymbol{d}}_{a,n1} = \begin{cases} \begin{bmatrix} 0 & 1 \\ -1 & 0 \end{bmatrix} \overline{\boldsymbol{x}}_a \overline{\alpha}_{n1} & \text{for } a \in \Omega^{e+} \\ \boldsymbol{0} & \text{otherwise} \end{cases} \tag{7.10}$$

$$\overline{\boldsymbol{u}}^h_{n1} = H_\Gamma(\boldsymbol{x}) \begin{bmatrix} 0 & 1 \\ -1 & 0 \end{bmatrix} \overline{\boldsymbol{x}}\overline{\alpha}_{n1} \tag{7.11}$$

$$\overline{\boldsymbol{u}}^h_{d,n1} = \sum_{a\in\Omega^{e+}} N_a \overline{\boldsymbol{d}}_{a,n1} \tag{7.12}$$

$$\boldsymbol{M}_{n1} = \frac{\overline{\boldsymbol{u}}^h_{n0} - \overline{\boldsymbol{u}}^h_{d,n0}}{\overline{\alpha}_{n0}} = H_\Gamma(\boldsymbol{x}) \begin{bmatrix} 0 & 1 \\ -1 & 0 \end{bmatrix} \overline{\boldsymbol{x}} - \sum_{a\in\Omega^{e+}} N_a \begin{bmatrix} 0 & 1 \\ -1 & 0 \end{bmatrix} \overline{\boldsymbol{x}}_a \tag{7.13}$$

- Constant tangential separation mode - "$m0$"

$$\overline{\boldsymbol{d}}_{a,m0} = \begin{cases} \boldsymbol{m}\overline{\alpha}_{m0} & \text{for } a \in \Omega^{e+} \\ \boldsymbol{0} & \text{otherwise} \end{cases} \tag{7.14}$$

$$\overline{\boldsymbol{u}}^h_{m0} = H_\Gamma(\boldsymbol{x})\boldsymbol{m}\overline{\alpha}_{m0} \tag{7.15}$$

$$\overline{\boldsymbol{u}}^h_{d,m0} = \sum_{a\in\Omega^{e+}} N_a \overline{\boldsymbol{d}}_{a,m0} \tag{7.16}$$

$$\boldsymbol{M}_{m0} = \frac{\overline{\boldsymbol{u}}^h_{m0} - \overline{\boldsymbol{u}}^h_{d,m0}}{\overline{\alpha}_{m0}} = \left(H_\Gamma(\boldsymbol{x}) - \sum_{a\in\Omega^{e+}} N_a \right) \boldsymbol{m} \tag{7.17}$$

- Linear tangential separation mode - "$m1$"

$$\overline{\boldsymbol{d}}_{a,m1} = \begin{cases} (\boldsymbol{m}\cdot\overline{\boldsymbol{x}}_a)\,\boldsymbol{m}\overline{\alpha}_{m1} & \text{for } a \in \Omega^{e+} \\ \boldsymbol{0} & \text{otherwise} \end{cases} \tag{7.18}$$

$$\overline{\boldsymbol{u}}^h_{m1} = H_\Gamma(\boldsymbol{x})\,(\boldsymbol{m}\cdot\overline{\boldsymbol{x}})\,\boldsymbol{m}\overline{\alpha}_{m1} \tag{7.19}$$

$$\overline{\boldsymbol{u}}^h_{d,m1} = \sum_{a\in\Omega^{e+}} N_a \overline{\boldsymbol{d}}_{a,m1} \tag{7.20}$$

$$\boldsymbol{M}_{m1} = \frac{\overline{\boldsymbol{u}}^h_{m1} - \overline{\boldsymbol{u}}^h_{d,m1}}{\overline{\alpha}_{m1}} = \left(H_\Gamma(\boldsymbol{x})\boldsymbol{m}\cdot\overline{\boldsymbol{x}} - \sum_{a\in\Omega^{e+}} N_a \boldsymbol{m}\cdot\overline{\boldsymbol{x}}_a \right) \boldsymbol{m} \tag{7.21}$$

Remark 7.1. *Motion of the Ω^{e+} region in the "m1" mode is not a rigid body motion but a stretch.*

Strains

We determine the strain field as the symmetric part of the gradient of the displacement field in (7.3) ($\boldsymbol{\epsilon} = \nabla^s \boldsymbol{u}^h = \frac{1}{2}[\nabla \boldsymbol{u}^h + (\nabla \boldsymbol{u}^h)^T]$) which can then be written in a vector form

$$\boldsymbol{\epsilon} = \left[\frac{\partial u_x^h}{\partial x}, \frac{\partial u_y^h}{\partial y}, \frac{\partial u_x^h}{\partial y} + \frac{\partial u_y^h}{\partial x}\right]^T \tag{7.22}$$

$$= \sum_{a=1}^{4} \boldsymbol{B}_a \boldsymbol{d}_a + \boldsymbol{G}_{n0}\alpha_{n0} + \boldsymbol{G}_{n1}\alpha_{n1} + \boldsymbol{G}_{m0}\alpha_{m0} + \boldsymbol{G}_{m1}\alpha_{m1}, \tag{7.23}$$

where

$$\boldsymbol{B}_a = \begin{bmatrix} \frac{\partial N_a}{\partial x} & 0 \\ 0 & \frac{\partial N_a}{\partial y} \\ \frac{\partial N_a}{\partial y} & \frac{\partial N_a}{\partial x} \end{bmatrix}, \boldsymbol{B}_n = \begin{bmatrix} n_x & 0 \\ 0 & n_y \\ n_y & n_x \end{bmatrix}, \boldsymbol{B}_m = \begin{bmatrix} m_x & 0 \\ 0 & m_y \\ m_y & m_x \end{bmatrix} \tag{7.24}$$

$$\boldsymbol{G}_{n0} = \underbrace{-\sum_{a\in\Omega^{e+}} \boldsymbol{B}_a \boldsymbol{n}}_{\overline{\boldsymbol{G}}_{n0}} + \underbrace{\delta_\Gamma \boldsymbol{B}_n \boldsymbol{n}}_{\overline{\overline{\boldsymbol{G}}}_{n0}}, \tag{7.25}$$

$$\boldsymbol{G}_{n1} = \underbrace{-\sum_{a\in\Omega^{e+}} \boldsymbol{B}_a \begin{bmatrix} 0 & 1 \\ -1 & 0 \end{bmatrix} \boldsymbol{x}_a}_{\overline{\boldsymbol{G}}_{n1}} + \underbrace{\delta_\Gamma \boldsymbol{B}_n \boldsymbol{n} \xi_\Gamma}_{\overline{\overline{\boldsymbol{G}}}_{n1}}, \tag{7.26}$$

$$\boldsymbol{G}_{m0} = \underbrace{-\sum_{a\in\Omega^{e+}} \boldsymbol{B}_a \boldsymbol{m}}_{\overline{\boldsymbol{G}}_{m0}} + \underbrace{\delta_\Gamma \boldsymbol{B}_n \boldsymbol{m}}_{\overline{\overline{\boldsymbol{G}}}_{m0}}, \tag{7.27}$$

$$\boldsymbol{G}_{m1} = \underbrace{H_\Gamma \boldsymbol{B}_m \boldsymbol{m} - \sum_{a\in\Omega^{e+}} \boldsymbol{B}_a (\boldsymbol{m}\cdot\overline{\boldsymbol{x}}_a)\boldsymbol{m}}_{\overline{\boldsymbol{G}}_{m1}} + \underbrace{\delta_\Gamma \boldsymbol{B}_n \boldsymbol{m} \xi_\Gamma}_{\overline{\overline{\boldsymbol{G}}}_{m1}}. \tag{7.28}$$

In above expressions we have used the folowing derivation rules (see e.g. [Mosler and Bruhns, 2004] and references therein for more details)

$$\nabla^s (H_\Gamma \boldsymbol{n}) = \underbrace{\delta_\Gamma (\boldsymbol{n}\otimes\boldsymbol{n})^s}_{\text{tensor form}} \equiv \underbrace{\delta_\Gamma \boldsymbol{B}_n \boldsymbol{n}}_{\text{vector form}}, \tag{7.29}$$

$$\nabla^s (H_\Gamma \boldsymbol{m}) = \underbrace{\delta_\Gamma (\boldsymbol{m}\otimes\boldsymbol{n})^s}_{\text{tensor form}} \equiv \underbrace{\delta_\Gamma \boldsymbol{B}_m \boldsymbol{n}}_{\text{vector form}}, \tag{7.30}$$

$$\delta_\Gamma(\boldsymbol{x}) = \begin{cases} \infty & \text{for } \boldsymbol{x}\in\Gamma^e \\ 0 & \text{otherwise} \end{cases}, \tag{7.31}$$

where $\nabla^s = \frac{1}{2}(\nabla + \nabla^T)$. Note that ξ_Γ is a coordinate along Γ^e, which has 0 value at $\boldsymbol{x}_\Gamma$ and is positive in the $\boldsymbol{m}$ direction. We further divide the strain field into a regular part

$\overline{\boldsymbol{\epsilon}}$ and a singular part $\overline{\overline{\boldsymbol{\epsilon}}}$

$$\boldsymbol{\epsilon} = \overline{\boldsymbol{\epsilon}} + \overline{\overline{\boldsymbol{\epsilon}}}, \tag{7.32}$$

$$\overline{\boldsymbol{\epsilon}} = \sum_{a=1}^{4} \boldsymbol{B}_a \boldsymbol{d}_a + \overline{\boldsymbol{G}}_{n0}\alpha_{n0} + \overline{\boldsymbol{G}}_{n1}\alpha_{n1} + \overline{\boldsymbol{G}}_{m0}\alpha_{m0} + \overline{\boldsymbol{G}}_{m1}\alpha_{m1}, \tag{7.33}$$

$$\overline{\overline{\boldsymbol{\epsilon}}} = \overline{\overline{\boldsymbol{G}}}_{n0}\alpha_{n0} + \overline{\overline{\boldsymbol{G}}}_{n1}\alpha_{n1} + \overline{\overline{\boldsymbol{G}}}_{m0}\alpha_{m0} + \overline{\overline{\boldsymbol{G}}}_{m1}\alpha_{m1} \tag{7.34}$$

We note that the singular part is just a particular representation of the localized inelastic deformation introduced at the displacement discontinuity.

7.2.2 Equilibrium equations

Interpolation of virtual strains is carried out according to

$$\hat{\boldsymbol{\epsilon}} = \sum_{a=1}^{4} \boldsymbol{B}_a \hat{\boldsymbol{d}}_a + \hat{\boldsymbol{G}}_{n0}\hat{\alpha}_{n0} + \hat{\boldsymbol{G}}_{n1}\hat{\alpha}_{n1} + \hat{\boldsymbol{G}}_{m0}\hat{\alpha}_{m0} + \hat{\boldsymbol{G}}_{m1}\hat{\alpha}_{m1}. \tag{7.35}$$

The discontinuity parameters can be viewed as additional (incompatible) degrees of freedom of the element. In that sense we use the following expression to compute the interpolation matrices of virtual strains (see e.g. [Ibrahimbegovic and Wilson, 1991]), which ensures the convergence in the spirit of the patch test

$$\hat{\boldsymbol{G}}_{mode} = \boldsymbol{G}_{mode} - \frac{1}{A_{\Omega^e}} \int_{\Omega^e} \boldsymbol{G}_{mode} d\Omega. \tag{7.36}$$

By introducing the last result in (7.36) into (7.25)-(7.28), we obtain

$$\hat{\boldsymbol{G}}_{n0} = \underbrace{\overline{\boldsymbol{G}}_{n0} - \frac{1}{A_{\Omega^e}} \int_{\Omega^e} \overline{\boldsymbol{G}}_{n0} d\Omega - \frac{l_\Gamma}{A_{\Omega^e}} \boldsymbol{B}_n \boldsymbol{n}}_{\overline{\hat{\boldsymbol{G}}}_{n0}} + \underbrace{\delta_\Gamma \boldsymbol{B}_n \boldsymbol{n}}_{\overline{\overline{\hat{\boldsymbol{G}}}}_{n0}}, \tag{7.37}$$

$$\hat{\boldsymbol{G}}_{n1} = \underbrace{\overline{\boldsymbol{G}}_{n1} - \frac{1}{A_{\Omega^e}} \int_{\Omega^e} \overline{\boldsymbol{G}}_{n1} d\Omega}_{\overline{\hat{\boldsymbol{G}}}_{n1}} + \underbrace{\delta_\Gamma \boldsymbol{B}_n \boldsymbol{n} \xi_\Gamma}_{\overline{\overline{\hat{\boldsymbol{G}}}}_{n1}}, \tag{7.38}$$

$$\hat{\boldsymbol{G}}_{m0} = \underbrace{\overline{\boldsymbol{G}}_{m0} - \frac{1}{A_{\Omega^e}} \int_{\Omega^e} \overline{\boldsymbol{G}}_{m0} d\Omega - \frac{l_\Gamma}{A_{\Omega^e}} \boldsymbol{B}_n \boldsymbol{m}}_{\overline{\hat{\boldsymbol{G}}}_{m0}} + \underbrace{\delta_\Gamma \boldsymbol{B}_n \boldsymbol{m}}_{\overline{\overline{\hat{\boldsymbol{G}}}}_{m0}}, \tag{7.39}$$

$$\hat{\boldsymbol{G}}_{m1} = \underbrace{\overline{\boldsymbol{G}}_{m1} - \frac{1}{A_{\Omega^e}} \int_{\Omega^e} \overline{\boldsymbol{G}}_{m1} d\Omega}_{\overline{\hat{\boldsymbol{G}}}_{m1}} + \underbrace{\delta_\Gamma \boldsymbol{B}_n \boldsymbol{m} \xi_\Gamma}_{\overline{\overline{\hat{\boldsymbol{G}}}}_{m1}}. \tag{7.40}$$

The weak form of the equilibrium equations or the principle of virtual work for an element e of a chosen finite element mesh with N_{el} finite elements, can be written as:

$$\delta\Pi^{int,(e)} - \delta\Pi^{ext,(e)} = 0. \tag{7.41}$$

By using (7.35) for the definition of the virtual strains, we can write a single element contribution to the virtual work of internal forces as:

$$\begin{aligned}\delta\Pi^{int,(e)} &= t^{(e)}\int_{\Omega^e}\hat{\boldsymbol{\epsilon}}^T\boldsymbol{\sigma}d\Omega \\ &= \underbrace{\sum_{a=1}^{4}t^{(e)}\int_{\Omega^e}\hat{\boldsymbol{d}}_a^{\,T}\boldsymbol{B}_a^T\boldsymbol{\sigma}d\Omega}_{\text{standard}}+ \\ &\quad \underbrace{t^{(e)}\int_{\Omega^e}\hat{\alpha}_{n0}\hat{\boldsymbol{G}}_{n0}^T\boldsymbol{\sigma}+\hat{\alpha}_{n1}\hat{\boldsymbol{G}}_{n1}^T\boldsymbol{\sigma}+\hat{\alpha}_{m0}\hat{\boldsymbol{G}}_{m0}^T\boldsymbol{\sigma}+\hat{\alpha}_{m1}\hat{\boldsymbol{G}}_{m1}^T\boldsymbol{\sigma}d\Omega,}_{\text{additional}} \qquad (7.42)\end{aligned}$$

where $t^{(e)}$ is the thickness of the element and

$$\boldsymbol{\sigma} = [\sigma_x, \sigma_y, \sigma_{xy}]^T \qquad (7.43)$$

is the stress vector. From the term "standard" in (7.42) we obtain the vector of element internal nodal forces

$$\boldsymbol{f}^{int,(e)} = \left[\boldsymbol{f}_a^{int,(e)^T}\right]^T, \quad \boldsymbol{f}_a^{int,(e)} = t^{(e)}\int_{\Omega^e}\boldsymbol{B}_a^T\boldsymbol{\sigma}d\Omega. \qquad (7.44)$$

From the virtual work of external forces $\delta\Pi^{ext,(e)}$ we can get the vector of element external nodal forces $\boldsymbol{f}^{ext,(e)}$, representing the consistent external load applied to the element's nodes. We note that the displacement discontinuity parameters do not contribute to the external load vector. The finite element assembly of vectors $\boldsymbol{f}^{int,(e)}$ and $\boldsymbol{f}^{ext,(e)}$, for all elements of the chosen mesh, leads to a set of global equilibrium equations

$$A_{e=1}^{N_{el}}\left(\boldsymbol{f}^{int,(e)} - \boldsymbol{f}^{ext,(e)}\right) = \boldsymbol{0}, \qquad (7.45)$$

where A is the assembly operator. Note that we have only used one part of the right side of equation (7.42) in (7.41) to get the set of global equations (7.45).

The other term in (7.42), denoted as "additional" (resulting from additional enriched kinematics due to embedded discontinuity), will also contribute to the weak form of the equilibrium. However, we will treat this contribution locally, element by element, only for those elements where the discontinuity was activated. Then, in view of (7.41), the

following four equations are obtained for each element of the chosen mesh

$$h_{n0}^{(e)} = t^{(e)} \left(\int_{\Omega^e} \overline{\hat{\boldsymbol{G}}}_{n0}^T \boldsymbol{\sigma} d\Omega + \int_{\Gamma^e} \underbrace{\boldsymbol{n}^T \boldsymbol{B}_n^T \boldsymbol{\sigma}}_{=t_n} d\Gamma \right) = \underbrace{t^{(e)} \int_{\Omega^e} \overline{\hat{\boldsymbol{G}}}_{n0}^T \boldsymbol{\sigma} d\Omega}_{h_{n0}^{\Omega^e}} + \underbrace{t^{(e)} \int_{\Gamma^e} t_n d\Gamma}_{h_{n0}^{\Gamma^e}} = 0, \tag{7.46}$$

$$h_{n1}^{(e)} = t^{(e)} \left(\int_{\Omega^e} \overline{\hat{\boldsymbol{G}}}_{n1}^T \boldsymbol{\sigma} d\Omega + \int_{\Gamma^e} \xi_\Gamma \underbrace{\boldsymbol{n}^T \boldsymbol{B}_n^T \boldsymbol{\sigma}}_{=t_n} d\Gamma \right) = \underbrace{t^{(e)} \int_{\Omega^e} \overline{\hat{\boldsymbol{G}}}_{n1}^T \boldsymbol{\sigma} d\Omega}_{h_{n1}^{\Omega^e}} + \underbrace{t^{(e)} \int_{\Gamma^e} \xi_\Gamma t_n d\Gamma}_{h_{n1}^{\Gamma^e}} = 0, \tag{7.47}$$

$$h_{m0}^{(e)} = t^{(e)} \left(\int_{\Omega^e} \overline{\hat{\boldsymbol{G}}}_{m0}^T \boldsymbol{\sigma} d\Omega + \int_{\Gamma^e} \underbrace{\boldsymbol{m}^T \boldsymbol{B}_n^T \boldsymbol{\sigma}}_{=t_m} d\Gamma \right) = \underbrace{t^{(e)} \int_{\Omega^e} \overline{\hat{\boldsymbol{G}}}_{m0}^T \boldsymbol{\sigma} d\Omega}_{h_{m0}^{\Omega^e}} + \underbrace{t^{(e)} \int_{\Gamma^e} t_m d\Gamma}_{h_{m0}^{\Gamma^e}} = 0, \tag{7.48}$$

$$h_{m1}^{(e)} = t^{(e)} \left(\int_{\Omega^e} \overline{\hat{\boldsymbol{G}}}_{m1}^T \boldsymbol{\sigma} d\Omega + \int_{\Gamma^e} \xi_\Gamma \underbrace{\boldsymbol{m}^T \boldsymbol{B}_n^T \boldsymbol{\sigma}}_{=t_m} d\Gamma \right) = \underbrace{t^{(e)} \int_{\Omega^e} \overline{\hat{\boldsymbol{G}}}_{m1}^T \boldsymbol{\sigma} d\Omega}_{h_{m1}^{\Omega^e}} + \underbrace{t^{(e)} \int_{\Gamma^e} \xi_\Gamma t_m d\Gamma}_{h_{m1}^{\Gamma^e}} = 0, \tag{7.49}$$

where t_n and t_m represent the normal and tangential components of the traction at the discontinuity

$$\boldsymbol{t} = [t_n, t_m]^T, \tag{7.50}$$

and $\int_{\Omega^e} \delta_\Gamma(\circ) d\Omega = \int_{\Gamma^e} (\circ) d\Gamma$ was used. We gather the equations (7.46) to (7.49) in a vector form to write the element-based residual as:

$$\boldsymbol{h}^{(e)} = \boldsymbol{h}^{\Omega^e} + \boldsymbol{h}^{\Gamma^e} = \begin{bmatrix} h_{n0}^{\Omega^e} \\ h_{n1}^{\Omega^e} \\ h_{m0}^{\Omega^e} \\ h_{m1}^{\Omega^e} \end{bmatrix} + \begin{bmatrix} h_{n0}^{\Gamma^e} \\ h_{n1}^{\Gamma^e} \\ h_{m0}^{\Gamma^e} \\ h_{m1}^{\Gamma^e} \end{bmatrix} = \mathbf{0}. \tag{7.51}$$

The dedicated solution procedure for a set of global equations in (7.45) together with a set of local (element) equations in (7.51) will be further addressed in Section 7.3.

7.2.3 Constitutive relations

In what follows we choose plane stress constitutive relations, although the derived 2D elements with embeded discontinuity could be also used for plane strain problems. We will describe the constitutive behavior of the bulk material $\Omega^e \backslash \Gamma^e$ with elastoplastic model with isotropic hardening, while the response of the discontinuity Γ^e is considered to be rigid-plastic with softening. The basic ingredients of the chosen constitutive relations are built upon the classical plasticity (e.g. [Ibrahimbegovic et al., 1998]) and can be summarized as:

- The regular strains $\overline{\boldsymbol{\epsilon}}$ (7.32) can be additively decomposed into elastic part $\overline{\boldsymbol{\epsilon}}^e$ and plastic part $\overline{\boldsymbol{\epsilon}}^p$
$$\overline{\boldsymbol{\epsilon}} = \overline{\boldsymbol{\epsilon}}^e + \overline{\boldsymbol{\epsilon}}^p, \tag{7.52}$$

- The free energy of the bulk material is assumed to be the sum of the strain energy function $\overline{W}$ and the hardening potential $\overline{\Xi}$
$$\overline{\Psi}(\overline{\boldsymbol{\epsilon}}^e, \overline{\xi}) := \overline{W}\left(\overline{\boldsymbol{\epsilon}}^e\right) + \overline{\Xi}(\overline{\xi}) = \frac{1}{2}\overline{\boldsymbol{\epsilon}}^{eT}\boldsymbol{C}\overline{\boldsymbol{\epsilon}}^e + \overline{\Xi}(\overline{\xi}), \tag{7.53}$$
where
$$\boldsymbol{C} = \frac{E}{1-\nu^2}\begin{bmatrix} 1 & \nu & 0 \\ \nu & 1 & 0 \\ 0 & 0 & \frac{1-\nu}{2} \end{bmatrix}, \tag{7.54}$$
E is the Young's modulus of the material, ν is the Poisson's ratio of the material and $\overline{\xi} \geq 0$ is strain-like hardening variable.

- The yield function is assumed to be based upon the von Mises yield criterion (see [Dujc and Brank, 2008] and references therein for more details), which can be written as
$$\overline{\phi}\left(\boldsymbol{\sigma}, \overline{q}\right) = \boldsymbol{\sigma}^T\boldsymbol{A}\boldsymbol{\sigma} - \left(1 - \frac{\overline{q}}{\sigma_y}\right)^2 \leq 0, \tag{7.55}$$
where
$$\boldsymbol{A} = \frac{1}{2\sigma_y^2}\begin{bmatrix} 2 & -1 & 0 \\ -1 & 2 & 0 \\ 0 & 0 & 6 \end{bmatrix}, \tag{7.56}$$
whereas $\overline{q}$ is the stress-like hardening variable conjugate to the equivalent plastic strain $\overline{\xi}$ and σ_y is the uniaxial yield stress.

- The traction $\boldsymbol{t}$ at a point at the discontinuity Γ^e is related to jump in displacements $\overline{\overline{\boldsymbol{u}}} = [\overline{\overline{u}}_n, \overline{\overline{u}}_m]^T$ (see Figure 7.3) at this particular point
$$\boldsymbol{t} = \boldsymbol{t}(\overline{\overline{\boldsymbol{u}}}). \tag{7.57}$$

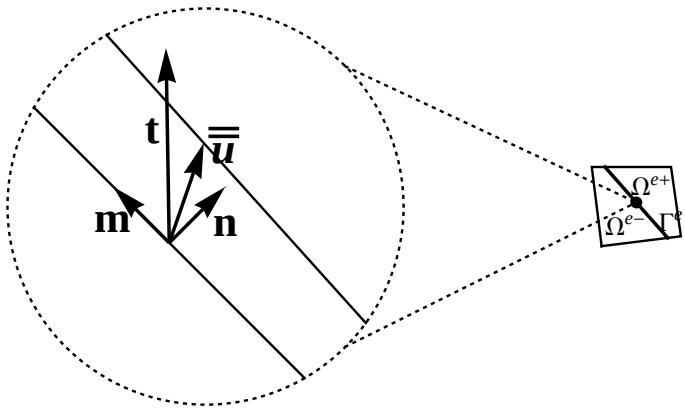

Figure 7.3: Neighborhood of a point of interest at the discontinuity Γ^e

Slika 7.3: Okolica obravnavane točke na nezveznosti

- The localization (failure) criterion that activates localized softening at discontinuity Γ^e is defined in terms of the traction $\boldsymbol{t}$ and the stress-like softening variable $\overline{\overline{q}}(\overline{\overline{\xi}})$ (the later is defined in terms of the strain-like softening variable $\overline{\overline{\xi}}$).

$$\overline{\overline{\phi}} = \overline{\overline{\phi}}(\boldsymbol{t}, \overline{\overline{q}}) \leq 0. \tag{7.58}$$

- The softening potential

$$\overline{\overline{\Xi}}(\overline{\overline{\xi}}), \tag{7.59}$$

  defined in terms of the strain-like softening variable $\overline{\overline{\xi}}$.

The remaining ingredients of the elastoplasticity with hardening,describing bulk material $\Omega^e \backslash \Gamma^e$, can be obtained from the standard consideration of thermodynamics for associative plasticity based upon the principle of maximum plastic dissipation (e.g. see [Lubliner, 1990], [Simo and Kennedy, 1992], [Ibrahimbegovic, 2009]). By using (7.52) and (7.53) the mechanical dissipation at a point $\boldsymbol{x} \in \Omega^e \setminus \Gamma^e$ can be further written as

$$0 \leq \overline{D} \overset{def.}{=} \boldsymbol{\sigma}^T \dot{\overline{\boldsymbol{\epsilon}}} - \dot{\overline{\Psi}}(\overline{\boldsymbol{\epsilon}}^e, \overline{\xi}) = (\boldsymbol{\sigma} - \frac{\partial \overline{\Psi}}{\partial \overline{\boldsymbol{\epsilon}}^e})^T \dot{\overline{\boldsymbol{\epsilon}}}^e + \boldsymbol{\sigma}^T \dot{\overline{\boldsymbol{\epsilon}}}^p - \frac{\partial \overline{\Psi}}{\partial \overline{\xi}} \dot{\overline{\xi}}, \tag{7.60}$$

where $(\dot{o}) = \partial (o) / \partial t$ denotes the derivative with respect to pseudo-time $t \in [0, T]$. By assuming that the elastic process is non-dissipative (i.e. $\overline{D} = 0$), with no change in plastic state variables, we obtain from (7.60) that

$$\boldsymbol{\sigma} = \frac{\partial \overline{\Psi}}{\partial \overline{\boldsymbol{\epsilon}}^e} = \boldsymbol{C} \overline{\boldsymbol{\epsilon}}^e. \tag{7.61}$$

We can also define the stress-like hardening variable $\overline{q}$ by further considering (7.60) and (7.53) as:

$$\overline{q} = -\frac{\partial \overline{\Psi}}{\partial \overline{\xi}} = -\frac{\partial \overline{\Xi}}{\partial \overline{\xi}}. \tag{7.62}$$

By replacing (7.61) and (7.62) in (7.60), the plastic dissipation can be obtained as

$$\overline{D}^p = \boldsymbol{\sigma}^T \dot{\overline{\boldsymbol{\epsilon}}}^p + \overline{q}\dot{\overline{\xi}}. \tag{7.63}$$

The principle of maximum plastic dissipation states that among all the variables ($\boldsymbol{\sigma}$, $\overline{q}$) that satisfy the yield criteria $\overline{\phi}\,(\boldsymbol{\sigma}, \overline{q}) \leq 0$, one should choose those that maximize plastic dissipation (at frozen rates $\dot{\overline{\boldsymbol{\epsilon}}}^p$ and $\dot{\overline{\xi}}$). This can be written as a constrained optimization problem:

$$\min_{\boldsymbol{\sigma},\overline{q}} \max_{\dot{\overline{\gamma}}} \left[\overline{L}^p(\boldsymbol{\sigma}, \overline{q}, \dot{\overline{\gamma}}) = -\overline{D}^p(\boldsymbol{\sigma}, \overline{q}) + \dot{\overline{\gamma}}\overline{\phi}(\boldsymbol{\sigma}, \overline{q}) \right], \tag{7.64}$$

where $\dot{\overline{\gamma}} \geq 0$ plays the role of Lagrange multiplier. By using (7.63) and (7.55), the last result can provide the evolution equations for internal variables that can be written as:

$$\frac{\partial \overline{L}^p}{\partial \boldsymbol{\sigma}} = -\dot{\overline{\boldsymbol{\epsilon}}}^p + \dot{\overline{\gamma}}\frac{\partial \overline{\phi}}{\partial \boldsymbol{\sigma}} = 0 \implies \dot{\overline{\epsilon}}^p = \dot{\overline{\gamma}} 2\boldsymbol{A}\boldsymbol{\sigma}, \tag{7.65}$$

$$\frac{\partial \overline{L}^p}{\partial \overline{q}} = -\dot{\overline{\xi}} + \dot{\overline{\gamma}}\frac{\partial \overline{\phi}}{\partial \overline{q}} = 0 \implies \dot{\overline{\xi}} = \dot{\overline{\gamma}}\frac{2}{\sigma_y}\left(1 - \frac{\overline{q}}{\sigma_y}\right) \overset{(7.55)}{=} \dot{\overline{\gamma}}\frac{2}{\sigma_y}\sqrt{\boldsymbol{\sigma}^T\boldsymbol{A}\boldsymbol{\sigma}}, \tag{7.66}$$

along with the Kuhn-Tucker loading/unloading conditions and the consistency condition

$$\dot{\overline{\gamma}} \geq 0, \quad \overline{\phi} \leq 0, \quad \dot{\overline{\gamma}}\overline{\phi} = 0, \quad \dot{\overline{\gamma}}\dot{\overline{\phi}} = 0. \tag{7.67}$$

To obtain the remaining ingredients of the rigid-plastic response, describing softening at the discontinuity Γ^e, we isolate one point at the discontinuity. We first define the strain energy function due to softening potential in this point as $\overline{\overline{\Psi}} = \overline{\overline{\Xi}}$. The dissipation can then be written as:

$$0 \leq \overline{\overline{D}} \overset{def.}{=} \boldsymbol{t}^T\dot{\overline{\overline{\boldsymbol{u}}}} - \dot{\overline{\overline{\Psi}}}(\overline{\overline{\xi}}) = \boldsymbol{t}^T\dot{\overline{\overline{\boldsymbol{u}}}} - \frac{\partial \overline{\overline{\Psi}}}{\partial \overline{\overline{\xi}}}\dot{\overline{\overline{\xi}}}. \tag{7.68}$$

where $\boldsymbol{t}$ is the traction defined in (7.57). Finally, by introducing the traction-like variable

$$\overline{\overline{q}} = -\frac{\partial \overline{\overline{\Psi}}}{\partial \overline{\overline{\xi}}} = -\frac{\partial \overline{\overline{\Xi}}}{\partial \overline{\overline{\xi}}}, \tag{7.69}$$

the result in (7.68) can be rewritten as

$$\overline{\overline{D}} = \overline{\overline{D}}^p = \boldsymbol{t}^T\dot{\overline{\overline{\boldsymbol{u}}}} + \overline{\overline{q}}\dot{\overline{\overline{\xi}}}. \tag{7.70}$$

The principle of maximum plastic dissipation at the rigid-plastic discontinuity can then be defined as:

$$\min_{\boldsymbol{t},\overline{\overline{q}}} \max_{\dot{\overline{\overline{\gamma}}}} \left[\overline{\overline{L}}^p(\boldsymbol{t},\overline{\overline{q}},\dot{\overline{\overline{\gamma}}}) = -\overline{\overline{D}}^p(\boldsymbol{t},\overline{\overline{q}}) + \dot{\overline{\overline{\gamma}}}\overline{\overline{\phi}}(\boldsymbol{t},\overline{\overline{q}}) \right], \tag{7.71}$$

where $\dot{\overline{\overline{\gamma}}} \geq 0$ is the Lagrange multiplier. By using (7.70) and (7.58), we get from (7.71) above the following evolution equations of displacement dicontinuity:

$$\frac{\partial \overline{\overline{L}}^p}{\partial \boldsymbol{t}} = -\dot{\overline{\overline{\boldsymbol{u}}}} + \dot{\overline{\overline{\gamma}}}\frac{\partial \overline{\overline{\phi}}}{\partial \boldsymbol{t}} = 0 \Longrightarrow \dot{\overline{\overline{\boldsymbol{u}}}} = \dot{\overline{\overline{\gamma}}}\frac{\partial \overline{\overline{\phi}}}{\partial \boldsymbol{t}}, \tag{7.72}$$

$$\frac{\partial \overline{\overline{L}}^p}{\partial \overline{\overline{q}}} = -\dot{\overline{\overline{\xi}}} + \dot{\overline{\overline{\gamma}}}\frac{\partial \overline{\overline{\phi}}}{\partial \overline{\overline{q}}} = 0 \Longrightarrow \dot{\overline{\overline{\xi}}} = \dot{\overline{\overline{\gamma}}}\frac{\partial \overline{\overline{\phi}}}{\partial \overline{\overline{q}}}, \tag{7.73}$$

accompanied by the Kuhn-Tucker loading/unloading conditions, and the consistency condition

$$\dot{\overline{\overline{\gamma}}} \geq 0, \quad \overline{\overline{\phi}} \leq 0, \quad \dot{\overline{\overline{\gamma}}}\overline{\overline{\phi}} = 0, \quad \dot{\overline{\overline{\gamma}}}\dot{\overline{\overline{\phi}}} = 0. \tag{7.74}$$

7.3 Computational procedure

In this section we present the details of a computational procedure for solving the set of global equilibrium equations along with the local (element based) equations, generated by the finite element with embedded discontinuity as presented in Section 7.2.

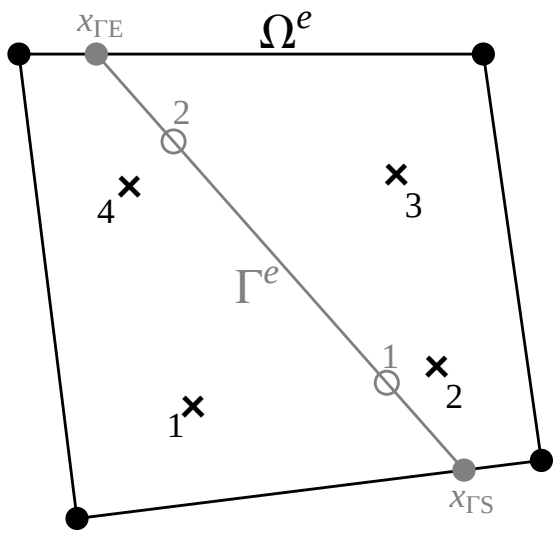

Figure 7.4: Numerical integration scheme

Slika 7.4: Numerična integracijska shema

The solution of the set of global nonlinear equations in (7.45) and the local nonlinear equations in (7.51) is obtained at discrete pseudo-time values $0, \tau_1, \tau_2, \ldots, \tau_{n-1}, \tau_n, \tau_{n+1}$,

$\ldots, T$ by means of the incremental-iterative scheme. We will consider a single-step scheme providing the solution in a typical pseudo-time increment from τ_n to τ_{n+1}. Let us assume that all the variables, related to an element e, its bulk integration points $bip = 1, 2, 3, 4$ and its discontinuity integration points $dip = 1, 2$ are given at τ_n, i.e.

$$\text{given: } \boldsymbol{d}_n^{(e)} = \left[\boldsymbol{d}_{a,n}^{(e)^T}\right]^T,\ \overline{\boldsymbol{\epsilon}}_n^{p,bip},\ \overline{\xi}_n^{bip},\ \boldsymbol{\alpha}_n^{(e)},\ \overline{\overline{\xi}}_n^{dip} \quad \text{and} \quad x_{\Gamma S},\ x_{\Gamma E}, \tag{7.75}$$

where $\boldsymbol{\alpha}_n^{(e)} = \left[\alpha_{n0,n}^{(e)}, \alpha_{n1,n}^{(e)}, \alpha_{m0,n}^{(e)}, \alpha_{m1,n}^{(e)}\right]^T$.

Remark 7.2. *4-point Gauss integration scheme is used for the bulk and 2-point Gauss integration scheme is used for the discontinuity, see Figure 7.4.*

We also need as indicated in (7.75): (i) the starting point of the discontinuity $x_{\Gamma S}$ (which is only true if the discontinuity in one of the neighboring elements ends at the common edge) and (ii) the end point of the discontinuity $x_{\Gamma E}$ (which is only true if softening has been activated so far). We will then iterate in the pseudo-time step in order to compute the converged values of the variables at τ_{n+1}, i.e.

$$\begin{aligned}&\text{find: } \boldsymbol{d}_{n+1}^{(e)},\ \overline{\boldsymbol{\epsilon}}_{n+1}^{p,bip},\ \overline{\xi}_{n+1}^{bip},\ \boldsymbol{\alpha}_{n+1}^{(e)},\ \overline{\overline{\xi}}_{n+1}^{dip} \text{ and}\\ &\text{if not given already and if the softening conditions are met: } x_{\Gamma E}.\end{aligned} \tag{7.76}$$

The computation of solution (7.76) is split into two phases:

(a) The global (mesh related) phase computes the current iterative values (with (i) as the iteration counter) of nodal generalized displacements at τ_{n+1} while keeping the other variables fixed, i.e.

$$\text{global phase: } \boldsymbol{d}_{n+1}^{(e),(i)} = \boldsymbol{d}_{n+1}^{(e),(i-1)} + \Delta\boldsymbol{d}_{n+1}^{(e),(i-1)}. \tag{7.77}$$

The computation of iterative update $\Delta\boldsymbol{d}_{n+1}^{(e),(i-1)}$ will be explained further below.

(b) The local (element and integration point related) phase computes the values of variables $\overline{\boldsymbol{\epsilon}}_{n+1}^{p,bip}$, $\overline{\xi}_{n+1}^{bip}$, $\boldsymbol{\alpha}_{n+1}^{(e)}$, $\overline{\overline{\xi}}_{n+1}^{dip}$ while keeping $\boldsymbol{d}_{n+1}^{(e),(i)}$ fixed. The computation procedure depends on weather the softening has been activated in the considered element or not. Therefore, the local computation procedure on the level of a single element can be based either on hardening plasticity procedure or on softening plasticity procedure (excluding each other).

In the rest of this section we will first describe in detail the phase (b). This will be followed by the description of the phase (a). The softening plasticity procedure is carried out only in those finite elements where:

- discontinuity has been active at the previous time step τ_n, i.e. $x_{\Gamma S}$ and $x_{\Gamma E}$ are provided and the local softening variables changed, or
- discontinuity has not been active in the previous time step but the discontinuity in one of the neighboring elements ends at the common edge, i.e. $x_{\Gamma S}$ is provided.

In the latter case we first compute the direction of the discontinuity by using the average stress field in the element

$$\boldsymbol{n} = \boldsymbol{n}\left(\boldsymbol{\sigma}^{avg}(\boldsymbol{d}_{n+1}^{(e)}, \overline{\boldsymbol{\epsilon}}_n^{p,bip})\right), \quad \boldsymbol{m} = \boldsymbol{m}\left(\boldsymbol{\sigma}^{avg}(\boldsymbol{d}_{n+1}^{(e)}, \overline{\boldsymbol{\epsilon}}_n^{p,bip})\right). \tag{7.78}$$

We determine the direction of the discontinuity in the direction of principal stress if the governing mode of separation is mode I, i.e. $\boldsymbol{n}$ is parallel to the maximum principal stress. If the governing mode of separation is mode II, we set $\boldsymbol{m}$ to be parallel to one of the directions of maximum shear stress. Once the direction of the discontinuity is determined we are able to obtain the end point of the discontinuity $x_{\Gamma E}$ and the complete description of the finite element with embedded discontinuity geometry (Ω^{e-}, Ω^{e+} and l_Γ). The main part of the softening plasticity procedure starts with the determination of the trial values of the traction in discontinuity integration points. Since we use the rigid plasticity law at the discontinuity, we are unable to determine the trial values by using the constitutive law. We use instead the local equilibrium equations in (7.51). Since stress in the bulk integration points is well defined we can always obtain the bulk contribution

$$\boldsymbol{h}_{n+1}^{\Omega^e,trial} = \begin{bmatrix} h_{n0,n+1}^{\Omega^e,trial} \\ h_{n1,n+1}^{\Omega^e,trial} \\ h_{m0,n+1}^{\Omega^e,trial} \\ h_{m1,n+1}^{\Omega^e,trial} \end{bmatrix} = \boldsymbol{h}^{\Omega^e}\left(\boldsymbol{\sigma}(\boldsymbol{d}_{n+1}^{(e)}, \overline{\boldsymbol{\epsilon}}_n^{p,bip}, \boldsymbol{\alpha}_n)\right). \tag{7.79}$$

We then further consider, that the integration at the discontinuity is carried out according to

$$\int_{-\frac{l_\Gamma}{2}}^{\frac{l_\Gamma}{2}} f(\xi_\Gamma)d\xi = \sum_{dip=1}^{2} f(\xi_\Gamma^{dip})w^{dip}\frac{l_\Gamma}{2}, \; \xi_\Gamma^{dip} = \pm\frac{l_\Gamma}{2\sqrt{3}}, \; w^{dip} = 1, \tag{7.80}$$

where $f(\xi_\Gamma)$ in an arbitrary scalar function, $f(\xi_\Gamma^{dip})$ is the value of this function evaluated at the Gauss quadrature point $dip = 1, 2$, ξ_Γ^{dip} is the coordinate of the quadrature point and w^{dip} is the corresponding weight. By using (7.80), the contribution of the discontinuity to equation (7.51) can then be written as

$$\boldsymbol{h}^{\Gamma^e} = \frac{t^{(e)}l_\Gamma}{2}\begin{bmatrix} t_n^1 + t_n^2 \\ \xi_\Gamma^1 t_n^1 + \xi_\Gamma^2 t_n^2 \\ t_m^1 + t_m^2 \\ \xi_\Gamma^1 t_m^1 + \xi_\Gamma^2 t_m^2 \end{bmatrix}, \tag{7.81}$$

where $\boldsymbol{t}^1 = [t_n^1, t_m^1]^T$ is the traction in the first discontinuity integration point and $\boldsymbol{t}^2 = [t_n^2, t_m^2]^T$ is the traction in the second discontinuity point. To satisfy the local equilibrium equations we solve the system of four algebraic equations

$$\boldsymbol{h}_{n+1}^{\Omega^e,trial} + \boldsymbol{h}^{\Gamma^e}(\boldsymbol{t}_{n+1}^{1,trial}, \boldsymbol{t}_{n+1}^{2,trial}) = \boldsymbol{0}, \tag{7.82}$$

and determine the four unknown components of the traction in the discontinuity integration points

$$\boldsymbol{t}_{n+1}^{1,trial} = \begin{bmatrix} t_{n,n+1}^{1,trial} \\ t_{m,n+1}^{1,trial} \end{bmatrix} = \begin{bmatrix} \frac{2(h_{n1,n+1}^{\Omega^e,trial} - h_{n0,n+1}^{\Omega^e,trial}\xi_\Gamma^2)}{(\xi_\Gamma^2 - \xi_\Gamma^1)l_\Gamma} \\ \frac{2(h_{m1,n+1}^{\Omega^e,trial} - h_{m0,n+1}^{\Omega^e,trial}\xi_\Gamma^2)}{(\xi_\Gamma^2 - \xi_\Gamma^1)l_\Gamma} \end{bmatrix}, \tag{7.83}$$

$$\boldsymbol{t}_{n+1}^{2,trial} = \begin{bmatrix} t_{n,n+1}^{2,trial} \\ t_{m,n+1}^{2,trial} \end{bmatrix} = \begin{bmatrix} \frac{2(h_{n1,n+1}^{\Omega^e,trial} - h_{n0,n+1}^{\Omega^e,trial}\xi_\Gamma^1)}{(\xi_\Gamma^1 - \xi_\Gamma^2)l_\Gamma} \\ \frac{2(h_{m1,n+1}^{\Omega^e,trial} - h_{m0,n+1}^{\Omega^e,trial}\xi_\Gamma^1)}{(\xi_\Gamma^1 - \xi_\Gamma^2)l_\Gamma} \end{bmatrix}. \tag{7.84}$$

Next we provide the trial values of the failure function at the discontinuity integration points

$$\underbrace{\overline{\overline{\phi}}^{1,trial} = \overline{\overline{\phi}}(\boldsymbol{t}_{n+1}^{1,trial}, \overline{\overline{q}}(\overline{\overline{\xi}}_n^1)) \leq 0 \text{ or } \overline{\overline{\phi}}^{2,trial} = \overline{\overline{\phi}}(\boldsymbol{t}_{n+1}^{2,trial}, \overline{\overline{q}}(\overline{\overline{\xi}}_n^2)) \leq 0}_{?}. \tag{7.85}$$

If the trial failure criterion (7.85) is satisfied, i.e. if the yield function is less or equal to zero in at least one discontinuity integration point, the values of softening plasticity local variables remain unchanged

$$\overline{\overline{\phi}}^{1,trial} \leq 0 \text{ or } \overline{\overline{\phi}}^{2,trial} \leq 0 \implies \boldsymbol{\alpha}_{n+1}^{(e)} = \boldsymbol{\alpha}_n^{(e)}, \quad \overline{\overline{\xi}}_{n+1}^1 = \overline{\overline{\xi}}_n^1, \ \overline{\overline{\xi}}_{n+1}^2 = \overline{\overline{\xi}}_n^2. \tag{7.86}$$

In the case of violation of the trial yield criterion (7.85), i.e. the yield function is greater than zero in both discontinuity integration points, the values of discontinuity integration point variables are updated by backward Euler integration scheme

$$\overline{\overline{\boldsymbol{u}}}_{n+1}^1 = \overline{\overline{\boldsymbol{u}}}_n^1 + \overline{\overline{\gamma}}_{n+1}^1 \frac{\partial \overline{\overline{\phi}}}{\partial \boldsymbol{t}}|_{\xi_\Gamma^1}, \qquad \overline{\overline{\xi}}_{n+1}^1 = \overline{\overline{\xi}}_n^1 + \overline{\overline{\gamma}}_{n+1}^1 \frac{\partial \overline{\overline{\phi}}}{\partial q}|_{\xi_\Gamma^1}, \tag{7.87}$$

$$\overline{\overline{\boldsymbol{u}}}_{n+1}^2 = \overline{\overline{\boldsymbol{u}}}_n^2 + \overline{\overline{\gamma}}_{n+1}^2 \frac{\partial \overline{\overline{\phi}}}{\partial \boldsymbol{t}}|_{\xi_\Gamma^2}, \qquad \overline{\overline{\xi}}_{n+1}^2 = \overline{\overline{\xi}}_n^2 + \overline{\overline{\gamma}}_{n+1}^2 \frac{\partial \overline{\overline{\phi}}}{\partial q}|_{\xi_\Gamma^2}, \tag{7.88}$$

where $\overline{\overline{\gamma}}_{n+1}^1 = \dot{\overline{\overline{\gamma}}}_{n+1}^1(\tau_{n+1} - \tau_n)$ and $\overline{\overline{\gamma}}_{n+1}^2 = \dot{\overline{\overline{\gamma}}}_{n+1}^2(\tau_{n+1} - \tau_n)$. Note that the relation between the jumps in displacements evaluated at the discontinuity integration points and the kinematic parameters related to discontinuity can be obtained as follows

$$\boldsymbol{\alpha}^{(e)}(\overline{\overline{\boldsymbol{u}}}^1, \overline{\overline{\boldsymbol{u}}}^2) = \left[\frac{\overline{\overline{u}}_n^1 + \overline{\overline{u}}_n^2}{2}, \frac{\overline{\overline{u}}_n^1 - \overline{\overline{u}}_n^2}{\xi_\Gamma^1 - \xi_\Gamma^2}, \frac{\overline{\overline{u}}_m^1 + \overline{\overline{u}}_m^2}{2}, \frac{\overline{\overline{u}}_m^1 - \overline{\overline{u}}_m^2}{\xi_\Gamma^1 - \xi_\Gamma^2} \right]^T, \tag{7.89}$$

where $\overline{\overline{\boldsymbol{u}}}^1 = \left[\overline{\overline{u}}^1_n, \overline{\overline{u}}^1_m\right]^T$ and $\overline{\overline{\boldsymbol{u}}}^2 = \left[\overline{\overline{u}}^2_n, \overline{\overline{u}}^2_m\right]^T$. By using (7.87)-(7.89), we can thus determine the updated values of discontinuity kinematic parameters

$$\boldsymbol{\alpha}^{(e)}_{n+1} = \boldsymbol{\alpha}^{(e)}\left(\overline{\overline{\boldsymbol{u}}}^1_{n+1}(\overline{\overline{\gamma}}^1_{n+1}), \overline{\overline{\boldsymbol{u}}}^2_{n+1}(\overline{\overline{\gamma}}^2_{n+1})\right). \tag{7.90}$$

The values of the plastic multipliers $\overline{\overline{\gamma}}^1_{n+1}$ and $\overline{\overline{\gamma}}^2_{n+1}$ are determined with an iteration solution to the system of the following two equations

$$\overline{\overline{\phi}}^1\left(\boldsymbol{t}^1_{n+1}\left(\boldsymbol{\alpha}^{(e)}_{n+1}\left(\overline{\overline{\gamma}}^1_{n+1}, \overline{\overline{\gamma}}^2_{n+1}\right)\right), \overline{\overline{q}}\left(\overline{\overline{\xi}}^1_{n+1}\left(\overline{\overline{\gamma}}^1_{n+1}\right)\right)\right) = \overline{\overline{\phi}}^1\left(\overline{\overline{\gamma}}^1_{n+1}, \overline{\overline{\gamma}}^2_{n+1}\right) = 0, \tag{7.91}$$

$$\overline{\overline{\phi}}^2\left(\boldsymbol{t}^2_{n+1}\left(\boldsymbol{\alpha}^{(e)}_{n+1}\left(\overline{\overline{\gamma}}^1_{n+1}, \overline{\overline{\gamma}}^2_{n+1}\right)\right), \overline{\overline{q}}\left(\overline{\overline{\xi}}^2_{n+1}\left(\overline{\overline{\gamma}}^2_{n+1}\right)\right)\right) = \overline{\overline{\phi}}^2\left(\overline{\overline{\gamma}}^1_{n+1}, \overline{\overline{\gamma}}^2_{n+1}\right) = 0. \tag{7.92}$$

New values of $\overline{\overline{\boldsymbol{u}}}^1_{n+1}$, $\overline{\overline{\boldsymbol{u}}}^2_{n+1}$, $\overline{\overline{\xi}}^1_{n+1}$ and $\overline{\overline{\xi}}^2_{n+1}$ are then computed by (7.87), (7.88) and the corresponding $\boldsymbol{\alpha}^{(e)}_{n+1}$ is computed by (7.89). Note, that we compute the traction in (7.91)-(7.92) in the same manner as in the case of trial values, i.e. by solving the system of four algebraic equations

$$\boldsymbol{h}^{\Omega^e}\left(\boldsymbol{\sigma}(\boldsymbol{d}^{(e)}_{n+1}, \overline{\boldsymbol{\epsilon}}^{p,bip}_n, \boldsymbol{\alpha}^{(e)}_{n+1})\right) + \boldsymbol{h}^{\Gamma^e}(\boldsymbol{t}^1_{n+1}, \boldsymbol{t}^2_{n+1}) = \boldsymbol{0} \quad \Rightarrow \quad \boldsymbol{t}^1_{n+1},\ \boldsymbol{t}^2_{n+1}. \tag{7.93}$$

The end result of the above described softening plasticity procedure are the new values of parameters $\boldsymbol{\alpha}^{(e)}_{n+1}$, which influence the stress state of the whole element by giving the new values of stress in the bulk integration points as

$$\boldsymbol{\sigma}^{bip}_{n+1} = \boldsymbol{C}\left(\overline{\boldsymbol{\epsilon}}(\boldsymbol{d}^{(e),(i)}_{n+1}, \boldsymbol{\alpha}^{(e)}_{n+1}) - \overline{\boldsymbol{\epsilon}}^{p,bip}_n\right). \tag{7.94}$$

The updated values of the plastic strains are $\overline{\boldsymbol{\epsilon}}^{p,bip}_{n+1} = \overline{\boldsymbol{\epsilon}}^{p,bip}_n$.

The hardening plasticity procedure is carried out at each integration point *ip* (e.g. [Dujc and Brank, 2008]). We first provide the trial value of the stress

$$\boldsymbol{\sigma}^{trial,bip}_{n+1} = \boldsymbol{C}(\overline{\boldsymbol{\epsilon}}(\boldsymbol{d}^{(e),(i)}_{n+1}, \boldsymbol{\alpha}^{(e)}_n) - \overline{\boldsymbol{\epsilon}}^{p,bip}_n), \tag{7.95}$$

and the trial value of the yield function $\overline{\phi}^{trial,bip}$. If the trial yield criterion

$$\overline{\phi}^{trial,bip}(\boldsymbol{\sigma}^{trial,bip}_{n+1}, \overline{q}(\overline{\xi}^{bip}_n)) \overset{?}{\leq} 0 \tag{7.96}$$

is satisfied, the values of hardening plasticity local variables remain unchanged (the step is elastic)

$$\overline{\phi}^{trial,bip} \leq 0 \quad \Longrightarrow \quad \overline{\boldsymbol{\epsilon}}^{p,bip}_{n+1} = \overline{\boldsymbol{\epsilon}}^{p,bip}_n, \quad \overline{\xi}^{bip}_{n+1} = \overline{\xi}^{bip}_n. \tag{7.97}$$

In the case of violation of the trial yield criterion (7.96), we first provide the updated values of stress

$$\boldsymbol{\sigma}^{bip}_{n+1} = \left[\boldsymbol{I}_3 + \overline{\gamma}^{bip}_{n+1} 2\boldsymbol{C}\boldsymbol{A}\right]^{-1} \boldsymbol{\sigma}^{trial,bip}_{n+1}, \tag{7.98}$$

(for more details on this computation see [Ibrahimbegovic and Frey, 1993a] and [Dujc and Brank, 2008]). By using the backward Euler integration scheme we can then determine the updated values of internal variables

$$\overline{\boldsymbol{\epsilon}}^{p,bip}_{n+1} = \overline{\boldsymbol{\epsilon}}^{p,bip}_{n} + \overline{\gamma}^{bip}_{n+1} 2\boldsymbol{A}\boldsymbol{\sigma}^{bip}_{n+1}, \quad \overline{\xi}^{bip}_{n+1} = \overline{\xi}^{bip}_{n} + \overline{\gamma}^{bip}_{n+1} \frac{2}{\sigma_y} \sqrt{\left(\boldsymbol{\sigma}^{bip}_{n+1}\right)^T \boldsymbol{A}\boldsymbol{\sigma}^{bip}_{n+1}}, \tag{7.99}$$

where $\overline{\gamma}^{bip}_{n+1} = \dot{\overline{\gamma}}^{bip}_{n+1}(t_{n+1} - t_n)$. The value of the plastic multiplier $\overline{\gamma}^{bip}_{n+1}$ is determined from

$$\overline{\phi}^{ip}(\boldsymbol{\sigma}^{bip}_{n+1}(\boldsymbol{d}^{(e),(i)}_{n+1}, \overline{\boldsymbol{\epsilon}}^{p,bip}_{n+1}(\overline{\gamma}^{bip}_{n+1})), \overline{q}(\overline{\xi}^{bip}_{n+1}(\overline{\gamma}^{bip}_{n+1}))) = \overline{\phi}^{bip}(\overline{\gamma}^{bip}_{n+1}) = 0. \tag{7.100}$$

The final result of the above described procedure for hardening plasticity is the plastically admissible value of the stress $\boldsymbol{\sigma}^{bip}_{n+1}$, computed as

$$\boldsymbol{\sigma}^{bip}_{n+1} = \boldsymbol{C}\left(\overline{\boldsymbol{\epsilon}}(\boldsymbol{d}^{(e),(i)}_{n+1}, \boldsymbol{\alpha}^{(e)}_{n}) - \overline{\boldsymbol{\epsilon}}^{p,bip}_{n+1}\right). \tag{7.101}$$

and the elastoplastic tangent operator $\partial\boldsymbol{\sigma}^{bip}_{n+1}/\partial\overline{\boldsymbol{\epsilon}}^{bip,(i)}_{n+1}$. The updated values of the discontinuity parameters are $\boldsymbol{\alpha}^{(e)}_{n+1} = \boldsymbol{\alpha}^{(e)}_{n}$.

Once the local variables are computed, we turn to the global phase (a) of the iterative loop in order to provide, if needed, new iterative values of nodal displacements. First, the set of global equilibrium equations (7.45) is checked with newly computed $\boldsymbol{\sigma}^{bip}_{n+1}$ from the local phase

$$\left\| A^{N_{el}}_{e=1}[\boldsymbol{f}^{int,(e)}_{n+1} - \boldsymbol{f}^{ext,(e),(i)}_{n+1}] \right\| \overset{?}{<} tol. \tag{7.102}$$

If the convergence criterion (7.102) is satisfied, we move on to the next pseudo-time incremental step. If the convergence criterion fails, we perform a new iterative sweep within the present pseudo-time incremental step. New iterative values of nodal generalized displacements of the finite element mesh are computed by accounting for each element contribution. A single element contribution can be written as

$$\begin{bmatrix} \boldsymbol{K}^{(e)} & \boldsymbol{K}^{f\alpha} \\ \boldsymbol{K}^{hd} & \boldsymbol{K}^{h\alpha} \end{bmatrix}^{(i)}_{n+1} \begin{pmatrix} \Delta\boldsymbol{d}^{(e),(i)}_{n+1} \\ \Delta\boldsymbol{\alpha}^{(e),(i)}_{n+1} \end{pmatrix} = \begin{pmatrix} \boldsymbol{f}^{ext,(e)}_{n+1} - \boldsymbol{f}^{int,(e),(i)}_{n+1} \\ \boldsymbol{0} \end{pmatrix}, \tag{7.103}$$

where the parts of the element stiffness matrix can be formally written as

$$\begin{aligned} \boldsymbol{K}^{(e),(i)}_{n+1} &= \left(\frac{\partial\boldsymbol{f}^{int,(e)}}{\partial\boldsymbol{d}^{(e)}}\right)^{(i)}_{n+1}, \quad \boldsymbol{K}^{f\alpha,(i)}_{n+1} = \left(\frac{\partial\boldsymbol{f}^{int,(e)}}{\partial\boldsymbol{\alpha}^{(e)}}\right)^{(i)}_{n+1}, \\ \boldsymbol{K}^{hd,(i)}_{n+1} &= \left(\frac{\partial\boldsymbol{h}^{(e)}}{\partial\boldsymbol{d}^{(e)}}\right)^{(i)}_{n+1}, \quad \boldsymbol{K}^{h\alpha,(i)}_{n+1} = \left(\frac{\partial\boldsymbol{h}^{(e)}}{\partial\boldsymbol{\alpha}^{(e)}}\right)^{(i)}_{n+1}. \end{aligned} \tag{7.104}$$

The static condensation in (7.103) above allows us to form the standard form of the element stiffness matrix $\widehat{\boldsymbol{K}}^{(e),(i)}_{n+1}$ that contributes to the finite element assembly

$$A^{N_{el}}_{e=1}\left(\widehat{\boldsymbol{K}}^{(e),(i)}_{n+1}\Delta\boldsymbol{d}^{(i)}_{n+1}\right) = A^{N_{el}}_{e=1}\left(\boldsymbol{f}^{ext,(e)}_{n+1} - \boldsymbol{f}^{int,(e),(i)}_{n+1}\right), \tag{7.105}$$

where

$$\widehat{\boldsymbol{K}}_{n+1}^{(e),(i)} = \boldsymbol{K}_{n+1}^{(e),(i)} - \boldsymbol{K}_{n+1}^{f\alpha,(i)} \left(\boldsymbol{K}_{n+1}^{h\alpha,(i)}\right)^{-1} \boldsymbol{K}_{n+1}^{hd,(i)}. \tag{7.106}$$

Solution of (7.105) gives the values of iterative update $\Delta\boldsymbol{d}_{n+1}^{(e),(i)}$, which should be performed as indicated in (7.77).

7.4 Examples

In this section we provide the results of a number of numerical simulations that can illustrate a very satisfying performance of the proposed finite element. The code was generated by using symbolic manipulation code AceGen and the examples were computed by using finite element program AceFem, see [Korelc, 2007b] and [Korelc, 2007a].

7.4.1 Tension test

In this example we consider a square block of 20 cm × 20 cm × 0.1 cm subjected to uniaxial tension, see Figure 7.6. The block is made of material with Young's modulus $E = 3000$ kN/cm^2, Poisson's ratio $\nu = 0.2$ and the ultimate tensile strength $\sigma_u = 3$ kN/cm^2. The softening response is governed by the cohesive law at the discontinuity presented in Figure 7.5. We can write the law in Figure 7.5 in terms of failure criterion

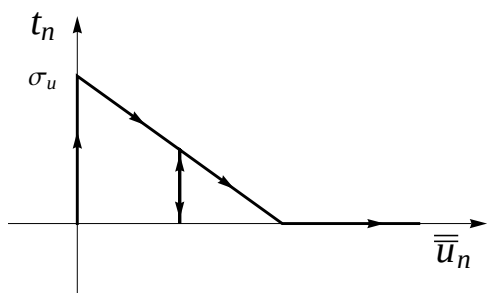

Figure 7.5: Rigid-plastic cohesive law with linear softening in tension

Slika 7.5: Kohezijski zakon (toga plastičnost z linearnim mehčanjem v nategu)

$$\overline{\overline{\phi}}(\boldsymbol{t}, \overline{\overline{q}}) = t_n - \left(\sigma_u - \overline{\overline{q}}\right) \leq 0, \tag{7.107}$$

and the bilinear softening response

$$\overline{\overline{q}} = \min\left[\sigma_u, -K_s\overline{\overline{\xi}}\right], \tag{7.108}$$

where $K_s = -45$ kN/cm^3 is the linear softening modulus and $\dot{\overline{\overline{\xi}}} = \dot{\overline{\overline{u}}}_n$, see (7.72), (7.73) and (7.107). We model the block with one finite element, which is supported at the left side

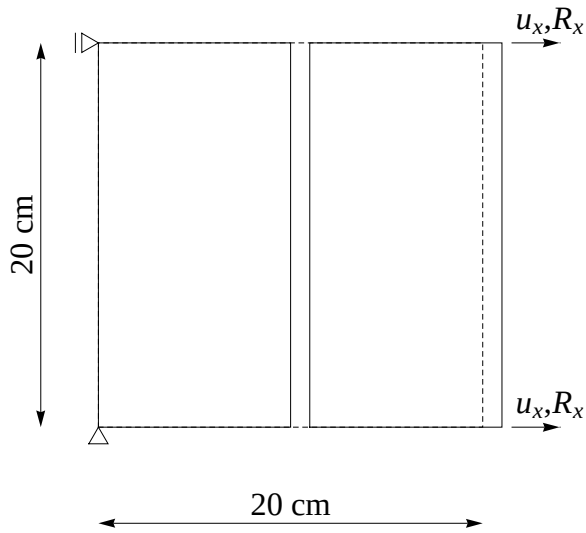

Figure 7.6: Tension test on a square block

Slika 7.6: Natezni preizkus kvadratnega bloka

and pulled, by imposing displacements, at the right side (see Figure 7.6). Once the tensile strength of the material is reached the discontinuity appears in the direction perpendicular to the maximum principal stress. Note that the behavior of the discontinuity is only defined for Mode I, i.e. the equations for the traction in the tangential direction and the corresponding jumps are not considered in the simulation. In Figure 7.7 we present the

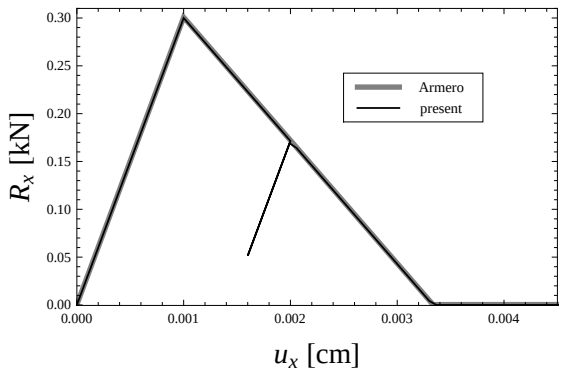

Figure 7.7: Reaction force versus imposed displacement curves

Slika 7.7: Krivulje reakcija - vsiljen pomik

reaction force versus imposed displacement diagram. Note that the results of the present formulation are in complete agreement with the results obtained in [Linder and Armero, 2007] for nonlinear elastic cohesive element, apart the local unloading branch that our

rigid-plastic formulation can capture.

7.4.2 Bending test

Next we consider the bending test of the block with the same material and geometrical properties as in the previous example. In Figure 7.8 we present the problem definition.

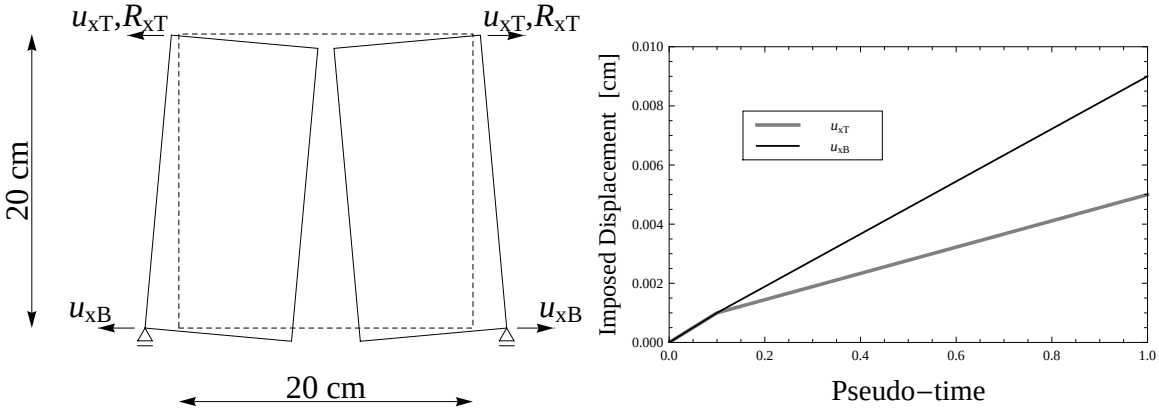

Figure 7.8: Geometry of the bending test of the square block and the imposed displacement versus pseudo-time curves

Slika 7.8: Geometrija pri upogibu kvadratnega bloka ter krivulje vsiljen pomik - psevdo čas

In the first part of loading the displacement at the top u_{xT} and the displacement at the bottom u_{xB} are applied with the same rate. The tensile strength of the material is reached at $u_{xT} = u_{xB} = 0.001$ cm and at that point the discontinuity in Mode I appears. This is followed by a non-uniform regime of loading with the rate of imposed displacement at the bottom being twice the rate of imposed displacement at the top, see right hand side of Figure 7.8. In Figure 7.9 we present the results of our simulation along with the results obtained in [Linder and Armero, 2007]. The differences in results are hardly noticeable up until the point when the first fibers of the discontinuity fail completely, resulting with $t_n = 0$. After that the results no longer coincide, since the integration scheme in [Linder and Armero, 2007] considered five integration points along the discontinuity and can therefore represent a smoother transition from the softening regime to the complete failure.

7.4.3 Partial tension test

In the above numerical examples we have evaluated the performance of the present formulation for the normal opening response. To evaluate the performance of the present

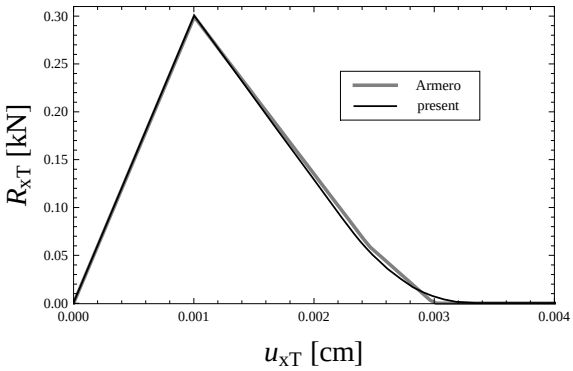

Figure 7.9: Top reaction force versus imposed top displacement curves

Slika 7.9: Krivulje reakcija na vrhu - pomik na vrhu

formulation for the tangential response, i.e. the Mode II response with linear softening at the discontinuity in its tangential direction, we consider the partial tension test presented in Figure 7.10. The block is of the same dimensions as in the previous sections, with the same value of Young's modulus $E = 3000$ kN/cm^2 but with a Poisson ratio $\nu = 0.0$. We consider a pre-existing discontinuity at the center of the block and from the beginning there is no resistance in the discontinuity, i.e. the discontinuity provides no stiffness in the tangential direction and the traction is always zero ($t_m = 0$). The equations involving the normal response are simply left out in this simulation. Again we model the block by using only one finite element. The block is supported at the two nodes on the left hand side and we pull apart the two nodes on the right hand side, thus causing a linear displacement distribution along the height of the Ω^+ region. In this way the only stress that develops is σ_{yy} which is only limited to Ω^+ region and all the other stress components remain zero throughout the test ($\sigma_{xx} = \sigma_{xy} = \sigma_{yy}^- = 0$).

In Figure 7.11 we present the stresses that develop in the element with the increase of imposed displacements. Again we compare the results of the present work with the results obtained in [Linder and Armero, 2007]. Note that the results presented in Figure 7.11 are in complete agreement. The stress component σ_{yy} in the Ω^- region is unaffected by the imposed displacements and is always equal to zero, while the stress component σ_{yy} in the Ω^+ changes with the increase of imposed displacement according to $\sigma_{yy}^+ = \frac{Eu_y}{b}$.

7.4.4 Three point bending test

In this example we consider a classical benchmark problem of a notched concrete beam under three point bending. In Figure 7.12 we present the geometry of the specimen, a

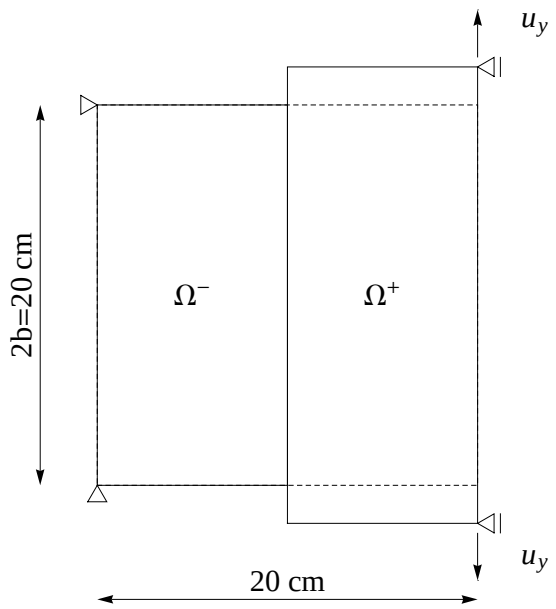

Figure 7.10: Partial tension test of the square block

Slika 7.10: Delni natezni preizkus kvadratnega bloka

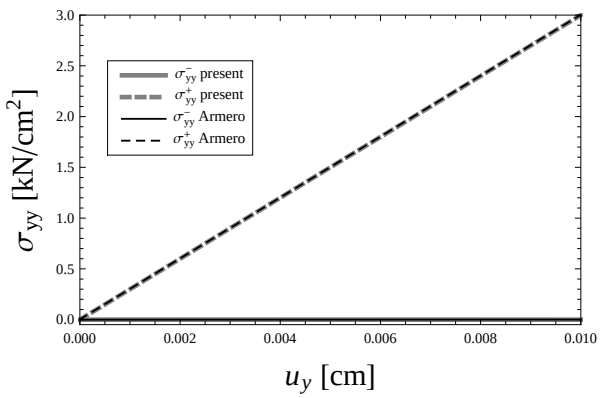

Figure 7.11: Stress at integration points in Ω^+ and Ω^- region versus imposed displacement curves

Slika 7.11: Krivulje napetosti v integracijskih točkah na območjih Ω^+ in Ω^- v odvisnosti od vsiljenega pomika

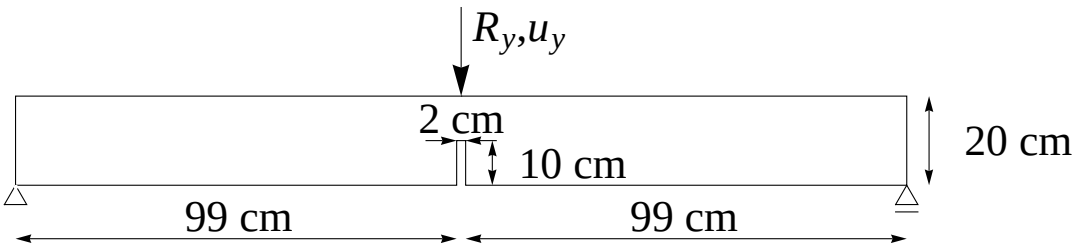

Figure 7.12: Three point bending test of a notched concrete beam

Slika 7.12: Tritočkovni upogib zarezanega betonskega nosilca

200 cm × 20 cm × 5 cm simply supported concrete beam with a 2 cm × 10 cm × 5 cm notch placed at the bottom of the beam. The beam is loaded by downward displacement imposed at the top in the center. The beam is made of material with Young's modulus $E = 3000$ kN/cm^2, Poisson's ratio $\nu = 0.2$ and the ultimate tensile strength $\sigma_u = 3.33$ kN/cm^2. The softening response is governed by the rigid-plastic cohesive law at the discontinuity presented in Figure 7.13. The law in Figure 7.13 can be also written in terms of failure

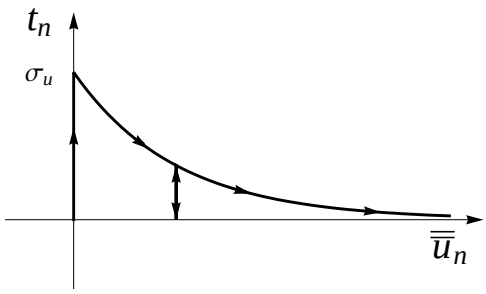

Figure 7.13: Rigid-plastic cohesive law with exponential softening in tension

Slika 7.13: Kohezijski zakon: toga plastičnost z eksponentnim mehčanjem v nategu

criterion (7.107) and the exponential softening law

$$\overline{\overline{q}} = \sigma_u \left(1 - \exp^{-\frac{\overline{\overline{\xi}}\sigma_u}{G_f}}\right), \tag{7.109}$$

where $G_f = 0.124 \cdot 10^{-2}$ kN/cm is the fracture energy. The response of the discontinuity in the tangential direction is not considered in the simulations. In Figure 7.14 we present the two different finite element meshes that were used in simulations. The coarser mesh is made of 530 finite elements and the finer one of 2186 finite elements. On the left hand side of Figure 7.15 we plot the reaction versus imposed displacement diagrams computed for both meshes. The discontinuity starts at the notch when the tensile strength of

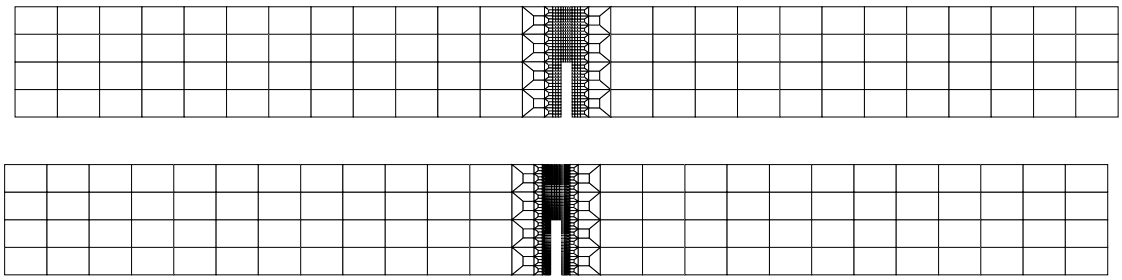

Figure 7.14: Coarse (top) and fine (bottom) finite element meshes for the three point bending test

Slika 7.14: Groba (zgoraj) in fina (spodaj) mreža končnih elementov pri tritočkovnem upogibu

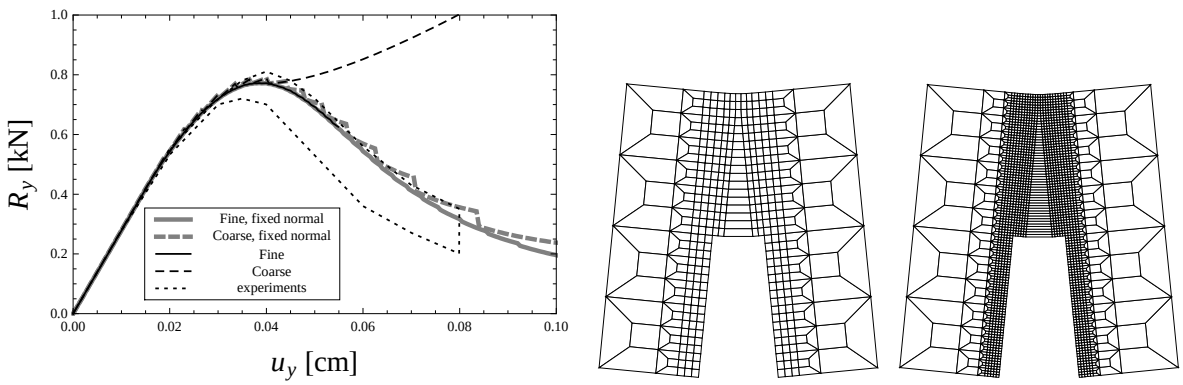

Figure 7.15: Reaction force versus imposed displacement curves and scaled (100 times) deformed meshes

Slika 7.15: Krivulje reakcija v odvisnosti od vsiljenega pomika ter povečana (100 krat) deformirana mreža

the material is reached and propagates in the direction perpendicular to the maximum principal stress, i.e. in the Mode I fashion. We have encountered a problem when using the above criterion to determine the discontinuity direction, namely the direction of the maximum principal stress at some point suddenly changes for 90 degrees. This causes a problem in convergence in the simulation with the fine mesh and a non-physical response when using the coarse mesh, see left hand side of Figure 7.15. The discontinuity direction problem was also reported in [Mosler and Meschke, 2003] and we direct the reader therein for further discussion. To obtain the solution without the discontinuity direction problem we considered a predetermined direction of the discontinuity, i.e. discontinuity can only propagate perpendicular to the length of the beam. With this modification we were able to obtain with both meshes the results that are within the experimentally established bounds of [Petersson, 1981] and [Rots et al., 1985]. The results of all simulations are given in Figure 7.15 (left). In the center and right hand side of Figure 7.15 we present the deformed configuration (scaled 100 times) of the area near the notch for both course and fine mesh.

7.4.5 Four point bending test

In this example we study the four point bending test on a beam with a notch. In Figure

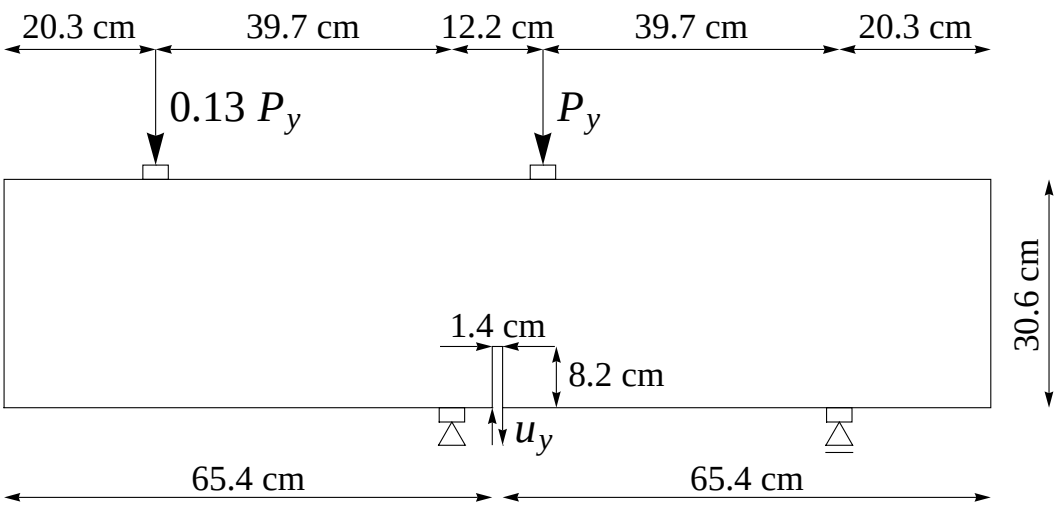

Figure 7.16: Four point bending test

Slika 7.16: Štiritočkovni upogibni test

7.16 we present the specimen geometry along with loading conditions and supports. The specimen is made of material with Young's modulus $E = 2880$ kN/cm^2, Poisson's ratio $\nu = 0.18$ and the ultimate tensile strength $\sigma_u = 2.8$ kN/cm^2. The behavior of the

discontinuity is governed by the failure criterion (7.107) and the softening law (7.108), with softening modulus being $K_s = -39.2$ kN/cm^3. In Figure 7.17 we present the mesh

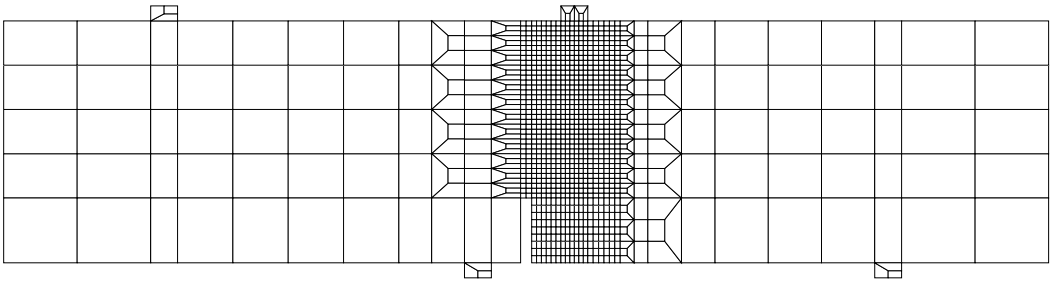

Figure 7.17: Finite element mesh for the four point bending test

Slika 7.17: Mreža končnih elementov pri štiritočkovnem upogibu

that we used in simulations. With respect to the description of the displacements jumps along the discontinuity line we considered three cases: (i) "n0 + m0" - the constant jump in displacements in both normal and tangential direction, (ii) "n0 + n1" - linear jump in displacement in normal direction only and (iii) "n0" - constant jump in displacements in normal direction only. In the mixed mode case ("n0 + m0") we considered a reduced shear stiffnes for the tangential response according to relation

$$\overline{\overline{\phi}}(t_m) = t_m - k_m \overline{\overline{u}}_m = 0, \tag{7.110}$$

where $k_m = 2.88$ kN/cm^3. The results of the simulations are presented in Figures 7.18 and

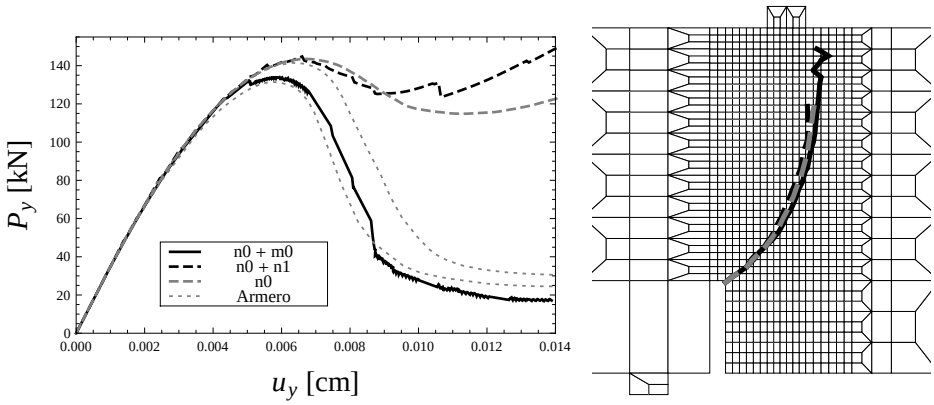

Figure 7.18: Load versus crack mouth sliding displacement curves and the corresponding crack paths

Slika 7.18: Krivulje obtežba v odvisnosti od relativnega zamika na ustju razpoke

7.19. On the left hand side of Figure 7.18 we plot the applied load - crack mouth sliding displacements curves of our simulations along with the envelope of results the we adopted from [Linder and Armero, 2007]. We can see that all the proposed formulations give a good prediction of the limit load of the structure, while only the mixed mode formulation can capture the true softening response of the structure. On the right hand side of Figure 7.18 we plot the crack paths that correspond to curves on the left hand side of the same figure.

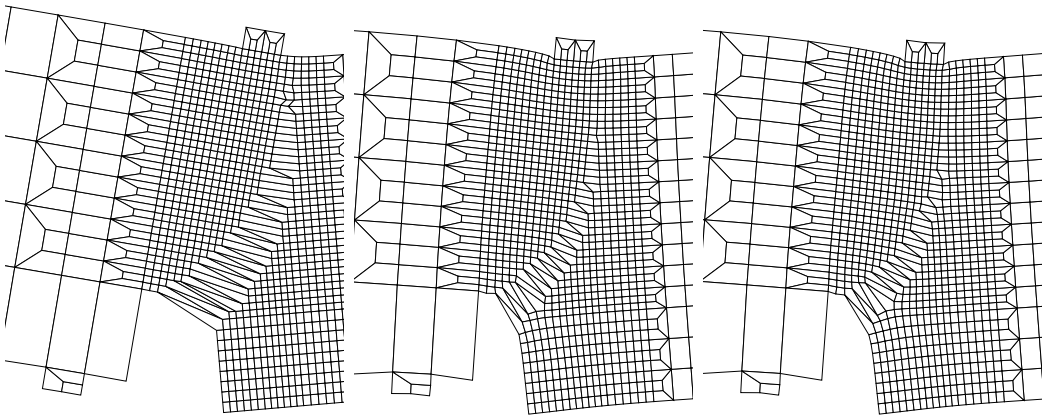

Figure 7.19: Scaled deformed mesh of the "n0 + m0" (left), "n0 + n1" (middle) and "n0" formulation

Slika 7.19: Povečane deformirane mreže za "n0 + m0" formulacijo (levo), "n0 + n1" formulacijo (sredina) in "n0" formulacijo (desno)

In Figure 7.19 we present the deformed (scaled 200 times) mesh of the area near the notch for all formulations. We claim that the crack paths presented in Figure 7.18 and the deformed meshes presented in 7.19 are in good agreement with those from [Linder and Armero, 2007].

7.4.6 Delamination

We consider a delamination test shown in Figure 7.20 as presented in [Manzoli and Shing, 2006]. The properties of the material are: Young's modulus $E = 50$ kN/cm^2 and Poisson ratio $\nu = 0.3$. We model the interface as an embedded discontinuity, whose properties are determined with the failure criterion (7.107), the ultimate tension stress $\sigma_u = 10^{-1}$ kN/cm^2, and the exponential softening law (7.109), with the fracture energy $G_f = 5 \cdot 10^{-3}$ kN/cm. The simulations are performed by using a coarse and a fine-type

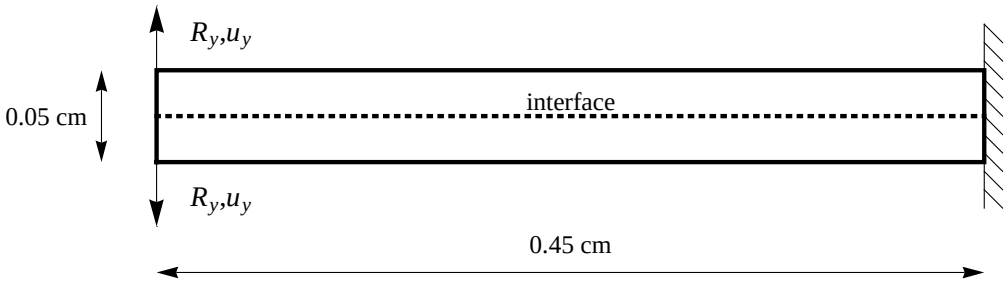

Figure 7.20: Delamination test data

Slika 7.20: Delaminacija: podatki

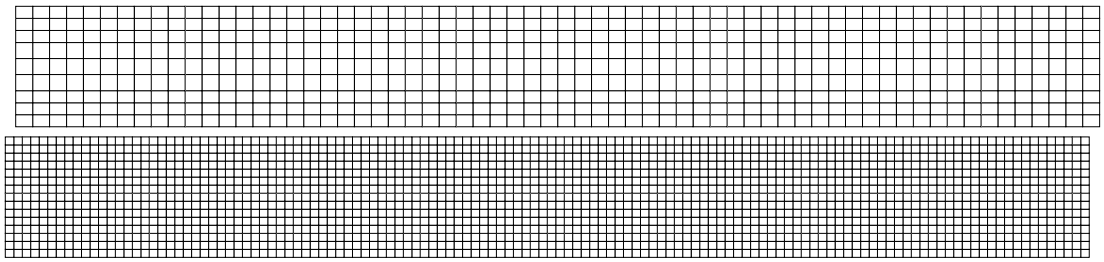

Figure 7.21: Coarse (top) and fine (bottom) finite element meshes for the delamination test

Slika 7.21: Groba (zgoraj) in fina (spodaj) mreža končnih elementov

finite element mesh, as presented in Figure 7.21. The reaction force versus imposed dis-

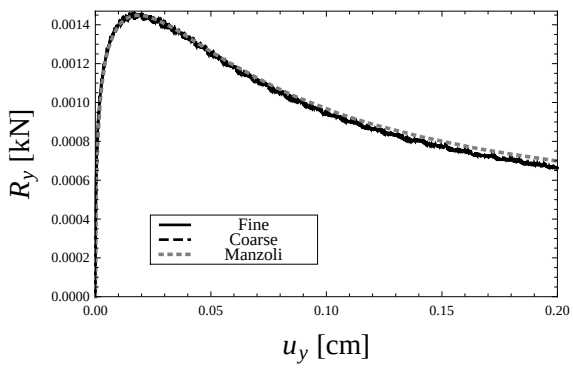

Figure 7.22: Reaction force versus imposed displacement diagram

Slika 7.22: Sila v odvisnosti od vsiljenega pomika

placement diagrams are presented in Figure 7.22. One can see, that the results of both coarse and fine mesh are in good agreement with the results obtained in [Manzoli and Shing, 2006] by using a fine mesh and a Q4SH-NU type finite element. Figure 7.23 depicts the deformed meshes that correspond to the imposed displacement $u_y = 0.2$ cm. Note that the deformed meshes are not scaled and one should for a more realistic representation use a geometrically non-linear framework, which is out of the scope of this work.

7.4.7 Elasto-plastic tension test

In the last example we consider a tension test of a metal strip. The geometry of the strip is presented in Figure 7.24 and the thickness is 0.055 cm. One of the shorter edges is built-in and the opposite edge is pulled by imposing the displacements as depicted in Figure 7.24. In this example we consider the bulk material as elastoplastic with the following properties: Young's modulus $E = 21000$ kN/cm^2, Poisson's ratio $\nu = 0.3$, yield stress $\sigma_y = 40$ kN/cm^2, ultimate stress $\sigma_u = 42$ kN/cm^2, and hardening modulus $K_h = 1000$ kN/cm^2 where we compute the stress-like variable related to isotropic hardening as

$$\overline{q} = -K_h \overline{\xi}. \tag{7.111}$$

The softening response is activated once the ultimate shear stress $\tau_u = \frac{\sigma_u}{2} = 21$ kN/cm^2 is reached and then the Mode II propagation of the discontinuity starts. The response of the discontinuity is governed by the cohesive law depicted in Figure 7.25, which one can also represent in the form of failure criterion

$$\overline{\overline{\phi}}(\boldsymbol{t}, \overline{\overline{q}}) = |t_m| - \left(\tau_u - \overline{\overline{q}}\right) \leq 0, \tag{7.112}$$

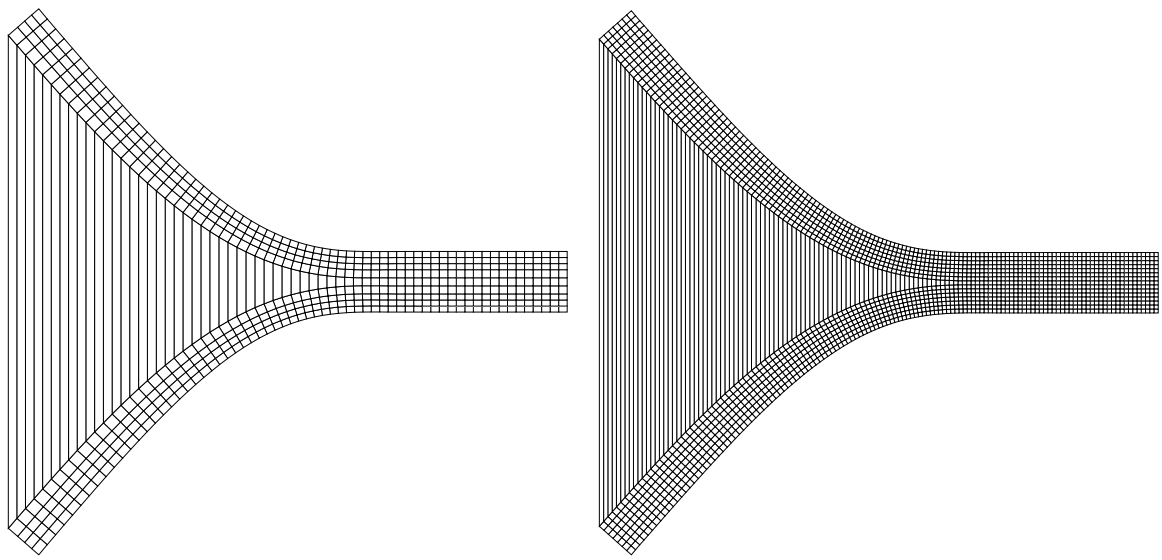

Figure 7.23: Deformed configuration of the coarse (left) and fine (right) mesh

Slika 7.23: Deformirana konfiguracija grobe (levo) in fine (desno) mreže

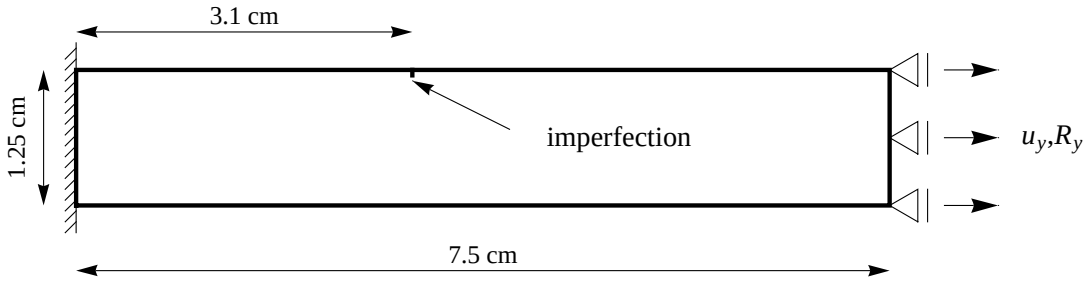

Figure 7.24: Tension test of a metal strip

Slika 7.24: Natezni preizkus metalnega traka

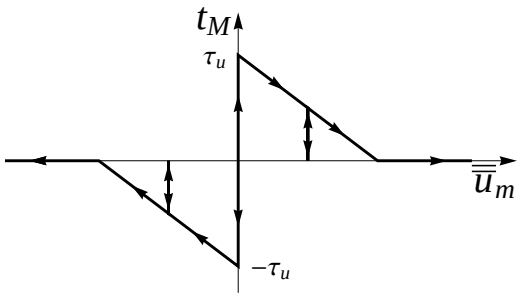

Figure 7.25: Rigid-plastic cohesive law with linear softening

Slika 7.25: Kohezijski zakon: toga plastičnost z linearnim mehčanjem

and the stress like softening variable

$$\overline{\overline{q}} = \min\left[\tau_u, -K_s\overline{\overline{\xi}}\right], \tag{7.113}$$

where $K_s = -400$ kN/cm^3 and $\dot{\overline{\overline{\xi}}} = |\dot{\overline{\overline{u}}}_n|$, see (7.72), (7.73) and (7.113). In our simulations we only considered constant jumps in the tangential direction. We assumed that there is a small imperfection in the metal strip which one can interpret as the starting point of the discontinuity (see Figure 7.24). Several simulations were made with different mesh

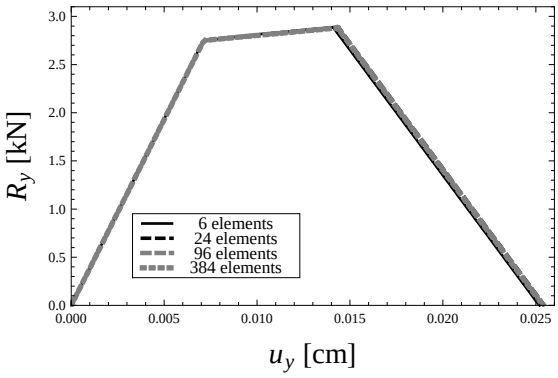

Figure 7.26: Total reaction force versus imposed displacement curves

Slika 7.26: Reakcija v odvisnosti od vsiljenega pomika

sizes ranging from 6 to 384 finite elements. The sum of reaction forces at the right edge versus imposed displacement diagrams are presented in Figure 7.26. One can see that the mesh size has very little influence on the results in this particular example. All the curves have three distinguished phases, namely the linear elastic phase, which is followed by the isotropic hardening phase and the final softening phase. Figure 7.27 depicts the

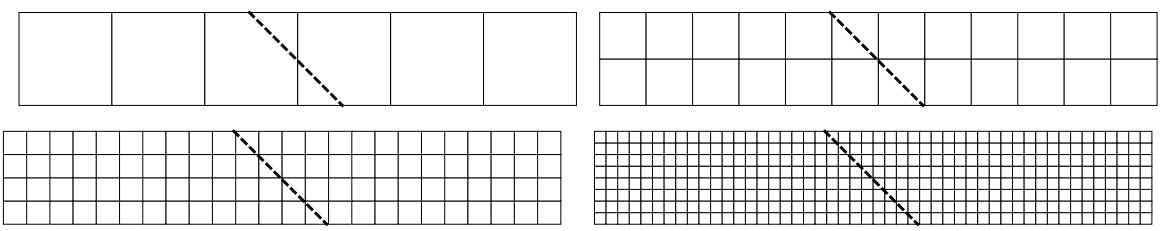

Figure 7.27: Discontinuity paths for several mesh sizes

Slika 7.27: Lega nezveznosti pri različnih mrežah

discontinuity paths for different mesh sizes. In Figure 7.28 we present the (scaled 10 times) deformed configurations for different mesh sizes.

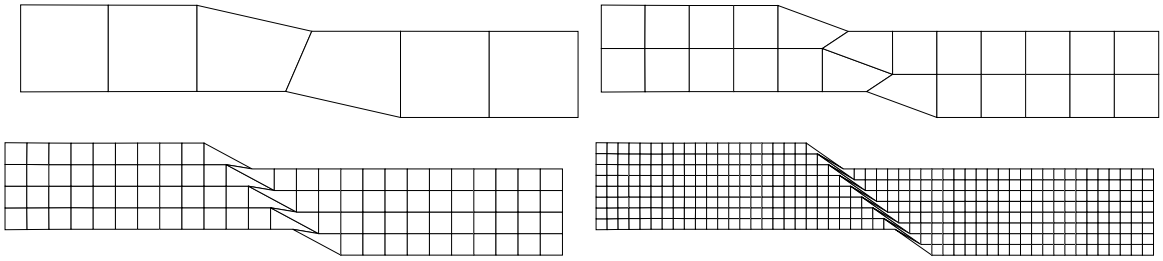

Figure 7.28: Scaled deformed configurations

Slika 7.28: Povečane deformirane konfiguracije

7.5 Concluding remarks and chapter summary

In this chapter we presented the quadrilateral two-dimensional elastoplastic finite element with embedded strong discontinuity. With the introduction of four additional parameters related to discontinuity line into the isoparametric 2D solid finite element we obtained the enriched displacement field

$$\boldsymbol{u}^h(\boldsymbol{\xi},\Gamma) = \underbrace{\sum_{a=1}^{4} N_a(\boldsymbol{\xi})\boldsymbol{d}_a}_{\boldsymbol{u}_d^h} + \underbrace{\sum_{mode} \boldsymbol{M}_{mode}(\boldsymbol{\xi},\Gamma^e)\alpha_{mode}}_{\boldsymbol{u}_\alpha^h}, \quad mode \in (n0, n1, m0, m1),$$

where we asociate the aditional parameters with the following modes of separation

- "n0" - the constant mode of separation in the normal direction,
- "n1" - the linear mode of separation in the normal direction,
- "m0" - the constant mode of separation in the tangential direction and
- "m1" - the linear mode of separation in the tangential direction.

By investigating the rigid body motion of the domains Ω^{e-} and Ω^{e+} separated with the discontinuity line Γ^e we determined the interpolation matrices for all additional modes as

$$\boldsymbol{M}_{mode} = \frac{\overline{\boldsymbol{u}}^h_{mode} - \overline{\boldsymbol{u}}^h_{d,mode}}{\overline{\alpha}_{mode}}.$$

The enriched strain field is determined as the symmetric part of the gradient of the displacement field

$$\boldsymbol{\epsilon} = \sum_{a=1}^{4} \boldsymbol{B}_a\boldsymbol{d}_a + \boldsymbol{G}_{n0}\alpha_{n0} + \boldsymbol{G}_{n1}\alpha_{n1} + \boldsymbol{G}_{m0}\alpha_{m0} + \boldsymbol{G}_{m1}\alpha_{m1}.$$

The virtual strains were determined according to

$$\hat{\boldsymbol{\epsilon}} = \sum_{a=1}^{4} \boldsymbol{B}_a \hat{\boldsymbol{d}}_a + \hat{\boldsymbol{G}}_{n0}\hat{\alpha}_{n0} + \hat{\boldsymbol{G}}_{n1}\hat{\alpha}_{n1} + \hat{\boldsymbol{G}}_{m0}\hat{\alpha}_{m0} + \hat{\boldsymbol{G}}_{m1}\hat{\alpha}_{m1},$$

where we used the following expression

$$\hat{\boldsymbol{G}}_{mode} = \boldsymbol{G}_{mode} - \frac{1}{A_{\Omega^e}} \int_{\Omega^e} \boldsymbol{G}_{mode} d\Omega,$$

in order to ensure the convergence in the spirit of the patch test. We introduced the virtual strains into the principle of virtual work and obtained the virtual work of internal forces as

$$\begin{aligned}
\delta\Pi^{int,(e)} &= t^{(e)} \int_{\Omega^e} \hat{\boldsymbol{\epsilon}}^T \boldsymbol{\sigma} d\Omega \\
&= \underbrace{\sum_{a=1}^{4} t^{(e)} \int_{\Omega^e} \hat{\boldsymbol{d}}_a^{\,T} \boldsymbol{B}_a^T \boldsymbol{\sigma} d\Omega}_{\text{standard}} + \\
&\quad \underbrace{t^{(e)} \int_{\Omega^e} \hat{\alpha}_{n0}\hat{\boldsymbol{G}}_{n0}^T\boldsymbol{\sigma} + \hat{\alpha}_{n1}\hat{\boldsymbol{G}}_{n1}^T\boldsymbol{\sigma} + \hat{\alpha}_{m0}\hat{\boldsymbol{G}}_{m0}^T\boldsymbol{\sigma} + \hat{\alpha}_{m1}\hat{\boldsymbol{G}}_{m1}^T\boldsymbol{\sigma} d\Omega,}_{\text{additional}}
\end{aligned}$$

and from the term "additional" we obtained four additional equations per finite element

$$\boldsymbol{h}^{(e)} = \boldsymbol{h}^{\Omega^e} + \boldsymbol{h}^{\Gamma^e} = \begin{bmatrix} h_{n0}^{\Omega^e} \\ h_{n1}^{\Omega^e} \\ h_{m0}^{\Omega^e} \\ h_{m1}^{\Omega^e} \end{bmatrix} + \begin{bmatrix} h_{n0}^{\Gamma^e} \\ h_{n1}^{\Gamma^e} \\ h_{m0}^{\Gamma^e} \\ h_{m1}^{\Gamma^e} \end{bmatrix} = \boldsymbol{0},$$

which ensure that all the components of the traction at the discontinuity are in equilibrium with the stress field in the element. The basic ingredients of the chosen constitutive relations for the bulk material and the discontinuity are the usual additive decomposition of regular strains into elastic and plastic part

$$\overline{\boldsymbol{\epsilon}} = \overline{\boldsymbol{\epsilon}}^e + \overline{\boldsymbol{\epsilon}}^p,$$

the free energy of the bulk material considering isotropic hardening

$$\overline{\Psi}(\overline{\boldsymbol{\epsilon}}^e, \overline{\xi}) := \overline{W}\left(\overline{\boldsymbol{\epsilon}}^e\right) + \overline{\Xi}(\overline{\xi}) = \frac{1}{2}\overline{\boldsymbol{\epsilon}}^{eT}\boldsymbol{C}\overline{\boldsymbol{\epsilon}}^e + \overline{\Xi}(\overline{\xi}),$$

the yield criterion for the bulk material

$$\overline{\phi}\left(\boldsymbol{\sigma}, \overline{q}\right) = \boldsymbol{\sigma}^T \boldsymbol{A} \boldsymbol{\sigma} - \left(1 - \frac{\overline{q}}{\sigma_y}\right)^2 \leq 0,$$

the cohesive law at the discontinuity written in terms of jump in displacements $\overline{\overline{\boldsymbol{u}}} = [\overline{\overline{u}}_n \quad \overline{\overline{u}}_m]^T$

$$\boldsymbol{t} = \boldsymbol{t}(\overline{\overline{\boldsymbol{u}}}),$$

which one can also write in terms of localization criterion

$$\overline{\overline{\phi}} = \overline{\overline{\phi}}(\boldsymbol{t}, \overline{\overline{q}}) \leq 0,$$

and the softening potential

$$\overline{\overline{\Xi}}(\overline{\overline{\xi}}).$$

The remaining ingredients of the bulk elastoplasticity were obtained by computing the plastic dissipation

$$\overline{D}^p = \boldsymbol{\sigma}^T \dot{\overline{\boldsymbol{\epsilon}}}^p + \overline{q}\dot{\overline{\xi}},$$

and by considering the principle of maximum plastic dissipation

$$\min_{\boldsymbol{\sigma}, \overline{q}} \max_{\dot{\overline{\gamma}}} \left[\overline{L}^p(\boldsymbol{\sigma}, \overline{q}, \dot{\overline{\gamma}}) = -\overline{D}^p(\boldsymbol{\sigma}, \overline{q}) + \dot{\overline{\gamma}}\overline{\phi}(\boldsymbol{\sigma}, \overline{q}) \right].$$

Similarly, we also defined the plastic dissipation at the discontinuity

$$\overline{\overline{D}} = \overline{\overline{D}}^p = \boldsymbol{t}^T \dot{\overline{\overline{\boldsymbol{u}}}} + \overline{\overline{q}}\dot{\overline{\overline{\xi}}},$$

and considered the principle of maximum plastic dissipation

$$\min_{\boldsymbol{t}, \overline{\overline{q}}} \max_{\dot{\overline{\overline{\gamma}}}} \left[\overline{\overline{L}}^p(\boldsymbol{t}, \overline{\overline{q}}, \dot{\overline{\overline{\gamma}}}) = -\overline{\overline{D}}^p(\boldsymbol{t}, \overline{\overline{q}}) + \dot{\overline{\overline{\gamma}}}\overline{\overline{\phi}}(\boldsymbol{t}, \overline{\overline{q}}) \right],$$

which is here limited to discontinuity line only. The computational procedure presented in Section 7.3 is split into the local and global phase. In the local phase we, if not already given, provide the discontinuity geometry

$$\boldsymbol{n} = \boldsymbol{n}\left(\boldsymbol{\sigma}^{avg}(\boldsymbol{d}^{(e)}_{n+1}, \overline{\boldsymbol{\epsilon}}^{p,bip}_n)\right), \quad \boldsymbol{m} = \boldsymbol{m}\left(\boldsymbol{\sigma}^{avg}(\boldsymbol{d}^{(e)}_{n+1}, \overline{\boldsymbol{\epsilon}}^{p,bip}_n)\right), \quad x_{\Gamma E},$$

by considering the average stress field in the element. The updates of the softening variables and the jumps in displacements at the discontinuity line integration points are determined by simultaneously solving the following equations

$$\overline{\overline{\phi}}^1\left(\boldsymbol{t}^1_{n+1}\left(\boldsymbol{\alpha}^{(e)}_{n+1}\left(\overline{\overline{\gamma}}^1_{n+1}, \overline{\overline{\gamma}}^2_{n+1}\right)\right), \overline{\overline{q}}\left(\overline{\overline{\xi}}^1_{n+1}\left(\overline{\overline{\gamma}}^1_{n+1}\right)\right)\right) = \overline{\overline{\phi}}^1\left(\overline{\overline{\gamma}}^1_{n+1}, \overline{\overline{\gamma}}^2_{n+1}\right) = 0,$$

$$\overline{\overline{\phi}}^2\left(\boldsymbol{t}^2_{n+1}\left(\boldsymbol{\alpha}^{(e)}_{n+1}\left(\overline{\overline{\gamma}}^1_{n+1}, \overline{\overline{\gamma}}^2_{n+1}\right)\right), \overline{\overline{q}}\left(\overline{\overline{\xi}}^2_{n+1}\left(\overline{\overline{\gamma}}^2_{n+1}\right)\right)\right) = \overline{\overline{\phi}}^2\left(\overline{\overline{\gamma}}^1_{n+1}, \overline{\overline{\gamma}}^2_{n+1}\right) = 0,$$

where we considered the following relation between the jumps in displacements evaluated at the discontinuity integration points and the kinematic parameters related to discontinuity

$$\boldsymbol{\alpha}^{(e)}(\overline{\overline{\boldsymbol{u}}}^1, \overline{\overline{\boldsymbol{u}}}^2) = \left[\frac{\overline{\overline{u}}_n^1 + \overline{\overline{u}}_n^2}{2}, \frac{\overline{\overline{u}}_n^1 - \overline{\overline{u}}_n^2}{\xi_\Gamma^1 - \xi_\Gamma^2}, \frac{\overline{\overline{u}}_m^1 + \overline{\overline{u}}_m^2}{2}, \frac{\overline{\overline{u}}_m^1 - \overline{\overline{u}}_m^2}{\xi_\Gamma^1 - \xi_\Gamma^2} \right]^T,$$

and we explicitly used the additional equilibrium equation to compute the traction at the integration points of the discontinuity

$$\boldsymbol{h}^{\Omega^e}\left(\boldsymbol{\sigma}(\boldsymbol{d}_{n+1}^{(e)}, \overline{\boldsymbol{\epsilon}}_n^{p,bip}, \boldsymbol{\alpha}_{n+1}^{(e)})\right) + \boldsymbol{h}^{\Gamma^e}(\boldsymbol{t}_{n+1}^1, \boldsymbol{t}_{n+1}^2) = \boldsymbol{0} \quad \Rightarrow \quad \boldsymbol{t}_{n+1}^1,\ \boldsymbol{t}_{n+1}^2.$$

In the local phase we also determine the updates for the hardening variables related to element integration points by solving the following equation

$$\overline{\phi}^{ip}(\boldsymbol{\sigma}_{n+1}^{bip}(\boldsymbol{d}_{n+1}^{(e),(i)}, \overline{\boldsymbol{\epsilon}}_{n+1}^{p,bip}(\overline{\gamma}_{n+1}^{bip})), \overline{q}(\overline{\xi}_{n+1}^{bip}(\overline{\gamma}_{n+1}^{bip}))) = \overline{\phi}^{bip}(\overline{\gamma}_{n+1}^{bip}) = 0.$$

In the global phase, where the single element contribution to the system of global equations is

$$\begin{bmatrix} \boldsymbol{K}^{(e)} & \boldsymbol{K}^{f\alpha} \\ \boldsymbol{K}^{hd} & \boldsymbol{K}^{h\alpha} \end{bmatrix}_{n+1}^{(i)} \begin{pmatrix} \Delta\boldsymbol{d}_{n+1}^{(e),(i)} \\ \Delta\boldsymbol{\alpha}_{n+1}^{(e),(i)} \end{pmatrix} = \begin{pmatrix} \boldsymbol{f}_{n+1}^{ext,(e)} - \boldsymbol{f}_{n+1}^{int,(e),(i)} \\ \boldsymbol{0} \end{pmatrix},$$

we determine the updates for the current iterative values of nodal displacements

$$\boldsymbol{d}_{n+1}^{(e),(i)} = \boldsymbol{d}_{n+1}^{(e),(i-1)} + \Delta\boldsymbol{d}_{n+1}^{(e),(i-1)}.$$

The static condensation allowed us to form the standard form of the element stiffness matrix

$$\widehat{\boldsymbol{K}}_{n+1}^{(e),(i)} = \boldsymbol{K}_{n+1}^{(e),(i)} - \boldsymbol{K}_{n+1}^{f\alpha,(i)} \left(\boldsymbol{K}_{n+1}^{h\alpha,(i)}\right)^{-1} \boldsymbol{K}_{n+1}^{hd,(i)},$$

thus the global solution procedure is completely the same as in the standard finite element formulation.

A finite element with embedded strong discontinuity has been presented and used to model the fracture process in two-dimensional concrete solids, delamination of composite materials and failure of ductile materials. The element has linear interpolations of the displacements jumps (in both normal and tangential directions), which are important for its locking-free response. In order to make the discontinuity propagation algorithm more robust the continuity of the discontinuity line between the elements has been enforced.

Chapter 8

Conclusion

The aim of this work is to increase the understanding of structural behavior at the limit loads and at loads that cause structural failure through the development of numerical methods like the finite element method with embedded discontinuity. In the thesis the emphasis was on the treatment of material nonlinearities and localized failure of material.

In the research work presented in the thesis we reached the following conclusions:

- We have revisited [Ibrahimbegovic et al., 1992], [Ibrahimbegovic and Frey, 1993b], [Ibrahimbegovic and Frey, 1994] and programmed a nonlinear elastic stress-resultant plate finite element for limit load analysis of reinforced concrete plates with Eurocode 2 [Eurocode 2, 2004] recommendations to describe the constitutive behavior of reinforced concrete. The results of the presented approach for the analysis of limit load of reinforced concrete plates are in good agreement with the available experimental results (which are available in the literature) for those plates, where the load is monotonically increased until the failure of the plate. The essence of this approach is that it takes into account the gradual degradation of reinforced concrete due to crushing of the concrete and the yielding of the reinforcement. Although the approach is based on the nonlinear finite element method it is relatively simple and robust. The advantage of this approach, compared to the theory of plastic lines, is the information on the displacements (limit ductility), which may be interesting for studies on limit state of serviceability.

- We have derived and programmed the small strain stress resultant elastoplastic and elastoviscoplastic plate finite element, where both isotropic and kinematic hardening were considered. We have also derived an algorithm, that unifies both inelastic formulations within one computational framework. Numerical results of the presented formulation have been compared with the stress formulation from Abaqus [Hobbit et al., 2007] as well as with the stress resultant formulation with α parameter that

takes into account gradual spreading of through-the-thickness plasticity. It has been shown that, regarding the accuracy of the limit load computation, the mesh density plays more important role than the type of elastoplastic formulation.

- We have revisited [Simo and Kennedy, 1992], [Brank et al., 1997] and programed the inelastic geometrically exact shell finite element, based on stress-resultant plasticity with isotropic and kinematic hardening. We have also derived a computational algorithm for the multi-surface plasticity of the shell stress-resultant formulation. Several numerical examples have been presented, which show a very satisfying performance of the presented approach compared to results from literature. In numerical example presented in Section 4.4.1 we have encountered some problems with convergence of the plasticity loop. We believe this was caused by the relatively large jumps between two equilibrated configurations that occur due to local buckling of the cylinder. This problem could be circumvented by a more sophisticated path following approach. In Section 4.4.3 we present the limit load analysis of rectangular plate. The comparison of the results obtained by the geometrically nonlinear shell formulation with the results of the geometrically linear plate formulation presented in Chapter 3 show that geometrically nonlinear effects can be significant when analyzing thin metal plates.

- We have derived and programmed the elastoplastic Euler-Bernoulli beam finite element with embedded discontinuity. We also presented a sequential multi-scale procedure to obtain the beam constitutive model parameters. The multi-scale procedure belongs to the class of weak coupling methods, since we carry out the sequential computations. The results of the shell model computations, accounting for material and geometric localized instability, are stored to be used within the beam model softening response. As presented by numerical simulations, performance of the proposed multi-scale computational approach is very satisfying. One of its main features is that detection and development of the softening plastic hinges in the frame is fully automatic, and spreads gradually in accordance with stress redistribution in the course of the nonlinear analysis. When analyzing frame structures, we noticed that the size of the load step has an influence on the results in the softening stage of the structure. If the step is too big, several discontinuities can appear simultaneously, which leads to convergence problems or to an equilibrated configuration, which would not have been encounter if smaller load steps had been used. In order to circumvent the above mentioned problems, we adapted the size of the load step, so that only one new discontinuity can appear in the frame within one load step. One possibility for the future work in the context of failure analysis

of frame structures is a development of a new formulation, where the multi-scale procedure is carried out simultaneously.

- We have derived and programmed an elastoplastic quadrilateral two-dimensional finite element with embedded strong discontinuity. The discontinuity kinematics allow to model linear jumps in both normal and tangential displacements along the discontinuity line. In one of the early versions of the derived formulation we allowed the appearance of the discontinuity in any finite element, if the stress level in that element triggered the softening response. This approach often led to convergence problems if several discontinuities appeared at once or to an over stiff response, if the discontinuities in the neighboring elements were not aligned properly. In order to make the discontinuity propagation algorithm more robust, the continuity of the discontinuity line between the elements has been enforced. We performed several numerical simulations where we modeled the crack growth in brittle materials and the delamination of the composite materials. The comparison shows that of our results are in good agreement with those from literature. The proposed formulation can be also used to model the failure of ductile materials where localized shear bands form. The results of our simulations show that the results are independent of the mesh. The convergence of the presented formulation depends on the problem of interest. When analyzing only one finite element, we did not encounter any problems, while the analyses of a more complex structures sometimes demanded a change of the load step (either smaller or larger) in order to obtain a converged configuration. It still remains an opened question, how to make the approach more robust. In numerical simulation presented in Section 7.4.4 we encountered a problem of determining the proper direction of the crack growth. This could be avoided with a formulation, where the direction of the crack growth would be determined by considering the stress state in the patch of the elements instead of only using one element. With some minor modifications of the present formulation one would obtain a formulation that is suitable for analysis of failure in soils.

- Finally, we should mention that all finite elements have been generated by the AceGen [Korelc, 2007b] computer program for symbolic expression manipulation and that all the numerical simulations have been preformed in the AceFem [Korelc, 2007a] computer program. These programs have been found to offer a versatile environment for fast production and testing of new finite element formulations.

Razširjeni povzetek

Najbolj pogosto uporabljeno orodje za računanje obnašanja konstrukcij je metoda končnih elementov. To je numerična metoda, s katero rešujemo robni problem (t.j. parcialne diferencialne enačbe s pripadajočimi robnimi pogoji), ki opisuje določen fizikalni problem. Osnovni gradnik te metode je t.i. končni element. Z mrežo končnih elementov iščemo aproksimacijo rešitve na območju, ki ga obravnavamo. V našem primeru opišemo z mrežo končnih elementov celo konstrukcijo ali pa samo del konstrukcije (konstrukcijski element), ki ga analiziramo. Popolna trodimezionalna analiza celotne konstrukcije, pri kateri bi upoštevali njeno točno geometrijo in bi vsebovala podrobne opise vseh geometrijsko in materialno nelinearnih pojavov (npr. plastifikacijo jekla, razpokanje betona, zdrs med betonom in jekleno ojačitvijo, lokalno odpoved materiala, velike pomike in rotacije, lokalni in globalni uklon, ...) je, kljub vedno bolj zmogljivim računalnikom in vedno boljšim modelom za opis omenjenih nelinearnih pojavov, še vedno neizvedljiva, hkrati pa tudi ni smiselna. Pri modeliranju tako privzamemo določeno mero fizikalne in matematične idealizacije. Ponavadi trorazsežno telo (v našem primeru konstrukcijski element), z upoštevanjem določenih kinematičnih predpostavk, modeliramo kot dvodimenzionalno (stene, plošče in lupine), oziroma kot enodimenzionalno (nosilci, palice). V ta namen uporabljamo končne elemente za stene, plošče, lupine, nosilce in palice. Nadalje si modeliranje obnašanja konstrukcij in konstrukcijskih elementov pogosto poenostavimo z uporabo približnih ali poenostavljenih konstitutivnih modelov.

V disertaciji so izpeljani različni končni elementi, ki so primeri za uporabo pri analizi obnašanja konstrukcije (ali konstrukcijskih elementov) vse do njene popolne porušitve. V ta namen se najprej ukvarjamo z neelastičnimi materialnimi modeli za opis dveh tipičnih gradbenih materialov - jekla in armiranega betona. Nato pa se ukvarjamo še z opisom lokalne odpovedi materiala, ki postopoma vodi k mehčanju konstrukcije, torej k takšnemu odzivu, ko se njeni pomiki povečujejo ob hkratnem zmanjševanju obtežbe. Za določitev mejne obtežbe (t.j. tiste obtežbe, ki jo konstrukcija še lahko prenese, preden se začne njeno mehčanje), smo tako razvili nelinearno elastične ter elastoplastične materialne modele za različne konstrukcijske elemente. Skupna lastnost vseh izpeljanih materialnih modelov je v tem, da so določeni na nivoju rezultant napetosti (t.j. notranjih sil), kar jih naredi

robustne in računsko manj zahtevne.

Ko pa se lotimo obravnavati obnašanje konstrukcije vse do njene popolne porušitve, pa uporaba nelinearno elastičnih oziroma elastoplastičnih modelov ne zadostuje več. Do začetka porušitve konstrukcije (oziroma njenega dela) ponavadi pride zaradi zelo lokalnih pojavov, ki jih z uporabo materialnih modelov za zvezno snov ni moč primerno opisati. Kot primer si lahko zamislimo večjo razpoko, ki nastane v betonski steni na mestih natezne odpovedi betona. Širina te razpoke je zelo majhna v primerjavi s preostalimi dimenzijami stene, vendar ima vpliv na obnašanje stene, saj v trdno telo vnese nezveznost. Le-to pa je zelo težko opisati s standardno metodo končnih elementov. Z vključitvijo singularnih polj, s katerimi opisujemo območja takšnih nezveznosti (t.j. območja lokalne porušitve materiala), v standardno metodo končnih elementov, pa lahko pridemo do robustnega načina za opis lokalne odpovedi materiala. Pridemo do t.i. metode končnih elementov z vključenimi nezveznostmi (angl. "embedded discontinuity finite element method").

V doktorski disertaciji smo si zastavili več nalog povezanih z analizo mejne nosilnosti konstrukcije, oziroma s porušno analizo konstrukcij. Reševanje vsake naloge je prikazano v svojem poglavju. Za prvo nalogo smo si izbrali izpeljavo končnega elementa za račun mejne nosilnosti armiranobetonskih plošč. V že obstoječo računalniško kodo za končni element na osnovi Reissner-Mindlinove teorije plošč, ki je predstavljen v [Bohinc et al., 2009], smo vgradili materialni model za armiranobetonske plošče, ki je opisan v [Ibrahimbegovic et al., 1992], [Ibrahimbegovic and Frey, 1993b] ter [Ibrahimbegovic and Frey, 1994], s tem da smo upoštevali določila Evrokoda 2 [Eurocode 2, 2004] za opis konstitutivnega obnašanja armiranega betona. S tem smo prišli do robustnega in relativno enostavnega modela za materialno nelinearno analizo armiranobetonskih plošč, s katerim lahko ocenimo njihovo mejno nosilnost, kar ima precejšnjo praktično vrednost.

Druga naloga je bila konsistentna izpeljava elastoplastičnega in elastoviskoplastičnega materialnega modela za plošče, ki upoštevata tako izotropno kot tudi kinematično utrjevanje in sta določena z rezultantami napetosti. Izpeljali smo nov numerični algoritem, ki hkrati zajema tako elastoplastično kot tudi elastoviskoplastično formulacijo. Oba materialna modela smo nato vgradili v že omenjeni končni element na osnovi Reissner-Mindlinove teorije plošč. S tem smo si omogočili materialno nelinearno analizo metalnih plošč, ki ima prav tako praktično vrednost.

Tretja naloga je bila izpeljava geometrijsko in materialno nelinearne (elastoplastične) formulacije za geometrijsko točne lupine, ki upošteva tako izotropno kot tudi kinematično utrjevanje in je določena z rezultantami nepetosti. Poseben poudarek je bil na izpeljavi točnega plastičnega algoritma za elastoplastičnost lupin z rezultantami napetosti, ki vsebuje dve funkciji tečenja. V obstoječi geometrijsko točni končni element za lupine (glej [Brank et al., 1995] in [Brank and Ibrahimbegovic, 2001]) smo nato vgradili nee-

lastični materialni model s pripadajočimi novimi algoritmi.

Prve tri naloge so se torej nanašale na materialno nelinearno analizo plošč in lupin iz kovin in armiranega betona. Modeli, ki omogočajo tovrstne analize imajo precejšnje praktične vrednosti, vendar ne omogočajo porušne analize, t.j. analize, ki bi omogočala popolno porušitev konstrukcije ali konstrukcijskega elementa. Takšnih analiz pa smo se lotili v naslednjih nalogah.

Četrta naloga se je tako nanašala na porušno analizo ravninskih okvirnih konstrukcij. Ta tema ima praktično vrednost pri sodobnem projektiranju, še posebej pri potresnem inženirstvu. Uporabili smo metodo končnih elementov z vgrajenimi nezveznostmi. Cilj je bil izpeljava novega elastoplastičnega končnega elementa za ravninske nosilce z vključeno nezveznostjo v rotaciji. Končni element je bil izpeljan na osnovi Euler-Bernoullijeve teorije nosilcev. Ker smo tudi v tem primeru neelastične materialne modele izpeljali na nivoju rezultant napetosti, smo se srečali s problemom določitve potrebnih materialnih parametrov. V ta namen smo uporabili geometrijsko in materialno nelinearne končne elemente za lupine. Izkazalo se je, da tako konsistentno izpeljani končni elementi lahko učinkovito nadomestijo standardne končne elemente, ki se uporabljajo za porušno analizo okvirjev, pri katerih se vsa nelinearnost veže na vzmeti (ponavadi locirane na obeh koncih končnega elementa).

Zadnja naloga v okviru doktorske disertacije se je nanašala na izpeljavo nove družine štirivozliščnih ravninskih končnih elementov, ki upoštevajo tako plastično utrjevanje kot tudi lokalno plastično mehčanje materiala. Zopet smo uporabili metodo končnih elementov z vgrajenimi nezveznostmi. Posebnost izpeljanih novih končnih elementov je v tem, da so skoki v pomikih na mestu nezveznosti linearni tako v smeri normale, kot v smeri tangente na nezveznost. Večina obstoječih ravninskih končnih elementov z vključenimi nezveznostmi namreč upošteva zgolj konstantne skoke v pomikih znotraj enega elementa. Poleg tega je ponavadi za odziv zvezne snovi upoštevan zgolj linearno elastični materialni model. Z novimi končnimi elementi je mogoče slediti nastanku in širjenju razpoke v krhkih dvodimenzijskih telesih ali formiranju lokaliziranega plastificiranega območja v duktilnih dvodimenzijskih telesih. Rešitve, ki jih dobimo z novimi končnimi elementi so neodvisne od mreže končnih elementov.

Analiza mejne obtežbe armiranobetonskih plošč

V drugem poglavju se ukvarjamo z materialno nelinearno analizo armiranobetonskih plošč z metodo končnih elementov. Za armirani beton uporabimo konstitutivni zakon, zapisan na nivoju rezultant napetosti. Ideja je povzeta po [Ibrahimbegovic et al., 1992], [Ibrahimbegovic and Frey, 1993b], [Ibrahimbegovic and Frey, 1994]; spremenimo jo v toliko, da

uporabimo priporočila Evrokoda 2 [Eurocode 2, 2004] za opis konstitutivnega modela betona.

S tem pristopom lahko identificiramo mejno stanje armiranobetonske plošče pri monotonem povečevanju obtežbe plošče; npr. pri obremenitvi zaradi lastne in stalne obtežbe. Če pa je obteževanje plošče takšno, da je prisotno veliko pomembnega razbremenjevanja in ponovnega obremenjevanja, se moramo omenjenemu načinu računanja mejne obtežbe odpovedati. Omeniti je potrebno, da je že pri monotonem povečevanju verjetno, da bo prišlo do lokalnega razbremenjevanja zaradi lokalne spremembe togosti plošče, vendar predpostavimo, da so neelastični efekti zaradi takšnega razbremenjevanja zanemarljivi. Poleg tega predpostavimo tudi, da pomiki plošče niso tako veliki, da bi prišli do izraza membranski efekti, povezani s pojavom osnih (membranskih) sil v plošči. Takšne pojave pri analizi mejnih nosilnosti armiranobetonskih plošč lahko obravnavamo kot sekundarne in zato zanemarljive.

Konstitutivni model za armirani beton je razdelejen na dve stanji: na stanje nerazpokanega betona (stanje I) in na stanje razpokanega betona (stanje II). Razpokano stanje se aktivira, ko pride do porušitve betona v natezno najbolj obremenjenem vlaknu prereza. V stanju I upoštevamo linearno elastične konstitutivne zveze za izotropen material

$$\boldsymbol{q} = \boldsymbol{C}_S \boldsymbol{\gamma}, \quad \boldsymbol{m} = \boldsymbol{C}_B \boldsymbol{\kappa},$$

kjer sta $\boldsymbol{m}$ in $\boldsymbol{q}$ vektorja momentov in prečnih sil, $\boldsymbol{C}_S$ in $\boldsymbol{C}_S$ pa sta matriki elastičnih konstant za plošče (glej (2.4)). Podobno kot v stanju I, tudi v stanju II upoštevamo linarno elastičen odziv za strižni del

$$\boldsymbol{q} = \boldsymbol{C}_S \boldsymbol{\gamma},$$

medtem ko pri upogibnem delu zanemarimo vpliv Poissonovega količnika in upoštevamo neodvisna odziva v dveh pravokotnih smereh, določenih s kotoma ϕ in $\phi + \frac{\pi}{2}$, v obliki

$$\overline{m} = \overline{m}(\overline{\kappa}),$$

kjer je $\overline{\kappa}$ vrednost ukrivljenosti v smeri ϕ oz. $\phi + \frac{\pi}{2}$, $\overline{m}$ pa pripadajoči moment. Odziv v teh dveh smereh je določen s količino efektivne armature v teh smereh (slika 2.4)

$$a_\phi = \sum_i a_i \cos^2(\phi - \alpha_i), \quad a_{\phi+\frac{\pi}{2}} = \sum_i a_i \cos^2(\phi + \frac{\pi}{2} - \alpha_i),$$

kjer je a_i količina armature v plošči položene v smeri α_i, in z odsekoma linearnim diagramom, ki je določen z naslednjimi stanji prereza:

- pojav prve razpoke v betonu (točka A na sliki 2.3),

- začetek plastifikacije armature (točka B na sliki 2.3),
- porušitev betona v tlaku (točka C na sliki 2.3).

Ločimo med izotropno armiranimi ploščami, pri katerih je efektivna količina armature enaka za vsak kot ϕ (razdelek 2.3.1)

$$a_{\phi}^{isotropic} = const.,$$

in anizotropno armiranimi ploščami, pri katerih efektivna količina armature ni konstantna

$$a_{\phi}(\phi) \neq const..$$

Pri slednjem obravnavamo dve možnosti (razdelek 2.3.2): s fiksno smerjo razpoke ter z rotirajočo smerjo razpoke. Glede na gornje kriterije določimo kot ϕ.

Uporabljen pristop za račun mejne obtežbe armiranobetonskih plošč se izkaže kot zelo zadovoljiv. Rezultati analiz se dobro ujemajo z razpoložljivimi eksperimentalnimi rezultati (ki so na voljo v strokovni literaturi) za tiste plošče, kjer se je obtežba monotono povečevala vse do porušitve (razdelek 2.4). Bistvo naše analize je, da upošteva postopno degradacijo armiranega betona zaradi razpokanja betona in zaradi plastifikacije armature. Čeprav analiza temelji na nelinearni metodi končnih elementov, je razmeroma preprosta in robustna in zato tudi uporabna v projektantski praksi.

Neelastična analiza metalnih plošč

V tretjem poglavju izpeljemo materialni model za elastoplastične plošče, ki upošteva tako izotropno kot tudi kinematično utrjevanje. Model je določen z rezultantami nepetosti (notranjimi silami). Elastoplastično formulacijo nadgradimo v elastoviskoplastično tipa Perzyna, glej npr. [Kojić and Bathe, 2005] in [Kleiber and Kowalczyk, 1996]. Oba neelastična modela sta izpeljana ob predpostavki hipnega elastičnega odziva in principa maksimalne plastične disipacije (za plastičnost) oz. kazenske oblike principa maksimalne plastične disipacije (za viskoplastičnost), glej npr. [Ibrahimbegovic et al., 1998].

Osnovni gradniki tega konstitutivnega modela so:

- Razcep celotnih deformacij $\boldsymbol{\varepsilon}$ na elastični $\boldsymbol{\varepsilon}^e$ in plastični $\boldsymbol{\varepsilon}^p$ (viskoplastični $\boldsymbol{\varepsilon}^{vp}$) del

$$\boldsymbol{\varepsilon} = \boldsymbol{\varepsilon}^e + \boldsymbol{\varepsilon}^{p,vp}.$$

- Predpostavka, da ima deformacijska energija naslednjo obliko, ki vsebuje tudi člena zaradi izotropnega in kinematičnega utrjevanja

$$\psi\left(\boldsymbol{\varepsilon}^e, \xi, \check{\varkappa}\right) = \frac{1}{2}\boldsymbol{\varepsilon}^{e,T}\boldsymbol{C}\boldsymbol{\varepsilon}^e + \Xi\left(\xi\right) + \frac{1}{2}\left(\frac{2}{3}H_{kin}\right)\check{\varkappa}^T\boldsymbol{D}\check{\varkappa},$$

kjer je $\boldsymbol{C}$ matrika elastičnih konstant za plošče (glej (3.9)), ξ parameter, ki določa izotropno utrjevanje, Ξ je funkcional povezan z izotropnim utrjevanjem, H_{kin} konstanta kinematičnega utrjevanja, $\boldsymbol{D}$ je matrika konstant za kinematično utrjevanje (glej (3.10)) in $\check{\varkappa}$ je vektor "zaostalih" deformacij (t.i. "back-strain").

- Funkcija tečenja ϕ, določena z rezultantami napetosti $\boldsymbol{\sigma}$, q in $\boldsymbol{\alpha}$

$$\phi\left(\boldsymbol{\sigma}, q, \boldsymbol{\alpha}\right) = \left(\boldsymbol{\sigma} + \boldsymbol{\alpha}\right)^T \boldsymbol{A}\left(\boldsymbol{\sigma} + \boldsymbol{\alpha}\right) - \left(1 - \frac{q}{\sigma_y}\right)^2 = 0,$$

kjer je q napetosti podoben parameter povezan z izotropnim utrjevanjem, $\boldsymbol{\alpha}$ vector napetosti podobnih količin povezanih s kinematičnim utrjevanjem, $\boldsymbol{A}$ je matrika konstant, s katerimi opišemo izotropno plastičnost pri ploščah (glej (3.12)), σ_y pa je napetost na meji tečenja pri enoosnem preizkusu.

- Princip maksimalne plastične disipacije $\mathcal{D}^p$, ki ga pri plastičnosti opišemo z iskanjem minimuma naslednjega funkcionala

$$\mathcal{L}^p\left(\boldsymbol{\sigma}, q, \boldsymbol{\alpha}, \dot{\gamma}\right) = -\mathcal{D}^p\left(\boldsymbol{\sigma}, q, \boldsymbol{\alpha}\right) + \dot{\gamma}\phi\left(\boldsymbol{\sigma}, q, \boldsymbol{\alpha}\right),$$

kjer je $\dot{\gamma}$ Lagrangev množitelj.

- Kazenska oblika principa maksimalne plastične disipacije, ki jo v primeru viskoplastičnosti zapišemo v obliki iskanja minimuma naslednjega funkcionala

$$\mathcal{L}^{vp}\left(\boldsymbol{\sigma}, q, \boldsymbol{\alpha}\right) = -\mathcal{D}^{vp}\left(\boldsymbol{\sigma}, q, \boldsymbol{\alpha}\right) + \frac{1}{\eta} g\left(\phi\left(\boldsymbol{\sigma}, q, \boldsymbol{\alpha}\right)\right),$$

kjer je η parameter viskoznosti in

$$g\left(\phi\right) = \begin{cases} \frac{1}{2}\phi^2 & \text{če } \phi \geq 0 \\ 0 & \text{če } \phi < 0 \end{cases},$$

kazenski funkcional.

Reševanje se izvede v časovnih korakih. Nove vrednosti plastičnih spremenljivk na koncu tipičnega časovnega koraka $[t_n, t_{n+1}]$ določimo z rešitvijo ene skalarne enačbe

$$\phi_{n+1}((\boldsymbol{\sigma}_{n+1} + \boldsymbol{\alpha}_{n+1})\left(\gamma_{n+1}\right), q_{n+1}\left(\gamma_{n+1}\right)) = \phi_{n+1}\left(\gamma_{n+1}\right) = 0 \rightarrow \overline{\gamma}_{n+1},$$

kjer je γ_{n+1} plastični množitelj, $\overline{\gamma}_{n+1}$ pa njegova skonvergirana vrednost na koncu koraka. V primeru viskoplastične analize zgornjo enačbo zamenjamo z

$$-\frac{\eta}{\Delta t}\gamma_{n+1} + \phi_{n+1}\left(\gamma_{n+1}\right) = 0 \rightarrow \overline{\gamma}_{n+1},$$

kjer je $\Delta t = t_{n+1} - t_n$. V kolikor v viskoplastični formulaciji postavimo viskozni parameter na $\eta = 0$, dobimo plastično formulacijo in tako z enim računskim algoritmom zajamemo obe neelastični formulaciji. Rezultate naših formulacij primerjamo (glej razdelek 3.4) z rezultati formulacije, ki je določena na nivoju napetosti [Hobbit et al., 2007], kakor tudi z rezultati formulacije, določene na nivoju rezultant napetosti s parametrom α, ki upošteva postopno širjenje plastificiranega območja v smeri debeline plošče. Pokazalo se je, da ima gostota mreže končnih elementov večji vpliv na nivo limitne obtežbe, kot pa izbira same formulacije.

Neelastična analiza metalnih lupin

V četrtem poglavju se ukvarjamo z elastoplastično analizo tankih metalnih lupin z metodo končnih elementov. Vse konstitutivne zveze so napisane na nivoju rezultat napetosti, s čemer se število integracijskih točk po debelini lupine zmanjša na vsega eno, kar naredi analizo mnogo hitrejšo v primerjavi s pristopom, ki je določen z napetostmi, glej npr. [Brank et al., 1997]. Podoben pristop je bil z uporabo nekoliko drugačnega končnega elementa in z drugačnim utrjevanjem že prikazan v [Simo and Kennedy, 1992].

Osnovni gradniki konstitutivnega modela so:

- Razcep celotnih deformacij $\boldsymbol{\varepsilon}$ na elastični $\boldsymbol{\varepsilon}^e$ in plastični $\boldsymbol{\varepsilon}^p$ del

$$\boldsymbol{\varepsilon} = \boldsymbol{\varepsilon}^e + \boldsymbol{\varepsilon}^p.$$

- Predpostavka, da ima deformacijska energija naslednjo obliko, ki vsebuje tudi člena zaradi izotropnega in kinematičnega utrjevanja

$$\psi\left(\boldsymbol{\varepsilon}^e, \xi^I, \check{\boldsymbol{\varkappa}}\right) = \frac{1}{2}\boldsymbol{\varepsilon}^{e,T}\boldsymbol{C}\boldsymbol{\varepsilon}^e + \Xi\left(\xi^I\right) + \frac{1}{2}\boldsymbol{\varkappa}^T\boldsymbol{D}\boldsymbol{\varkappa},$$

  kjer je $\boldsymbol{C}$ matrika elastičnih konstant za lupine (glej (4.31)), ξ^I parameter, ki določa izotropno utrjevanje, Ξ je funkcional povezan z izotropnim utrjevanjem, $\boldsymbol{D} = \frac{2}{3}H_{kin}\boldsymbol{I}_8$ je matrika konstant za kinematično utrjevanje, H_{kin} je konstanta kinematičnega utrjevanja, $\boldsymbol{I}_8$ je enotska matrika velikosti 8×8 in $\check{\boldsymbol{\varkappa}}$ je vektor "zaostalih" deformacij.

- Funkcija tečenja ϕ, določena z rezultantami napetosti $\boldsymbol{\sigma}$, ki jo omejujeta dve ploskvi (slika 4.1)

$$\phi_\mu\left(\boldsymbol{\sigma}, q, \boldsymbol{\alpha}\right) = \left(\boldsymbol{\sigma} + \boldsymbol{\alpha}\right)^T \boldsymbol{A}_\mu\left(\boldsymbol{\sigma} + \boldsymbol{\alpha}\right) - \left(1 - \frac{q}{\sigma_y}\right)^2 \qquad \mu = 1, 2,$$

kjer je q napetosti podoben parameter povezan z izotropnim utrjevanjem, $\boldsymbol{\alpha}$ vector napetosti podobnih količin povezanih s kinematičnim utrjevanjem, $\boldsymbol{A}_\mu$ je matrika konstant, s katerimi opišemo izotropno plastičnost pri lupinah (glej (4.33)), σ_y pa je napetost na meji tečenja pri enoosnem preizkusu.

- Plastična disipacija
$$\mathcal{D}^p = \boldsymbol{\sigma}^T \dot{\boldsymbol{\varepsilon}}^p + q\dot{\xi}^I + \boldsymbol{\alpha}^T \dot{\boldsymbol{\varkappa}} \geqslant 0.$$

- Princip maksimalne plastične disipacije, ki ga opišemo z iskanjem minimuma naslednjega funkcionala
$$\mathcal{L}^p\left(\boldsymbol{\sigma}, q, \boldsymbol{\alpha}, \dot{\gamma}_1, \dot{\gamma}_2\right) = -\mathcal{D}^p\left(\boldsymbol{\sigma}, q, \boldsymbol{\alpha}\right) + \sum_{\mu=1}^{2} \dot{\gamma}_\mu \phi_\mu\left(\boldsymbol{\sigma}, q, \boldsymbol{\alpha}\right),$$
kjer sta $\dot{\gamma}_1$ in $\dot{\gamma}_2$ Lagrangeva množitelja.

Notranje spremenljivke računamo na dva načina (glej razdelek 4.3.2). Pri prvem načinu rešujemo le enačbe povezane s funkcijo tečenja
$$\boldsymbol{R}^p\left(\gamma_{1,n+1}, \gamma_{2,n+1}\right) = \begin{bmatrix} \phi_1(\gamma_{1,n+1}, \gamma_{2,n+1}) \\ \phi_2(\gamma_{1,n+1}, \gamma_{2,n+1}) \end{bmatrix} = \mathbf{0},$$
ki jih zapišemo v vektor $\boldsymbol{R}^p$. Z rešitvijo za plastična množitelja $\gamma_{1,n+1}$ in $\gamma_{2,n+1}$ nato določimo nove vrednosti plastičnih spremenljivk. Pri drugem načinu pa v vektorju $\boldsymbol{R}^p$ nastopajo tudi evolucijske enačbe
$$\boldsymbol{R}^p\left(\boldsymbol{\varepsilon}^p_{n+1}, \xi^I_{n+1}\gamma_{1,n+1}, \gamma_{2,n+1}\right) = \begin{bmatrix} -\boldsymbol{\varepsilon}^p_{n+1} + \boldsymbol{\varepsilon}^p_n + \sum_{\mu=1}^{2} \gamma_{\mu,n+1}\boldsymbol{\nu}_{\mu,n+1} \\ -\xi^I_{n+1} + \xi^I_n + \sum_{\mu=1}^{2} \gamma_{\mu,n+1}\beta_{n+1} \\ \phi_{1,n+1} \\ \phi_{2,n+1} \end{bmatrix} = \mathbf{0},$$
tako da tudi plastične spremenljivke določimo neposredno. Ko imamo opravka z večploskovnimi funkcijami tečenja, nimamo vedno informacije o tem, katera ploskev bo v skonvergiranem stanju aktivna (v zgornjih enačbah smo predstavili le možnost, ko sta obe ploskvi aktivni). Tako pri dveh ploskvah ločimo med tremi možnimi sistemi enačb
$$\boldsymbol{R}^p_{12} = \begin{bmatrix} \phi_{1,n+1} \\ \phi_{2,n+1} \end{bmatrix} = \mathbf{0},\ \boldsymbol{R}^p_1 = \begin{bmatrix} \phi_{1,n+1} \\ \gamma_{2,n+1} \end{bmatrix} = \mathbf{0},\ \boldsymbol{R}^p_2 = \begin{bmatrix} \gamma_{1,n+1} \\ \phi_{2,n+1} \end{bmatrix} = \mathbf{0},$$
s katerimi pokrijemo vse možne končne izide ($\boldsymbol{R}^p_{12}$ obe ploskvi sta aktivni, $\boldsymbol{R}^p_1$ le prva ploskev je aktivna in $\boldsymbol{R}^p_2$ le druga ploskev je aktivna). Predstavljeni sta dve proceduri za določitev pravilne rešitve (glej razdelek 4.3.2). Pri prvi proceduri poiščemo rešitve za vse tri možne sisteme enačb in na koncu izberemo tisto rešitev, ki zadošča Kuhn-Tuckerjevim

pogojem obremenjevanja in razbremenjevanja ($\gamma_{\mu,n+1} \geq 0,\ \phi_{\mu,n+1} \leq 0$). Pri drugi proceduri pa iščemo rešitev le enega sistema enačb, ki pa se lahko med postopkom spreminja, in sicer upoštevamo, da morajo biti pri vseh aktivnih ploskvah plastični množitelji vedno nenegativni ($\gamma_{\mu,n+1} \geq 0$). Predstavljenih je več numeričnih primerov (glej razdelek 4.4), ki kažejo dobro ujemanje naše formulacije z rezultati iz literature.

Predstavitev koncepta vključene nezveznosti

V petem poglavju je na primeru končnega elementa za palico predstavljen koncept vključene nezveznosti (angl. "embedded discontinuity"). Obravnavamo natezni test idealizirane palice, ki je predstavljen na sliki 5.1. Odziv palice je linearno elastičen dokler ni dosežena nosilnost materiala, nato pa se nosilnost palice linearno manjša z večanjem pomika, glej sliko 5.1 desno spodaj. Na zgornjem levem delu slike 5.1 je prikazana ključna lastnost porušitve, in sicer, da pride do zmanjšanja nosilnosti zaradi zelo lokalnih efektov, ki so skoncentrirani v okolici najšibkejše točke palice (mi smo izbrali sredino palice). Na sliki 5.1 levo spodaj je prikazana porušitev zaradi t.i. "necking efekta", ki je značilen pri natezni porušitvi metalnih palic. Omeniti je potrebno, da je razen sredine idealne palice, kjer se pojavijo nepovratne (plastične) deformacije, celotna palica v elastičnem območju. Tako je celoten odziv palice v mehčanju odvisen le od obnašanje sredinske točke palice. Na zgornjem desnem delu slike 5.1 je predstavljena razporeditev pomikov vzdolž osi palice, ko nosilnost palice še ni v celoti izčrpana. Skok v pomikih $\overline{\overline{u}}$ si lahko razlagamo tudi kot lokalno plastično deformacijo na mestu nezveznosti.

Izpeljave končnega elementa, ki je predstavljen v petem poglavju, sledi naslednjemu postopku. V standarni izoparametrični končni element za palico dodamo parameter α, s katerim opišemo kinematiko nezveznosti ter dobimo obogateno polje vzdolžnih pomikov

$$u^h(\xi) = \underbrace{\sum_{a=1}^{2} N_a(\xi) d_a}_{u^h_{\mathrm{MKE}}} + \underbrace{M_\alpha(\xi)\alpha}_{\text{obogatitev}},$$

kjer s h označimo diskretno aproksimirano količino, $\xi \in [-1, 1]$ je brezdimenzionalna lokalna koordinata, $a = 1, 2$ je indeks vozlišca, N_a je interpolacijska funkcija (glej (5.2)), d_a je vozliščni pomik in M_α je interpolacijska funkcija povezana z nezveznostjo (glej (5.5)). Z u^h_{MKE} označimo izraz, ki izhaja iz standardne metode končnih elementov. Z odvajanjem polja pomikov po koordinati x (glej (5.1) in sliko 5.3) pridemo do polja deformacij

$$\epsilon = \frac{du^h}{dx} = \underbrace{\sum_{a=1}^{2} B_a(\xi) d_a}_{\epsilon_d} + \underbrace{G_\alpha(\xi)\alpha}_{\epsilon_\alpha},$$

kjer je B_a deformacijski operator, ki ga povezujemo z vozliščnimi pomiki (glej (5.7)), $G_\alpha = \overline{G}_\alpha + \overline{\overline{G}}_\alpha$ je deformacijski operator, ki ga povezujemo s kinematiko nezveznosti in ga razdelimo na zvezni $\overline{G}_\alpha$ in nezvezni $\overline{\overline{G}}_\alpha$ del (glej (5.7)), ϵ_d je del deformacij, ki izhaja iz vozliščnih pomikov, ϵ_α pa del deformacij, ki izhaja iz nezveznosti. Upoštevamo, da se virtualne deformacije znotraj končnega elementa interpolirajo kot

$$\hat{\epsilon} = \sum_{a=1}^{2} B_a(\xi)\hat{d}_a + \hat{G}_\alpha \hat{\alpha},$$

kjer je $\hat{d}_a$ virtualni vozliščni pomik, $\hat{\alpha}$ je virtualni parameter nezveznosti ter

$$\hat{G}_\alpha = G_\alpha - \frac{1}{L^e}\int_{\Omega^e} G_\alpha dx,$$

operator, s katerim zagotovimo konvergenco elementa v smislu patch testa. Če v princip virtualnega dela notranjih sil vstavim nastavek za virtualne deformacije, dobimo

$$\delta\Pi^{int,(e)} = \underbrace{\sum_{a=1}^{2} A^{(e)} \int_{\Omega^e} \hat{d}_a B_a \sigma dx}_{\text{standardna MKE}} + \underbrace{A^{(e)} \int_{\Omega^e} \hat{\alpha}\hat{G}_\alpha \sigma dx}_{\text{dodatno}},$$

kjer je $A^{(e)}$ površina prečnega prereza elementa e, Ω^e območje elementa in σ napetost v elementu. Iz izraza "dodatno" tako dobimo eno dodatno ravnotežno enačbo

$$h^{(e)} = A^{(e)}\left(\int_{\Omega^e} \overline{G}_\alpha \sigma dx + t\right) = 0,$$

ki zagotavlja, da je napetost na nezveznosti t v ravnotežju z napetostnim stanjem v končnem elementu. Togi plastični kohezijski zakon, predstavljen na sliki 5.5, gradimo na osnovi kriterija začetka nezveznosti

$$\overline{\overline{\phi}}(t, \overline{\overline{q}}) = t - (\sigma_u - \overline{\overline{q}}) \leq 0,$$

ter potenciala, povezanega z mehčanjem materiala

$$\overline{\overline{\Xi}}(\overline{\overline{\xi}}) = \frac{1}{2} K_s \overline{\overline{\xi}}^2,$$

kjer je σ_u nosilnost materiala, $\overline{\overline{q}}$ napetosti podobna količina povezana z mehčanjem, $\overline{\overline{\xi}}$ je parameter, ki opisuje mehčanje materiala, K_s pa je modul linearnega mehčanja. Preostale sestavine kohezijskega zakona določimo z upoštevanjem plastične disipacije

$$\overline{\overline{D}}^p = t\dot{\alpha} + \overline{\overline{q}}\dot{\overline{\overline{\xi}}},$$

ter principa maksimalne plastične disipacije, ki ga zapišemo kot

$$\min_{t,\overline{\overline{q}}} \max_{\dot{\overline{\overline{\gamma}}}} \left[\overline{\overline{L}}^p(t, \overline{\overline{q}}, \dot{\overline{\overline{\gamma}}}) = -\overline{\overline{D}}^p(t, \overline{\overline{q}}) + \dot{\overline{\overline{\gamma}}}\overline{\overline{\phi}}(t, \overline{\overline{q}}) \right],$$

kjer je $\dot{\overline{\overline{\gamma}}}$ Lagrangev množitelj. Reševanje se izvede v časovnih korakih, računski postopek pa je razdeljen na lokalni in na globalni del. V lokalnem delu na koncu časovnega koraka $[\tau_n,\ \tau_{n+1}]$ določimo popravke k spremenljivkam mehčanja z rešitvijo ene skalarne enačbe

$$\overline{\overline{\phi}} = t_{n+1}\left(\overline{\overline{\gamma}}_{n+1}\right) - \left(\sigma_u - \overline{\overline{q}}_{n+1}\left(\overline{\overline{\gamma}}_{n+1}\right)\right) = \overline{\overline{\phi}}\left(\overline{\overline{\gamma}}_{n+1}\right) = 0,$$

kjer je $\overline{\overline{\gamma}}_{n+1}$ množitelj povezan s togo plastičnostjo na nezveznosti. Da določimo napetost na nezveznosti, eksplicitno upoštevamo dodatno ravnotežno enačbo

$$t_{n+1} = -\int_{\Omega^e} \overline{G}_\alpha \sigma_{n+1} dx = \sigma^G_{n+1},$$

kjer s σ^G_{n+1} označimo vrednost napetosti v integracijski točki elementa. V globalni fazi določimo popravke $\Delta \boldsymbol{d}^{(e),(i-1)}_{n+1}$ za trenutne vrednosti vozliščnih pomikov

$$\boldsymbol{d}^{(e),(i)}_{n+1} = [d_1, d_2]^{(e),(i)^T}_{n+1} = \boldsymbol{d}^{(e),(i-1)}_{n+1} + \Delta \boldsymbol{d}^{(e),(i-1)}_{n+1},$$

kjer je i števec globalne iteracijske sheme. Prispevek enega končnega elementa k sistemu globalnih enačb je

$$\begin{bmatrix} \boldsymbol{K}^{(e)} & \boldsymbol{K}^{f\alpha} \\ \boldsymbol{K}^{hd} & K^{h\alpha} \end{bmatrix}^{(i)}_{n+1} \begin{pmatrix} \Delta \boldsymbol{d}^{(e),(i)}_{n+1} \\ \Delta \alpha^{(e),(i)}_{n+1} \end{pmatrix} = \begin{pmatrix} \boldsymbol{f}^{ext,(e)}_{n+1} - \boldsymbol{f}^{int,(e),(i)}_{n+1} \\ 0\ (= h^{(e),(i)}_{n+1}) \end{pmatrix},$$

kjer so $\boldsymbol{K}^{(e)}$, $\boldsymbol{K}^{f\alpha}$, $\boldsymbol{K}^{hd}$ in $K^{h\alpha}$ podmatrike tangentne matrike elementa (glej (5.49)-(5.55)), $\boldsymbol{f}^{int,(e),(i)}_{n+1}$ so notranje vozliščne sile (glej (5.47)), $\boldsymbol{f}^{ext,(e)}_{n+1}$ pa zunanja vozliščna obtežba. S pomočjo statične kondenzacije pridemo do tangentne matrike končnega elementa

$$\widehat{\boldsymbol{K}}^{(e),(i)}_{n+1} = \boldsymbol{K}^{(e),(i)}_{n+1} - \boldsymbol{K}^{f\alpha,(i)}_{n+1} \left(K^{h\alpha,(i)}_{n+1}\right)^{-1} \boldsymbol{K}^{hd,(i)}_{n+1},$$

ki je povsem enake oblike kot v standardni metodi končnih elementov in je s tem globalni sistem reševanja nespremenjen. V prvem numeričnem primeru v razdelku 5.4 je prikazan konvergenčni test enega končnega elementa, medtem ko v drugem numeričnem primeru analiziramo konstrukcijo sestavljeno iz štirih vzporednih palic.

Porušna analiza metalnih nosilcev in okvirjev

V šestem poglavju obravnavamo porušno analizo metalnih nosilcev in okvirjev. Tipičen primer porušne analize je t.i. "push-over" analiza pri potresnem inženirstvu. To je nelinearna statična analiza konstrukcije na katero nanesemo potresno ekvivalentno horizontalno obtežbo, ki konstrukcijo poriva preko njene nosilnosti, glej npr. [Fajfar et al., 2006].

Poškodbe, ki so jih utrpele konstrukcije pri potresih, kakor tudi eksperimentalna dognanja, kažejo, da pride do porušitve kostrukcij sestavljenih iz prečk in stebrov zaradi lokalne odpovedi materiala na omejenem številu kritičnih mest. Ta mesta se ponavadi opisuje s plastičnimi (neelastičnimi) členki. Običajni pristop za določitev nosilnosti, oziroma za določitev obnašanja okvirne konstrukcije v primeru porušne analize, je uporaba plastičnih členkov, ki se modelirajo z neelastičnimi vzmetmi. Neelastične vzmeti se vključi v običajno mrežo končnih elementov na vnaprej določena kritična mesta (npr. [Wilson, 2002]) ali pa se uporabi končne elemente, v katerih je že upoštevana vzmet v obeh vozliščih (npr. [Powell, 1986]).

V šestem poglavju predstavimo alternativo zgoraj omenjenim pristopom, ki temelji na nelinearni analizi z uporabo končnih elementov z vključenimi nezveznostmi. Predstavljen je tudi pristop za določitev materialnih parametrov za nosilce, ki sloni na predhodni analizi dela konstrukcije s podrobnejšim računskim modelom za lupine. S tem združimo pozitivne lastnosti obeh računskih modelov, t.j. robustnost in učinkovitost končnih elementov za nosilce, s katerimi modeliramo celotno konstrukcijo, ter podroben opis dogajanja na kritičnih mestih ki ga omogočajo končni elementi za lupine. Pri slednjem upoštevamo tako geometrijsko kot tudi materialno nelinearnost.

Izpeljava končnega elementa za nosilce sledi naslednjemu postopku. Z vpeljavo dodatnih parametrov $\boldsymbol{\alpha} = [\alpha_u, \alpha_\theta]^T$, ki določata skok v osnih pomikih α_u oz. skok v rotaciji α_θ na mestu nezveznosti (plastičnega členka), v Euler-Bernoullijeve kinematične enačbe dobimo polje obogatenih deformacij $\boldsymbol{\epsilon}$, ki jih delimo na zvezni $\overline{\boldsymbol{\epsilon}}$ in nezvezni del $\overline{\overline{\boldsymbol{\epsilon}}}$

$$\boldsymbol{\epsilon} = \overline{\boldsymbol{\epsilon}} + \overline{\overline{\boldsymbol{\epsilon}}},\ \overline{\boldsymbol{\epsilon}} = \boldsymbol{B}\boldsymbol{d} + \boldsymbol{G}\boldsymbol{\alpha},\ \overline{\overline{\boldsymbol{\epsilon}}} = \delta_{x_d}\boldsymbol{\alpha},$$

kjer je $\boldsymbol{B}$ deformacijski operator, ki ga povezujemo z vektorjem vozliščnih pomikov (glej (6.11)), δ_{x_d} je Diracova delta, $\boldsymbol{G}$ pa operator vezan na dodatne parametre, ki je določen ob zahtevi, da je končni element zmožen opisati brezdeformacijsko stanje (glej (6.12) in (6.13))

$$\boldsymbol{G} = -\boldsymbol{B}\boldsymbol{D}_{hinge}.$$

Da bi zajeli geometrijsko nelinearne efekte, povezane z globalno nestabilnostjo konstrukcij, uporabimo von Karmanove nastavke (glej (6.18) in (6.19)) za določitev osnih virtualnih deformacij $\delta\overline{\varepsilon}$

$$\begin{bmatrix} \delta\overline{\varepsilon} = \delta\overline{\varepsilon}^{VK} \\ \delta\overline{\kappa} \end{bmatrix} = \underbrace{\begin{bmatrix} \boldsymbol{B}^u & \boldsymbol{B}^{u,w} & \boldsymbol{B}^{u,w'} \\ \boldsymbol{0} & \boldsymbol{B}^w & \boldsymbol{B}^{w'} \end{bmatrix}}_{\boldsymbol{B}^{VK}} \delta\boldsymbol{d} + \boldsymbol{G}\delta\boldsymbol{\alpha},$$

kjer je $\delta\overline{\varepsilon}^{VK}$ von Karmanova virtualna deformacija, $\delta\overline{\kappa}$ zvezni del virtualne ukrivljenosti, $\delta\boldsymbol{d}$ je vektor virtualnih vozliščnih pomikov, $\delta\boldsymbol{\alpha}$ je vektor virtualnih parmetrov nezveznosti,

komponente deformacijskega operatorja $\boldsymbol{B}^{VK}$ so pa določene v (6.20). Če v princip virtualnega dela vstavimo nastavek za virtualne deformacije, dobimo

$$\delta\Pi^{int,(e)} = \underbrace{\int_0^{L^{(e)}} \delta\boldsymbol{d}^T \left(\boldsymbol{B}^{VK}\right)^T \boldsymbol{\sigma} dx}_{\text{standardna MKE}} + \underbrace{\int_0^{L^{(e)}} \delta\boldsymbol{\alpha}^T (\boldsymbol{G}^T\boldsymbol{\sigma} + \delta_{x_d}\boldsymbol{\sigma}) dx}_{\text{dodatno}},$$

kjer je $L^{(e)}$ dolžina elementa e, $\boldsymbol{\sigma} = [N, M]^T$ je vektor notranjih sil, N je osna sila, M pa upogibni moment. Iz izraza "dodatno" dobimo dve dodatni ravnotežni enačbi

$$h_N^{(e)} = \int_0^{L^{(e)}} G^u N dx + t_N = 0, \; h_M^{(e)} = \int_0^{L^{(e)}} G^\theta M dx + t_M = 0,$$

ki zagotavljata, da sta osna sila v nezveznosti t_N in upogibni moment v nezveznosti t_M v ravnotežju z napetostnim stanjem v končnem elementu. Osnovni gradniki konstitutivnega modela so:

- Aditivni razcep celotnih deformacij $\overline{\boldsymbol{\epsilon}}$ na elastične $\overline{\boldsymbol{\epsilon}}^e$ in plastične $\overline{\boldsymbol{\epsilon}}^p$

$$\overline{\boldsymbol{\epsilon}} = \overline{\boldsymbol{\epsilon}}^e + \overline{\boldsymbol{\epsilon}}^p, \quad \overline{\boldsymbol{\epsilon}}^e = [\overline{\varepsilon}^e, \overline{\kappa}^e]^T, \quad \overline{\boldsymbol{\epsilon}}^p = [\overline{\varepsilon}^p, \overline{\kappa}^p]^T,$$

- pri čemer plastičnost omejimo samo na upogibni del

$$\varepsilon = \overline{\varepsilon} = \overline{\varepsilon}^e, \quad \overline{\overline{\varepsilon}} = 0 \quad \Longleftrightarrow \quad \overline{\varepsilon}^p = 0, \quad \alpha_u = 0.$$

- Predpostavka, da je prosta energija zvezne snov sestavljena iz deformacijske energije elastičnih deformacij $\overline{W}\left(\overline{\boldsymbol{\epsilon}}^e\right)$ in člena zaradi izotropnega utrjevanja $\overline{\Xi}(\overline{\xi})$

$$\overline{\Psi}(\overline{\boldsymbol{\epsilon}}^e, \overline{\xi}) := \overline{W}\left(\overline{\boldsymbol{\epsilon}}^e\right) + \overline{\Xi}(\overline{\xi}) = \frac{1}{2}\overline{\boldsymbol{\epsilon}}^{eT}\boldsymbol{C}\overline{\boldsymbol{\epsilon}}^e + \frac{1}{2}K_h\overline{\xi}^2,$$

  kjer je $\boldsymbol{C} = DIAG\left[EA, EI\right]$, E je elastični modul, A je površina prečnega prereza, I je vztrajnostni moment prereza, $\overline{\xi} \geq 0$ je parameter povezan z utrjevanjem materiala, $K_h \geq 0$ pa linearni modul utrjevanja.

- Funkcija tečenja za zvezno snov

$$\overline{\phi}(M, \overline{q}) = |M| - (M_y - \overline{q}) \leq 0,$$

  kjer je $M_y > 0$ upogibni moment na meji tečenja, $\overline{q}$ pa upogibnemu momentu podobna količina povezana z linearnim utrjevanjem materiala.

- Kriterij začetka nezveznosti

$$\overline{\overline{\phi}}(t_M, \overline{\overline{q}}) = |t_M| - (M_u - \overline{\overline{q}}) \leq 0,$$

  kjer je $M_u > 0$ upogibna nosilnost prereza, $\overline{\overline{q}}$ pa upogibnemu momentu podobna količina povezana z mehčanjem.

- Potencial, povezan z mehčanjem

$$\overline{\overline{\Xi}}(\overline{\overline{\xi}}) = \frac{1}{2} K_s \overline{\overline{\xi}}^2 ,$$

kjer je $K_s \leq 0$ linearni modul mehčanja, $\overline{\overline{\xi}}$ pa količina, ki opiše mehčanje.

Preostale sestavine za elastoplastični odziv materiala določimo z upoštevanjem plastične disipacije

$$\overline{D}^p = M\dot{\overline{\kappa}}^p + \overline{q}\dot{\overline{\xi}},$$

ter principa maksimalne plastične disipacije, ki ga zapišemo kot

$$\min_{M,\overline{q}} \max_{\dot{\overline{\gamma}}} \left[\overline{L}^p(M, \overline{q}, \dot{\overline{\gamma}}) = -\overline{D}^p(M, \overline{q}) + \dot{\overline{\gamma}}\overline{\phi}(M, \overline{q}) \right] ,$$

kjer je $\dot{\overline{\gamma}}$ Lagrangev množitelj. Podobno definiramo tudi plastično disipacijo na nezveznosti

$$\overline{\overline{D}} = \overline{\overline{D}}^p = t_M \dot{\alpha}_\theta + \dot{\overline{\overline{q}}}\dot{\overline{\overline{\xi}}},$$

ter tudi tu upoštevamo princip maksimalne plastične disipacije

$$\min_{t_M,\overline{\overline{q}}} \max_{\dot{\overline{\overline{\gamma}}}} \left[\overline{\overline{L}}^p(t_M, \overline{\overline{q}}, \dot{\overline{\overline{\gamma}}}) = -\overline{\overline{D}}^p(t_M, \overline{\overline{q}}) + \dot{\overline{\overline{\gamma}}}\overline{\overline{\phi}}(t_M, \overline{\overline{q}}) \right] ,$$

kjer je $\dot{\overline{\overline{\gamma}}}$ Lagrangev množitelj.

Materialno nelinearni odziv končnega elementa za nosilce, je določen s parametri: M_y, K_h, M_u in K_s. Upogibni moment, ki oznanja začetek materialno nelinearnega odziva, je določen z momentom, ki povzroči plastifikacijo najbolj obremenjenaga vlakna v prečnem prerezu in je odvisen od nivoja osne sile

$$M_y\,(N) = W\sigma_y(1 - \frac{|N|}{A\sigma_y}),$$

kjer je W upogibna odpornost prereza. Da dobimo ustrezne vrednosti za preostale tri parametre, se obrnemo na modeliranje dela konstrukcije s podrobnejšim modelom, ki v našem primeru sloni na geometrijsko in materialno nelinearnih končnih elementih za lupine. Maksimalna upogibna nosilnost nosilca M_u je tako določena z maksimalno nosilnostjo, ki smo jo zabeležili pri analizi z lupinastimi končnimi elementi $M_u^{ref}(N)$

$$M_u\,(N) = M_u^{ref}(N).$$

Ta vrednost nam tudi pomaga, da v rezultatih lupinastega modela ločimo med režimom utrjevanja in režimom mehčanja, do katerega lahko pride zaradi odpovedi materiala (mehčanja) ali pa lokalne geometrijske nestabilnosti (uklona). Nadalje predpostavimo,

da mora biti plastično delo (glej (6.53) in (6.54)), ki ga opravi model nosilca, enako plastičnemu delu, ki ga opravi model lupine. Ker pa plastično delo poteka v dveh režimih (utrjevanje in mehčanje), zagotovimo, da je tudi v posameznem režimu plastično delo pri obeh modelih enako

$$E^{\overline{W}^p}(N) = E^{\overline{W}^{p,ref}}(N), \quad E^{\overline{\overline{W}}^p}(N) = E^{\overline{\overline{W}}^{p,ref}}(N),$$

kjer je $E^{\overline{W}^p}$ plastično delo pri utrjevanju za model z nosilci, $E^{\overline{W}^{p,ref}}$ plastično delo pri utrjevanju za model z lupinami, $E^{\overline{\overline{W}}^p}$ plastično delo pri mehčanju za model z nosilci ter $E^{\overline{\overline{W}}^{p,ref}}$ plastično delo pri mehčanju za model z lupinami. Če upoštevamo, da so vsi prečni prerezi v vzorcu dolžine L^{ref} pod (približno) enakim napetostnim stanjem, dobimo naslednji izraz za modul utrjevanja

$$K_h(N) = \frac{(M_u^2(N) - M_y^2(N))L^{ref}}{2E^{\overline{W}^{p,ref}}(N)}.$$

Nasprotno pa v primeru mehčanja upoštevamo, da se vse zgodi le v enem prerezu in tako dobim modul mehčanja kot

$$|K_s(N)| = \frac{M_u^2(N)}{2E^{\overline{\overline{W}}^{p,ref}}(N)}, \quad K_s \leq 0.$$

Reševanje se izvede v časovnih korakih, računski postopek pa je razdeljen na lokalni in na globalni del. V lokalnem delu na koncu tipičnega časovnega koraka $[t_n, t_{n+1}]$ določimo nove vrednosti spremenljivk povezanih z utrjevanjem materiala z rešitvijo enačbe

$$\overline{\phi}^{ip}(M_{n+1}^{ip}(\boldsymbol{d}_{n+1}^{(e),(i)}, \overline{\kappa}_{n+1}^{p,ip}(\overline{\gamma}_{n+1}^{ip})), \overline{q}(\overline{\xi}_{n+1}^{ip}(\overline{\gamma}_{n+1}^{ip}))) = \overline{\phi}^{ip}(\overline{\gamma}_{n+1}^{ip}) = 0,$$

kjer je $ip = 1, 2, 3$ indeks integracijske točke, i števec globalne iteracijske sheme, $\overline{\gamma}_{n+1}^{ip}$ pa plastični množitelj povezan z utrjevanjem. Spremenljivke, povezane z mehčanjem, pa določimo z rešitvijo naslednje enačbe

$$\overline{\overline{\phi}}^{(e)}(t_{M,n+1}^{(e)}(\alpha_{\theta,n+1}^{(e)}(\overline{\overline{\gamma}}_{n+1}^{(e)})), \overline{\overline{q}}(\overline{\overline{\xi}}_{n+1}^{(e)}(\overline{\overline{\gamma}}_{n+1}^{(e)}))) = \overline{\overline{\phi}}^{(e)}(\overline{\overline{\gamma}}_{n+1}^{(e)}) = 0,$$

kjer je $\overline{\overline{\gamma}}_{n+1}^{(e)}$ plastični množitelj povezan z mehčanjem. Upogibni moment na nezveznosti določimo z uporabo dodatne ravnotežne enačbe

$$t_{M,n+1}^{(e)} = -\int_{\Omega^e} G^{\theta}(x_d^{(e)}, x) M(\boldsymbol{d}_{n+1}^{(e),(i)}, \overline{\kappa}_n^{p,ip}, \alpha_{\theta,n+1}^{(e)}) dx.$$

V globalni fazi določimo popravke $\Delta\boldsymbol{d}_{n+1}^{(e),(i-1)}$ za trenutne vrednosti vozliščnih pomikov

$$\boldsymbol{d}_{n+1}^{(e),(i)} = \boldsymbol{d}_{n+1}^{(e),(i-1)} + \Delta\boldsymbol{d}_{n+1}^{(e),(i-1)}.$$

Prispevek enega končnega elementa k sistemu globalnih enačb je

$$\begin{bmatrix} \boldsymbol{K}^{(e)} & \boldsymbol{K}^{f\alpha} \\ \boldsymbol{K}^{hd} & K^{h\alpha} \end{bmatrix}_{n+1}^{(i)} \begin{pmatrix} \Delta \boldsymbol{d}_{n+1}^{(e),(i)} \\ \Delta \alpha_{\theta,n+1}^{(e),(i)} \end{pmatrix} = \begin{pmatrix} \boldsymbol{f}_{n+1}^{ext,(e)} - \boldsymbol{f}_{n+1}^{int,(e),(i)} \\ 0 \end{pmatrix},$$

kjer so $\boldsymbol{K}^{(e)}$, $\boldsymbol{K}^{f\alpha}$, $\boldsymbol{K}^{hd}$ in $K^{h\alpha}$ podmatrike tangentne matrike končnega elementa (glej (6.82)), $\boldsymbol{f}_{n+1}^{int,(e),(i)}$ so notranje vozliščne sile (glej (6.25)), $\boldsymbol{f}_{n+1}^{ext,(e)}$ pa zunanja vozliščna obtežba. S pomočjo statične kondenzacije pridemo do tangentne matrike končnega elementa

$$\widehat{\boldsymbol{K}}_{n+1}^{(e),(i)} = \boldsymbol{K}_{n+1}^{(e),(i)} - \boldsymbol{K}_{n+1}^{f\alpha,(i)} \left(K_{n+1}^{h\alpha,(i)} \right)^{-1} \boldsymbol{K}_{n+1}^{hd,(i)},$$

ki je povsem enake oblike kot v standardni metodi končnih elementov, zato je globalni sistem reševanja nespremenjen. V prvem numeričnem primeru v razdelku 6.5 je prikazan izračun s končnimi elementi za lupine in z rezultati tega izračuna smo določili bilinearno aproksimacijo za upogibno nosilnost

$$M_u(N) = \widetilde{M}_u^{ref}(N) = \begin{cases} M_u^{ref,0}(1.03 + 0.85\frac{N}{N_y}) & \text{if } N < -0.035N_y \\ M_u^{ref,0} & \text{if } N \geq -0.035N_y \end{cases},$$

medtem ko smo za modula utrjevanja in mehčanja upoštevali kar konstantni vrednosti

$$K_h(N) = 1.06 \cdot 10^7 \text{ kN/cm}^2, \; K_s(N) = -3.28 \cdot 10^5 \text{ kN/cm}^2,$$

kjer z $\widetilde{M}_u^{ref}$ označimo aproksimirano funkcijo na osnovi analize z lupinami, $M_u^{ref,0}$ je upogibna nosilnost prereza določena pri analizi z lupinami pri nični vrednosti osne sile in $N_y = A\sigma_y$. Materialni parametri določeni pri analizi z lupinami so bili nato uporabljeni v vseh nadaljnih numeričnih primerih z uporabo končnih elementov za nosilce.

Predstavljen pristop spada v kategorijo simulacij na več nivojih (angl. "multi-scale"), kjer najprej izvedemo izračun na podrobnejšem modelu in dobljene rezultate nato nesemo v bolj robustni makro model. Rezultati analize z lupinami, kjer so upoštevane tako materialne kot tudi geometrijske nelinearnosti, so tako shranjeni in upoštevani v modelu za nosilce. Ena glavnih lastnosti tega pristopa je avtomatsko zaznavanje in razvoj plastičnih členkov (nezveznosti), ki se pojavijo postopoma, v skladu s prerazporeditvijo obremenitev tekom nelinearne analize. Pri mnogih standardnih postopkih za račun t.i. "push-over" analiz je namreč potrebno vnaprej določiti kritična mesta ter njihov odziv.

Porušna analiza z ravninskimi končnimi elementi

V sedmem poglavju obravnavamo družino štirivozliščnih elastoplastičnih ravninskih elementov z vgrajeno nezveznostjo. Izdelava učinkovitih štirivozliščnih končnih elementov z vgrajeno nezveznostjo, ki niso podvrženi blokiranju, je mnogo bolj zahtevna (glej

npr. [Linder and Armero, 2007] in [Manzoli and Shing, 2006]), kot pa v primeru trikotnih elementov, ki so sposobni opisati zgolj konstantno napetostno stanje. Morda je tu potrebno iskati vzrok, da je bila do sedaj večina raziskav povezanih z vključevanjem nezveznosti v ravninske končne elemente izvedena ravno s trikotnimi elementi, glej npr. [Sancho et al., 2007], [Ibrahimbegovic and Brancherie, 2003], [Brancherie and Ibrahimbegovic, 2008], [Mosler, 2005], [Jirasek and Zimmermann, 2001]. Kinematika discontinuitete omogoča linearna skoke tako v smeri normale kot tudi v smeri tangente nezveznosti.

S predstavljenim končnim elementom lahko analiziramo natezno porušitev ravninskih betonskih vzorcev s pripadajočim širjenjem razpoke. Ista formulacija se lahko uporabi tudi za analizo porušitve duktilnih materialov, pri katerih pride do pojava strižnih pasov in tudi za analizo delaminacije pri kompozitnih materialih.

Izpeljava končnega elementa, ki je predstavljen v sedmem poglavju, sledi naslednjemu postopku. Z vpeljavo štirih dodatnih parametrov (α_{n0}, α_{n1}, α_{m0} in α_{m1}), povezanih s kinematiko nezveznosti, v izoparametrični ravninski končni element, pridemo do obogatenega polja pomikov

$$\boldsymbol{u}^h(\boldsymbol{\xi},\Gamma^e) = \underbrace{\sum_{a=1}^{4} N_a(\boldsymbol{\xi})\boldsymbol{d}_a}_{\boldsymbol{u}_d^h} + \underbrace{\sum_{mode} \boldsymbol{M}_{mode}(\boldsymbol{\xi},\Gamma^e)\alpha_{mode}}_{\boldsymbol{u}_\alpha^h}, \quad mode \in (n0, n1, m0, m1),$$

kjer povezujeme dodatne parametere z eno od naslednjih oblik obnašanja nezveznosti

- "n0" - konstaten skok pomikov v smeri normale nezveznosti,
- "n1" - linearen skok pomikov v smeri normale nezveznosti,
- "m0" - konstaten skok pomikov v smeri tangente nezveznosti,
- "m1" - linearen skok pomikov v smeri tangente nezveznosti.

S h označimo diskretno aproksimirano količino, $\boldsymbol{\xi} = [\xi, \eta]^T \in [-1, 1] \times [-1, 1]$ je brezdimenzionalana koordinata znotraj elementa, z Γ^e označimo nezveznost znotraj elementa e, $a = 1, 2, 3, 4$ je indeks vozlišča, N_a je interpolacijska funkcija (glej (7.2)), $\boldsymbol{d}_a = [u_x, u_y]^T$ so vozliščni pomiki, M_{mode} je interpolacijska matrika povezana s parametri nezveznosti, z $\boldsymbol{u}_d^h$ označimo del polja pomikov, ki izhaja iz interpolacije vozliščnih vrednosti, z $\boldsymbol{u}_\alpha^h$ pa del, ki izhaja iz parametrov nezveznosti. S preučevanjem togih pomikov območji Ω^{e-} in Ω^{e+} ($\Omega^e = \Omega^{e-} \cup \Omega^{e+}$), ki sta ločeni z nezveznostjo Γ^e (glej sliko 7.2), določimo interpolacijske matrike povezane s parametri nezveznosti kot

$$\boldsymbol{M}_{mode} = \frac{\overline{\boldsymbol{u}}_{mode}^h - \overline{\boldsymbol{u}}_{d,mode}^h}{\overline{\alpha}_{mode}},$$

kjer sta $\overline{\boldsymbol{u}}^h_{mode}$ in $\overline{\boldsymbol{u}}^h_{d,mode}$ določena v (7.4), $\overline{\alpha}_{mode}$ pa je vrednost togega pomika na nezveznosti. Polje obogatenih deformacij dobimo s simetričnim gradientom polja pomikov

$$\boldsymbol{\epsilon} = \sum_{a=1}^{4} \boldsymbol{B}_a \boldsymbol{d}_a + \boldsymbol{G}_{n0}\alpha_{n0} + \boldsymbol{G}_{n1}\alpha_{n1} + \boldsymbol{G}_{m0}\alpha_{m0} + \boldsymbol{G}_{m1}\alpha_{m1},$$

kjer je $\boldsymbol{B}_a$ deformacijski operator povezan z vozliščnimi pomiki (glej (7.24)), $\boldsymbol{G}_{n0}$, $\boldsymbol{G}_{n1}$, $\boldsymbol{G}_{m0}$ in $\boldsymbol{G}_{m1}$ pa so deformacijski operatorji, ki so povezani s kinematiko nezveznosti (glej (7.25)-(7.28)). Upoštevamo, da se virtualne deformacije znotraj končnega elementa interpolirajo kot

$$\hat{\boldsymbol{\epsilon}} = \sum_{a=1}^{4} \boldsymbol{B}_a \hat{\boldsymbol{d}}_a + \hat{\boldsymbol{G}}_{n0}\hat{\alpha}_{n0} + \hat{\boldsymbol{G}}_{n1}\hat{\alpha}_{n1} + \hat{\boldsymbol{G}}_{m0}\hat{\alpha}_{m0} + \hat{\boldsymbol{G}}_{m1}\hat{\alpha}_{m1},$$

kjer so $\hat{\boldsymbol{d}}_a$ vozliščni virtualni pomiki, $\hat{\alpha}_{n0}$, $\hat{\alpha}_{n1}$, $\hat{\alpha}_{m0}$ in $\hat{\alpha}_{m1}$ so virtualni parametri nezveznosti ter $\hat{\boldsymbol{G}}_{n0}$, $\hat{\boldsymbol{G}}_{n1}$, $\hat{\boldsymbol{G}}_{m0}$ in $\hat{\boldsymbol{G}}_{m1}$ operatorji, ki jih določimo kot

$$\hat{\boldsymbol{G}}_{mode} = \boldsymbol{G}_{mode} - \frac{1}{A_{\Omega^e}} \int_{\Omega^e} \boldsymbol{G}_{mode} d\Omega,$$

da zagotovimo konvergenco v smislu t.i. "patch" testa. Če v princip virtualnega dela vstavimo izraz za virtualne deformacije, dobimo

$$\begin{aligned}
\delta\Pi^{int,(e)} &= t^{(e)} \int_{\Omega^e} \hat{\boldsymbol{\epsilon}}^T \boldsymbol{\sigma} d\Omega \\
&= \underbrace{\sum_{a=1}^{4} t^{(e)} \int_{\Omega^e} \hat{\boldsymbol{d}}_a^{\,T} \boldsymbol{B}_a^T \boldsymbol{\sigma} d\Omega}_{\text{standardna MKE}} + \\
&\quad \underbrace{t^{(e)} \int_{\Omega^e} \hat{\alpha}_{n0} \hat{\boldsymbol{G}}_{n0}^T \boldsymbol{\sigma} + \hat{\alpha}_{n1} \hat{\boldsymbol{G}}_{n1}^T \boldsymbol{\sigma} + \hat{\alpha}_{m0} \hat{\boldsymbol{G}}_{m0}^T \boldsymbol{\sigma} + \hat{\alpha}_{m1} \hat{\boldsymbol{G}}_{m1}^T \boldsymbol{\sigma} d\Omega}_{\text{dodatno}},
\end{aligned}$$

kjer je $t^{(e)}$ debelina elementa in $\boldsymbol{\sigma} = [\sigma_x, \sigma_y, \sigma_{xy}]^T$ vektor komponent napetosti. Iz izraza "dodatno", ki se pojavi v principu virtualnega dela, tako dobimo štiri dodatne ravnotežne enačbe (glej (7.46)-(7.49))

$$\boldsymbol{h}^{(e)} = \boldsymbol{h}^{\Omega^e} + \boldsymbol{h}^{\Gamma^e} = \begin{bmatrix} h_{n0}^{\Omega^e} \\ h_{n1}^{\Omega^e} \\ h_{m0}^{\Omega^e} \\ h_{m1}^{\Omega^e} \end{bmatrix} + \begin{bmatrix} h_{n0}^{\Gamma^e} \\ h_{n1}^{\Gamma^e} \\ h_{m0}^{\Gamma^e} \\ h_{m1}^{\Gamma^e} \end{bmatrix} = \boldsymbol{0},$$

ki zagotavljajo, da je vektor napetosti na nezveznosti $\boldsymbol{t} = [t_n, t_m]^T$, kjer je t_n komponenta napetosti v smeri normale nazveznosti in t_m komponenta napetosti v smeri tangente nazveznosti, v ravnotežju z napetostnim stanjem v elementu. Osnovni gradniki materialnega modela za zvezno snov, kakor tudi za nezveznost so:

- Razcep celotnih (zveznih) deformacij $\overline{\boldsymbol{\epsilon}}$ na elastični $\overline{\boldsymbol{\epsilon}}^e$ in plastični $\overline{\boldsymbol{\epsilon}}^p$ del

$$\overline{\boldsymbol{\epsilon}} = \overline{\boldsymbol{\epsilon}}^e + \overline{\boldsymbol{\epsilon}}^p.$$

- Predpostavka, da je prosta energija zvezne snov sestavljena iz deformacijske energije elastičnih deformacij $\overline{W}\left(\overline{\boldsymbol{\epsilon}}^e\right)$ in člena zaradi izotropnega utrjevanja $\overline{\Xi}(\overline{\xi})$

$$\overline{\Psi}(\overline{\boldsymbol{\epsilon}}^e, \overline{\xi}) := \overline{W}\left(\overline{\boldsymbol{\epsilon}}^e\right) + \overline{\Xi}(\overline{\xi}) = \frac{1}{2}\overline{\boldsymbol{\epsilon}}^{eT}\boldsymbol{C}\overline{\boldsymbol{\epsilon}}^e + \overline{\Xi}(\overline{\xi}),$$

  kjer je $\boldsymbol{C}$ matrika elastičnih konstant (glej (7.54)), $\overline{\xi} \geq 0$ pa parameter povezan z utrjevanjem materiala.

- Funkcija tečenja za zvezno snov

$$\overline{\phi}\left(\boldsymbol{\sigma}, \overline{q}\right) = \boldsymbol{\sigma}^T\boldsymbol{A}\boldsymbol{\sigma} - \left(1 - \frac{\overline{q}}{\sigma_y}\right)^2 \leq 0,$$

  kjer je $\boldsymbol{A}$ matrika konstant, s katerimi opišemo izotropno plastičnost pri ravninskih problemih (glej (7.56)), σ_y je napetost na meji tečenja pri enoosnem preizkusu, $\overline{q}$ pa napetosti podoben parameter povezan z izotropnim utrjevanjem.

- Kohezijski zakon na nezveznosti zapisan s skoki v pomikih na nezveznosti $\overline{\overline{\boldsymbol{u}}} = [\overline{\overline{u}}_n, \overline{\overline{u}}_m]^T$

$$\boldsymbol{t} = \boldsymbol{t}(\overline{\overline{\boldsymbol{u}}}),$$

  ki ga lahko zapišemo tudi s kriterijem začetka nezveznosti

$$\overline{\overline{\phi}} = \overline{\overline{\phi}}(\boldsymbol{t}, \overline{\overline{q}}) \leq 0,$$

  in potencialom povezanim z mehčanjem materiala

$$\overline{\overline{\Xi}}(\overline{\overline{\xi}}),$$

  kjer je $\overline{\overline{\xi}}$ količina, ki opiše mehčanje.

Preostale sestavine za elastoplastični odziv materiala določimo z upoštevanjem plastične disipacije

$$\overline{D}^p = \boldsymbol{\sigma}^T\dot{\overline{\boldsymbol{\epsilon}}}^p + \overline{q}\dot{\overline{\xi}},$$

ter principa maksimalne plastične disipacije, ki ga zapišemo kot

$$\min_{\boldsymbol{\sigma}, \overline{q}} \max_{\dot{\overline{\gamma}}} \left[\overline{L}^p(\boldsymbol{\sigma}, \overline{q}, \dot{\overline{\gamma}}) = -\overline{D}^p(\boldsymbol{\sigma}, \overline{q}) + \dot{\overline{\gamma}}\overline{\phi}(\boldsymbol{\sigma}, \overline{q})\right],$$

kjer je $\dot{\overline{\gamma}}$ Lagrangev množitelj. Podobno definiramo tudi plastično disipacijo na nezveznosti

$$\overline{\overline{D}} = \overline{\overline{D}}^p = \boldsymbol{t}^T \dot{\overline{\overline{\boldsymbol{u}}}} + \overline{\overline{q}} \dot{\overline{\overline{\xi}}},$$

ter tudi tu upoštevamo princip maksimalne plastične disipacije

$$\min_{\boldsymbol{t},\overline{\overline{q}}} \max_{\dot{\overline{\overline{\gamma}}}} \left[\overline{\overline{L}}^p(\boldsymbol{t}, \overline{\overline{q}}, \dot{\overline{\overline{\gamma}}}) = -\overline{\overline{D}}^p(\boldsymbol{t}, \overline{\overline{q}}) + \dot{\overline{\overline{\gamma}}} \overline{\overline{\phi}}(\boldsymbol{t}, \overline{\overline{q}}) \right],$$

kjer je $\dot{\overline{\overline{\gamma}}}$ Lagrangev množitelj. Reševanje se izvede v časovnih korakih, računski postopek pa je razdeljen na lokalni in na globalni del. V lokalnem delu na koncu tipičnega časovnega koraka $[\tau_n, \tau_{n+1}]$, če ni že določeno, najprej, z upoštevanjem povprečnega napetostnega stanja v končnem elementu, določimo geometrijo nezveznosti

$$\boldsymbol{n} = \boldsymbol{n}\left(\boldsymbol{\sigma}^{avg}(\boldsymbol{d}^{(e)}_{n+1}, \overline{\boldsymbol{\epsilon}}^{p,bip}_n)\right), \quad \boldsymbol{m} = \boldsymbol{m}\left(\boldsymbol{\sigma}^{avg}(\boldsymbol{d}^{(e)}_{n+1}, \overline{\boldsymbol{\epsilon}}^{p,bip}_n)\right), \quad x_{\Gamma E},$$

kjer je $\boldsymbol{n}$ normala nezveznosti, $\boldsymbol{m}$ tangenta nezveznosti, $\boldsymbol{\sigma}^{avg}$ povprečna napetost v elementu, določena na osnovi napetostnega stanja v integracijskih točkah $bip = 1, 2, 3, 4$, ter $x_{\Gamma E}$ končna točka nezveznosti v elementu (glej sliko 7.4). Nove vrednosti spremenljivk za mehčanje materiala ter skokov v pomikih v dveh integracijskih točkah nezveznosti, določimo s hkratnim reševanjem naslednjih enačb

$$\overline{\overline{\phi}}^1\left(\boldsymbol{t}^1_{n+1}\left(\boldsymbol{\alpha}^{(e)}_{n+1}\left(\overline{\overline{\gamma}}^1_{n+1}, \overline{\overline{\gamma}}^2_{n+1}\right)\right), \overline{\overline{q}}\left(\overline{\overline{\xi}}^1_{n+1}\left(\overline{\overline{\gamma}}^1_{n+1}\right)\right)\right) = \overline{\overline{\phi}}^1\left(\overline{\overline{\gamma}}^1_{n+1}, \overline{\overline{\gamma}}^2_{n+1}\right) = 0,$$

$$\overline{\overline{\phi}}^2\left(\boldsymbol{t}^2_{n+1}\left(\boldsymbol{\alpha}^{(e)}_{n+1}\left(\overline{\overline{\gamma}}^1_{n+1}, \overline{\overline{\gamma}}^2_{n+1}\right)\right), \overline{\overline{q}}\left(\overline{\overline{\xi}}^2_{n+1}\left(\overline{\overline{\gamma}}^2_{n+1}\right)\right)\right) = \overline{\overline{\phi}}^2\left(\overline{\overline{\gamma}}^1_{n+1}, \overline{\overline{\gamma}}^2_{n+1}\right) = 0,$$

kjer z indeksom 1 opišemo količino, ki se nanaša na prvo integracijsko točko, z indeksom 2 opišemo količino, ki se nanaša na drugo integracijsko točko, $\overline{\overline{\gamma}}^1_{n+1}$ in $\overline{\overline{\gamma}}^2_{n+1}$ pa sta plastična množitelja povezana z mehčanjem. Upoštevali smo naslednje zveze med skoki v pomikih v integracijskih točkah nezveznosti ter kinematičnimi parametri nezveznosti

$$\boldsymbol{\alpha}^{(e)}(\overline{\overline{\boldsymbol{u}}}^1, \overline{\overline{\boldsymbol{u}}}^2) = \left[\frac{\overline{\overline{u}}^1_n + \overline{\overline{u}}^2_n}{2}, \frac{\overline{\overline{u}}^1_n - \overline{\overline{u}}^2_n}{\xi^1_\Gamma - \xi^2_\Gamma}, \frac{\overline{\overline{u}}^1_m + \overline{\overline{u}}^2_m}{2}, \frac{\overline{\overline{u}}^1_m - \overline{\overline{u}}^2_m}{\xi^1_\Gamma - \xi^2_\Gamma}\right]^T,$$

kjer sta ξ^1_Γ in ξ^2_Γ koordinati integracijskih točk na nezveznosti (glej (7.80)). Pri izračunu napetosti v integracijskih točkah nezveznosti smo eksplicitno uporabili dodatne ravnotežne enačbe

$$\boldsymbol{h}^{\Omega^e}\left(\boldsymbol{\sigma}(\boldsymbol{d}^{(e)}_{n+1}, \overline{\boldsymbol{\epsilon}}^{p,bip}_n, \boldsymbol{\alpha}^{(e)}_{n+1})\right) + \boldsymbol{h}^{\Gamma^e}(\boldsymbol{t}^1_{n+1}, \boldsymbol{t}^2_{n+1}) = \boldsymbol{0} \quad \Rightarrow \quad \boldsymbol{t}^1_{n+1},\ \boldsymbol{t}^2_{n+1}.$$

V lokalni fazi določimo tudi nove vrednosti spremenljivk v integracijskih točkah elementa, ki so povezane z utrjevanjem materiala, z rešitvijo naslednje enačbe

$$\overline{\phi}^{ip}(\boldsymbol{\sigma}^{bip}_{n+1}(\boldsymbol{d}^{(e),(i)}_{n+1}, \overline{\boldsymbol{\epsilon}}^{p,bip}_{n+1}(\overline{\gamma}^{bip}_{n+1})), \overline{q}(\overline{\xi}^{bip}_{n+1}(\overline{\gamma}^{bip}_{n+1}))) = \overline{\phi}^{bip}(\overline{\gamma}^{bip}_{n+1}) = 0,$$

kjer je i števec globalne iteracijske sheme, $\overline{\gamma}_{n+1}^{bip}$ pa plastični množitelj povezan z utrjevanjem. V globalni fazi določimo popravke $\Delta \boldsymbol{d}_{n+1}^{(e),(i-1)}$ za trenutne vrednosti vozliščnih pomikov

$$\boldsymbol{d}_{n+1}^{(e),(i)} = \boldsymbol{d}_{n+1}^{(e),(i-1)} + \Delta \boldsymbol{d}_{n+1}^{(e),(i-1)}.$$

Prispevek enega končnega elementa k sistemu globalnih enačb je

$$\begin{bmatrix} \boldsymbol{K}^{(e)} & \boldsymbol{K}^{f\alpha} \\ \boldsymbol{K}^{hd} & \boldsymbol{K}^{h\alpha} \end{bmatrix}_{n+1}^{(i)} \begin{pmatrix} \Delta \boldsymbol{d}_{n+1}^{(e),(i)} \\ \Delta \boldsymbol{\alpha}_{n+1}^{(e),(i)} \end{pmatrix} = \begin{pmatrix} \boldsymbol{f}_{n+1}^{ext,(e)} - \boldsymbol{f}_{n+1}^{int,(e),(i)} \\ \boldsymbol{0} \end{pmatrix},$$

kjer so $\boldsymbol{K}^{(e)}$, $\boldsymbol{K}^{f\alpha}$, $\boldsymbol{K}^{hd}$ in $\boldsymbol{K}^{h\alpha}$ podmatrike tangentne matrike končnega elementa (glej (7.104)), $\boldsymbol{f}_{n+1}^{int,(e),(i)}$ so notranje vozliščne sile (glej (7.44)), $\boldsymbol{f}_{n+1}^{ext,(e)}$ pa zunanja vozliščna obtežba. S pomočjo statične kondenzacije pridemo do tangentne matrike končnega elementa

$$\widehat{\boldsymbol{K}}_{n+1}^{(e),(i)} = \boldsymbol{K}_{n+1}^{(e),(i)} - \boldsymbol{K}_{n+1}^{f\alpha,(i)} \left(\boldsymbol{K}_{n+1}^{h\alpha,(i)} \right)^{-1} \boldsymbol{K}_{n+1}^{hd,(i)},$$

ki je povsem enake oblike kot v standardni metodi končnih elementov in je s tem globalni sistem reševanja nespremenjen.

V razdelku 7.4 so prikazani numerični primeri, kjer analiziramo dvodimenzionalne betonske vzorce, delaminacijo kompozitnih materialov ter porušitev duktilnih materialov. Element omogoča opis linearnih skokov pomikov tako v smeri tangente kot tudi normale. Da je postal postopek širjenja razpoke bolj robusten, smo povezali nezveznosti med dvema sosednjima elementoma.

Zaključki

Namen dela je poglobitev znanja o obnašanju konstrukcij v okolici mejne nosilnosti, ter pri obremenitvah, ki povzročijo porušitev konstrukcije, z uporabo numeričnih metod, kot je na primer metoda končnih elementov z vključenimi nezveznostmi. V disertaciji smo se osredotočali predvsem na modeliranje materialnih nelinearnosti in na modeliranje lokalne porušitve materiala v kontekstu omenjene numerične metode.

V raziskovalnem delu, ki je predstavljeno, smo izvedli naslednja dela in prišli do naslednjih ugotovitev:

- Izpeljali in sprogramirali smo nelinearno elastičen končni element za račun mejne obtežbe plošč, ki je definiran z rezultantami, njegovo delovanje smo pa preverili z računskimi primeri. Upoštevali priporočila Evrokoda 2 [Eurocode 2, 2004] za opis konstitutivnih zvez armiranega betona. Rezultati računskih primerov se dobro ujemajo z razpoložljivimi eksperimentalnimi rezultati (ki so na voljo v strokovni literaturi) za tiste plošče, kjer se je obtežba monotono povečevala vse do porušitve.

Bistvo uporabljene analize je, da upošteva postopno degradacijo armiranega betona zaradi razpokanja betona in zaradi plastifikacije armature. Čeprav analiza temelji na nelinearni metodi končnih elementov, je razmeroma preprosta in robustna. Prednost prikazanega pristopa, glede na precej uporabljano teorijo plastičnih linij, je informacija o velikosti pomikov pri doseženi mejni nosilnosti, ki je lahko zanimiva za študij mejnega stanja uporabnosti.

- Izpeljali smo elastoplastično in elastoviskoplastično formulacijo za plošče in ju, z novim algoritmom, ki hkrati zajame obe neelastični formulaciji, vgradili v končni element za Reissner-Mindlinove plošče. Obe formulaciji sta definirani z rezultantami napetosti in upoštevata tako izotropno kot tudi kinematično utrjevanje materiala. Končni element smo preverili z računskimi primeri, kjer smo rezultate naše formulacije primerjali s formulacijo, ki je določena na nivoju napetosti in s formulacijo z rezultantami napetosti, ki upošteva postopno plastifikacijo v smeri debeline plošče. Ugotovili smo, da ima gostota mreže končnih elementov večji vpliv na nivo mejne obtežbe, kot pa izbira same formulacije.

- Izpeljali smo geometrijsko in materialno nelinearno (elastoplastično) formulacijo za geometrijsko točne lupine, ki vsebuje tako izotropno kot tudi kinematično utrjevanje in je določena z rezultantami nepetosti. Razvili smo tudi algoritem za elastoplastične lupine z rezultantami napetosti, ki vsebuje dve funkciji tečenja. V obstoječi geometrijsko točni končni element za lupine smo vgradili neelastični materialni model s pripadajočimi novimi algoritmi in ga preverili z računskimi primeri. Primerjava rezultatov naše formulacije z rezultati iz literature kaže dobro ujemanje. Pri računskem primeru v razdelku 4.4.1, smo imeli nekaj težav s konvergenco plastične zanke, ki najverjetneje nastane zaradi velikih skokov med dvemi ravnotežnimi konfiguracijami, zaradi pojava lokalnih uklonov. Z uporabo boljšega pristopa za sledenje obtežne poti bi se problemom s konvergenco izognili. V razdelku 4.4.3 smo na primeru jeklene plošče primerjali elastoplastično formulacijo za lupine z elastoplastično formulacijo za plošče, ki je predstavljena v tretjem poglavju. Ugotovili smo, da so lahko geometrijsko nelinearni efekti pri analizi tankih plošč zelo veliki.

- Izpeljali in sprogramirali smo elastoplastično formulacijo z vključenimi nezveznostmi za analizo ravninskih nosilcev. Formulacija je izpeljana na osnovi Euler-Bernoullijeve teorije nosilcev in vsebuje tako utrjevanje materiala kot tudi njegovo lokalno mehčanje. Izpeljan je tudi postopek zaporednega računa na več nivojih, s katerim določimo konstitutivne parametre za nosilce. Z rezultati analize, ki je izvedena s končnimi elementi za lupine, zajamemo materialne in geometrijske nelinearnosti, vključno z

lokalnimi efekti. Te rezultate shranimo in jih uporabimo pri analizi s končnimi elementi za nosilce. Z numeričnimi testi smo ugotovili dobro delovanje predstavljenega pristopa. Ena glavnih lastnosti tega pristopa je avtomatsko zaznavanje in razvoj plastičnih členkov (nezveznosti), ki se pojavljajo postopoma v skladu s prerazporeditvijo obremenitev tekom nelinearne analize. Pri analizi ravninskih okvirjev se je izkazalo, da lahko velikost obtežnega koraka vpliva na rešitev v območju mehčanja konstrukcije. Če je korak prevelik, se lahko nezveznosti naenkrat pojavijo na več mestih, kar lahko privede do problemov s konvergenco ali pa je posledica prevelikih korakov neka nova ravnotežna lega, ki je drugačna od tiste, ki bi jo dobili z manjšim korakom. Tako smo pri računskih primerih uporabili tako velikost koraka, da je v enem obtežnem koraku nastala kvečjemu ena nova nezveznost. Naslednji korak pri analizi okvirjev bi lahko bil razvoj nove formulacije, kjer bi večnivojska analiza potekala istočasno.

- Izpeljali smo elastoplastično formulacijo z vgrajenimi nezveznostmi za analizo ravninskih problemov. Formulacijo smo vgradili v izoparametrični štirivozliščni končni element in ga preverili z računskimi testi. Pri opisu kinematike nezveznosti smo upoštevali linearne skoke v pomikih, tako v smeri tangente kot tudi normale nezveznosti. V prvih različicah formulacije se je lahko nezveznost pojavila v kateremkoli končneme elementu, če je tako narekovalo napetostno stanje v njem. Tak pristop je privedel do problemov pri konvergenci ali pa je zaradi različno orientiranih nezveznosti v sosednjih elementih prišlo do pretogega odziva. Da je postal postopek širjenja razpoke bolj robusten, smo povezali nezveznost med dvema sosednjima elementoma. Primerjava rezultatov naše formulacije pri analizi porušitve betonskih vzorcev ter analizi delaminacije kompozitnih materialov kaže dobro ujemanje z rezultati iz literature. Na primeru analize elastoplastičnega vzorca z duktilno porušitvijo smo z različnimi gostotami mrež pokazali, da je rezultat neodvisen od mreže končnih elementov. Konvergenca predstavljenega pristopa je zelo odvisna od obravnavanega problema. Analize z enim končnim elementom delujejo brez težav, medtem ko je pri analizi bolj kompliciranih konstrukcij včasih potrebna intervencija in je potrebno spremeniti dolžino obtežnega koraka, da pridemo do uravnotežene konfiguracije. Zaenkrat obstaja še odprto vprašanje, kako narediti računski postopek še bolj robusten. Pri računskem primeru v razdelku 7.4.4 smo imeli težave z določitvijo pravilne smeri širjenja nezveznosti. Temu problemu bi se lahko izognili z razvojem formulacije, ki bi za kriterij smeri širjenja nezveznosti, upoštevala napetostno stanje v širši okolici elementa in ne le v enem elementu. Z manjšimi spremembami že obstoječe formulacije, pa bi dobili orodje, ki bi bilo primerno za analizo drsin pri

zemljinah.

- Vsi, v tej disertaciji predstavljeni končni elementi, so bili pripravljeni v programskem okolju AceGen [Korelc, 2007b]. Vsa testiranja končnih elementov so bila izvedena v programskem okolju AceFem [Korelc, 2007a]. Obe programski okolji sta se izkazali za vsestranski orodji, ki omogočata hitro "proizvodnjo" in testiranje novih formulacij končnih elementov.

Bibliography

Armero, F., Ehrlich, D. 2004. An analysis of strain localization and wave propagation in plastic models of beams at failure. Comput. Meth. Appl. Mech. Eng., 193: 3129-3171.

Armero, F., Ehrlich, D. 2006a. Finite element methods for the multi-scale modeling of softening hinge lines in plates at failure. Comput. Meth. Appl. Mech. Eng., 195: 1283-1324.

Armero, F., Ehrlich, D. 2006b. Numerical modeling of softening hinges in thin Euler-Bernoulli beams. Computers and Structures, 84: 641-656.

Auricchio, F., Taylor, R.L. 1994. A generalized elastoplastic plate theory and its algorithmic implementation. International Journal for Numerical Methods in Engineering, 37: 2583-2608.

Basar, Y., Itskov, M. 1999. Constitutive model and finite element formulation for large strain elasto-plastic analysis of shells. Computational Mechanics, 23: 466-481.

Bažant, Z.P., Oh, BH. 1983. Crack band theory for fracture of concrete. Materials and Structures, 16: 155-177.

Bažant, Z.P., Belytschko, T., Chang, T.P. 1984. Continuum model for strain softening. Journal of Engineering and Mechanics 110, 12: 1666-1691.

Babuška, I., Melenk, J.M. 1997. The partition of unity method. International Journal for Numerical Methods in Engineering, 40: 727-758.

Bathe, K.J., Dvorkin, E. 1985. A four-node plate bending element based on Mindlin-Reissner plate theory and a mixed interpolation. Int J Numer Meth Engng, 21: 367-383.

Bittencourt, T.N., Wawrzynek, P.A., Ingraffea, A.R., Sousa, J.L. 1996. Quasi-automatic simulation of crack propagation for 2D LEFM problems. Engineering Fracture Mechanics, 55 :321-334.

Bohinc, U., Ibrahimbegovic, A. 2005. Robustni končni elementi za plošče. Zbornik Kuhljevi dnevi 2005, 33-40.

Bohinc, U., Ibrahimbegovic, A., Brank, B. 2009. Model adaptivity for finite element analysis of thin and thick plates based on equilibrated boundary stress resultants. Engineering Computations, 26: 69-99.

Brancherie, D., Ibrahimbegovic, A. 2008. Novel anisotropic continuum-discrete damage model capable of representing localized failure of massive structures. Part I: theoretic formulation and numerical implementation. Engineering Computations 26, 1/2: 100-27.

Brancherie, D. 2003. Modeles continus et discrets pour les problemes de localisation et de rupture fragile et/ou ductile. Doctoral Thesis, Cachan, ENS Cachan: 180 p.

Brank, B. 1994. Velike deformacije lupin pri nelinearnih materialnih modelih. Doktorska disertacija. Ljubljana, Univerza v Ljubljani, Fakulteta za gradbeništvo in geodezijo: 201 str.

Brank, B. 2005. Nonlinear shell models with seven kinematic parameters. Comput. Meth. Appl. Mech. Eng., 194: 2336-2362.

Brank, B., Ibrahimbegovic, A. 2001. On the relation between different parametrizations of finite rotations for shells. Engineering Computations, 18: 950-973.

Brank, B., Perić, D., Damjanić, F.B. 1995. On implementation of a nonlinear four node shell finite element for thin multilayered elastic shells. Comput. mech., 16: 341-359.

Brank, B., Perić, D., Damjanić, F.B. 1997. On large deformation of thin elastoplastic shells: Implementation of a finite rotation model for quadrilateral shell elements. International Journal for Numerical Methods in Engineering, 40: 689-726.

Camacho, G.T., Ortiz, M. 1996. Computational modeling of impact damage in brittle materials. International Journal of Solids and Structures, 33: 2899-2938.

Carter, B.J., Wawrzynek, P.A., Ingraffea, A.R. 2000. Automated 3-D crack growth simulation. International Journal for Numerical Methods in Engineering, 47: 229-253.

Coleman, B.D., Hodgon, M.L. 1985. On shear bands in ductile materials. Archive for Rational Mechanics and Analysis, 90: 219-247.

Crisfield, M.A., Peng, X. 1992. Efficient nonlinear shell formulations with large rotations and plasticity. In: D.R.J. Owen et al. Computational plasticity: models, software and applications, Part 1, Pineridge Press, Swansea, p. 1979-1997.

Crisfield, M.A. 1981. Finite element analysis for combined material and geometric nonlinearities. In: W. Wundelich (ed.), Nonlinear Finite Element Analysis in Structural Mecanics. Springer-Verlag, p. 325-338.

Darvall, P.L., Mendis, P.A. 1985. Elastic-plastic-softening analysis of plane frames. Journal of Structural Engineering, 111: 871-888.

de Borst, R., Sluys, L.J. 1991. Localization in a cosserat continuum under static and dynamic loading conditions. Computer Methods in Applied Mechanics and Engineering, 90: 805-827.

de Borst, R., Remmers, J.J.C., Needleman, A., Abellan, M.A., 2004. Discrete vs smeared crack models for concrete failure: bridging the gap. International Journal for Numerical and Analytical Methods in Geomechanics, 28: 583-607.

Dujc, J., Brank, B. 2006. Limit load analysis of steel plates. Gradbeni vestnik, 55: 288-299.

Dujc, J., Brank, B. 2008. On stress resultant plasticity and viscoplasticity for metal plates. Finite Elements in Analysis and Design, 44: 174-185.

Dujc, J., Brank, B., Ibrahimbegovic, A. 2009. Multi-scale computational model for failure analysis of metal frames that includes softening and local buckling, Comput. Methods Appl. Mech. Engrg. 199, 21: 1371-1385.

Dujc, J., Brank, B., Ibrahimbegovic, A., Brancherie, B. 2010. An embedded crack model for failure analysis of concrete solids, Computers and Concrete, submitted January 2010.

Dvorkin, E., Cuitiño, A., Goia, G. 1990. Finite elements with displacement interpolated embedded localization lines insensitive to mesh size and distortions. International Journal for Numerical Methods in Engineering, 30: 541-564.

Ehrlich, D., Armero, F. 2005. Finite element methods for the analysis of softening plastic hinges in beams and frames. Comput. Mech., 35: 237-264.

Eurocode 2: Design of concrete structures - Part 1-1: General rules and rules for buildings, 2004.

Eurocode 3: Design of shell structures - Part 1-6: General rules - Supplementary rules for the shell structures, 2007.

Fajfar, P., Dolšek, M., Marušič D., Stratan, A. 2006. Pre- and post-test mathematical modelling of a plan-asymmetric reinforced concrete frame building. Earthquake Engng. and Struct. Dyn., 35: 1359-1379.

Hobbit, Karlsson, Sorensen. 2007. Abaqus manuals.

Hillerborg, A., Modeer, M., Petersson, P.E. 1976. Analysis of crack formation and crack growth in concrete by means of fracture mechanics and finite elements. Cement and Concrete Research, 6: 773-782.

Ibrahimbegovic, A. 1993. Quadrilateral finite elements for analysis of thick and thin plates. Computer Methods in Applied Mechanics and Engineering, 110: 195-209.

Ibrahimbegovic, A. 2006. Mécanique non linéare des solides déformables: formulation théorique et implatantion éléments finis. Paris. Hermes Science-Lavoisier: 558 p.

Ibrahimbegovic, A. 2009. Nonlinear Solid Mechanics: Theoretical Formulations and Finite Element Solution Methods. Dordrecht. Springer: 574 p.

Ibrahimbegovic, A., Brancherie, D. 2003. Combined hardening and softening constitutive model of plasticity: precursor to shear slip line failure. Comput. Mech., 31: 88-100.

Ibrahimbegovic, A., Frey, F. 1993. An efficient implementation of stress resultant plasticity in analysis of Reissner-Mindlin plates. International Journal for Numerical Methods in Engineering, 36:303-320.

Ibrahimbegovic, A., Frey, F. 1993. Stress resultant finite element analysis of reinforced concrete plates. Engineering Computations, 10: 15-30.

Ibrahimbegović, A., Frey, F. 1994. An efficient approach to serviceability analysis and ultimate load design of reinforced concrete plates. Computational modelling of concrete structures (H. Mang, N. Bićanić,R. de Borst, uredniki), Pineridge Press, 875-884.

Ibrahimbegovic, A., Melnyk, S. 2007. Embedded discontinuity finite element method for modelling of localized failure in heterogeneous materials with structured mesh: an alternative to extended finite element method. Comput. Mech., 40: 149-155.

Ibrahimbegovic, A., Wilson, E.L. 1991. A modified method of incompatible modes. Commun. Appl. Numer. Meth., 7: 187-194.

Ibrahimbegovic, A., Frey, F., Sarf, J.L. 1992. Limit load analysis of plates with particular reference to steel and reinforced concrete. Engineering Modeling 5, 3-4: 75-82.

Ibrahimbegovic, A., Gharzeddine, F., Chorfi, L. 1998. Classical plasticity and viscoplasticity models reformulated: Theoretical basis and numerical implementation. International Journal for Numerical Methods inEngineering, 42: 1499-1535.

Ingraffea, A.R., Saouma, V. 1985. Numerical modelling of discrete crack propagation in reinforced and plain concrete. In Fracture mechanics of concrete: Structural application and numerical calculation, eds. Sih GC, Tomasso D, 171-225.

Jirasek, M., Zimmermann, T. 2001. Embedded crack model: I. Basic formulation. International journal for numerical methods in engineering, 50: 1269-1290.

Jirasek, M. 1997. Analytical and numerical solutions for frames with softening hinges. ASCE J. Eng. Mech. Din., 123: 8-14.

Jirasek, M. 2000. Comparative study on finite elements with embedded discontinuities. Comput. Methods Appl. Mech. Engrg., 188: 307-330.

Khan, A.S., Huang, S. 1995. Continuum Theory of Plasticity. New York. John Wiley: 440 p.

Kleiber, M., Kowalczyk, P. 1996. Sensitivity analysis in planestress elasto-plasticity and elasto-viscoplasticity. Computer Methods in Applied Mechanics and Engineering, 137: 395-409.

Koechlin, P., Potapov, S. 2007. Global Constitutive Model for Reinforced Concrete Plates. Journal of engineering mechanics 133, 3: 257-266.

Kojić, M., Bathe, K.J. 2005. Inelastic Analysis of Solids and Structures. Berlin. Springer: 414 p.

Korelc, J. 1997. Automatic generation of finite element code by simultaneous optimization of expressions. Theor Comput Sci, 187: 231-248.

Korelc, J. 2002. Multi-language and multi-environment generation of nonlinear finite element codes, Engineering with computers 18, 4: 312-327.

Korelc, J. 2007a. AceFem. http://www.fgg.uni-lj.si/Symech, 2007.

Korelc, J. 2007b. AceGen. http://www.fgg.uni-lj.si/Symech, 2007.

Kučerova, A., Brancherie, D., Ibrahimbegovic, A., Zeman, J., Bittnar, Z. 2009. Novel anisotropic continuum-discrete damage model capable of representing localized failure of massive structures. Part II: identification from tests under heterogeneous stress field. Engineering Computations, 26: 128-144.

Linder, C. 2007. New finite elements with embedded strong discontinuities for the modeling of failure in solids. Doctoral Thesis. Berkeley. University of California: 321 p.

Linder, C., Armero, F. 2007. Finite elements with embedded strong discontiunuities for the modeling of failure in solids. Int. J. Numer. Meth. Engng., 72: 1391-1433.

Lubliner, J. 1990. Plasticity Theory. New York. MacMillian: 495 p.

Manzoli, O.L., Shing, P.B. 2006. A general technique to embed non-uniform discontinuities into standard solid finite elements. Computers and Structures, 84: 742-757.

Marusich, T.D., Ortiz, M. 1995. Modelling and simulation of high-speed machining. International Journal for Numerical Methods in Engineering, 38: 3675-3694.

Melenk, J.M., Babuška, I. 1996. The partition of unity finite element method: basic theory and applications. Computer Methods in Applied Mechanics and Engineering, 139: 289-314.

Mosler, J., Bruhns, O.T. 2004. A 3D anisotropic elastoplastic-damage model using discontinuous displacement fields. Int. J. Numer. Meth. Engng., 60: 923-948.

Mosler, J., Meschke, G. 2003. 3D modelling of strong discontinuities in elastoplastic solids: fixed and rotating localization formulations. Int. J. Numer. Meth. Engng, 57: 1553-1576.

Mosler, J. 2005. On advanced solution strategies to overcome locking effects in strong discontinuity approaches. Int. J. Numer. Meth. Engng., 63: 1313-1341.

Moy, S.J. 1996. Plastic methods for stell and concrete structures. London. MacMillian: 271 p.

Needleman, A. 1987. A continuum model for void nucleation by inclusion debonding. Journal of Applied Mechanics, 54: 525-531.

Ngo, D., Scordelis, A.C. 1967. Finite element analysis of reinforced concrete beams. Journal of the American Concrete Institute, 64: 152-163.

Nielsen, M.P. 1984. Limit analysis and concrete plasticity. Englewood Cliffs. Prentice-Hall: 420 p.

Oliver, J. 1995. Continuum modelling of strong discontinuities in solid mechanics using damage models. Computational Mechanics, 17: 49-61.

Oliver, J. 1996. Modelling strong discontinuities in solid mechanics via strain softening constitutive equations. Parts 1: Fundamentals. International Journal for Numerical Methods in Engineering, 39: 3575-3600.

Oliver, J. 1996. Modelling strong discontinuities in solid mechanics via strain softening constitutive equations. Part 2: Numerical simulation. International Journal for Numerical Methods in Engineering, 39: 3601-3623.

Oliver, J., Simo, J.C. 1994. Modelling strong discontinuities by means of strain softening constitutive equations. In Proceedings EURO-C Computer Modelling of Concrete Structures, eds. Mang H, Bicanic N, de Borst R, 363-372.

Ortiz, M., Pandolfi, A. 1999. Finite deformation irreversible cohesive elements for three-dimensional crack-propagation analysis. International Journal for Numerical Methods in Engineering, 44: 1267-1282.

Ortiz, M., Quigley, J.J. 1991. Adaptive mesh refinement in strain localization problems. Computer Methods in Applied Mechanics and Engineering, 90: 781-804.

Ortiz, M., Leroy, Y., Needleman, A. 1987. A finite element method for localized failure analysis. Computer Methods in Applied Mechanics and Engineering, 61: 189-214.

Park, R., Gamble, W. L. 2000. Reinforced concrete slabs. Wiley.

Petersson, P.E. 1981. Crack growth and development of fracture zones in plain concrete and similar materials. Report No. TVBM-1006. Lund, Sweden, University of Lund, Division of Building Materials.

Powell, G.H. 1986. Nonlinear structural analysis by computer code INSA, UC Berkeley reports SEMM 86-15.

Press, W.H., Teukolsky, S.A., Vetterling, W.T., Flannery, B.P. 1992. Numerical Recipes in Fortran. 2nd edition, Cambridge University Press.

Radosavljević, Ž., Bajić, D. 1990. Armirani beton knjiga 3, Elementi armiranobetonskih konstrukcija. Beograd. Građevinska knjiga: 431 str.

Rashid, R. 1968. Analysis of prestressed concrete pressure vessels. Nuclear Engineering and Design 7, 4: 334-355.

Reddy, J.N. 2004. An introduction to nonlinear finite element analysis. Oxford. Oxford University Press: 463 p.

Rots, J.G., Nauta, P., Kusters, G.M.A., Blaauwendraad, J. 1985. Smreared crack approach and fracture localization in concrete. Heron 30, 1: 1-48.

Sancho, J.M., Planas, J., Cendón, D.A., Reyes, E., Gálvez, J.C. 2007. An embedded crack model for finite element analysis of concrete structure. Engineering Fracture Mechanics, 74: 75-86.

Save, M.A., Massonet, C.E. 1972. Plastic analysis and design of plates, shells and disks. Amsterdam. Nort-Holland: 478 p.

Sawczuk, A. 1989. Mechanics and Plasticity of Structures. Chichester. Ellis Horwood: 203p.

Shi, G., Voyiadjis, G.Z. 1992. A simple non-layered finite element for the elastoplastic analysis of shear flexible plates. International Journal for Numerical Methods in Engineering, 33: 85-100.

Simo, J.C., Hughes, T.J.R. 1998. Computational Inelasticity. New York. Springer: 392 p.

Simo, J.C., Kennedy, J.G. 1992. On a stress resultant geometrically exact shell model. Part V. Nonlinear plasticity: formulation and integration algorithms. Computer Methods in Applied Mechanics and Engineering, 96: 133-171.

Simo, J.C., Oliver, J. 1994. A new approach to the analysis and simulation of strong discontinuities. In Fracture and Damage in Quasibrittle Structures, eds. Bažant ZP, Bittnar Z, Jirasek M, Mazars J, 2-6: 25-39, Boundary Row, London.

Simo, J.C., Oliver, J., Armero, F. 1993. An analysis of strong discontinuities induced by strain-softening in rate independent inelastic solids. Computational Mechanics,12: 277-296.

Skallerud, B., Myklebust, L.I., Haugen, B. 2001. Nonlinear response of shell structures: effects of plasticity modelling and large rotations. Thin-Walled Structures, 39: 463-482.

Tvergaard, V. 1990. Effect of fibre debonding in a whisker-reinforced metal. Material Science and Engineering A, 125: 203-213.

Voyiadjis, G.Z., Woelke, P. 2006. General non-linear finite element analysis of thick plates and shells. International Journal of Solidsand Structures, 43: 2209-2242.

Wackerfuss, J. 2008. Efficient finite element formulation for the analysis of localized failure in beam structures. Int. J. Numer. Meth. Engng., 73: 1217-1250.

Wilson, E.L. 2002. Three dimensional static and dynamic analysis of structures. Berkley. Computers and Structures, Inc.: 423 p.

Xu, X.P., Needleman, A. 1994. Numerical simulations of fast crack growth in brittle solids. Journal of the Mechanics and Physics of Solids, 42: 1397-1434.

Zahlten, W. 1993. A contribution to the Physically and Geometrically Nonlinear Computer Analysis of General Reinforced Concrete Shells. Ruhr - Universitaet Bochrum, 212 - 215.

Zeng, Q., Combescure, A., Arnaudeau, F. 2001. An efficient plasticity algorithm for shell elements application to metal forming simulation. Computers and Structures, 79: 1525-1540.